ISSN 0974-1267 (Online)
ISSN 0972-4257 (Print)

Journal of

METALLURGY AND MATERIALS SCIENCE

Special Issue on Advanced Materials

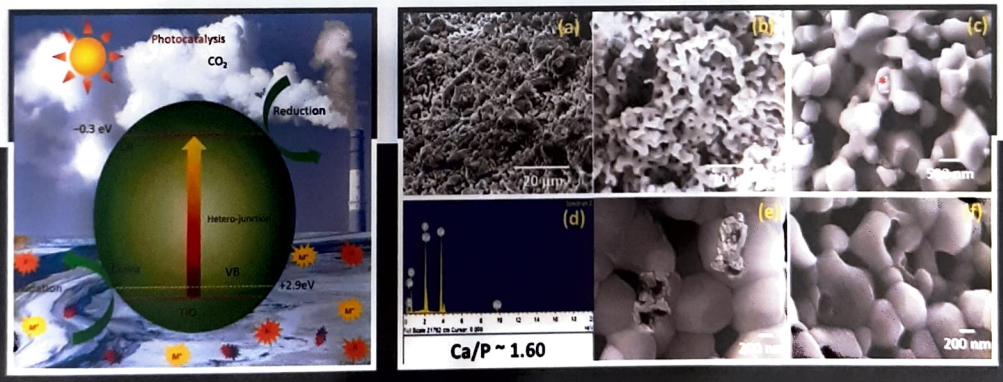

(J. Met. Mater. Sc.)

Vol. 62, No. 3-4, July-December 2020

Journal of Metallurgy and Materials Science

ISSN : 0972-4257 (Print version)

ISSN : 0974-1267 (Electronic version)

www.indianjournals.com

Scope of the Journal

Journal of Metallurgy and Materials Science (JMMS) publishes original articles, review reports and short communications in the areas of minerals, metals and materials tracing the overall life cycle of structural as well as functional materials. The journal lays special emphasis on fundamental sciences related to metallic materials and their applications.

The scope of JMMS may be enumerated as: Mineral processing; Extractive metallurgy: ferrous and non ferrous; Processing of metals; Advanced joining of metals ; Mechanical behaviour of materials; Materials failure mechanisms including Creep, Fatigue, Fracture and Corrosion; Characterization of materials; Non Destructive Techniques; Functional materials; Computational materials engineering; Metallurgical waste recycling and utilization of metallurgical and electronic wastes.

Copyright

- On acceptance of manuscript for publication, the copyright is automatically transferred to publisher by authors.
- Only unpublished work and the paper not submitted for publication elsewhere will be published. Papers presented in conference where full papers not submitted, work published in reports, reviews, or thesis may be considered.
- Consent from all co-authors is mandatory prior to submission of the manuscript. On receiving the manuscript, it is presumed that the corresponding author has taken consent from co-authors.

Plagiarism policy

- Authors are requested to submit unique manuscript free form plagiarism.
- We follow the guideline of UGC for handling plagiarism as per rule published here: https://www.ugc.ac.in/pdfnews/7771545_academic-integrity-Regulation2018.pdf
- Manuscripts within 10% similarity will be accepted for review.
- Authors will be asked to resubmit manuscript if the similarity is above 10 to 40%.
- For more than 40% similarity, the manuscript will be rejected.

Published by : Director, CSIR-National Metallurgical Laboratory, Jamshedpur-831007, India

www.nmlindia.org

Journal of Metallurgy and Materials Science, Vol. 62, No. 3-4, July-December 2020
Printed in India, © NML, ISSN 0972-4257

Editorial Note

I am extremely delighted to publish a special issue of the Journal of Metallurgy and Materials Science on "Advanced Materials" to commemorate the completion of 70 years of CSIR-National Metallurgical Laboratory (NML).

The Journal of Metallurgy and Materials Science (JMMS), is one of the oldest journals among Indian Metallurgical Journals, first published in 1959. Dr. Balraj Nijhawan, the first Indian Director of the laboratory, conceived the idea of publishing a scholarly journal in the fields of metallurgy and materials science. This Journal was earlier known as the NML Technical Journal and in 2000, it was renamed as the Journal of Metallurgy & Materials Science. JMMS aims to provide a forum for communication among metallurgists and materials scientists. All the important indexing and abstracting services of the world devoted to materials science take cognizance of this journal.

I am thankful to Dr. Arvind Sinha, Chief Scientist, CSIR-NML, for his co-ordination as the Guest Editor, in bringing out this special issue on "Advanced Materials", in which the state-of-the-art R&D knowledge by eminent researchers working in this field are documented. I acknowledge with gratitude all the authors featured in this issue, for contributing their research experiences and knowledge.

I sincerely acknowledge the contribution of the editorial advisory board members and the editorial team for their editorial services for improving the technical content and overall presentation of this journal.

Indranil Chattoraj
Editor-in-Chief

Journal of Metallurgy and Materials Science, Vol. 62, No. 3-4, July-December 2020
Printed in India, © NML, ISSN 0972-4257

Foreword

I am delighted to pen this foreword for the special issue on Advanced Materials of the Journal of Metallurgy and Materials Science (JMMS), brought out in the 70th anniversary year of CSIR- National Metallurgical Laboratory. My heartfelt thanks to all the authors of the papers published in this special issue, who accepted our invitation and submitted their manuscripts within a short duration during the unprecedented testing times of the pandemic Covid-19.

Materials are at the heart of technology based growth of contemporary society, ensuring a good quality of socio-economic life while covering the spectrum from impliments to implants. Scientific developments in the field of materials leading to the advent of Functionally Advanced Materials, vis-a-vis conventional materials, has not only been possible by diffusing the artificial boundaries among different scientific disciplines, it has also made "materials" an important tool for addressing and solving problems associated with "grand challenges", be it energy, safe drinking water, health, resource depletion or safe environment.

The present issue of the journal reports the role of advanced and functional materials in the fields of health, environment and energy, highlighting advancement made both in conventional (metals, alloys and bio-ceramics) and non-conventional advanced materials (nanomaterials, hydrogels, graphene and other 2d materials), processed conventionally as well as by non-conventional methods.

I once again express my gratitude to all the contributors for their cooperation.

(Arvind Sinha)
Chief Scientist
CSIR-National Metallurgical Laboratory
Jamshedpur 831007, India

ISSN 0974-1267 (Online)
ISSN 0972-4257 (Print)

Journal of Metallurgy and Materials Science
(Formerly NML Tech. Journal)

Vol. 62, No. 3-4, July-December 2020

Contents

		Pages
1	The role of nanomedicine in the treatment of osteosarcoma and in the prevention of infections ADA TAYMOORI and THOMAS WEBSTER	1 - 12
2	An opinion on hydroxyapatite based bio-composites as bone-scaffolds KANTESH BALANI	13 - 19
3	Synthesis of fully interconnected multiporous hydroxyapatite block for orthopedic application CHANDRANI SARKAR and ARVIND SINHA	21 - 29
4	Effect of dual crosslinking on physico-chemical properties of hydrogels prepared from chitosan and alginate SANTANU GHOSH, PRITIRANJAN MONDAL, B. RATHINA VEL and KAUSHIK CHATTERJEE	31 - 40
5	Limiting platelet adhesion in stainless steel bio-implants through microstructural modification G. PERUMAL, A. CHAKRABARTI, S. PATI, S. SINGH, V. REDDY, H.S. GREWAL, G. MANIVASAGAM and H.S.ARORA,	41 - 48
6	Technology glimpse of bioceramic implants developed by CSIR-CGCRI, Kolkata BISWANATH KUNDU, VAMSI K. BALLA and K. MURALEEDHARAN	49 - 57
7	Mg-based biodegradable alloys for orthopedic implants - A review ANSU J KAILATH and ARVIND SINHA	59 - 70
8	Tuning surface resistivity and thermal conductivity of water resistant fly ash waste based polymer composite via tailoring the interfacial polarization SANDHYA SINGH TRIPALIYA, MANOJ KUMAR GUPTA, RIYA SAHU, ASOKAN PAPPU, CHARU SHARMA, ASHISH KUMAR CHATURVEDI and AVANISH KR SRIVASTAVA	71 - 80
9	Rapidly quenched magnetic materials for functional and sensor applications ASHIS K. PANDA, RAJAT K. ROY, PREMKUMAR M, SOMNATH DAS, TARUN K. DAS and AMITAVA MITRA	81 - 88
10	Spectroscopic changes in conventional magnetorheological fluid and graphene oxide based magnetorheological fluid with combustion method KUNAL SINGH BISHT and KAVERI SAH	89 - 93

11	Electrochemical application of shape and phase dependant copper sulphide for cost-effective next generation supercapacitive energy storage: A review ARYA DAS, MAMATA MOHAPATRA and SUDDHASATWA BASU	95 - 102
12	Recent advances in photodetection applications of two dimensional MoS_2 nanostructures BISHNU PADA MAJEE and ASHISH KR MISHRA	103 - 126
13	Weakly coupled metal-semiconductor plasmonic nanoparticles in solution BHASKAR SAHA1, SALIL S. VAIDYA, KAUSTAV BHATTACHARJEE and BHAGAVATULA L. V. PRASAD	127 - 133
14	Prospective of titania based photocatalyst for environmental reduction reactions TRILOCHAN MISHRA	135 - 146
15	Some notable experiments of graphene RANJAN K SAHU	147 - 153

Journal of Metallurgy and Materials Science, Vol. 62, No. 3-4, July-December 2020, pp. 1-12
Printed in India, © NML, ISSN 0972-4257

The role of nanomedicine in the treatment of osteosarcoma and in the prevention of infections

ADA TAYMOORI[1] and THOMAS WEBSTER[2*]
[1] Northeastern University, Boston, MA 029115 USA
[2] Ph D, Professor, Art Zafiropoulo Chair in Engineering, Chemical Engineering, Northeastern University, Boston, MA 029115 USA

Abstract: Osteosarcoma is the most common bone cancer in children and the third most common cancer in adolescence. The current survival rate for osteosarcoma is 60-70% which has not improved over the past two decades. The treatment of osteosarcoma is complicated by cytotoxicity and side effects of various therapeutic drugs and osteosarcoma can also be accompanied with infection which can happen post-surgical resection or can be associated with implants causing graft rejection. The goal of utilizing nano-medicine in the treatment of osteosarcoma is to take advantage of nanocarriers for specific targeted drug delivery to cancer cells and to lower the negative impact of drugs on normal cells. Further, nanoparticles can prevent infections in patients. In this paper, we review specific nanomaterials, various micelleplexes, and their role in targeted drug delivery to osteosarcoma cells. We will also review the anti-cancer effect of nanoparticles that should replace chemotherapy in the future. This paper also reviews the role of nanoparticles in passive and active targeting of osteosarcoma cells and the role of nanocomposites in cancer treatment and infection prevention in the osteosarcoma.

Keywords: *Nanomedicine, Nanoparticles, Osteosarcoma, Nanocarriers, Micelleplexes, Active Targeting, Passive Targeting*

OSTEOSARCOMA: A DEBILITATING CANCER PREVALENT IN CHILDREN

Osteosarcoma (OS) is the most malignant bone cancer in which immature bone cells (in osteoids) are produced by tumor cells. Although OS is a rare bone tumor with a global incidence of only 3.4 cases per million people per year, it is the most common bone cancer in children and the third most common cancer in adolescence. From the 1000 new cases of osteosarcoma diagnosed each year in the United States[25], 450 occur in children. OS is the most common in the second decade of one's life. Further, the current survival rate for OS is about 65%. [8] [25] 70% of cases show chromosomal abnormalities and a few cases have cell cycle regulation defects. Mutations in tumor-suppressor genes and DNA helicases show abnormalities in OS. tumor samples.[14] What makes OS even more detrimental is that it is often a secondary cancer type where cancer from other parts of the body often metastasize to bone, making treatment and recovery even more complicated.

CURRENT OS DIAGNOSIS

For every bone lesion, the imaging protocol to determine if OS exists starts with X-ray analysis and is followed up by MRI imaging and CT scans. The X-ray protocol includes at least 2 angles and each X-ray must show two adjacent joints on two sides of the lesion. OS on an X-ray image appears as an ill-defined lesion usually in the long bones, arising from the metaphysis of bone, including osteoblastic and osteolytic areas, with a periosteal reaction and soft tissue mass[23]

MRI imaging is used to evaluate the soft tissue mass, the extension of the tumor and possibly bone marrow invasions along with neurovascular structures. CT scans can reveal cortical invasion, fracture sites and the extent of involvement and metastasis [23]. The final diagnosis of OS is through a biopsy.

* Corresponding Author : email: ada.mty.md@gmail.com

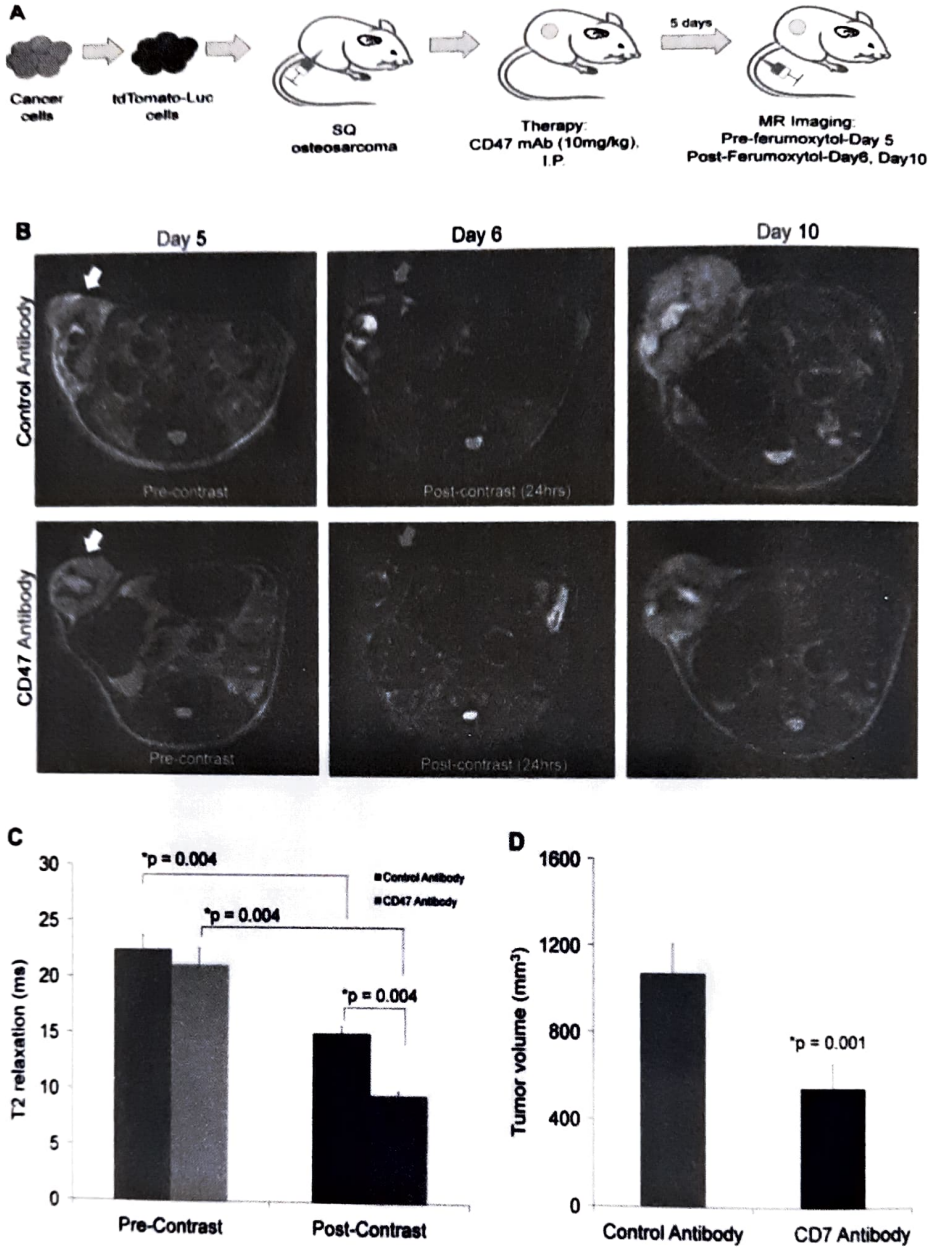

Fig 1. ***Ferumoxytol-enhanced MRI images by Mohanty et al demonstrating the promise of nanomaterials to improve osteosarcoma diagnosis, Credited to Mohanty, et.al. 2019*** [25]

Nanoparticles have provided new aspects for the usability for MRI imaging in research and visualization of the macrophage response to immunotherapy in osteosarcoma. CD47 monoclonal antibodies (mAbs) induce an immunological response by activating tumor-associated macrophages (TAMs) through which TAMs will be able to remove osteosarcoma cells through phagocytosis. These immunological responses to CD47 antibodies have to be monitored with specific diagnostic tests to prove the efficiency of CD47 mAbs. For example, Mohanty et al. used Ferumoxytol, a nanoparticle, as a contrast agent that could be phagocytosed by TAMs and be detected by MRI (Figure 1). Ferumoxytol-enhanced MRI successfully detected TAM responses to CD47 mAbs in mouse models of OS and was suggested to be used in clinical trials to monitor CD47 mAbs treatment [26, 27].

A. The study started vis for Figure 1 subcutaneous injection of human osteosarcoma tumor cells to mouse models. After the detection of tumors with bioluminescent imaging, control antibodies and anti-CD47

mAbs were given to the control and case groups, respectively. Ferumoxytol-enhanced MRI was performed on days 5, 6 and 10.

B. T2-Weighted MRI images of osteosarcoma in mice treated with the control or CD47 mAbs. The tumor is bright (hyperintense) in pre-contrast MRI images whereas after administration of ferumoxytol, the tumors seem hypo-intense enhancement (dark, red arrows).

C. Tumor MRI enhancement is measured by T2 relaxation time. The T2 relaxation time is significantly shorter in CD47-treated tumors on ferumoxytol-enhanced images, showing that the ferumoxytol enhanced MRI is more efficient in detecting the tumor response to CD47 antibodies.

D. Tumor sizes on day 10, as represented by ferumoxytol-enhanced MRI scans, were significantly lower in the group treated with CD47 mAbs compared to the control group [26].

Photo credited to Mohanty et al., 2019 [26].

CURRENT OS TREATMENT

The American Cancer Society recommends OS treatment based on its extent of growth in the body. There are several factors involved in choosing the best treatment method for OS including extent of growth, grade, location, the person's age, overall health and accompanying conditions.

The extent of OS is referred to as its 'spread' which is determined through staging the cancer. Staging is done physically through exams, imaging, lab tests and biopsies. The goal is to determine how much cancer is in the body, how far it has spread and what organs are involved.

The simplest level of staging is by categorizing OS into localized and metastatic as described below:

Localized OS. OS is considered localized if it is limited to the bone from which it started based on radiology images and biopsies, with the possibility of extension to the tissues immediately adjacent to the bone such as muscles, tendons and fat tissues. Most of the cases of OS sarcoma start as a localized cancer. However, since in every patient, there is a possibility of long distance metastases that are not visible in imaging studies and are not immediately detectable through lab tests, conventional chemotherapy is a main part of the treatment.

Surgical Treatment for Localized OS. Surgical treatment for localized OS depends on whether the cancer is resectable or non-resectable. If the entire visible tumor can be removed by surgery, it is a resectable tumor. Non-resectable tumors are the ones that cannot be completely removed by surgery.

Metastatic OS. When OS spreads to other parts of the body, the treatment and prognosis will be more challenging. The most common sites for OS metastasis are other bones, lungs and the brain. Unfortunately, 1/5 of all OS have long distance metastasis at the time of diagnosis.

STAGING AND GRADING OF OS

OS stage can be determined by a physical exam, imaging and biopsies. It is a systematic system to classify the cancer based on how far it has spread. Based on the Musculoskeletal Tumor Society (MSTS) staging system, also known as the Enneking system, 3 factors are used to determine the stage of osteosarcoma:

1 The Grade (G) of the tumor: Tumor grade is determined under the microscope. Tumor cells can be classified as low-grade and high-grade. Low-grade tumor cells are closer in appearance to normal cells and usually have a lower chance to metastasize quickly. High-grade tumor cells are more abnormal and represent a tumor that can spread fast.

2 The extent of the primary tumor (T): Classified as intracompartmental or extracompartmental. Intracompartmental tumors remain in the organ or structure where they formed, while extra compartmental tumors are the ones that extend to nearby structures.

3 Metastases (M): Meaning whether the tumor has spread or is nearby or farther away from organs. Tumors with no metastases to any nearby or farther away organs or lymph nodes, are considered M0, whereas tumors that have spread locally or over a long distance, are classified as M1.

The staging of a tumors uses Roman numerics. Stages I and II are divided into A (intracompartmental tumor) and B (extracompartmental tumors) (American Cancer Society, 2020) (Table 1).

Table 1.

Stage	Grade	Tumor	Metastasis
IA	G1	T1	M0
IB	G1	T2	M0
IIA	G2	T1	M0
IIB	G2	T2	M0
III	G1 or G2	T1 or T2	M1

Osteosarcoma Staging.

Credited to the American Cancer Society.

Chemotherapy Regimens for OS

Despite the existence of some low-grade variants, most OSs are highly malignant. There are multi-modal treatment regimens for high grade OS, and specifically, preoperative chemotherapy has improved the prognosis and achieved a long-term survival in 2/3 of the patients [3]. Prior to the introduction of chemotherapy in the 1970s, the treatment for OS was limited to surgical resection which led to a <20% cure rate in patients. The leading cause of mortality in patients who underwent surgical resection without chemotherapy was lung metastasis. After the introduction of chemotherapy, the use of a combination of surgery and chemotherapy has led the 5-year survival rate to reach 70%. This rate of survival has not improved over the past two decades and the majority of survivals are among pediatric patients. The prognosis for adults remains poor [29].

The chemotherapy regimen for high-grade OS usually has a duration of 6-12 months. Doxorubicin is a main chemotherapeutic component of this treatment regimen along with Cisplatin and high-dose Methotrexate. The major concerns with the current chemotherapy regimen (despite its achievements in improving the prognosis and increasing the survival rate from 20% before 1970s to 70% mostly in pediatric patients today[29]) is the toxicity associated with each of the mentioned drugs. Doxorubicin's use must be limited and closely monitored because of its cardiotoxicity while Cisplatin has shown some renal toxicity and high doses of Methotrexate has the potential of life-threatening toxicity but it is usually tolerated by younger patients. [3] Other complications of chemotherapy include the suppression of bone marrow cell growth, inflammation of mucosal surfaces, impaired renal function, cardiotoxicity and hypomagnesemia which can lead to arrhythmia, hearing loss, gonadal dysfunction and ultimately, infertility.[3] In approximately 1/3 of patients who have a complete positive response to treatment, a relapse can occur. For example, in a study that followed up on 37 patients with localized OS of the extremities and relapsed, unfortunately, 31 patients died (29 within 6 years of the recurrence and 2 more than 6 years from the recurrence). 6 of the 37 patients with an OS relapse lived between 6-24 years from the first recurrence and 5 of them lived disease free for this period of time and 1 with the disease. [7] Therefore, for OS, metastasis and

recurrence of a bone tumor at the site of resection are two major challenges in the treatment of OS and in the patient's prognosis.

On the other hand, the plateau of a 60%-70% rate of a 5-year survival in OS for the past 2 decades is related to chemotherapy drug resistance [21]. The relatively high chance of distant metastases and a lack of improvement in the survival rate since the 1980s, point to a strong need for new technologies for drug delivery and this need is undeniable.

Another serious concern in the treatment of OS is postoperative infection and how it can affect the survival in OS patients. In general, post-treatment complications in OS include infection, local recurrence, wound infection, pathological fractures, and prosthetic loosening. The incidence of infection in OS patients is 5.3-13% making it a major complication. These infections can have a range of severity from mild to very severe and deep infections are the cause of readmission, revision surgeries and amputations. According to the association of postoperative infection and improved survival in osteosarcoma patients, although postoperative infections in osteosarcoma patients can be associated in prolonged survival, the quality of life and outcomes remain controversial [6].

THE DEFINITION OF NANOTECHNOLOGY IN MEDICINE AND ITS ROLE IN IMPROVING THE SURVIVAL RATE AND QUALITY OF LIFE

Nanotechnology involves the application of particles in the nanoscale regime (1-100 nanometers) to create new solutions for all different scientific fields including medicine, chemistry, physics, agriculture and different areas of engineering [28].

Nanomedicine or the implication of nanotechnology in medicine is a progressive field with high potential in research and medical technology and treatment as nano-materials and nano-devices have been well studied in vitro and in vivo. Nanoparticles can be used for targeted drug delivery, especially where drug delivery is challenging such as across the blood brain barrier or across the placenta. Nanoparticles can be used as drug carriers not only to transfer drugs across more specific biological barriers but to protect healthy cells from the side effects of drugs by improving bio-distribution of drugs. Nanotechnology can also be used in the regenerative medicine and in manufacturing implants resistant to infections [2].

Nanotechnology may be that answer to what has complicated the treatment and the survival rate of OS. Nanotechnology has provided the possibility of loading high doses of drugs and other molecules into nanocarriers that are capable of targeting specific receptors on cells and even entering the cells to release its drug payload. These methods, by specific targeting and by lowering the required dose of the drugs can increase drug efficiency and reduce side effects [3].

Most importantly, the successful delivery of chemotherapy drugs and RNAi are challenges that can be addressed by utilizing micelleplexes. Micelleplexes are complexes of cationic amphiphilic blocks copolymers with a micelle-formed configuration. Genetic materials such as nucleic acids (NAs) including plasmidic DNA (pDNA), small interfering RNA (siRNA) and micro RNA (miRNA) can be loaded into micelleplexes as the nanocarrier to deliver NAs to osteosarcoma cells [3]. Micelleplexes are attracting attention as successful nano-platforms for the effective and targeted delivery of NAs and chemotherapy drugs [3], [1].

Several nanoparticles have been used to optimize the treatment of OS (Table 2), including but not limited to:

1 - Alendronate-modified polydomaine-coated paclitaxel nanoparticles:

Paclitaxel (PTX) is an approved medicine for several types of cancer, however, there is not enough evidence to prove its efficacy for the treatment of OS. Nevertheless, PTX was used by Leo and his team as a model drug

for the targeted treatment of OS cells in vitro. The efficacy of PTX is limited by its low bioavailability and high toxicity and low water solubility. However, in the above mentioned study, nanocarriers were created for PTX. These nanocarriers were made by synthesizing new nanoparticles that were coated with polydopamine (PDA) and then alendronate (ALN) was grafted to them as a ligand with an affinity for OS cells. The conjugation of PDA-NPs with ALN ligands created nanocarriers for PTX. These nanoparticles showed higher in vitro affinity and cytotoxicity for K7M2 OS cells. They also showed lower side effects and a higher therapeutic efficacy than PTX alone (82.51% vs 66.63%). The authors concluded that PTX-PDA-ALN-NPs could be a potential drug for the treatment of OS [20].

2 - Gold nanoparticles:

Gold nanoparticles (AuNPs) have shown size-dependent cytotoxicity on OS cells. The cytotoxicity and uptake of gold nanoparticles can vary based on their size. In a study focused on gold nanoparticles of 40-60 nm, increasing the concentration of the 46 nm AuNPs enhanced apoptosis in MG63 cells. This enhancement in apoptosis was achieved by the disruption of mitochondrial membrane potential. Higher cancer cell death rate was observed for the 46 and 60 nm AuNPs compared to 38 nm at 200, 400 and 800 ng/ml concentrations. Cellular apoptosis was assessed by surface enhanced Raman scattering (SERS) [4].

3 - Tangeretin-assisted platinum nanoparticles:

Doxorubicin (DOX) is a common chemotherapeutic drug for the treatment of OS. Its severe side effects though, still limits its use. The anticancer activity of a combination of platinum nanoparticles (PtNPS) and DOX on human OS epithelial cells (U_2OS) was investigated. The combination of PtNPS characterized by tangeritin and DOX significantly lowered U_2OS viability and proliferation in a dose-dependent manner. This combination also increased lactate dehydrogenase leakage, reactive oxygen species (ROS) generation, and caused mitochondrial dysfunction detectable by a reduced mitochondrial membrane potential (MMP)[12].

4 - Hydroxyapatite nanoparticles:

Hydroxyapatite nanoparticles (nano-HAPs) synthesized by Wang and colleagues, reduced the viability of OS-732 cells in mouse tumor models and decreased the migration and invasion of normal cells in vivo. The down regulation of OS-732 cells by nano-HAPs was achieved by slowing the FAK/PI3K/Akt signaling pathway (a signaling pathway activated by the platelet-derived growth factor). This study showed the efficacy of nanoHAPs in suppressing OS-732 cells in vitro and in vivo [40].

Table 2

NPs	Role	Effect	Reference
PTX-PDA-ALN-NPs	Nanocarrier for PXT	Lower side effects and higher efficacy than PTX alone (82.51% vs 66.63%).	[36]
AuNPs	Anti-cancer nanoparticles	Size-dependent cytotoxicity on OS cells.	[37]
PtNPS	Nanocarrier for DOX	Reduced U_2OS viability & mitochondrial dysfunction in MG63 cells.	[38]
nano-HAPs	Anti-cancer nanoparticles	Reduced OS-732 cells viability, migration and invasion.	[39]
ANPs	Drug delivery system for DOX	Cytotoxicity close to DOX alone with fewer side effects.	[40]

5 - Aragonite nanoparticles:

Another drug delivery system utilizing nanotechnology has used cockle shell-derived aragonite nanoparticles (ANPs) and loaded them with doxorubicin (DOX). DOX-ANPs showed a faster DOX release at a pH of 4.8 compared to pH of 7.4. Flow cytometric analysis showed cell cycle arrest in OS cells induced by DOX-ANPs. The cytotoxicity of DOX-ANPs was close to the cytotoxicity efficacy of DOX alone. The researchers concluded that DOX-ANPs could act as a pH-sensitive drug delivery system for the treatment of OS. This study was conducted in vitro [9].

Passive Targeting OS Nano Therapies

Targeted drug delivery is the process of drugs being selectively delivered to targeted cells. Passive targeting uses cellular mechanisms to uptake the drug, such as endocytosis instead of actively transferring the drug into the cells.

Passive targeting uses lipid-based nanoparticles, such as liposomes, polymeric micelles, and gold nanorods to name a few (Table 3), which will be described next.

Liposomes: Liposomes are particularly useful for the delivery of Doxorubicin. Liposomal Doxorubicin is formed when Doxorubicin is encapsulated in a liposome. In this vesicular structure, Doxorubicin is inside a lipid hydrophobic shell that is coated with PEG for stability. These liposomes can be ingested easily by OS cells and overall, improve drug delivery, and elimination of OS cells [1].

Table 3

Nanocarrier	Composition	Findings
ZnO Nanoparticles	Zinc oxide nanoparticles	Induce autophagy and apoptosis in OS cells [15].
PLGA Nanoparticles	Polylactic co-glycolic acid + PEGylated Polylactic co-glycolic acid	Controlled release profile and enhanced cell cycle inhibition activities [39].
Dextran-based Nanoparticles	Lipid modified dextran	Delivery of siRNA to OS cells [43].
Lipid-coated Polymeric Nanoparticles	Lipid-coated polymers	By delivery of microRNA, they inhibit the growth and proliferation of OS cells [43].
Hydroxyapatite Nanoparticles	Hydroxyapatite coating, polyvinyl alcohol conjugated methotrexate	Supporting proliferation to normal bone cells and inducing apoptosis in OS cells [43].

Passive Targeting Strategies in OS treatment

Polymeric Micelles: Polymeric micelles are colloidal suspensions that can be used both in cancer diagnosis and treatment. Micelles are used as nano sized cylindrical, spherical, or ellipsoid structures composed of hydrophobic and hydrophilic components. Recently, hybrid nanomicelles have been formed by integration with metal nanoparticles such a gold, iron-oxide, and silver. Gold nanoparticles in the size range of 40-60 nm have shown noticeable cytotoxicity on OS cells at 200,400, and 800 ng/ml concentrations [4]. According to recent studies, the interaction between immune cells (macrophages) and iron oxide nanoparticles can lead to anti-tumor immune responses. This effect is in addition to the efficacy of iron oxide nanoparticles in treating anemia in patients suffering from different types of cancer, including OS [35]. 5 nm and 35 nm citrate-coated silver nanoparticles (AgNPs) can induce death in OS cells (U_2OS and Saos-2 Cells) regardless of their p53 status. Therefore, AgNPs are attractive novel candidates for chemotherapeutic treatments of OS [19]. Polymeric micelles can deliver water insoluble or poorly water soluble drugs, lengthen their stability, and enhance their potency (therapeutic efficiency) through site-specificity and increased anti-cancer drug penetration [13].

Gold Nanorods: Polyacrylic acid-coated gold nanorods have been used in photo thermal therapy to treat OS. In a study by Pan et. al., it was demonstrated that polyacrylic acid (PAA) - coated gold nanorods (GNRs) when stimulated with a 808 nm laser, increased the efficiency of hyperthermia therapy for MG63 human osteosarcoma cells. It was shown that GNRs-PAA can increase the efficiency of photo thermal therapy by damaging cell membranes causing DNA integration that leads to apoptosis in OS cells. This experiment was conducted in vitro by planting MG63 cells into 96-well plates with H-DMEM medium and the effect was proven to be dose-dependent [31].

Active Targeting

Multiple nanoparticles have been used for active targeting to OS cells. The mechanism of active targeting is bonding molecules (such as ligands and antibodies) to the surface of nano-carriers, some of the same ones mentioned above for passive targeting. Therefore, they enhance cellular uptake of drugs by targeting compatible cell receptors and cell membrane channels. These mechanisms take advantage of the over-expression of receptors on the surface of cancer cells. These receptors include folate receptors that are over-expressed in OS xenograft samples, $\alpha v\beta 3$ and $\alpha v\beta 5$ integrins, type-A receptor 2 (EphA2), a surface molecule over expressed in OS cells, CD133, epidermal growth factor receptor (EGFR) and CD44 [41].

Ligand-targeted drug delivery nano systems currently rely mostly on folic acid receptors and transferring receptors [18]. Although folate α receptors are over-expressed on the surface of OS cells, there are also folate uptake mechanisms inside OS cells that can increase cellular resistance to chemotherapy. In order to overcome multi-drug resistance in cancer cells, the co-delivery of drugs and nucleic acids (NA) is considered a method to increase the intracellular concentration of chemotherapy drugs and/or activating apoptotic pathways. Micelleplexes are nanostructures used to achieve this goal showing much promise and will be described next.

Micelleplexes

Multifunctional nanostructures that deliver genetic material and chemotherapy to OS cells are promising [32]. Micelleplexes are nanocarriers formed from polymer-based nanosystems. Since RNA interference (RNAi) technology has started a new approach in treating cancer through the use of nucleotide interfering molecules to inhibit different phases of cancer, micelleplexes are valuable in cancer treatment and specifically in OS as a nanocarrier for nucleic acids and for chemotherapy delivery [32]. This method is fairly new. In a study in 2018, researchers decided to use a nanosystem to deliver genetic material to repress the expression of mutated genes in the regulatory pathway of OS. An efficient micellar nanosystem was developed by conjugating the amphiphilic copolymer Pluronic® L64 and the cationic polymer polyethileneimine (PEI). This combination was used to deliver miRNA-145 into the OS cells which resulted into the arrest of proliferation and migration and ultimately induced apoptosis in OS cells [22].

Polymers

Polymers, such as Methotrexate conjugated with poly glycerol adipate, can self-assemble into nanoparticles. The size of the nanoparticles depend on the dose of the conjugates, MTX and the pH of the medium. The MTX-PGA conjugates containing high molar MTX content (27.5 mole) showed a higher toxicity for Saos-2 cells compared to free MTX. These nano particles were physically stable at a pH of 5-9 and chemically stable at a pH of 7.4 against hydrolysis for 30 days. However, they can be degraded by enzymes to release MTX [37].

Suppressive Treatment

Suppressive therapy in cancer is a course or multiple courses of treatment to prevent the growth of any remaining cancer cells [10]. Magnetic gene carriers made of polyethylenimine, dextran and iron oxide nanoparticles (PDIs) have been used for the in vitro and in vivo transfection of miR-302b [8]. miR-302b belongs to a group of short non-coding RNAs or microRNAs (miRNAs). MiRNAs have a rssss der-expressed in OS cell lines while it is expressed more predominantly, in healthy osteoblasts cell lines. miR-302b can in fact, limit the proliferation of OS cells and induce apoptosis in these cells [42]. PDIs have shown mild toxicity in mice. By the use of a magnetic field, PDI/pmiR302b entering the OS cells of mice showed effective anti-cancer effects with low toxicity [11].

Curcumin-loaded Self-assembled Arginine-rich-RGD Nanospheres

Curcumin shows anticancer affects through different mechanisms. However, its low water solubility is a challenge for using curcumin in vivo.

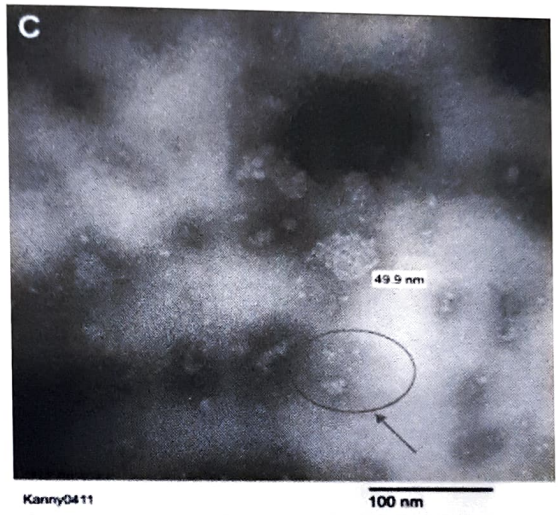

Fig. 2: ***Aggregates of amphiphilic nanoparticles without sonication. Photo credited to Chang et al., 2015[5].***

Therefore, an amphiphilic peptide C18GR7RGDS was recently used as a carrier for curcumin in water-based solutions. The combination of amphiphilic nanoparticles and curcumin APNP/curcumin showed significant toxicity against MG-63 OS cells compared to control cells (normal osteoblasts) (Fig. 2) [5].

Selenium Nanocomposites

The recurrence of OS at the site of tumor resection is a major challenge for a patient's survival and quality of life. An in vitro study, using selenium nanoparticles (SeNP), lowered the recurrence of OS cells and enhanced the function of healthy osteoblasts. SeNPs for this study were formed on poly-L lactic acid (PLLA). Selenium coated PLLA showed increased osteoblast activity (increased ALP) compared to osteoblasts on control tissue culture plates without the use of any chemotherapy or other medicine. These results suggest that selenium coated PLLA should be further examined as a potential graft material to replace cancerous bone tissue [36].

Magnetic ZnF_2O_4-hydroxyapatite nanocomposite particles

Infections are a well-known complication of OS, post-surgical resection and they are also associated with bone implants and are a major reason for amputation and graft rejection. Multifunctional ZnF_2O_4-hydroxyapatite nanocomposite particles were formed through the co-precipitation method. At the concentration of 0.078mg/L, ZnF_2O_4HAp had the highest inhibitory effect on bacterial proliferation and growth on gram positive bacteria.

These nanoparticles could penetrate bacterial cells through endocytosis. Iron-oxide nanoparticles can penetrate bacterial cells due to the fact that their size is smaller than the membrane pores. These nanoparticles can then inhibit the DNA and protein synthesis inside the bacterial cells. Additionally, when zoledronic acid (ZA) was loaded into ZnF_2O_4HAp as nanocarriers, for primary ZA concentrations of 0.01, 0.02, and 0.04 mg/L, the drug-loaded nanocomposite particles showed an early burst release through the first 20h followed by a slow drug release until 170h. Based on these experiments, ZnF_2O_4HAp are multifunctional nanocomposite particles that can inhibit bacterial growth at the site of osteosarcoma and can also be used as localized anticancer drug delivery systems [34].

Conclusion and Future Directions

To increase life expectancy and the quality of life in patients with OS, more specific and targeted therapeutic methods are required. In this article, we reviewed current passive and active targeting OS therapies through nanoparticles. Although there are several benefits to using nanoparticles for drug delivery and increasing the potency and bioavailability of chemotherapeutic medicines for OS, there are concerns about the potential side effects that mandate further and deeper in vitro and in vivo studies. Of note, Micelleplexes have showed significant capabilities in drug and NA delivery into OS cells, however, there are serious concerns about their cytotoxicity [30].

Hydroxyapatite nanoparticles on the other hand, can be a major breakthrough in the treatment of OS through the dual role they play in enhancing healthy bone cells while killing OS cells. They increase the proliferation in normal bone cells while inducing apoptosis in OS cells. These nanoparticles should be the focus of improved OS treatment in future nano medicine studies; although, several more studies are required to assure the absence of cytotoxicity.

From among the active targeting therapies, selenium nanoparticles have shown an effect very similar to HANPs. They also increase the proliferation in healthy osteoblasts and have an inhibitory effect on OS cells.

The use of nanocomposties can revolutionize cancer treatment in osteosarcoma since these particles can have a dual effect of anticancer treatment and infection inhibition. Considering that infection is a major factor that impacts the quality of life and also causes complications in the treatment of OS, nano medicine with the use of nanoparticles, nanocarriers and nanocomposites has the potential to revolutionize the treatment of OS in the future.

References

[1] Aulton M.E, Taylor K. Aulton's Pharmaceutics: The Design and Manufacture of Medicines Ch 45: Pharmaceutical nanotechnology and nanomedicines 4th ed., 2013 Elsevier, Churchill Livingstone.

[2] Boiseau P, Loubaton B. Nanomedicine, nanotechnology in medicine. 12: 620-636, 2011.

[3] Carrle D, Bielack SS. Current strategies of chemotherapy in osteosarcoma. Int Orthop. Dec, 30(6):445-51, 2006.

[4] Chakrabortty A, Das A, Raha S, Barui A. Size-dependent apoptotic activity of gold nanoparticles on osteosarcoma cells correlated with SERS signal. Journal of Photochemistry and Photobiology B: Biology. Jan. 203: 111778, 2020.

[5] Chang R, Sun L, Webster TJ. Selective inhibition of MG-63 osteosarcoma cell proliferation induced by curcumin-loaded self-assembled arginine-rich-RGD nanospheres. Int J Nanomedicine. May 5;10:3351-65, 2015.

[6] Chen YU, Xu SF, Xu M, Yu XC. Postoperative infection and survival in osteosarcoma patients: Reconsideration of immunotherapy for osteosarcoma. Mol Clin Oncol. May, 3(3) : 495-500 2015.

[7] Crompton BD, Goldsby RE, Weinberg VK, Feren R, O'Donnell RJ, Ablin AR. Survival after recurrence of osteosarcoma: a 20-year experience at a single institution. Pediatr Blood Cancer. Sep, 47(3): 255-9 2006.

[8] Diseases and Conditions. Osteosarcoma. The American Academy of Orthopedic Surgeons. Retrieved from: https://orthoinfo.aaos.org/en/diseases--conditions/osteosarcoma/.

[9] Fu W, Noor MHM, Yusof LM, Ibrahim TAT, Keong YS, Jaji AZ, Zakaria MZ. In vitro evaluation of a novel pH sensitive drug delivery system based cockle shell-derived aragonite nanoparticles against osteosarcoma. Journal of Experimental Nanoscience. Jan. Vol 12, 2017. https://www.tandfonline.com/doi/full/10.1080/17458080.2017.1287965.

[10] Gavrila A. Thyroid Hormone Treatment, Suppressive therapy with levothyroxine does not impair cognitive function. Clinical Thyroidology For The Public. 7: 6-7, 2020.

[11] Gong M, Liu H, Sun N, Xie Y, Yan F, Cai L. Polyethylenimine-dextran-coated magnetic nanoparticles loaded with miR-302b suppress osteosarcoma in vitro and in vivo. Nanomedicine. Mar. 15(7): 2020.

[12] Gurunathan S, Jeyaraj M, Kang MH, Kim JH. Tangeretin-Assisted Platinum Nanoparticles Enhance the Apoptotic Properties of Doxorubicin: Combination Therapy for Osteosarcoma Treatment. Nanomaterials. 9(8): 1089, 2019.doi.org/10.3390/nano9081089.

[13] Hanafy, N.A.N.; El-Kemary, M.; Leporatti, S. Micelles Structure Development as a Strategy to Improve Smart Cancer Therapy. Cancers 10: 238, 2018.

[14] Hayden JB, Hoang BH Osteosarcoma: basic science and clinical implications. Orthop Clin North Am. Jan; 37(1):1-7,2006.

[15] He G, Ma Y, Zhu Y, Yong L, Liu X, Wang P, Liang C, Yang C, Zhao Z, Hai B, Pan X, Liu Z, Liu X, Mao C. Cross Talk Between Autophagy and Apoptosis Contributes to ZnO Nanoparticle Induced Human Osteosarcoma Cell Death. Wiley Online Library. 2018 Jun. https://onlinelibrary.wiley.com/doi/abs/10.1002/adhm.201800332.

[16] Huang W, Chen L, Kang L, Jin M, Sun P, Xin X, Gao Z, Bae YH. Nanomedicine-based combination anticancer therapy between nucleic acids and small-molecular drugs. Adv Drug Deliv Rev. Jun 1;115: 82-97, 2017.

[17] Ifergan I, Meller I, Issakov J, Assaraf YG. Reduced folate carrier protein expression in osteosarcoma: implications for the prediction of tumor chemosensitivity. Cancer. Nov 1; 98(9):1958-66, 2003.

[18] Kolhatkar, R. A, Khambati L.H. 2011. Active tumor targeting of nanomaterials using folic acid, transferrin and integrin receptors. Curr. Drug Discov. Technol., 8(3): 197-206, 2011.

[19] Kovács D, Igaz N, Keskeny C, Bélteky P, Tóth T, Gáspár R, Madarász D, Rázga Z, Kónya Z, Boros IM, Kiricsi M. Silver nanoparticles defeat p53-positive and p53-negative osteosarcoma cells by triggering mitochondrial stress and apoptosis. Sci Rep. Jun 13; 6: 27902, 2016

[20] Lei Z, Mengying Z, Yifei G, Xiangtao W, Meihua H. Alendronate-modified polydopamine-coated paclitaxel nanoparticles for osteosarcoma-targeted therapy. Journal of Drug Delivery Science and Technology. Oct. 53: 101133, 2019.

[21] Liu, Q., Xu, B., Zhou, W."Correlation between chemotherapy resistance in osteosarcoma patients and PAK5 and Ezrin gene expression". Oncology Letters 15.1: 879-884, 2018.

[22] Magalhães M, Almeida M, Tavares-da-Silva E, Roleira FMF, Varela C, Jorge J, Gonçalves AC, Carvalho RA, Veiga F, Santos AC, Figueiras A. miR-145-loaded micelleplexes as a novel therapeutic strategy to inhibit proliferation and migration of osteosarcoma cells. Eur J Pharm Sci. Oct 15; 123:28-42, 2018.

[23] Majó J, Cubedo R, Pardo N Treatment of osteosarcoma. A review. Rev Esp Cir Ortop Traumatol, 54: 329–336, 2010.

[24] Messerschmitt PJ, Garcia RM, Abdul-Karim FW, Greenfield EM, Getty PJ J Am Acad Orthop Surg. Aug; 17(8):515-27, 2009.

[25] Misaghi A, Goldin A, Awad M, Kulidjian AA. Osteosarcoma: a comprehensive review. SICOT J. 4:12, 2018. doi: 10.1051/sicotj/2017028. Epub 2018 Apr 9. PMID: 29629690; PMCID: PMC5890448.

[26] Mohanty, S., Yerneni, K., Theruvath, J.L. et al. Nanoparticle enhanced MRI can monitor macrophage response to CD47 mAb immunotherapy in osteosarcoma. Nature Cell Death Dis 10: 36, 2019.

[27] Mohanty S, Yerneni K, Theruvath JL, Graef CM, Nejadnik H, Lenkov O, Pisani L, Rosenberg J, Mitra S, Cordero AS, Cheshier S, Daldrup-Link HE. Nanoparticle enhanced MRI can monitor macrophage response to CD47 mAb immunotherapy in osteosarcoma. Cell Death Dis. Jan 15:10(2):36, 2019.

[28] Nano.gov. What is nanotechnology 2020. https://www.nano.gov/nanotech-101/what/definition.

[29] O'Kane GM, Cadoo KA, Walsh EM, Emerson R, Dervan P, O'Keane C, Hurson B, O'Toole G, Dudeney S, Kavanagh E, Eustace S, Carney DN. Perioperative chemotherapy in the treatment of osteosarcoma: a 26-year single institution review. Clin Sarcoma Res. Jul 14; 5:17, 2015.

[30] Oskuee RK, Dabbaghi M, Gholami L, Taheri-Bojd S, Balali-Mood M, Mousavi SH, Nikkei BM. Investigating the influence of polyplex size on toxicity properties of polyethylenimine mediated gene delivery. Life Sciences. Mar. 97: 101-108, 2018.

[31] Pan S, Xing H, Fu X, Yu H, Yang Z, Yang Y, Sun W. The Effect of Photothermal Therapy on Osteosarcoma With Polyacrylic Acid–Coated Gold Nanorods. Dose-Response. 2018. Aug. https://doi.org/10.1177/1559325818789841.

[32] Pereira-Silva M, Alvarez-Lorenzo C, Cocheiro A, Santos A.C, Veiga F, Figueiras A. Nanomedicine in osteosarcoma therapy; Miscelleplexes for delivery of nucleic acids and drugs toward osteosarcoma-targeted therapies. European Journal of Pharmaceutics and Biopharmaceutics. 148: 88-106, 2020.

[33] Qing, F., Wang, Z., Hong, Y. et al. Selective effects of hydroxyapatite nanoparticles on osteosarcoma cells and osteoblasts. J Mater Sci: Mater Med. 23: 2245–2251, 2012.

[34] Seyfoori A, Ebrahimi S, Omidian S, Naguib SM. Multifunctional magnetic $ZnFe_2O_4$-hydroxyapatite nanocomposite particles for local anti-cancer drug delivery and bacterial infection inhibition: An in vitro study. Journal of the Taiwan Institute of Chemical Engineers. Mar. 96: 503-508, 2019.

[35] Soetaert F, Korangath P, Senates D, Fiering S, Ivkov R. Cancer therapy with iron oxide nanoparticles: Agents of thermal and immune therapies. Advanced Drug Delivery Reviews. 2020 Jun. doi.org/10.1016/j.addr.2020.06.025.

[36] Stolzoff M, Webster T. Reducing bone cancer cell functions using selenium nanocomposites. Journal of Biomedical Materials Research. 2015 Oct. https://doi.org/10.1002/jbm.a.35583.

[37] Suksiriworapong J, Taresco V, Ivanov DP, Styliari ID, Sakchaisri K, Junyaprasert VB, Garnett MC. Synthesis and properties of a biodegradable polymer-drug conjugate: Methotrexate-poly(glycerol adipate). Colloids Surf B Biointerfaces. Jul 1; 167:115-125, 2018 .

[38] The American Cancer Society Medical and Editorial Content Team. Osteosarcoma stages. 2020. Retrieved from https://www.cancer.org/cancer/osteosarcoma/detection-diagnosis-staging/staging.html.

[39] Wang, B., Yu, X., Xu, S. et al. Paclitaxel and etoposide co-loaded polymeric nanoparticles for the effective combination therapy against human osteosarcoma. J Nanobiotechnol 13: 22, 2015. .

[40] Wang R, Liu W, Wang Q, Li G, Wan B, Sun Y, Niu X, Chen D, Tian W. Anti-osteosarcoma effect of hydroxyapatite nanoparticles both in vitro and in vivo by downregulating the FAK/PI3K/Akt signaling pathway. Biomaterials Science. 16, 2020.

[41] Wang SY, Hu HZ, Qing XC, Zhang ZC, Shao ZW. Recent advances of drug delivery nanocarriers in osteosarcoma treatment. J Cancer. Jan. 11(1):69-82, 2020.

[42] Xie, Y., Sun, W., Deng, Z. et al. MiR-302b Suppresses Osteosarcoma Cell Migration and Invasion by Targeting Runx2. Sci Rep 7:13388,2017.

[43] Zhang L, Lyer AK, Yang X, Kobayashi E, Guo Y, Mankin H, Hornicek FJ, Amiji MM, Duan Z. Polymeric nanoparticle-based delivery of microRNA-199a-3p inhibits proliferation and growth of osteosarcoma cells. Int J Nanomedicine. Apr 15;10:2913-24, 2015.

Journal of Metallurgy and Materials Science, Vol. 62, No. 3-4, July-December 2020, pp. 13-19
Printed in India. © NML, ISSN 0972-4257

An opinion on hydroxyapatite based bio-composites as bone-scaffolds

KANTESH BALANI*
Professor, Department of Materials Science and Engineering, Indian Institute of Technology Kanpur, Kanpur-208016, Uttar Pradesh, India

Abstract: Hydroxyapatite (HA, $Ca_{10}(PO_4)_6(OH)_2$) is regarded as one among most bioactive materials for bone and hard-tissue replacement due to its chemical and structural similarity as that of apatite with Ca/P ratio of 1.67. But, the use of HA is limited due to its poor fracture toughness to the order of 0.5-1.5 MPa.$m^{1/2}$. Therefore, usually, some additives, such as Al_2O_3, YSZ, ZnO, Fe_3O_4, TiO_2, Ti, Ag, carbon nanotubes (CNTs), Ti, etc have been incorporated. It is observed that the metallic reinforcement is a better toughening agent than the ceramic reinforcement, but the release of metal ions may also hamper the key metabolic pathways of human cell. Further, β-tricalcium phosphate (β-TCP) and bioglass addition can be used for attaining controlled resorption of material under in vivo conditions so the natural bone can replace the artificial scaffold during healing process. Many additives, such as Ag, ZnO, CuO, TiO_2, etc have been incorporated to provide antibacterial efficacy to the scaffolds. The aspect of antioxidant activity obtained from aliovalent ceramics (such as CeO_2) may also assist in expedited healing. The design of porosity at multi-length scales can also be envisaged as means of incorporating cell-material interaction at bulk scale (~150-250 μm size, for vascularisation), at micrometer length scale (~10s of μm for cellular alignment) and at molecular length scale (~ few nm for surface protein interaction with implant substrate). Hence, the onus is on interdisciplinary biomedical engineers to aspire and design multifunctional bone-scaffolds with required mechanical integrity, antibacterial efficacy, bioactive response, biosorption for accommodating natural healing, and inducting expedited restoration.

Keywords: *Hydroxyapatite; Bone-scaffold; Toughness; Porosity; Protein Adhesion.*

INTRODUCTION

Healthcare advancements manage the ageing population and assists in retaining the social activity via offering total-hip joint arthroplasty (THA). For year 2015, with more than 12 lakhs THA annual surgeries [1], 4.7 lakh THA surgeries are performed in India [1]. And surgeries are on rise, and THA in the United States is ~ 1.2 lakhs in year 2015 [2], and, it is expected that around 10 lakhs may need such replacements in the year 2020. The success of hip implant is mainly governed by completing 15-20 years of successful service without any failures and with proper osseointegration (i.e. bone growth in the adjoining area of the femoral stem of hip implant). As the bioactivity is expressed in terms of osteogenesis (bone-formation), osteoconduction (bone-growth), to result bone healing (or osteoinduction) and osseointegration (integrating artificial implant with natural bone). Thus, from material selection to result bone formation requires a bioactive material like hyhydroxyapatite (HA, $Ca_{10}(PO_4)_6(OH)_2$)/ β-Tricalcium phosphate (TCP) or bioglass (BG). Bioglass is typically calcium-sodium-phosphosilicates, and their use is limited by their very low fracture toughness and rapid dissolution in aqueous medium (and loss of structural integrity before natural bone formation). It is important to mention that the crystallinity and material resorption are very important aspects to decide on the applications. For example, high crystallinity of HA may prompt its application in load-bearing application and where the bone-remodelling may be minimal in elderly persons, whereas BG and β-TCP may be very attractive for porous-scaffolds and where material-resorption will be replaced by new bone cells, especially in younger patients. Nonetheless, these concepts have evolved for engineer to appropriately choose the composition and design the composites into complex shapes as porous/ 3-D printed scaffolds. Towards achieving osteoconduction, the introduction of macro-porosity assists in letting formation of fibrous tissues and accommodating vascularisation. The osseointegration highly depends on the surface of the implanted surface, and the assimilated surface bioactivity and continuous porosity allows formation of a unified interface between an implant and natural bone. The biodegrading species like bioglass, amorphous

* Corresponding Author Email : kbalani@iitk.ac.in

calcium phosphate or Mg-based alloys may also be utilised for replacing the implant material with natural bone in due course of time. It may also be mentioned that the healing process depends a lot on the metabolism and age of individual as the healing can be very rapid in young patients (and use of biodegradable materials becomes feasible), whereas the delayed or restricted healing process in elderly persons may mandate the use of bio-inert materials and the implant material may have to be completely bio-inert in making up for the lost functionality.

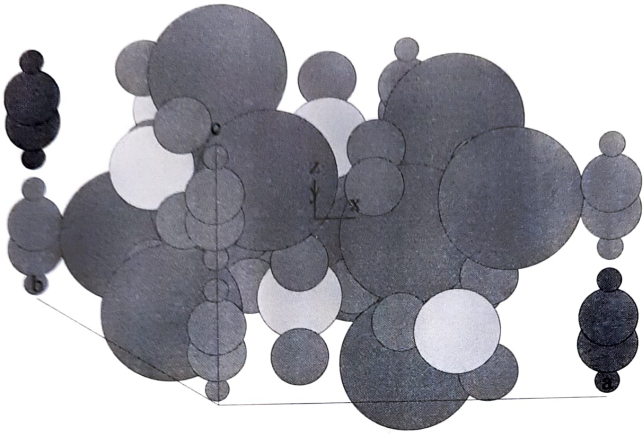

Fig. 1: ***Schematic of hydroxyapatite crystal showing Ca atoms (pink), oxygen atoms (green), phosphorous (yellow) and hydrogen (orange).***

For the same, hydroxyapatite Fig. 1 is deposited (usually via plasma spraying) for achieving surface bioactivity on the surface of femoral stem and assisting bone-integration after THA. Otherwise, a bone-cement (called polymethyl meth acrylate, PMMA) is utilized as glue to attach the femoral stem with the surrounding bone. But, due to lack of bone-material interaction, this bone cement loosens with time and mandates a revision surgery, which is highly painful and costlier. Currently, plasma sprayed hydroxyapatite[3] is the only industrially scalable coating on femoral stem that is approved by Food and Drug Administration (FDA). Thus, bioactive nature of HA allows enhanced osseointegration due to its chemical similarity with that of apatite found in bone and teeth (Ca/P ratio of 1.67)[4].

TOUGHENING EFFECTS

Brittleness of HA is one of the major concerns (fracture toughness to the tune of ~ 0.5-1 $MPa.m^{1/2}$,[5] , thus, many researchers have proposed multi-pronged approaches of utilizing various reinforcements (e.g. bioinert Al_2O_3[6],Yttria stabilized zirconia (YSZ)[7], or bioactive carbon nanotubes (CNTs)[5] in order to enhance its fracture toughness. Ceramics are known to be brittle, nonetheless a limited toughening enhancement in ceramics can be obtained by grain size refinement, incorporating micro-porosity (to blunt/terminate the propagating cracks), crack branching, incorporating pinning agents, adding phase-transformation toughening agents, and inducing crack-bridging phenomena. CNTs have elicited crack deflection, crack-branching, CNT-pull-out and crack-bridging mechanisms to sustain enhanced damage tolerance[8]. It may be noted that Ag and other metallic reinforcements have shown to be a superior additive in achieving enhanced toughening even when compared to that of CNT[9, 10]. Herein, with CNT reinforcement, the fracture toughness is ~ 1 $MPa.m^{1/2}$, which increased to above 2.5 $MPa.m^{1/2}$ upon addition of Ag[9]. As the surface requires bioactivity, whereas the bulk requires structural toughness, a mere layering of these two composites will not work. Thus, an attempt of achieving surface bioactivity with HA-dominated surface and YSZ-bulk was interfaced with Al_2O_3-YSZ based cushioning layer as a functionally graded structure in sufficing both the requirements[11].

ANTIMICROBIAL EFFECTS

In order to extend the functionality of the bone-scaffold, it is preferred to add antibacterial agents to avoid post-surgical infections. Though the post-surgical infections are usually to the tune of 5%, but the pain and trauma to the patient can be twice as that of first surgery and the cost of revision surgery can be as high as up to 2-3 times. Thus, antibacterial agents such as Ag, Cu, Co, TiO_2, ZnO, Fe_3O_4, etc have been incorporated. On one hand, like for Ag, its ions permeate through bacterial membrane and denature DNA, whereas agents like ZnO or CuO can assist the release of reactive oxygen species (ROS) and rupture the bacterial wall. These killing mechanism of bacteria also extend to the use of AMPs (anti-microbial peptides) inducting opsonisation (of formation of localised porous regions in bacteria) and hamper their key pathways and eventually kill the bacteria. Further, an enhanced functionality with incorporation of ferromagnetic (Fe_2O_3/Fe_3O_4)[12] or antibacterial ZnO [13,14, 15], Cu, Ag etc.[16] have been incorporated in HA matrix. Utilisation of processing in controlling the incorporation of Cu in HA matrix [17] or site specific anti-bacterial efficacy of Zn [18] or Co [19] in HA matrix or even the effects of co-doping of Zn and Co in HA matrix [20] well elucidate and establish Co as superior antibacterial agent (than Zn), and also enunciate a stronger release of Co when doped at Ca site compared to that at OH site of HA.

EFFECT OF POROSITY

Though there have been various reports on controlling porosity on isolated micro-, nano-length-scale, or its combination [21], or even at bulk length scale [22] the induction of porosity, whether at a micro-meter length scale or nanometer, length scale does allow an enhanced number of binding sites to encourage cell-proliferation. Nonetheless, a synergistic approach to consolidate these to enunciate amino acid interaction at molecular length scale, attain directional cell-growth in micro-textured surface and allow osseointegration at bulk length scale needs attention. Our research group has earlier elicited the control of bi-modal porosity via adopting different processing technique and utilization of porogen (pore forming agent) during processing of HA-based composites [23]. The bi-modal nature of porosity (i.e. sub-micrometer and micrometer sized pores) allows interaction of amino acids with enhanced interaction points, and an enhanced cellular growth is observed for the same [24].

It may also be noted that the macro porosity to the tune of 40-70% is mandated to permit vascularisation. In addition, the porosity size must be big enough (~ 100-250 μm). Further, micro-porosity similar to the size of human cell (~10s of μm) is required to permit directional growth of the cell. Also, it is observed by researchers that presence of nano-porosity (~nm size) permits an enhanced interaction of surface proteins with the cell surface at atomistic level. The protein interaction is originated at atomic length scale and allows sensing of 'surface-compatibility' of artificial implant material with the cells. Hence and amalgamation of nano-porosity (for molecular protein interaction), micro-porosity (for cell-directionality), and macro-porosity (for vascularisation) is needed for the bone-scaffolds.

ROLE OF ANTIOXIDANTS

Antioxidants, which are also present in fruits, assist in the expedited healing. Antioxidants take up the ROS and minimize the damage to the cell-walls. The aliovalent oxidation state of various cations allows trapping the ROS and restricting the damage it may cause to the living cells. During healing, the immune response triggers the release of ROS to clear out the debris and restrict infections. Without distinguishing between the anti-bacterial or site-cleaning process, ROS also becomes deleterious for human cells in the vicinity. The antioxidants assist in restricting ROS damage by combining with it and making it bearable for human cell. Just the larger size and membrane enclosed organelles in human cell permit sustenance while the anti-infection process is carried out by ROS. In summary, the M^{n+} oxidation state changes to $M^{(n+1)}$ when combining with ROS, which then restricts the damage to the protective cell lipid bilayer. Typically, cerium oxide has been used as an antioxidant and has shown

to enhance the cell-proliferation process. Enhanced cellular affinity and growth in HA-CeO_2-Ag-CNT based samples [25], confirmed via absorbance is attributed to enhanced anti-oxidant capability (due to incorporation of CeO_2) that is elicited in scaled-up plasma sprayed coatings. Further, the balance of mechanical, biological and anti-bacterial properties must be sought to ensure enhanced service life of the femoral stems during THA [25].

ROLE OF EXTERNAL FIELDS

Both, magnetic [26,27,28] and electric fields [29,30] have been utilised to control the cell-fate processes. It is interesting to note that the ion-exchange and cell-permeation is controlled by the surface charges, which can be manipulated by the external fields. In addition, it is not only the magnitude, but also the pulsing (or frequency) that requires synchronised response from the cell to control the ion-permeation response. On one hand, where ferro-magnetic additives in HA can provide antibacterial efficacy supplemented with magnetic fields [26], on the other hand the ferro-magnetic responsive nature of cells [27,28] can be utilised in assisting osteogenesis with ferro-magnetic reinforcements. Similarly, the gene expression and cell-fate can also be tailored using complementing electric fields [29-33] or along with substrate conductivity [34-35] for obtaining enhanced cell-proliferation and directing the ensuing cellular-response forwards tissue engineering.

WETTING, PROTEIN ADSORPTION AND ADHESION OF BACTERIA/CELLS

A good scaffold material is also dictated by the wettability of the material as the subsequent protein adsorption is followed by cell-attachment and consequent cell growth. As an implant is inserted, protein attachment occurs almost immediately. Then, the nature of protein adhesion [36] on that substrate dictates what portion of that protein is available to attach (as ligand) with integrins (surface protein receptors of cells). Though cellular attachment is to be promoted, the 'friendliness' of the substrate may also allow adhesins (bacterial surface proteins) to initiate infection. Nonetheless, integrins allow attachment of cells by binding to ligands (e.g. fibronectin, collagen, laminin in bone cells) on an implanted surface. In order to observe role of these surface proteins, gene-expression may be undertaken to utilise these markers in linking it to bone growth. It may be noted that both, hydrophilic and hydrophobic surfaces may promote protein attachment. Earlier, cellular attachment and bacterial attachment events on substrates have been quantified by various researchers [36, 37]. Porosity has shown to encourage fibrous cell-ingrowth for additional mechanical interlocking, but it is the substrate chemistry that dominates in dictating if the protein is configured to allow a surface towards promoting cell-attachment and growth (i.e. Al_2O_3 bio-inert ceramic may not promote cell-growth, but bioactive HA promotes chemical binding with cells). As the attachment and adhesion events of cells can be qualitatively compared from centrifugation, or spinning disc or plate and wash assays, etc., whereas qualitative adhesion strength can be evaluated from optical tweezers, nano-scratching or atomic force microscopy, etc. Nonetheless, visualisation of the protein adhesion (or de-adhesion event of bacterial protein) requires molecular dynamics simulations.

The computational modelling is not only demanding, but also highly complex. First, the protein may have numerous stable confirmations in 3-D space, so selecting an appropriate profile may require multiple and repeated simulations. Second, only a portion of the protein (Fig. 2) may participate in the adhesion process, but with molecular weight of protein running in 100s of kilo-Daltons becomes highly computationally demanding to accommodate so many atoms. Moreover, the aqueous environment also changes the protein confirmation and requires appropriate stabilisation with the pH and salts. Then, an enough simulation space needs to be created to ensure that the protein is always under a water environment, and its stretching will always be accommodated in the simulation volume (and without affecting its mirror atom if it appears in the periodic boundary conditions). Nonetheless, visualization of these events may allow integration of the number of events (with multiple protein chains) with the magnitude of de-adhesion force can help comment on the strength of protein binding with various bio-surfaces.

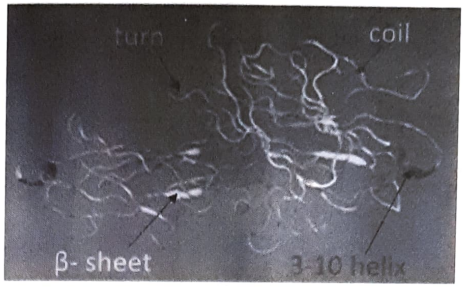

Fig. 2: A schematic showing portion of highly complex bacterial surface protein structure. It comprises of various helices and β-sheet structures and can undertake numerous 3-D conformations. (Courtesy: Mr. Arindam Raj, Yale University).

With advancements in the manufacturing technology, 3-D printing has emerged as a leading processing tool for constructing porous bone-scaffolds [38]. These constructs may be applied to cranial segments, skull, manibular portions, etc. The porosity design allows promoting enhanced capillarity/wetting along with enhanced surface area for biological/bioactive fixation. In addition, scaffold structures may be loaded with multifunctional additives during the 3-D printing process [39]. Further, the multi-functional scaffolds may restrict cancerous cell growth and provide therapeutic effects [39] and extend new opportunities in taking the bone-scaffolds as superior replacement to natural bone.

SUMMARY AND CONCLUSIONS

In summary, the approach of creating multifunction hydroxyapatite (HA) based scaffolds, Fig. 3, require appropriate combination of surface bioactivity, structural integrity, and porosity at multiple length scales. Further, antibacterial aspects may be incorporated with various additives such as Ag, ZnO, TiO_2, Fe_3O_4, or even anti-microbial peptides. The size and morphology of these additives may be highly important in promoting antibacterial effects. The healing events can be expedited with the addition of antioxidants (such as CeO_2) in order to curb the damage by reactive oxygen species. Damage tolerance of the HA-based composites may be promoted with addition of carbon nanotubes (CNTs), though metallic additives (such as Ag and Ti) may be more probable toughening agents. The presence of porosity at different length scales is mandated from promoting amino acid adhesion at molecular length scale to promoting vascularisation at macro-length scale. Functional gradation may also be envisaged to account for surface activity clubbed with bulk toughness of the HA-based bioactive composites. Visualisation of the protein attachment and bacterial de-adhesion events call for computational modelling approach, which can then be linked with its adhesion strength on various bio-substrates. Accounting for wettability aspects and protein adhesion, the cell-attachment must eventually ensure a successful osseointegration.

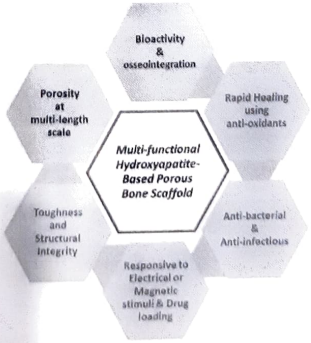

Fig. 3: The requirements of a multi-functional porous hydroxyapatite-based bone-scaffold.

ACKNOWLEDGMENTS

Author acknowledges funding from Swarnajayanti fellowship, DST, Govt. of India (project no. DST/SJF/ETA-02-2016-17). Author thanks Prof. Bikramjit Basu (IISc Bangalore), Prof. Arvind Agarwal (FIU, USA), Prof. Indranil Manna (IIT Kharagpur), Dr. H.S. Maiti, Prof. Sourabh Ghosh (IIT Delhi), Prof. Abhijit Mukherjee (Curtin University), and Prof. Navdeep Dhami (Curtin University) for collaborative efforts. Author also thanks Dr. Sushma Kalmodia, Dr. Mohammad Atif Faiz Afzal, Dr. Fahad Alam, Dr. Aditi Pandey, Dr. Satish Kanhed, Mr. Arjak Bhattacharjee, Ms. Shivani Gour, Mr. Arindam Raj, and Mr. Niraj Dhandia for their inputs.

REFERENCES

[1] Statistics by Country for Hip Replacement. Available from: https://www.rightdiagnosis.com/h/hip_replacement/stats-country.htm.

[2] G. Shaw, Hip and Knee Replacements on the Rise, Available from: https://www.webmd.com/arthritis/features/hip-knee-replacements-rise#1.

[3] R.B. Heimann, Plasma-Sprayed Hydroxylapatite-Based Coatings: Chemical, Mechanical, Microstructural, and Biomedical Properties, Journal of Thermal Spray Technology 25(5): 827-850, 2016.

[4] A.M. Ballo, W. Xia, A. Palmquist, C. Lindahl, L. Emanuelsson, J. Lausmma, H. Engqvist, P. Thomsen, Bone tissue reactions to biomimetic ion-substituted apatite surfaces on titanium implants, J Royal Soc Interface 9(72): 1615-24, 2012.

[5] K. Balani, R. Anderson, T. Laha, M. Andara, J. Tercero, E. Crumpler, A. Agarwal, Plasma-sprayed carbon nanotube reinforced hydroxyapatite coatings and their interaction with human osteoblasts in vitro, Biomaterials 28(4): 618-624, 2007.

[6] Y.M. Kong, S. Kim, H. Kim, Reinforcement of hydroxyapatite bioceramic by addition of ZrO_2 coated with Al_2O_3, Journal of American Ceramic Society 82(11):2963-2968, 1999 .

[7] Y.W. Gu, K. A. Khor, D. Pan, P. Cheang, Activity of plasma sprayed yttria stabilized zirconia reinforced hydroxyapatite/Ti–6Al–4V composite coatings in simulated body fluid, Biomaterials 25(16): 3177-3185, 2004.

[8] Z. Xia, L. Riester, W.A. Curtin, H. Li, B. W. Sheldon, J. Liang, B. Chang, J.M. Xu, Direct observation of toughening mechanisms in carbon nanotube ceramic matrix composites, Acta Materialia 52(4): 931-944,2004.

[9] K. Herkendell, V.R. Shukla, A.K. Patel, K. Balani, Domination of volumetric toughening by silver nanoparticles over interfacial strengthening of carbon nanotubes in bactericidal hydroxyapatite biocomposite, Materials Science and Engineering C, 34: 455-467 2014.

[10] A. Kumar, T.J. Webster, K. Biswas, B. Basu, Flow cytometry analysis of human fetal osteoblast fate processes on spark plasma sintered hydroxyapatite–titanium biocomposites, Journal of Biomedical Materials Research A 101A(10): 2925-2938, 2013

[11] M.A.F. Afzal, P. Kesarwani, K.M. Reddy, S. Kalmodia, B. Basu, K. Balani, Functionally graded hydroxyapatite-alumina-zirconia biocomposite: synergy of toughness and biocompatibility, Materials Science and Engineering C, 3(5): 1164-1173, 2012.

[12] I. Bajpai, K. Balani, B. Basu, Spark Plasma Sintered HA-Fe_3O_4Based Multifunctional Magnetic Biocomposites, Journal of the American Ceramic Society, 9(7): 2100-2108, 2013.

[13] M. Roeinfard, A. Bahari, "Nanostructural Characterization of the Fe_3O_4/ZnO Magnetic Nanocomposite as an Application in Medicine, Journal of Superconductivity and Novel Magnetism, 30(12): 3541-3548, 2017.

[14] G. Bajpai, T. Srivastava, N. Patra, I. Moirangthem, S.N. Jha, D. Bhattacharyya, S. Riyajuddin, K. Ghosh, D.R. Basaula, M. Khan, S. Liu, S. Biring, S. Sen, Effect of ionic size compensation by Ag+ incorporation in homogeneous Fe-substituted ZnO: studies on structural, mechanical, optical, and magnetic properties, The Royal Society of Chemistry, 8(43): 24355-24369, 2018.

[15] N. Saha, A.K. Dubey, and B. Basu, Cellular proliferation, cellular viability, and biocompatibility of HA-ZnO composites, J. Biomed Mater Res B: Applied Biomater, 100(1): 256-264, 2012.

[16] H. Jing, Z. Yu, L. Li, Antibacterial properties and corrosion resistance of Cu and Ag/Cu porous materials, Journal of Biomedical Materials Research Part A,87(1), :33-37 2008 .

[17] A. Bhattacharjee, Y. Fang, T.J.N. Hooper, N.L. Kelly, D. Gupta, K. Balani, I. Manna, T. Baikie, P.T. Bishop, T.J. White, J. V. Hanna, Crystal Chemistry and Antibacterial Properties of Cuperiferous Hydroxyapatite, Materials,12(11): 1814 (17pp) 2019.

[18] A. Bhattacharjee, A. Gupta, M. Verma, M. Prem Anand, P. Sengupta, M. Saravanan, I. Manna, K. Balani, Site-Specific Antibacterial Efficacy and Cyto/Hemocompatibility of Zinc Substituted Hydroxyapatite, Ceramics International, 45(9): 12225-12233, 2019.

[19] A. Bhattacharjee, A. Gupta, M. Verma, M. Prem Anand, P. Sengupta, M. Saravanan, I. Manna, and K. Balani, Antibacterial and Magnetic Response of Site-Specific Cobalt Incorporated Hydroxyapatite, Ceramics International 46(1) : 513-522, 2020.

[20] A. Bhattacharjee, R. Hassan, A. Gupta, M. Verma, M. Prem Anand, P. Sengupta, M. Saravanan, I. Manna, K. Balani, Effect of Zn and Co Doping on Antibacterial Efficacy and Cytocompatibility of Spark Plasma Sintered Hydroxyapatite, Journal of American Ceramic Society 103: 4090–4100, 2020.

[21] M.J. López-Bosque, E. Tejeda-Montes, M. Cazorla, J. Linacero, Y. Atienza, K.H. Smith, A. Lladó, J. Colombelli, E. Engel, A. Mata, Fabrication of hierarchical micro-nanotopographies for cell attachment studies, Nanotechnology 24: 255305 (12pp), 2013.

[22] Molteno Ophthalmic (https://www.molteno.com/m-sphere-natural-hydroxy-apatite- orbital-implants).

[23] S. Kalmodia, S. Goenka, T. Laha, D. Lahiri, B. Basu, K. Balani, Microstructure, mechanical properties, and in vitro biocompatibility of spark plasma sintered hydroxyapatite–aluminum oxide–carbon nanotube composite, Materials Science and Engineering C, 30(8): 1162-1169, 2010.

[24] S. Kanhed, S. Awasthi, S. Goel, A. Pandey, R. Sharma, A. Upadhyaya, K. Balani, Porosity distribution affecting mechanical and biological behaviour of hydroxyapatite bioceramic composites, Ceramics International 43(13): 10442-10449, 2017.

[25] A. Pandey, S. Midha, R.K. Sharma, R. Maurya, V.K. Nigam, S. Ghosh, K. Balani, Antioxidant and antibacterial hydroxyapatite-based biocomposite for orthopedic applications, Materials Science and Engineering C 88: 13-24, 2018.

[26] I. Bajpai, N. Saha, B. Basu, Moderate intensity static magnetic field has bactericidal effect on E. coli and S. epidermidis on sintered hydroxyapatite, Journal of Biomedical Materials Research Part B: Applied Biomaterials 100(5): 1206-1217, 2012.

[27] S.K. Boda, G. Thrivikraman, B. Basu, Magnetic field assisted stem cell differentiation–role of substrate magnetization in osteogenesis, Journal of Materials Chemistry B 3(16): 3150-3168, 2015.

[28] I. Bajpai, K. Balani, B. Base, Synergistic effect of static magnetic field and HA-Fe_3O_4 magnetic composites on viability of S. aureus and E. coli bacteria, J. Biomed. Mater. Res. Part B 102(3): 524–532, 2014.

[29]. A.K. Dubey, S.D. Gupta, B. Basu, Optimization of electrical stimulation parameters for enhanced cell proliferation on biomaterial surfaces, Journal of Biomedical Materials Research Part B: Applied Biomaterials 98(1): 18-29, 2011.

[30] G. Thrivikraman, S.K. Boda, B. Basu, Unraveling the mechanistic effects of electric field stimulation towards directing stem cell fate and function: A tissue engineering perspective, Biomaterials 150: 60-86, 2018.

[31] A. K. Dubey, B. Basu, "Pulsed electrical stimulation and surface charge induced cell growth on multistage spark plasma sintered hydroxyapatite-barium titanate piezobiocomposite, J. Am. Cer. Soc. 97(2): 481-489, 2014.

[32] A.K. Dubey, P.K. Mallik, S. Kundu, B. Basu, Dielectric and electrical conductivity properties of multi-stage spark plasma sintered HA-$CaTiO_3$ composites and comparison with conventionally sintered materials, J. Eur. Cer. Soc. 33: 3445–3453, 2013.

[33] S.K. Boda, I. Bajpai, B. Basu, Inhibitory effect of direct electric field and HA-ZnO composites on S. aureus biofilm formation, J. Biomed. Mat. Res.: B, 104B : 1064–1075 2016.

[34] K. Ravikumar, B. Sunilkumar and B. Basu, Synergy of substrate conductivity and intermittent electrical stimulation towards osteogenic differentiation of human mesenchymal stem cells, Bioelectrochemistry 116: 52–64, 2017 .

[35] G. Thrivikraman, P.K. Mallik, B. Basu, Substrate conductivity dependent modulation of cell proliferation and differentiation in vitro, Biomaterials 34:7073-7085, 2013.

[36] F. Alam, Kantesh Balani, Adhesion Force of Staphylococcus aureus on Various Biomaterial Surfaces, Journal of the Mechanical Behavior of Biomedical Materials 65:872-880, 2017.

[37] D. Lahiri, A.P. Benaduce, L. Kos, A. Agarwal, Quantification of carbon nanotube induced adhesion of osteoblast on hydroxyapatite using nano-scratch technique, Nanotechnology 22(35): 355703 (9pp), 2011.

[38] S. Bose, S. Vahabzadeh, A. Bandyopadhyay, Bone tissue engineering using 3D Printing, Materials Today 16(12): 496-503, 2013.

[39] N. Sarkar, S. Bose, Liposome-Encapsulated Curcumin-Loaded 3D Printed Scaffold for Bone Tissue Engineering, ACS Appl. Mater. Interfaces 11: 17184−17192, 2019.

Journal of Metallurgy and Materials Science, Vol. 62, No. 3-4, July-December 2020, pp. 21-29
Printed in India, © NML, ISSN 0972-4257

Synthesis of fully interconnected multiporous hydroxyapatite block for orthopedic application

CHANDRANI SARKAR[1,2] and ARVIND SINHA[1*]
[1]Advanced Materials and Processes Division, CSIR-National Metallurgical Laboratory, Jamshedpur-831007, Jharkhand, India
[2]Department of Chemistry, Mahila College, Kolhan University, Chaibasa- 833201, Jharkhand, India

Abstract : In the present work, three dimensional multiporous hydroxyapatite block has been synthesized by a novel process which comprises of two steps. At first, three dimensional polymer-hydroxyapatite nanocomposite was synthesized by mimicking matrix mediated in situ biomineralization process. Second is sintering step where synthesized polymer-hydroxyapatite composite was sintered at 1200°C under atmospheric pressure. After sintering, a structurally stable fully interconnected multiporous hydroxyapatite block was obtained. Detailed structural and chemical characterization revealed the role of polymer matrix in the formation of three dimensional multiporous hydroxyapatite block. Cytocompatibility of sintered hydroxyapatite block was evaluated by MTT assay and cell adhesion test. Results evidenced the non-toxic nature of sintered hydroxyapatite block.

Keywords*: Hydroxyapatite; Three dimensional; Biomimetic; Block; Sintering*

INTRODUCTION

Hydroxyapatite [HA, $Ca_{10}(PO_4)_6(OH)_2$], a calcium phosphate ceramic is extensively researched in water treatment plant, fertilizers and pharmaceuticals industries. Since decades, it has received tremendous attention in biomedical field because the chemical composition is very similar to the inorganic component of bone. Moreover, it has excellent biological properties such as highly biocompatible and bioactive. On material point of view, HA is stiff, brittle and fragile in nature [1, 2]. So, it is very difficult to contour as three dimensional (3D) structure. Hence, its clinical applications are limited as powder material especially for cavity filler and coating material of alloy or metallic implants [3, 4].

To be used as bone grafts or bone implants, HA must be in stable 3D shaped with porous structure. Porous structure is required for cell motility and survivability, tissue infiltration and vascularization [5, 6]. Many attempts have been made by researchers to develop 3D porous HA blocks. Most of these developed processes are gel casting, foaming, replication and sacrificial templating [4, 6-8]. Mbarki et. al. have demonstrated gelatin as a pore forming agent and synthesized 3D porous HA block [9]. The common limitations in above mentioned methods are formation of isolated pores, lack of interconnectivity in pores and non-uniform dispersion of pores/ HA [6-8]. Chen et. al. fabricated 3D HA scaffold with hierarchical porosity by extrusion deposition with porogen foaming technique. In this technique, they had used various chemicals particularly for dispersing HA particles [10].

On the other side, our group synthesized interconnected macroporous HA granules by biomimetic mineralization process coupled with sintering [11]. This is a powerful approach which is basically based on in situ nucleation and growth of HA particles in polymeric matrix that leads uniform distribution of HA particles in the matrix resulted in the generation of complex hierarchical macroporous granular structure after sintering [11]. In recent years, researchers try to develop synthetic strategies that mimic this process. The aim of present work is also to develop an interconnected multiporous HA block by adapting this process. In this work, we have selected carboxymethyl cellulose (a cellulose derivative) and polyethylene glycol (a polyether) as organic matrix. Both the polymers are hydrophilic and nontoxic in nature. They are approved by the U.S. Food and Drug Administration (FDA) for use in different pharmaceutical formulations [12-13]. These features contribute to their broad application in biomedical research particularly in drug delivery and tissue engineering field. Researchers also demonstrated that

* Corresponding Author E-mail: arvind@nmlindia.org

polyethylene glycol (PEG) efficiently crosslinked with cellulose and formed a homogenous stable structure [14, 15]. In our study, we aimed to use this homogenous stable CMC-PEG blend as hybrid polymeric matrix for in-situ mineralization of HA. By this simple polymer matrix mediated biomimetic route, three dimensional polymer-HA nanocomposite has been synthesized. Finally, interconnected multiporous HA block was obtained by removal of polymers after sintering. The detailed structural and chemical characterizations along with the mechanical performance of the synthesized block have been studied. Results showed that a fully interconnected multiporous HA block has been successfully synthesized by this process.

EXPERIMENTAL DETAILS

Materials

Polyethylene glycol (PEG), carboxymethyl cellulose [CMC, DS (degree of substitution) ~ 0.9], calcium salt (calcium nitrate tetrahydrate), phosphate salt (diammonium hydrogen phosphate) and ammonia (30%) were procured from Merck, India.

Synthesis of three dimensional hydroxyapatite block (s-HA)

In this work, mutiporous hydroxyapatite block (s-HA) has been simply synthesized by sintering 3D polymer-hydroxyapatite composite (p-HA) at 1200°C under atmospheric pressure. At first, 3D polymer-hydroxyapatite composite was synthesized by biomineralization process [16, 17]. Details of synthetic procedure are as follows- 600 mL CMC (1 wt%) and 300 mL PEG (1 wt%) aqueous solutions were prepared in different vessels. After that, PEG solution was slowly added to CMC solution with constant stirring for 15 min, and a homogenous CMC-PEG blend was formed. Later, 400 mL calcium nitrate solution (0.99 M) was gently added to polymers blend and stirred for 15 min. The pH of the mixture was maintained at 10 with ammonia solution and kept ageing for 24 h at 30 ±2°C. Next day, 200 mL phosphate solution (0.56 M) was prepared and gradually added to the calcium containing polymer solution. The final mixture was allowed to age for a week at a temperature of 30±2°C. After a week the white slurry was washed with deionized (DI) water and dried in an oven at 60°C for 72 h. At the final step, dried polymer-HA blocks were sintered at 1200°C for 2 h (rate ~4°C min^{-1}) in a tubular furnace under atmospheric pressure, and finally 3D multiporous HA block was obtained.

Characterization

X-ray diffraction [XRD Bruker, D8 Discover, Cu Kα radiation with λ=0.154 nm, 40 kV, 40 mA] was used to characterize the crystallographic phases present in the synthesized samples. Fourier transform infrared (FTIR) spectra of CMC, PEG, p-HA and s-HA were recorded in the range of 4000-400 cm^{-1} at a resolution of 4 cm^{-1} using JASCO-FTIR, Model 410. JEOL 2100 transmission electron microscope (TEM) at 200 kV was used for microstructural evaluation. Nova nano scanning electron microscope (SEM) equipped with the analyzer of energy dispersive spectroscopy (EDS) was used for morphological characterization and element investigation. Dissolution study was carried out in simulated body fluid (SBF), the ionic concentrations of SBF is (Na+ 142.0 mM, K^+ 5.0 mM, Mg^{2+} 1.5 mM, Ca^{2+} 2.5 mM, Cl- 147.8 mM, HCO_2^{3-} 4.2 mM, HPO_4^{2-} 1.0 mM and SO_4^{2-} 0.5 mM) nearly equal to those of human blood plasma [4, 17]. Sintered HA blocks were immersed in 30 mL SBF (pH 7.40) for different time periods (7 days and 14 days). After that, samples were withdrawn, rinsed with DI water and dried for characterization. The Mercury Porosimeter, Pascal 140/440 was used to measure the porosity and pore size distribution of the sintered HA block. Density is measured by Sartorius balance and the data is used for the computation in mercury porosimetry. The compressive mechanical properties of the sintered HA blocks were tested using Universal Mechanical Testing Machine [Hounsfield H10KS-0290] at 0.2 mm min^{-1} crosshead speed. The dimensions of the blocks were 20 mm × 10 mm × 10 mm.

Cell culture

In-vitro cell study of sintered HA was carried out in Shree Chitra Tirunal Institute for Medical Sciences and Technology, Thiruvananthapuram, Kerela, India. Bone marrow mesenchymal stem cells (BMSCs) at third passage were used for in-vitro experiments.

MTT assay and cell adhesion study

3-[4,5-dimethylthiazol-2-yl]-2,5-diphenyltetrazolium bromide (MTT) assay was performed with extract method as per ISO-10993-5 [16, 17]. The extract of sintered blocks [2 mm × 2 mm × 0.2 mm] was prepared by incubating in 1 mL culture medium [α-MEM containing FBS and antibiotic] at 37°C for 24 h. In the meantime, BMSCs (5×10^3 cells per well) were seeded in 96-well plates and maintained at 37°C under humidified atmosphere containing 5% CO_2 for 24 h. After that, 200 µL of the sample extract was added to the cell-seeded wells and incubated for 24 h and 48 h. At the day of test, 50 µL MTT solution (1 mg mL^{-1}) was added into each well and left it for 2 h at 37°C. After 2 h, MTT solution was discarded and isopropanol (100 µL) was added to each well for dissolving the formazan crystals. The developed color was quantified by measuring absorbance at 570 nm using a micro plate reader (Power Wave-XS micro plate spectrophotometer BioTek -Reader).

For In-vitro cell adhesion test, the test materials (0.5 cm × 0.5 cm × 0.5 cm) were conditioned in culture medium. BMSCs were seeded on pre-conditioned materials at a density of 5×10^3 and incubated for 48 h at 37°C under humidified atmosphere containing 5 % CO_2. After 48 h of incubation, cells with test materials were stained with working FDA solution (10 µg mL^{-1}) and examined under fluorescent microscope (Leica DMI6000B).

STATISTICAL ANALYSIS

Experiments were performed three times and data represented as mean standard deviation. Data were statistically processed using one way analysis of variance (ANOVA); $p \leq 0.05$ was considered statistically significant.

RESULTS AND DISCUSSION

The present study demonstrated a simple biomimetic process coupled with sintering for the synthesis of tailor-made 3D HA block for orthopedic application. It is based on in situ biomineralization of HA particles in CMC-PEG polymeric matrix, and then its conversion to fully interconnected multiporous HA block after sintering at 1200°C. Scheme of synthetic procedure is given in Fig.1. At 1200°C the polymers decomposed out but left their impression, as a result sintered HA with interconnected multiporous three dimensional structure was obtained.

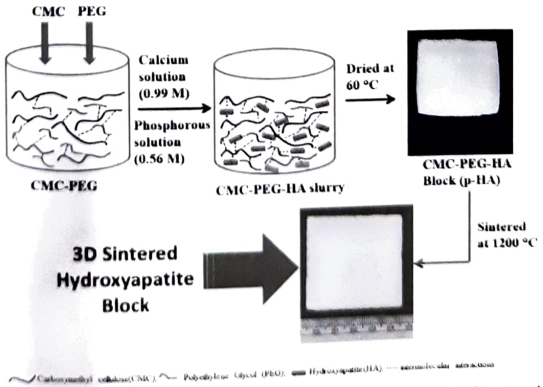

Fig.1. Scheme of synthetic procedure of fully interconnected multiporous hydroxyapatite block.

X-ray Diffraction

XRD patterns of CMC-PEG-HA (p-HA) and sintered HA (s-HA) are shown in Fig. 2. The diffraction peaks in the XRD spectrum of p-HA are assigned as (002), (102), (211), (202), (310), (222), (004), (213) and (511) planes of hydroxyapatite as per the JCPDS card number: 09-432 [4, 11]. All the above mentioned diffraction peaks of hydroxyapatite are also found in s-HA pattern, however, few extra peaks are observed at $2\theta^0 \sim 28.9^0$, 32.2^0, 32.9^0, 34.1^0, 35.5^0 correspond to (120), (112), (300), (202) and (301) planes of HA. It is clearly seen that the peaks became sharped and distinctly separate from each other after sintering at 1200°C, indicating the formation of well-developed HA crystals in s-HA [18, 19, 20]. Besides these, very small peaks are observed at $2\theta^0 \sim 25.4^0$, 31.5^0 indexed as (1010), (0210) planes of β- TCP [20-22].

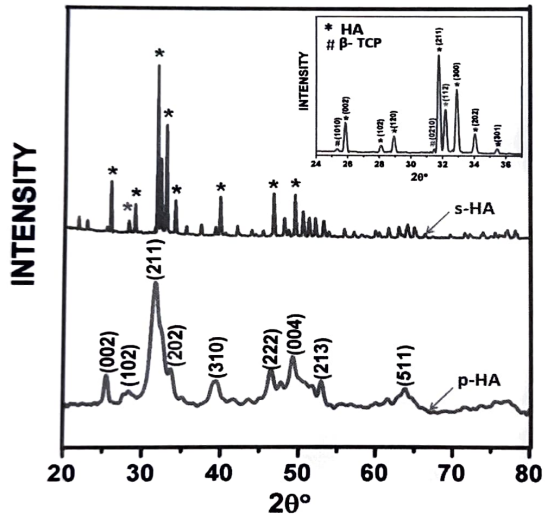

Fig.2. XRD patterns of synthesized samples.

FTIR spectroscopy

FTIR spectra of PEG, CMC, CMC-PEG-HA [p-HA] and sintered HA [s-HA] are presented in Fig. 3. In Fig. 3a and 3b, the broad band of –OH vibration was found at 3440 cm^{-1} in the spectrum of both PEG and CMC [15, 16]. In addition, two bands at 2880 cm^{-1} and 1352 cm^{-1} were observed in the FTIR spectrum of PEG (Fig. 3a) assigned to –C-H stretching and CH_2 wagging, respectively. Moreover, the bands associated with C-C, C-O, C-O-C and C-H vibrations of PEG (Fig. 3a) were detected at 1287 cm^{-1}, 1250 cm^{-1}, 1108 cm^{-1} and 951 cm^{-1} [14, 15, 19]. In Fig. 3b, the major vibrational bands related to carboxylate (COO−) stretching of CMC were observed at 1598 cm^{-1} (asymmetric) and 1417 cm^{-1} (symmetric). The –C-OH band and β-1,4 glycoside bands of CMC were detected at 1062 cm^{-1} and 599 cm^{-1}, respectively [14, 15]. In the spectrum of CMC-PEG-HA (p-HA) [Fig. 3c], the -O-H vibration gave an overlapped broad band at 3155 cm^{-1}, which was slightly shifted from the position of hydroxyl band of CMC and PEG [Fig. 3a,b]. Similarly, asymmetric and symmetric stretching bands of COO^- group of CMC were also shifted to 1633 cm^{-1} and 1398 cm^{-1}, respectively. These shifting in vibrational bands implied the existence of intermolecular interactions among the three different constituents (CMC, PEG and HA) in CMC-PEG-HA composite [14-16, 18, 19]. The vibrational bands of phosphate (PO_4^{3-}) groups were occurred at 1035 cm^{-1} (stretching), 954 cm^{-1} (stretching), 604 cm^{-1} (bending) and 566 cm^{-1} (bending), confirming the formation of in-situ HA in CMC-PEG matrix [16, 18-19]. In addition, a small band appeared at 829 cm^{-1} corresponds to HPO_4

group[23]. In the FTIR spectrum of sintered HA [Fig. 3d], it was observed that the stretching vibration of -OH group shifted to higher wavenumber at 3570 cm^{-1}, and phosphate (PO_4^{3-}) bands were occurred at 1088 cm^{-1}, 1053 cm^{-1}, 602 cm^{-1}, 571 cm^{-1} and 474 cm^{-1}. However, no characteristic vibrational bands of CMC and PEG were found, indicating the complete decomposition of polymers during sintering[9].

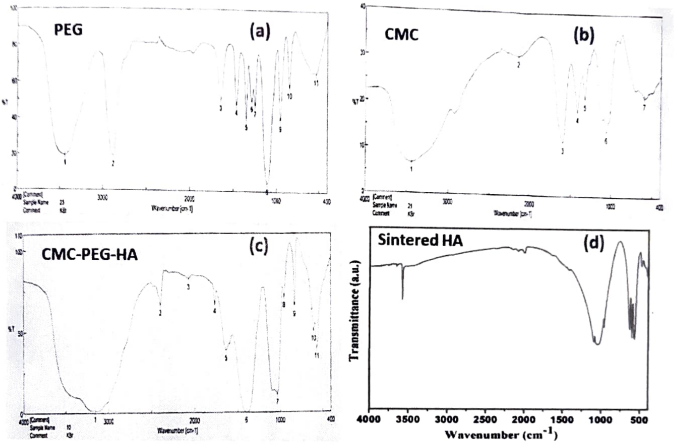

Fig.3. FTIR spectra of (a) PEG, (b) CMC, (c) CMC-PEG-HA and (d) sintered HA.

TEM analysis

The TEM images of CMC-PEG-HA (p-HA) and sintered-HA (s-HA) are presented in Fig.4. The morphology of p-HA consists of clustered spherical particles [Fig. 4a], approximately 20-40 nm in size. On the other hand, the s-HA morphology [Fig. 4b] is highly fused and agglomerated with individual particle size ranging from 200 nm to 400 nm. After sintering, it was noticed that the spherical particles had diffused to bigger particles (almost 10 times in size) and formed agglomerated HA particles. It can be concluded that during sintering, HA particles approached to each other and neck formations occurred between them and the heat treatment temperature favored the particles to enlarge. Hence, particles grow and the grain boundaries became clearer in sintered HA[24, 25].

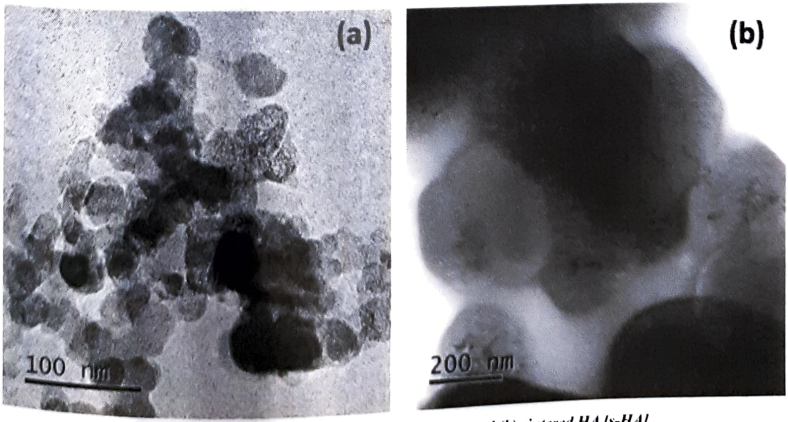

Fig.4. TEM image of (a) CMC-PEG-HA [p-HA] and (b) sintered HA [s-HA].

Microstructural analysis

The SEM microstructure of the as-synthesized CMC-PEG-HA (p-HA) composite from biomimetic process and sintered HA (s-HA) are shown in Fig. 5a-c. Biomimetic p-HA composite (Fig. 5a) consists of irregular shaped small and large aggregates. These aggregates were made up with nanosized HA particles (20- 40 nm) as shown in TEM image (Fig. 4a). This aggregation of nanoparticles is due to the intermolecular interactions among CMC, PEG and HA[14-16, 19]. Moreover, the surface properties associated with HA nanoparticles caused these particles to clump together and formed different size of agglomerates[3, 18, 26].

Fig. 5b exhibits the interconnected porous structure of sintered sample. This porous structure may be attributed to the elimination of polymers during sintering[11]. A closer look at the microstructure evidenced the presence of a hierarchy in pores [Fig. 5c], all the primary pores consists of secondary pores in their volume. This study confirmed that the fully interconnected multiporous HA block was formed by this simple process (biommetic method coupled with sintering). In Fig. 5c, few small and immature clusters of particles were found at the edge of grain boundaries. The elemental analysis (EDS) data showed that these clusters are made up with calcium (Ca), Phosphorous (P), Oxygen (O) and Carbon (C), mainly deficient calcium phosphate minerals (Ca/P ~1.60). It is known that calcium deficient minerals are generally water soluble[4]; hence, the solubility of sintered sample was checked in SBF (simulated body fluid) for 7 days and 14 days [Fig. 5e, f]. At day 7, calcium deficient parts were started to solubilize, however, at day 14 those were completely solubilized.

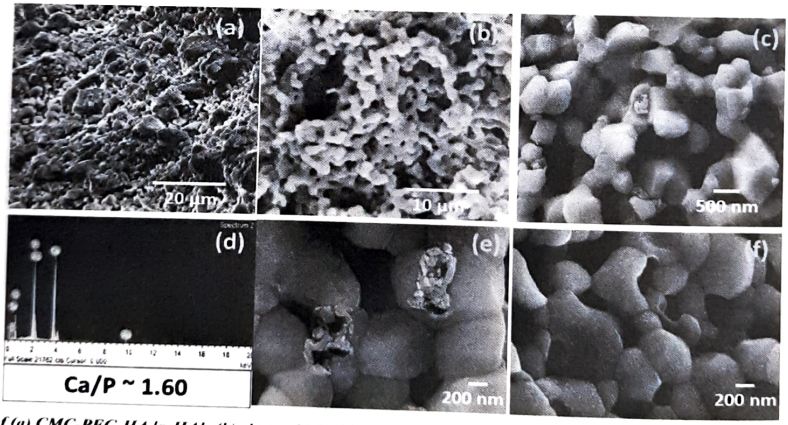

Fig. 5. SEM image of (a) CMC-PEG-HA [p-HA]; (b) sintered HA [s-HA]; (c) high resolution image of s-HA; (d) point EDS of s-HA; images of simulated body fluid treated s-HA [(e) 7 days and (f) 14 day].

Porosity and mechanical properties of sintered HA

The performance of bone implant mainly depends on its structure and strength, generally porous structure having wide range of pores with sufficient strength is more effective after implantation[8-9]. So, the porosity and compressive strength of sintered HA block have been evaluated. The pore size distribution pattern of sintered HA are presented in Fig. 6a. It shows that the pores diameter ranges from 4 -100 µm and the porosity is ~ 55%. The compressive stress-strain curve of sintered HA is shown in Fig. 6b. The curve exhibits a typical behavior of porous ceramic material, and sample failed at 3.6 MPa (stress) with lower strain percentage (6.3%) under compression[4]. Porous sintered HA block possesses compressive strength ~ 3.22±0.35 MPa and elastic modulus ~ 242±15 MPa, which are both in the range of human cancellous bone[4, 14]. These results showed that the sintered multiporous HA block can support bone tissue regeneration at the site of implantation, and can maintain sufficient integrity.

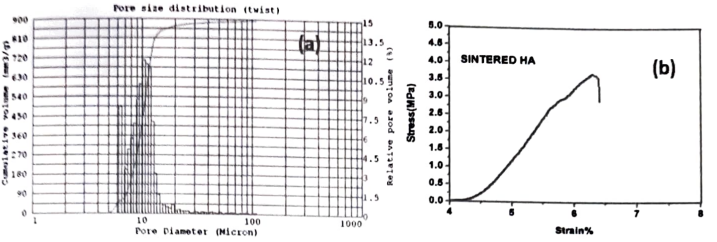

Fig.6. (a) Pore size distribution curve and (b) stress-strain curve of sintered HA.

MTT assay and cell adhesion study

Sintered HA (s-HA) was subjected to MTT assay with BMSCs. This study exhibits the cell metabolic activity where MTT absorbance corresponds to the number of viable cells [6-7, 17]. Results evidenced the proliferation of cells with culture time, and no significant toxicity was observed. Cell adhesion study revealed the behavior of cells on direct interaction with test material [16]. A representative image of cell adhesion test is shown in Fig. 7b, number of cells was observed on the surface of sintered HA which revealed that the sintered HA block do not interfere in cellular mechanism suggesting its cytcompatible nature[27]. Therefore, it can be concluded that sintered multiporous HA block may be used as an efficacious bone construct in future.

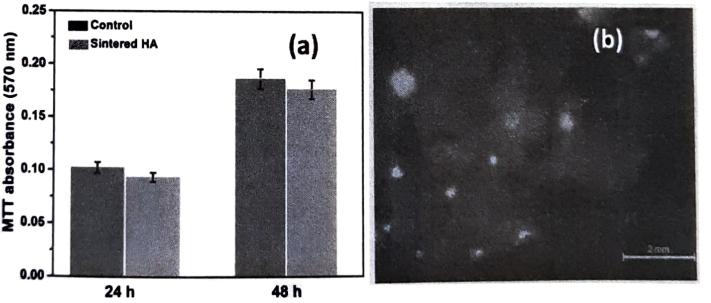

Fig.7. (a) MTT assay of sintered HA scaffold, (b) Fluorescent microscopy image after BMSCs were cultured with sintered HA for 48 h

CONCLUSION

In this study, fully interconnected multiporous hydroxyapatite block was successfully synthesized by a simple and cost effective process. The process is based on the concept of biomineralization, which demonstrates good control over the microstructural features of the block. Structural characterization clearly evidenced the formation of fully interconnected multiporous HA block. The microstructural features of sintered HA is a function of hybrid polymers matrix where the nucleation, growth and aggregation of HA nanoparticles were occurred. During sintering, polymers decomposed out and left their impression in sintered sample, as a result fully interconnected multiporous HA block was formed.

ACKNOWLEDGMENTS

Authors are thankful to Late Dr. Subhadra Garai (Principal Scientist, CSIR-National Metallurgical Laboratory, Jamshedpur) for the initiation of this work and her valuable contribution in this work. This work was supported by CSIR network project ESC103 and in house project support group (OLP-228), CSIR-National Metallurgical Laboratory, Jamshedpur.

REFERENCES

[1] C.Y. Tang, P.S. Uskokovic, C.P. Tsui, D. Veljovic, R. Petrovic, D. Janackovic: Influence of microstructure and phase composition on the nanoindentation characterization of bioceramic materials based on hydroxyapatite, Ceram Int 35: 2171–2178, 2009.

[2] S. Nayar, M.K. Sinha, D. Basu, A. Sinha: Synthesis and sintering of biomimetic hydroxyapatite nanoparticles for biomedical applications, J Mater Sci Mater Med 17: 1063–1068, 2006.

[3] S. K. Loghmani, M. Farrokhi-Rad, T. Shahrabin: Effect of polyethylene glycol on the electrophoretic deposition of hydroxyapatite nanoparticles in isopropanol, Ceram Int 39 : 7043–7051, 2013.

[4] S. Garai, A. Sinha: Three dimensional biphasic calcium phosphate nanocomposites for loadbearing bioactive bone grafts, Mater Sci Eng C 59:375-383, 2016.

[5] L. Roseti, V. Parisi, M. Petretta, C. Cavallo, G. Desando, I. Bartolotti, B. Grigolo: Scaffolds for Bone Tissue Engineering: State of the art and new perspectives, Mater Sci Eng C 78: 1246–1262, 2017.

[6] C. Sarkar, K. Anuvrat, S. Garai, S. K. Sahu, J. Chakraborty: One pot method to synthesized three dimensional porous hydroxyapatite nanocomosite for bone tissue engineering, J Porous Mater, 27: 225-235, 2020.

[7] S. Kanhed, S. Awasthi, S. Goel, A. Pandey, R. Sharma, A. Upadhyaya, K. Balani: Porosity distribution affecting mechanical and biological behaviour of hydroxyapatite bioceramic Composites, Ceram Int 43: 10442-10449, 2017.

[8] X. Wang, J. Li, Y. Xie, H. Zhang: Three-dimensional fully interconnected highly porous hydroxyapatite scaffolds derived from particle-stabilized emulsions, Ceram Int 42 : 5455-5460, 2016.

[9] M. Mbarki, P. Sharrock, M. Fiallo, H. ElFeki: Hydroxyapatite bioceramic with large porosity, Mater Sci Eng C 76: 985-990, 2017.

[10] Z. Chen, X. Zhang, Y. Yang, K. Zhou, N. Wragg, Y. Liu, M. Lewis, C. Liu: Fabrication and characterization of 3D complex hydroxyapatite scaffolds with hierarchical porosity of different features for optimal bioactive performance, Ceram Int 43: 336-344,2017.

[11] A. Sinha, S. Nayar, A. Kar, M.K. Gunjan, B. Mahato, G. Das: Microhydrogel-Mediated Synthesis of Sintered Hydroxyapatite Granules, Int J Appl Ceram Technol, 5: 458–463 2008.

[12] H. Konoa: Characterization and properties of carboxymethyl cellulose hydrogels crosslinked by polyethylene glycol, Carbohydr Polym, 106: 84-93, 2014.

[13] D. Varma, G.T. Gold, P.J. Taub, S.B. Nicoll: Injectable carboxymethyl cellulose hydrogels for soft tissue filler applications, Acta Biomater, 10: 4996-5004, 2014.

[14] N.S.V. Capanema, A. A. P. Mansur, A.C. Jesus, S. M. Carvalho, L.C. Oliveira, H.S. Mansur: Superabsorbent crosslinked Carboxymethyl cellulose-PEG hydrogels for potential wound dressing applications, Int J Biol Macromol 106: 1218-1234, 2018.

[15] S. Liang, J. Wu, H. Tian, L. Zhang, J. Xu: High-Strength Cellulose/Poly(ethylene glycol) Gels, Chem Sus Chem 1:558–563,2008.

[16] S. Garai, A. Sinha: Biomimetic nanocomposites of carboxymethyl cellulose-hydroxyapatite: novel three dimensional load bearing bone grafts, Colloid Surf B, 115: 182-190, 2014.

[17] C. Sarkar, P. Kumari, K. Anuvrat, S. K. Sahu, J. Chakraborty, S. Garai: Synthesis and characterization of mechanically strong carboxymethyl cellulose- gelatin-hydroxyapatite nanocomposite for load-bearing orthopedic application, J Mater Sci, 53: 230-246, 2018.

[18] Y. Wang, D. Liang, F. Liu, W. Zhang, X. Di, C. Wang: A polyethylene glycol/ hydroxyapatite composite phase change material for thermal energy storage, Appl Therm Eng 113: 1475-1482, 2017.

[19] C. Qiu, X. Xiao, R. Liu: Biomimetic synthesis of spherical nano-hydroxyapatite in the presence of polyethylene glycol, Ceram Int. 34:1747–1751, 2008.

[20] S. Lala, B. Satpati, S.K. Pradhan: Sintering behavior and growth mechanism of β-TCP in nanocrystalline hydroxyapatite synthesized by mechanical alloying, Ceram Int 42: 13176-13182, 2016.

[21] N. Monmaturapoj, W. Soodsawang, W. Thepsuwan: Porous hydroxyapatite scaffolds produced by the combination of the gel-casting and freeze drying techniques, J Porous Mater: 19: 441–447, 2012.

[22] P. Feng, M. Niu, C. Gao, S. Peng, C. Shuai: A novel two-step sintering for nano-hydroxyapatite scaffolds for bone tissue engineering, Sci Rep, 4: 5599, 2014,

[23] P. Kumar, B.S. Dehiya, A. Sindhu, Synthesis and characterization of nHA-PEG and nBG-PEG scaffolds for hard tissue engineering applications, Ceram Int 45: 8370-8379, 2019.

[24] K.T. Chu, S.F. Ou, S.Y. Chen, S.Y. Chiou, H.H. Chou, K.L. Ou: Research of phase transformation induced biodegradable properties on hydroxyapatite and tricalcium phosphate based bioceramic, Ceram Int 39: 1455–1462,2013.

[25] X. Pei, L. Ma, B. Zhang, J. Sun, Y. Sun, Y. Fan, Z. Gou, C. Zhou, X. Zhang: Creating hierarchical porosity hydroxyapatite scaffold with osteoinduction by three-dimensional printing and microwave sintering, Biofabrication 9: 045008, 2017.

[26] A.W. Xu, Y. Ma, H. Colfen: Biomimetic mineralization, J Mater Chem, 17: 415–449, 2007.

[27] C. Zhou, P. Xie, Y. Chen, Y. Fan, Y. Tan, X. Zhang: Synthesis, sintering and characterization of porous nano-structured CaP bioceramics prepared by a two-step sintering method, Ceram Int, 41: 4696-4705,2015.

Journal of Metallurgy and Materials Science, Vol. 62, No. 3-4, July-December 2020, pp. 31-40
Printed in India, © NML, ISSN 0972-4257

Effect of dual crosslinking on physico-chemical properties of hydrogels prepared from chitosan and alginate

SANTANU GHOSH, PRITIRANJAN MONDAL, B. RATHINA VEL and KAUSHIK CHATTERJEE*
Department of Materials Engineering, Indian Institute of Science, C.V. Raman Avenue, Bangalore, Karnataka- 560012, India

Abstract : Hydrogels have established their utility in the field of biomedical science and technology including drug delivery and tissue engineering, among other applications. Crosslinking density critically affects the resultant physical property of the hydrogels. Here, we have successfully synthesized carboxymethylchitosan (CMC) and oxidized alginate (AA) from chitosan and sodium alginate, respectively. CMC and AA were used to fabricate CMC-AA-single network (CMC-AA-SNH) and CMC-AA-double network (CMC-AA-DNH) hydrogels. Crosslinking of CMC-AA-SNH was done by dynamic covalent bonding, that is, imine bond formation, whereas CMC-AA-DNH was crosslinked via covalent imine bond and Ca^{2+} mediated ionic interactions. Fourier transform infrared spectroscopy (FTIR) and proton nuclear magnetic resonance (^{1}H NMR) studies were employed to characterize the components of the hydrogels. Effect of dual crosslinking over the single crosslinked hydrogel was extensively analyzed by rheological studies. Scanning electron microscopy revealed that the CMC-AA-DNH was more densely packed with interconnected structure than CMC-AA-SNH. Swelling study demonstrated that the degree of swelling of CMC-AA-DNH was significantly less than CMC-AA-SNH due to more crosslinking density. Compressive mechanical test of the hydrogels further indicated that CMC-AA-DNH exhibits fracture stress of 79.5 kPa. These results indicate how the physical and mechanical properties of a polymeric hydrogel system can be tuned through control of crosslinking, which have important implications for the use of these gels for biomedical applications.

Keywords: *hydrogels; chitosan; alginate; covalent crosslinking; ionic crosslinking; biopolymers; biomaterials*

INTRODUCTION

Hydrogels have gained enormous interest owing to their potential in diverse fields of biomedical science including drug delivery, peptide delivery, gene delivery, and tissue engineering, etc. [1, 2, 3] Over the years, researchers have proposed various definitions of hydrogels [4]. The simplest definition of hydrogels is that they are cross-linked three-dimensional (3D) polymeric networks, which may contain one or more polymers and are capable of holding a large amount of water. Cross-linking of hydrogels is known to be an important parameter as it plays a critical role in determining their physical integrity, swelling, and stiffness as well as other properties such as release behavior and degradation. Hydrogels can be crosslinked by different methods including chemical (covalent conjugations, enzyme mediated crosslinking, etc.) and physical (hydrogen bond formation, ionic interaction, stereocomplex formation, etc.) cross-linking [5]. A higher cross-linking density typically yields a much stiffer hydrogel than the lower cross-linked one. However, the degree of cross-linking can be tailored and depends on the target applications.

Various biodegradable, non-toxic polymers such as chitosan [6], sodium alginate[7], kappa carrageenan [8], guar gum [9], and gelatin [10], etc., have been used to prepare hydrogels for diverse biomedical applications. Among them, chitosan, which is a partially deacetylated form of chitin, is widely used in the food industries and medical applications such as wound healing and tissue engineering owing to its favorable properties such as biocompatibility, biodegradability, and antibacterial activity [11]. Sodium alginate, another naturally-derived biopolymer, has drawn enormous interests as it possesses properties similar to chitosan and can readily interact with different divalent cations such as Ca^{2+}, Sr^{2+}, and Mg^{2+} etc. to form hydrogels through ionic cross-linking [12]. Till now, several studies have been reported, wherein both chitosan and sodium alginate were used to develop hydrogels for different biomedical applications [13, 14, 15].

*Corresponding Author E-mail: kchatterjee@iisc.ac.in,

Recently, injectable hydrogels have been drawing increasing attention owing to their ability to readily form hydrogels and ease of delivery[16]. However, mechanical properties of these hydrogels are a concern limiting their use when employed as tissue adhesives or scaffolds for soft tissue regeneration. Mismatch in the elastic modulus of the hydrogel and the target tissue can result in poor biological outcomes.[17] Cross-linking is an important paramaters as it determines the mechanical properties of the hydrogels. Several research studies have been reported with double network hydrogels to explore different biomedical applications[18, 19]. However, there are few studies that have systematically compared the difference between single network hydrogel (SNH) and double network hydrogels (DNH) for a given polymeric system. Thus, in this study, we aimed to develop single cross-linked hydrogel (CMC-AA-SNH) and double cross-linked hydrogel (CMC-AA-DNH) prepared using CMC and AA and evaluate the effect of the crosslinking on their rheological behavior, swelling, and mechanical properties.

MATERIALS AND METHODS

Materials

Chitosan and sodium alginate were purchased from Sigma-Aldrich. Monochloroacetic acid and sodium periodate was procured from SD Fine Chemicals. Solvents used for this work were all analytical grade.

Synthesis of carboxymethyl-chitosan (CMC)

CMC was synthesized according to Bukzem et al with slight modification[20]. Briefly, 2 g of chitosan was suspended in 20 ml of 4:1 v/v isopropanol: water containing 2.7 g of sodium hydroxide and stirred for 1 h. Next, 3 g of monochloroacetic acid dissolved in isopropanol (4 ml) was added dropwise into the mixture above with continuous stirring for 30 min and the final mixture was stirred for 4 h at 60°C. Thereafter, the reaction was quenched by adding excess 70% ethanol and neutralized with glacial acetic acid followed by filtration. The solid mass was repeatedly washed with increased ethanol content (70%, 80%, 90%) and finally dried under vacuum for 24 h.

Synthesis of oxidized alginate (AA)

AA was synthesized by the oxidation of alginate[21]. Briefly, 1 g of sodium alginate was dissolved in 100 ml of deionized water with continuous stirring. Subsequently, 5 μM of sodium periodate was added to the mixture above and the stirring was continued for 6 h in the dark. 1.5 ml of ethylene glycol was used to quench the reaction followed by dialysis (3.5 kDa MWCO) against deionized water for 3 days with regular change of deionized water. Next, the dialyzed sample was freeze-dried to obtain dried AA as the final product. AA was stored in -20° C until use.

Preparation of Hydrogels

CMC and AA based SNH (CMC-AA-SNH) was prepared by mixing the 4.5% w/v aqueous solution of CMC and 20% w/v aqueous solution of AA at the ratio of 3:2 into a cylindrical mold at room temp. CMC and AA based DNH (CMC-AA-DNH) was prepared in a similar way where 20 nM of $CaCl_2$ solution was added additionally to introduce the second crosslinking. In both the cases, the inverted tube method was employed to determine the gelation time.

Chemical Characterization

The synthesized CMC and AA were characterized by Fourier transform infrared (FTIR) spectroscopy (Perkin-Elmer, USA) using attenuated total reflection (ATR) mode, where the spectra were recorded within the range 4000 to 650 cm^{-1} with 4 cm^{-1} resolutions and 32 consecutive scans. ^1H nuclear magnetic resonance (^1H NMR) was

also performed at 400 MHz to confirm the successful synthesis of CMC and AA using D_2O and tetramethylsilane (TMS) as solvent and internal standard, respectively. Moreover, both CMC-AA-SNH and CMC-AA-DNH hydrogels were characterized by FTIR analysis.

Swelling Study

Swelling study was done by immersing CMC-AA-SNH and CMC-AA-DNH hydrogels in PBS 7.4 at 37°C. Sample weight was measured at predetermined time points until it did not change any further. Triplicate samples of each type of hydrogel were used for each measurement. Swelling ratio was calculated by the following equation.

$$\text{Swelling ration} = \frac{W_t - W_i}{W_i}$$

Where, W_t and W_i are the weight of the hydrogel at individual time points and initial weight of the hydrogels, respectively.

Rheology study

The dynamic rheological behaviors, including dynamic frequency sweep, dynamic strain sweep and dynamic temperature sweep were studied using the Discovery Hybrid Rheometer (DHR-3 from TA Instruments) using cone and plate geometry (diameter 40 mm, angle: 40 degree geometry gap: 200 μm). The lower plate was a Peltier device with a specifically designed temperature control system and the upper plate was made of stainless steel. For each measurement, each sample was carefully loaded onto the Peltier plate and the upper plate was set at a desired distance above the Peltier plate. Thereafter, dynamic frequency and strain sweep samples were equilibrated without pre-shearing or oscillating for 2 min at 37°C before conducting the experiments. For the temperature sweep, the sample was equilibrated at 25°C for 2 min.

(i) Dynamic Strain sweep

Before the dynamic viscoelastic measurements, the dynamic strain sweep from 1 to 800% at a fixed angular frequency 10 rad s^{-1} was first performed to identify the linear viscoelastic region (LVR) in which the storage modulus is independent of the strain amplitude and the gel to sol transition point. 1% strain was selected for the low amplitude oscillation test to ensure that the dynamic oscillatory deformation of each sample was in the LVR.

(ii) Dynamic frequency sweep

Shear storage modulus (G') and loss modulus (G") were measured as functions of angular frequency (ω) over the range of 0.01 to 100 rad s^{-1} at 1 % strain at 37° C. The loss tangent (tanδ) was calculated by the equation (tan δ = G'/G") and plotted as function of angular frequency.

(iii) Dynamic temperature sweep

To test the temperature stability of the hydrogel samples, G' and G" were measured through a heating process 25°C to 60°C at ω = 10 rad s^{-1} and γ = 1%. Heating rate was 5°C / min.

Scanning electron microscopy

Longitudinal and cross-sectional regions of CMC-AA-SNH and CMC-AA-DNH were imaged using a scanning electron microscope (SEM, Ultra55 FE-SEM Karl Zeiss by Karl Zeiss SEM). For SEM imaging, both the hydrogel samples were freeze-dried followed by immersion into liquid nitrogen for few seconds prior to cutting into desired sections. Before imaging, samples were sputter coated with gold.

Mechanical Characterization

Compressive mechanical properties of hydrogels were evaluated using cylinder-shaped hydrogels (diameter of 7 mm and height of 2 mm) using the micro-universal testing machine (Mecmesin). A load cell of 25 N was used at a constant displacement rate of 1 mm/min until fracture. Triplicates of each type of hydrogel were measured.

RESULTS AND DISCUSSION

CMC and AA synthesis and characterization

CMC and AA were synthesized from chitosan and sodium alginate, respectively, and characterized by FTIR and ^{1}H NMR spectroscopic techniques. Fig 1(a) shows the characteristic broad FTIR absorption peaks of chitosan at 3600 to 3100 cm^{-1} for O-H and N-H stretching. The C=O stretching could be observed at 1656 cm^{-1}. The peaks at 1560 cm^{-1} and 1368 cm^{-1} correspond to N-H angular deformation and symmetric deformation of CH_3, respectively. Absorption at 1068 cm^{-1} corresponds to the C-O stretch. The FTIR spectra of CMC (Fig 1(a)) indicates the presence of COO^- as an intense absorption spectrum at 1584 cm^{-1}. The absorption band at 1410 cm^{-1} is observed, which is attributed to the symmetric and asymmetric deformations of COO^-, respectively. These results are in agreement with previously published work of Bukzem et al [20] and confirmed the successful formation of CMC.

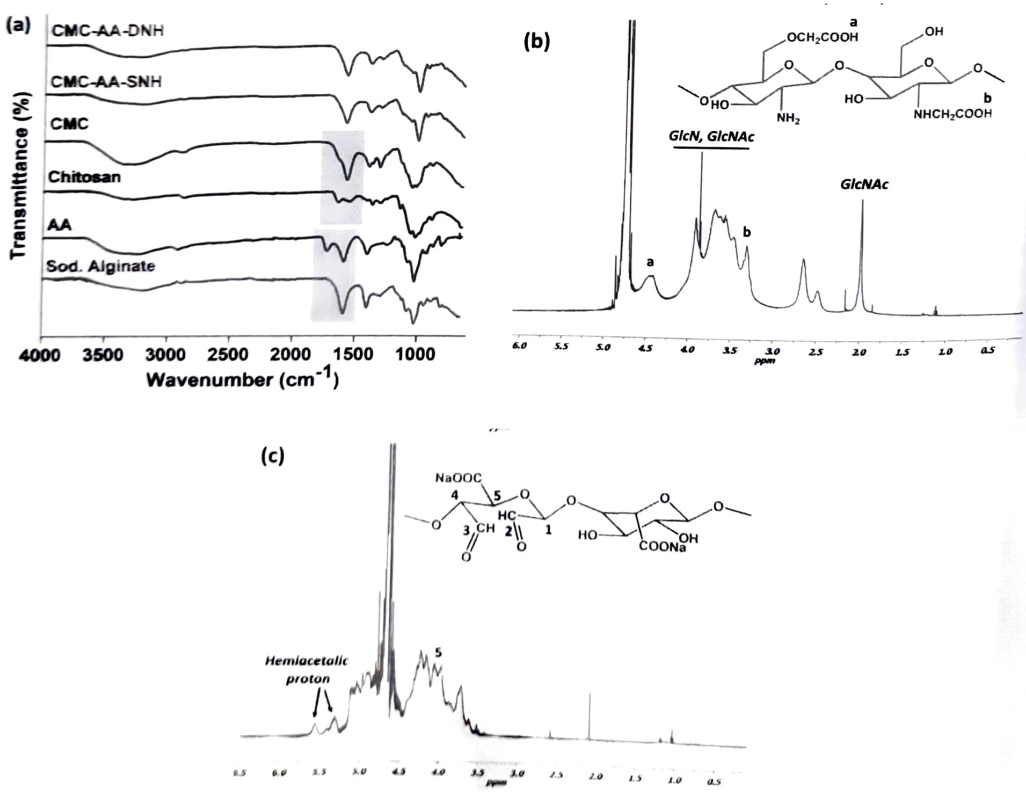

Fig 1. (a) FTIR spectra of sod. alginate, AA, chitosan, CMC, CMC-AA-SNH and CMC-AA-DNH; (b, c) 1H NMR spectra of (b) CMC and (c) AA.

The synthesis of CMC was further confirmed by ^{1}H NMR (Fig 1(b)). Chitosan is a copolymer, consisting of glucosamine (GlcN) and acetylglucosamine (GlcNAc) units. The characteristic methyl proton could be observed at 2.0 ppm, whereas peaks at the range of 3.4 to 4.1 ppm indicated the presence of hydrogens of GlcN and GlcNAc units. A broad peak at 4.3 to 4.6 ppm (a) is seen for the carboxymethyl protons and the adjacent protons of CH_2 indicating the O-carboxymethylation. Moreover, evidence of the formation of N-carboxymethylation could be observed as the peak around 3.3 ppm (b) indicated the protons of carboxymethyl group attached to nitrogen group of chitosan. [20]

Similarly, the formation of AA was confirmed by FTIR spectra (Fig 1(a)) and ^{1}H NMR spectra (Fig 1 (c)). Fig 1(a) presents the characteristic absorption spectrum of alginate. The broad peak at 3400 cm^{-1} indicates the O-H stretching vibration. The weak C-H stretching vibration could be observed at 2909 cm^{-1}. The asymmetric and symmetric stretching vibrations of COO^- could be found at 1596 cm^{-1} and 1404 cm^{-1}, respectively. All characteristic peaks could be observed for AA. However, a new absorption peak appeared around 1728 cm^{-1} that corresponds to the C=O stretching vibration of the aldehyde group, which indicated the formation of AA.[22] 1H NMR analysis further confirmed the formation of AA. Fig 1 (c) depicts the 1H NMR spectra of AA, where the appearance of two prominent signals at around 5.25 and 5.55 ppm indicate the presence of hemiacetalic protons, which formed from aldehyde and the neighbouring hydroxyl groups. Similar observations were reported by Gomez et al [23] and thus, corroborate the results presented here confirming the formation of AA.

Hydrogel formation and gelation time

Fig 2 (a) shows the schematic representation of hydrogel preparation for CMC-AA-SNH ad CMC-AA-DNH. Figs 2 (b) and (c) present the digital photographs of the two hydrogels formed in the vials. Schiff base chemistry was employed to develop CMC-AA-SNH, wherein the hydrogel was rapidly formed by the homogeneous mixing of aqueous CMC and AA solutions in proportions listed in Table 1. The amine groups of CMC readily reacted with the aldehyde group of AA to produce dynamic covalent imine bonds. Similarly, Schiff base chemistry was used to prepare CMC-AA-DNH hydrogels along with the introduction of a secondary crosslinker, i.e., Ca^{2+} ions at a predetermined concentration as listed in Table 1. Divalent Ca^{2+} ions rapidly reacted with the carboxylic acid groups of AA polymeric chains through ionic cross-linking. The resultant hydrogels were characterized by FTIR spectroscopy, which confirmed the formation of the imine bond in both hydrogels, as revealed by the absorption at around 1700 cm^{-1} (Fig 1(a)). The gelation time was calculated by tube inversion method for both CMC-AA-SNH and CMC-AA-DNH and is tabulated in Table 1. The gelation time of 20s for CMC-AA-SNH here is significantly faster than for similar hydrogels reported by others. For example, Lei et al [24] utilized the Schiff base reaction to prepare dynamic self-healing hydrogels from amino-gelatin and dialdehyde carboxymethyl cellulose with gelation time of approximately 2 h. Furthermore, the gelation time decreased to 10 s for CMC-AA-DNH (Table 1) indicating that the ionic bonds formed faster than the dynamic imine bonds.

Table 1. Composition of different hydrogels and their corresponding gelation time

	CMC (4.5% w/v): AA (20% w/v)	**$CaCl_2$ aqueous solution (nM)**	**Gelation time (s)**
CMC-AA-SNH	3:2	0	20
CMC-AA-DNH	3:2	20	10

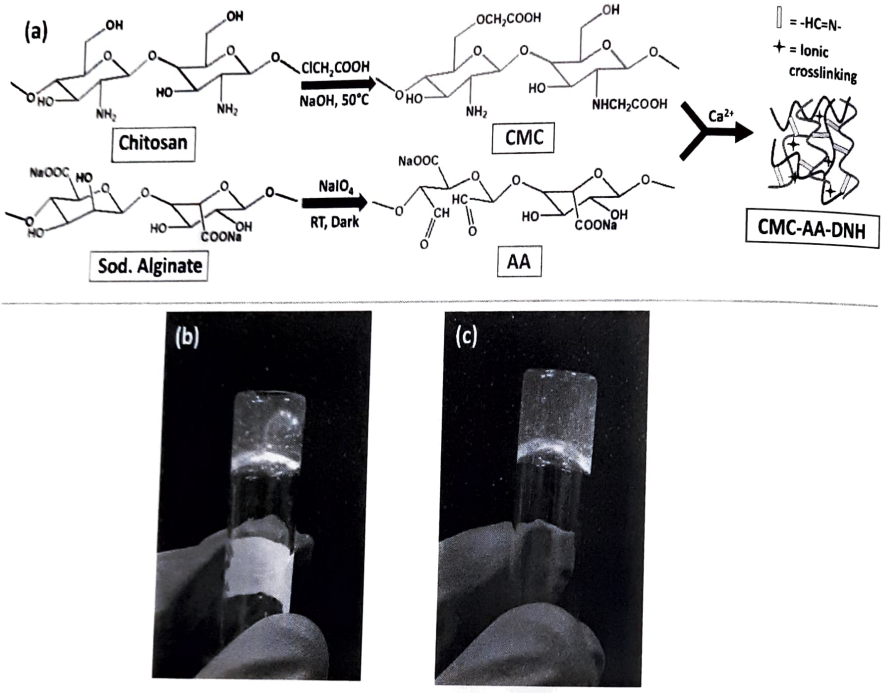

Fig 2. (a) Schematic representation of the CMC-AA-DNH gel formation; (b, c) Digital photographs of gels formed in inverted tubes of (b) CMC-AA-SNH and (c) CMC-AA-DNH.

Rheological study

Fig 3(a) shows the G' and G" as a function of % strain for both CMC-AA-SNH and CMC-AA-DNH hydrogels, which are the characteristic of the elastic response of hydrogels. In the LVR region, G' values of both hydrogels are essentially independent of the applied strain. The linear viscoelastic behavior deviated beyond a critical strain. The strain where the G' values of the hydrogels deviated by more than 5% from the linear region indicated the critical strains (γc) for each hydrogel [25]. Above γc, the G' values then rapidly decreased and crossed over the G" plot indicating the gel-to-sol transition point (γt). This transition point indicates a transformation from the quasi-solid state to quasi-liquid sol state. As shown, in Table 2, The γc values of CMC-AA-SNH and CMC-AA-DNH hydrogels are 6.33 and 4.12 %, respectively. Therefore, $\gamma = 1\%$ was used for the subsequent low amplitude oscillation tests, The corresponding G'max of CMC-AA-SNH and CMC-AA-DNH are 289 Pa and 737 Pa, respectively (Table 2 and Fig 3 a). The G'max of CMC-AA-DNH is 2.5 times more than G'max of CMC-AA-SNH due to the addition of a small amount of Ca^{2+} ions. In the presence of Ca^{2+} ions, more chelation happened in the CMC-AA-DNH system and as a result, the viscoelasticity and stiffness of the CMC-AA-DNH increased noticeably compared to CMC-AA-SNH. It can be observed that CMM-AA-DNH presented a moderately higher G'max compared to CMC-AA-SNH, as well as shorter LVR window and therefore, lower γc. These observations indicate that CMC-AA-DNH was a much stiffer and stronger hydrogel than CMC-AA-SNH.

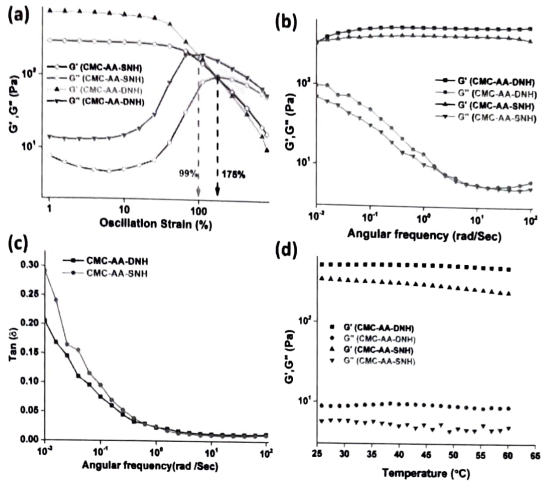

Fig 3. Dynamic viscoelasticity performance of both hydrogels at 37°C (a) The G' and G" of the hydrogel from strain amplitude sweep (γ = 1%–800%) at a fixed angular frequency (10 rad s^{-1}) (b) Frequency dependence (0.01 to 100 rad s-1) of G' and G" at γ = 1% (c) frequency dependence of tan δ for both hydrogel (d) temperature dependence of G' and G" during heating (25 to 60° C, 5°C / min) at γ = 1% and ω = 10 rad s^{-1}.

To understand the influence of Ca^{2+} ions on the viscoelastic properties of hydrogels, low amplitude oscillatory measurements were carried out at 37°C for CMC-AA-SNH & CMC-AA-DNH (Fig 3b). It can be seen that G'(ω) and G"(ω) of both hydrogels followed a similar trend. As ω increased, there is nearly a monotonic increase in G' and decrease in G", which begins to suggest more entanglement network together with a strong elastic gel network. [26] Throughout the experimental frequency window (0.01 to 100 rad s^{-1}), G'is greater than G"and tan δ is also less than 1.0 (Fig 3c), which demonstrates the solid-like elastic behavior of hydrogels. This feature is consistent with the response observed typically for viscoelastic materials with a narrow distribution of relaxation time.[27] The marginal increase of moduli in CMC-AA-DNH is indicative of the rearrangement of Ca^{+2} ions to form higher-order network structure under shear stress. The magnitude of G'(ω) values of CMC-AA-DNH was more than the magnitude of G'(ω) values of CMC-AA-SNH in the measured window (0.01 to 100 rad s^{-1}), again signifying stronger gel-like behavior of CMC-AA-DNH due to the additional ionic crosslinking in the system resulting from the Ca^{2+} ions.

Table 2: Rheological characteristics of the hydrogels

Parameters	CMC-AA-SNH	CMC-AA-DNH
Critical Strains (γ_c) %	6.33	4.12
Transition point (γ_t) %	175	99
Maximum G' within LVR, G'_{max} (Pa)	289	737
Crossover modulus, G_c (Pa)	99	202

To understand the behavior of hydrogel with temperature, temperature sweep studies have been performed. Fig 3d shows the temperature dependence of moduli (G' and G") for both hydrogels. Both hydrogels exhibited similar behavior. The moduli were nearly independent of temperature within the temperature range examined. G' of CMC-AA-SNH decreased marginally with an increase of temperature from 50° to 60°C, unlike the steady response of CMC-AA-DNH, which is suggestive of less stable crosslinking structure in CMC-AA-SNH than in CMC-AA-DNH.

SEM study

The surface morphology and internal structure of the lyophilized gels are shown in Fig 4(a) to (d). It was observed that both gels had a highly porous structure. The average pore size of CMC-AA-DNH (140 ± 32 μm, calculated from Fig 4a) was lower than the average pore size of CMC-AA-SNH (174 ± 39 μm, calculated from Fig 4c). This observation may be attributed to the fact that CMC-AA-DNH was stiffer and denser than the CMC-AA-SNH resulting from the higher crosslinking density in the presence of Ca^{2+} ions. From the micrograph of Fig 4b & 4d (longitudinal section of the sample), it was also observed that pores are highly interconnected. This interconnecting and irregular porous structure of 3D hydrogel is well suited for cell adhesion and proliferation.

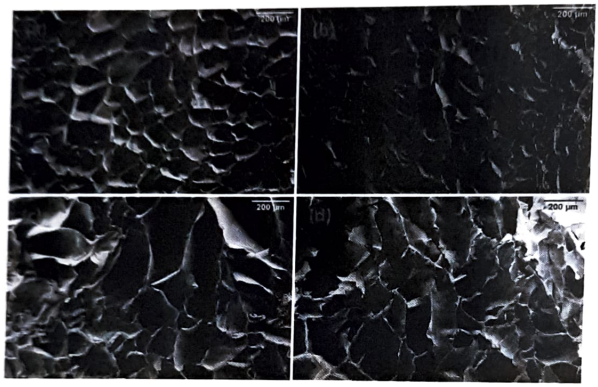

Fig 4. Scanning electron micrographs of (a) CMC-AA-DNH in cross-section, (b) CMC-AA-DNH in longitudinal direction, (c) CMC-AA-SNH in cross-section and (d) CMC-AA-SNH in longitudinal section.

Swelling study

The ability of the hydrogels for water uptake and resultant swelling was characterized for their use in biomedical applications. Fig 5 (a) compiles the swelling behavior of both hydrogels. CMC-AA-DNH almost reached equilibrium within 24 h and the swelling ratio was calculated to be 2.3. In contrast, CMC-AA-SNH swelled to reach equilibrium after 36 h and the swelling ratio was 5.5. This observation may be again being attributed to the fact that CMC-AA-DNH is relatively more tightly cross-linked than CMC-AA-SNH. When crosslinking density is less, the swelling swollen ratio is high. In CMC-AA-DNH, cross-linked density is more due to the additional Ca^{2+} -mediated ionic cross-linking.

Mechanical Property

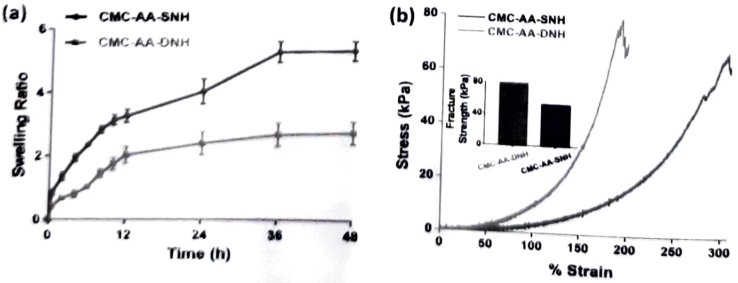

Fig 5. Comparative study of CMC-AA-SNH and CMC-AA-DNH (a) swelling, (b) compressive mechanical behavior

The mechanical properties of the hydrogels were assessed under compression. From the stress-strain curves in

Fig 5 (b), it is seen that CMC-AA-DNH exhibits higher modulus and maximum stress (79.5 kPa vs. 53.4 kPa) prior to failure but lower strain to failure (192% vs. 305%) than CMC-AA-SNH. These results are consistent with the data from rheology and a consequence of the increased cross-linking in CMC-AA-DNH compared to CMC-AA-DNH. Wei et al [21] also studied chitosan and alginate based hydrogels and the resulting hydrogel exhibited strength of 33 kPa. Lu et al [28] examined the effect of ionic concentration on dopamine modified 4 armed poly (ethylene glycol) hydrogel. They observed that the strength of the hydrogel was 65 kPa. In this work, we were able to achieve hydrogels with good strength by introduction of double network system using a combination of ionic and covalent bonding.

CONCLUSION

CMC and AA were synthesized and characterized by FTIR and ^{1}H NMR. Both pre-polymers were used to fabricate CMC-AA-SNH and CMC-AA-DNH hydrogels, where, CMC-AA-SNH was prepared by single covalent crosslinking whereas, covalent as well as ionic crosslinking were employed to prepare dual cross-linked CMC-AA-DNH. Faster gelation was observed for CMC-AA-DNH. Rheological properties were extensively studied for both the hydrogels and it was observed that CMA-AA-DNH is more viscoelastic as well as stiffer than CMC-AA-SNH. Denser and interconnected pores were observed for dual crosslinked CMC-AA-DNH hydrogel. Due to the higher crosslinking density, CMC-AA-DNH showed less swelling and higher strength than the single cross-linked CMC-AA-SNH hydrogel. It can be concluded that the presence of dual crosslinking CMC-AA-DNH yields much stiffer and stronger hydrogels than the single crosslinked CMC-AA-SNH. These results demonstrate how the physico-chemical properties of hydrogels derived from biopolymers may be tuned to meet the needs for different biomedical applications through careful selection of cross-links.

ACKNOWLEDGEMENTS

Funding from the Nanomission Programme of the Department of Science and Technology (DST), Government of India (Project DST/NM/NB/2018/119) is gratefully acknowledged. S.G. acknowledge SERB for the National Postdoctoral Fellowship (PDF/2019/000553). We thank Prof. Suryasarathi Bose for access to the rheometer.

DECLARATION

The authors declare no conflict of interest.

REFERENCES

[1] J. Li, D. J. Mooney: Designing hydrogels for controlled drug delivery. Nature Reviews Materials. 1: 1-7, 2016.

[2] N. Carballo-Pedrares, I. Fuentes-Boquete, S. Díaz-Prado, A. Rey-Rico: Hydrogel-Based Localized Nonviral Gene Delivery in Regenerative Medicine Approaches—An Overview. Pharmaceutics. 12: 752, 2020.

[3] S.H. Parekh, K. Chatterjee, S. Lin-Gibson, N.M. Moore, M.T. Cicerone, M.F. Young, C.G. Simon, Jr.: Modulus-driven differentiation of marrow stromal cells in 3D scaffolds that is independent of myosin-based cytoskeletal tension. Biomaterials. 32: 2256-2264, 2011.

[4] E.M. Ahmed: Hydrogel: Preparation, characterization, and applications: A review. Journal of Advanced Research 6: 105-121, 2015.

[5] W.E. Hennink, C.F. van Nostrum: Novel crosslinking methods to design hydrogels. Advanced drug delivery reviews. 64: 223-236, 2012.

[6] Z. Shariatinia, A.M. Jalali: Chitosan-based hydrogels: preparation, properties and applications. International journal of biological macromolecules. 115: 194-220, 2018.

[7] A.C. Hernández-González, L. Téllez-Jurado, L.M. Rodríguez-Lorenzo: Alginate hydrogels for bone tissue engineering, from injectables to bioprinting: A review. Carbohydrate Polymers. 229:115514, 2020.

[8] A. Rasool, S. Ata, A. Islam, R.U. Khan: Fabrication of novel carrageenan based stimuli responsive injectable hydrogels for controlled release of cephradine. RSC advances. 9: 12282-12290:2019.

[9] S. Das, U. Subuddhi: Guar gum–poly (N-isopropylacrylamide) smart hydrogels for sustained delivery of 5-fluorouracil. Polymer Bulletin. 76: 2945-2963, 2019.

[10] K. Dey, S. Agnelli, M. Serzanti, P. Ginestra, G. Scarì, P. Dell'Era, L. Sartore: Preparation and properties of high performance gelatin-based hydrogels with chitosan or hydroxyethyl cellulose for tissue engineering applications. International Journal of Polymeric Materials and Polymeric Biomaterials. 68: 183-192, 2019.

[11] P. Domalik-Pyzik, J. Chłopek, K. Pielichowska: Chitosan-based hydrogels: preparation, properties, and applications. Cellulose-Based Superabsorbent Hydrogels, MIH Mondal, Editor. 1665-1693, 2019.

[12] Q. Zhou, H. Kang, M. Bielec, X. Wu, Q. Cheng, W. Wei, H. Dai: Influence of different divalent ions cross-linking sodium alginate-polyacrylamide hydrogels on antibacterial properties and wound healing. Carbohydrate polymers. 197: 292-304, 2018.

[13] J. Chalitangkoon, M. Wongkittisin, P. Monvisade: Silver loaded hydroxyethylacryl chitosan/sodium alginate hydrogel films for controlled drug release wound dressings. International Journal of Biological Macromolecules. 159: 194-203, 2020.

[14] G. Wang, X. Wang, L. Huang: Feasibility of chitosan-alginate (Chi-Alg) hydrogel used as scaffold for neural tissue engineering: a pilot study in vitro. Biotechnology & Biotechnological Equipment. 31: 766-773, 2017.

[15] L. Xing, J. Sun, H. Tan, G. Yuan, J. Li, Y. Jia, D. Xiong, G. Chen, J. Lai, Z. Ling, Y. Chen: Covalently polysaccharide-based alginate chitosan hydrogel embedded alginate microspheres for BSA encapsulation and soft tissue engineering. International journal of biological macromolecules. 127: 340-348, 2019.

[16] Y. Sun, D. Nan, H. Jin, X. Qu: Recent advances of injectable hydrogels for drug delivery and tissue engineering applications. Polymer Testing. 81: 106283, 2020.

[17] K. Chatterjee, S. Lin-Gibson, W.E. Wallace, S.H. Parekh, Y.J. Lee, M.T. Cicerone, M.F. Young, C.G. Simon, Jr.: The effect of 3D hydrogel scaffold modulus on osteoblast differentiation and mineralization revealed by combinatorial screening. Biomaterials 31: 5051-5062, 2010.

[18] M.A. Haque, T. Kurokawa , J.P. Gong: Super tough double network hydrogels and their application as biomaterials. Polymer. 53: 1805-1822, 2012.

[19] J.P. Gong: Why are double network hydrogels so tough?. Soft Matter. 6: 2583-2590, 2010.

[20] A.L. Bukzem, R. Signini, D.M. dos Santos, L. M. Lião, D.P. Ascheri: Optimization of carboxymethyl chitosan synthesis using response surface methodology and desirability function. International journal of biological macromolecules. 85: 615-624, 2016.

[21] Z. Wei, J.H. Yang, Z.Q. Liu, F. Xu, J. X. Zhou, M. Zrínyi, Y. Osada, Y.M. Chen: Novel biocompatible polysaccharide-based self-healing hydrogel. Advanced Functional Materials. 25: 1352-1359, 2015.

[22] M. Tian, X. Chen, H. Li, L. Ma, Z. Gu, X. Qi, X. Li, H. Tan, C. You: Long-term and oxidative-responsive alginate–deferoxamine conjugates with a low toxicity for iron overload. RSC advances. 6: 32471-32479, 2016.

[23] C.G. Gome, M. Rinaudo, M. A. Villar: Oxidation of sodium alginate and characterization of the oxidized derivatives. Carbohydrate Polymers. 67: 296-304, 2007.

[24] J. Lei, X. Li, S. Wang, L. Yuan, L. Ge, D. Li, C. Mu: Facile fabrication of biocompatible gelatin-based self-healing hydrogels. ACS Applied Polymer Materials. 1: 1350-1358, 2019.

[25] S. Gao, J. Guo, K. Nishinari: Thermoreversible konjac glucomannan gel crosslinked by borax. Carbohydrate Polymers. 72: 315-325, 2008.

[26] Y. Wang, L. Chen: Impacts of nanowhisker on formation kinetics and properties of all-cellulose composite gels. Carbohydrate Polymers. 83: 1937-1946, 2011.

[27] T. Inoue, K. Osaki: Rheological properties of poly(vinyl alcohol)/sodium borate aqueous solutions. Rheol Acta. 32: 550-555, 1993.

[28] L. Lu, T. Tian, S. Wu, T. Xiang, S. Zhou: A pH-induced self-healable shape memory hydrogel with metal-coordination cross-links. Polymer Chemistry. 10: 1920-1929, 2019.

Journal of Metallurgy and Materials Science, Vol. 62, No. 3-4,July-December2020, pp. 41-48
Printed in India, © NML, ISSN 0972-4257

Limiting platelet adhesion in stainless steel bio-implants through microstructural modification

G. PERUMAL[1], A. CHAKRABARTI[2], S. PATI[2], S. SINGH[3], V. REDDY[4], H.S. GREWAL[1], G. MANIVASAGAM[4] and H. S. ARORA[1,*]

[1]Surface Science and Tribology Laboratory, School of Mechanical Engineering, Shiv Nadar University, Uttar Pradesh 201314, India

[2]Department of Life Sciences, School of Natural Sciences, Shiv Nadar University, Uttar Pradesh 201314, India

[3]Special Center for Molecular Medicine, Jawaharlal Nehru University, New Delhi 110067, India

[4]Centre for BioMaterials, Cellular and Molecular Theranautics, Vellore Institute of Technology (VIT), Vellore, Tamil Nadu 632014, India

Abstract : Thrombosis, resulting from platelet adhesion and attachment is one of the major issues with blood contacting implants. Limiting platelet adhesion is highly desirable to ensure the usefulness of implants in blood contacting applications. In this work, we report on simplistic low-temperature high strain-rate processing to minimize the platelet adhesion on biomedical grade stainless steel. In addition, processing was also done at low rotational speed to study the effect of strain rate during processing. At high rotational speed, the processed steel resulted in single-phase ultra-fine grain structure along with significantly lower metal ion-release and better hemocompatibility. In addition, increased cellular viability with no significant morphological aberrations were observed in processed specimen in Human Wharton's jelly derived mesenchymal stem cells (HW-MSCs). Higher resistance for platelet adhesion for the processed steel is explained by favorable electronic characteristics of the metal-oxide and short-range polar interactions at the cell-substrate interface. Higher stability of the metal-oxide on processed steel contributed towards reducing the metal-ion release and ensure better hemocompatibility.

Keywords: *Biomaterials; Interfaces; Microstructure; Grain boundaries; Platelet*

INTRODUCTION

Stainless steel and titanium are amongst most widely used materials for bio-implant applications. This is mainly driven by their high strength, toughness, satisfactory corrosion and wear resistance as well as superior biocompatibility[1-3]. These materials also find applications in intravascular components such as blood pumps, pacemaker leads, heart valves and stents[4, 5]. However, one of the major issues with the use of these materials for blood contacting applications is the adsorption of blood constituents i.e. proteins and platelets on the implant surface [6-8]. The protein-implant interaction occur spontaneously as soon as blood contacts the implant surface followed by platelet attachment and blood coagulation. The consequence of adsorption of blood constituents on an implant involves severe complications such as thrombosis, vasculitis, and inflammation[7]. Limiting protein and platelet adhesion on an implant surface is highly desirable to ensure their usefulness for blood contacting applications.

The interaction of implant with blood components is a complex phenomenon and is primarily driven by its surface characteristics. Surface charge, wettability and surface topography significantly influence the protein, platelet adhesion and attachment. Negative surface charge and hydrophilicity are known to impede the platelet adhesion[8]. Various approaches including microstructural refinement[9, 10], tailoring the surface chemistry[11] and surface texturing[12, 13] have been reported to control the cellular response as well as diminish protein and platelet adhesion. The existing pattering techniques for crystalline metals, offer limited control over morphology and length-scale. In contrast, microstructural refinement approach is highly versatile in that context. Here, we demonstrate a versatile high strain-rate processing technique for limiting platelet adhesion on stainless steel surface through microstructure control. In addition, the processed stainless steel surface showed reduced metal ion-release and slightly better hemocompatibility. Improved thromboresistance properties of processed stainless-steel surface is explained based on favorable electronic characteristics of the metal-oxide and short-range polar interactions at the cell-substrate interface.

*E-mail: harpreet.arora@snu.edu.in, Phone: (+91)-8130625504

EXPERIMENTAL DETAILS

Biomedical grade stainless steel, SS316L, was used in the current study. The surface properties of stainless steel were tailored using low-temperature high strain-rate deformation process known as submerged friction stir processing. The details about the process are given elsewhere [14]. Processing was done at two different tool rotational speeds of 388 rpm (designated as 388-RS henceforth) and 1800 rpm (designated as 1800-RS henceforth). All samples were polished down to 3000 grit followed by electro-polishing in 10% oxalic acid solution. Electron back scatter diffraction (EBSD), performed using FEI Quanta 3D FEG, was used to reveal the grain size and phase distribution for all specimens. The semiconductor properties of the thin oxide layer formed on base SS316L and processed specimen was obtained using Mott-schottky analysis [15]. A standard three electrode electrochemical system (Gamry, Interface 1000E) was used along with the ringer solution as an electrolyte. For Mott-schottky analysis, AC signal of 10 mV amplitude at 1000 Hz frequency and a step potential of 50 mV is swept in the cathodic direction from 0.25V to -0.5V to measure the capacitance, C. Cell assay was performed using Human Wharton's jelly derived mesenchymal stem cells (HW-MSCs, Hi Media, India). A colorimetric assay (MTT, Thermo Fisher Scientific) was performed to evaluate the cytotoxicity of the as-received SS316L and processed specimens. In addition, the morphological aberrations were studied using fluorescence microscopy analysis after staining with DAPI, PI, and Phalloidin as described elsewhere [16]. Hemolysis assay was performed as described by Lale et. Al [17] while platelet isolation was performed as explained by Verhuel [18]. In addition, the fibrinogen adhesion of the specimens was determined by ELISA assay (enzyme-linked immunosorbent). The specific details of these assay were given elsewhere [14]. Inductively coupled plasma mass spectrometry (ICP-MS; Thermo fisher Scientific Inc., USA) was used to trace ion concentration of iron, chromium and nickel ions in the ringer solution. One-way analysis of variance method followed by a Student's t-test was used to compare the various means of the triplicate samples of individual experiments and to identify the statistical significance. All the statistical analysis has been done using the statistical tool GraphPad Prism 7.0 and $*p < 0.05$, $**p < 0.01$, $***p < 0.001$ were considered as statistically significant.

RESULTS

Microstructure

The grain size got significantly refined from 22 μm for the base steel to 0.6 μm and 0.9 μm for 388-RS and 1800-RS specimen. The detailed information regarding microstructure analysis and details is given elsewhere [19]. As shown by the EBSD analysis, the base steel has austenite structure while 1800-RS has nearly 8% martensite phase. The fraction of martensite phase is significantly high at nearly 45% for the 388-RS specimen.

Contact Angle

The contact angle of the base SS316L, 388-RS and 1800-RS specimens was found to be $60^\circ \pm 3^\circ$, $50^\circ \pm 9^\circ$, $46^\circ \pm 2^\circ$ respectively. Thus, both the processed samples show lower contact angle compared to the base steel. The decrease in contact angle with grain refinement has been shown previously as well [20]. Higher contact angle and large variation in the value for 388-RS specimen is likely due to high martensite fraction. This might be also due to the difference in the nature or percentage composition of oxide layer formed on the surface of the specimen [21, 22].

Mott Schottky Analysis

The electronic properties of the metal in a metal-electrolyte environment were determined using Mott Schottky (M-S) analysis, a capacitive measurement technique [15, 23].

This technique is used to study the interface reactions between the specimen surface and biological moieties. Here, all the specimen shows n-type semiconductor behavior with positive slope and the flat band potential of the same is calculated using the M-S equation [22, 24]. The curves obtained are shown in Figure 1 and the results comprising rest potential and flat band potential of all the tested specimens were tabulated in Table 1.

Tested Specimen	Open circuit potential Eocp (mV)	Flat band potential, Efb (mV)	Difference (mV)
SS316L	-250±5	-430±6	180
388-RS	-258±12	-432±9	174
1800-RS	-440±7	-298±4	-142

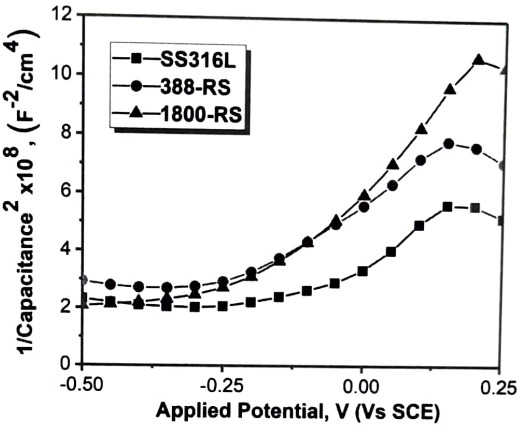

Fig.1: I/C² Vs E plot (Mott-Schottky) for stainless steel SS316L, low rotational speed friction processed SS316L (388-RS) and high rotational speed friction processed SS316L (1800-RS) at low temperature submerged conditions. Curves were obtained at 37° C in simulated body fluid environment (Ringer solution as electrolyte) using three-electrode electrochemical setup.

Table 1: Semi conducting properties of SS316L steel, low rotational speed friction processed SS316L (388-RS) and high rotational speed friction processed SS316L (1800-RS) at low temperature submerged conditions. Curves were obtained at 37°C in simulated body fluid environment (Ringer solution as electrolyte) using three-electrode electrochemical setup.

Interestingly, 1800-RS reported higher flat band potential and lower open circuit potential. Thus, the difference between the rest potential and flat band potential was calculated to be negative whereas other positive difference was observed in other specimens. Further, the consequences of this condition resulted in lesser platelet and fibrinogen adhesion on 1800-RS specimen which is discussed in forthcoming sections.

Hemocompatibility

The samples treated with human RBC reports minimal hemolysis for both the base SS316L and the processed samples (Figure 2(a)). Whereas total hemolysis was observed in the positive control (deionized water), < 5% hemolysis was detected for all the steel specimens. Although, all samples are hemocompatible, the percentage hemolysis is least for 1800-RS specimen.

Protein Adsorption and Platelet Adhesion

The adsorption of protein was determined by the adsorbed fibrinogen percentage which is shown in Figure 2(b). Here, polystyrene plate was used as the control. Both the processed specimen reported least fibrinogen adsorption compared to the base stainless-steel alloy with high statistical significance of $^{**}p < 0.05$. In addition, the release

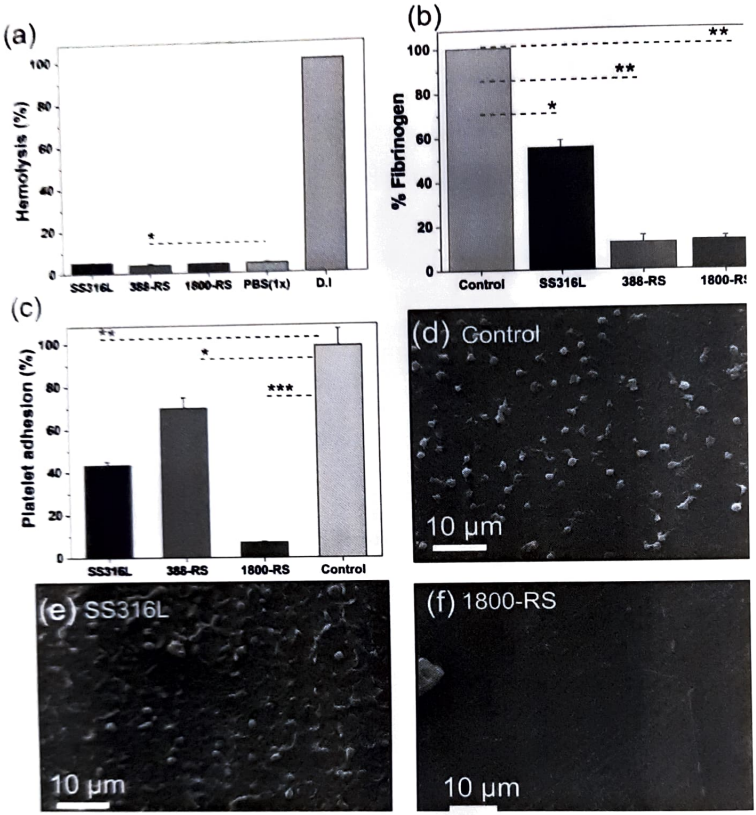

*Fig. 2: Hemocompatibility and platelet adhesion activity of the tested specimens: (a) hemolysis percentages, (b) % Fibrinogen adsorption obtained by ELISA, (c) % platelet adhesion obtained by LDH assay. Scanning electron microscopy (SEM) images of platelets adhering to (d) the control (polystyrene 24 well plate), (e) base stainless steel, SS316L and (f) high rotational speed friction processed SS316L (1800-RS). Data is presented along with error bar which represents standard deviation. *$p < 0.05$, **$p < 0.01$, ***$p < 0.001$ is considered to be statistically significant performed using student t-test.*

of lactate dehydrogenase (LDH) by the platelets on the samples was used to determine the platelet adhesion property and the results are shown in Figure 2(c). Platelets adhered on treated polystyrene plates were used as a control. 1800-RS specimen showed lowest platelet adhesion, nearly 7% compared to 43% for the base alloy. In contrast, 388-RS showed higher platelet adhesion of nearly 69%. Thus, the 1800-RS specimen exhibited exceptionally lower affinity for platelet adhesion, signifying its desirable attribute for blood-contacting implants. The statistical significance of *$p < 0.05$ in variation with respect to control is reported in all of the samples. However, higher statistical difference in 1800-RS was denoted using ***$p < 0.001$. SEM images of control polystyrene plate, SS316L and the 1800-RS specimen, shown in Figure 2(d) and (e) and Figure 2(f) respectively, support minimal platelet adhesion on 1800-RS.

Cellular response - Cytotoxicity and Fluorescence microscopy Analysis

The results of cellular response of Human Wharton's jelly derived mesenchymal stem cells (HW-MSCs) is shown in Figure 3. Figure 3(a) shows the evaluated percentage of dead cells after MTT assay. It is seen that 1800-RS processed specimen shows less toxic nature compared to 388-RS and base SS316L alloy. In addition, the dead and live cells were stained using DAPI and PI respectively.

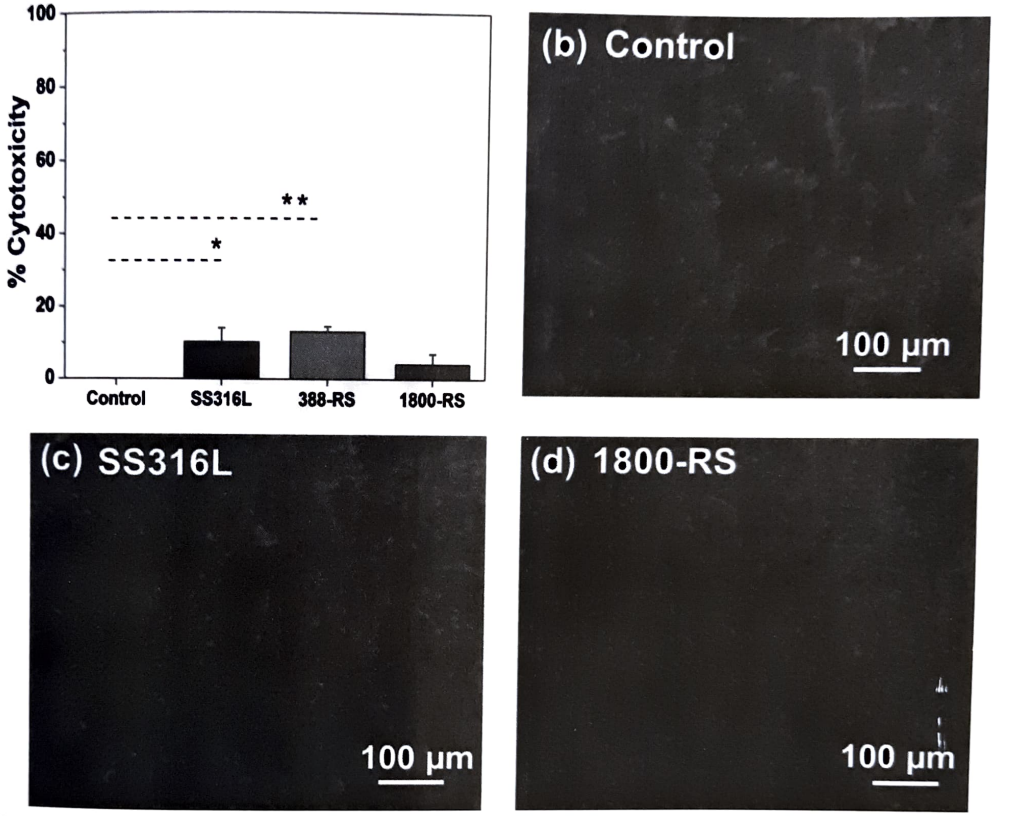

*Fig. 3: Cellular activity of the tested specimens: (a) % Toxicity obtained from MTT Assay, Fluorescence images of Human Wharton's jelly derived mesenchymal stem cells (HW-MSCs) cultured with respective conditioned media from the (b) control (media without specimen), (c) base SS316L alloy, (d) high rotational speed friction processed SS316L (1800-RS) for 48 h: Cells were stained DAPI , PI and phalloidin representing live cells (blue), dead cells (red) and actin filaments (green) respectively. Data is presented along with error bar which represents standard deviation. *p < 0.05, **p < 0.001 is considered to be statistically significant performed using student t-test.*

It is shown in Figure 3(b)-3(d) which indicates there is no significant difference in cell morphology after processing. Further, there was no red color fluorescence observed indicating processing does not affect the HW-MSCs morphology. Thus, providing safe condition as implant material for blood contacting applications.

ICP-MS Analysis

The results of ICP-MS testing for the base SS316L, 388-RS and 1800-RS specimens are given in Figure 4. Here, both the processed specimens released lesser ion compared to the base SS316L alloy.

In correlation with the weight percentage of the stainless steel, iron leached out the maximum compared to chromium and nickel. 1800-RS shows the lowest rate of ion release which corroborates the ability of 1800-RS to form a more stable passive layer in the ringer solution. These released ions from the implants results and inflammation [25, 26]. In addition, these elements can also lead to carcinogenic and mutagenic reactions [27, 28]. Thus, the reduction of leaching of ions using high rotational speed processing (1800-RS) from implant material might play a particular significance especially in blood contacting applications. in allergic reactions in the human body resulting in toxicity to the cells

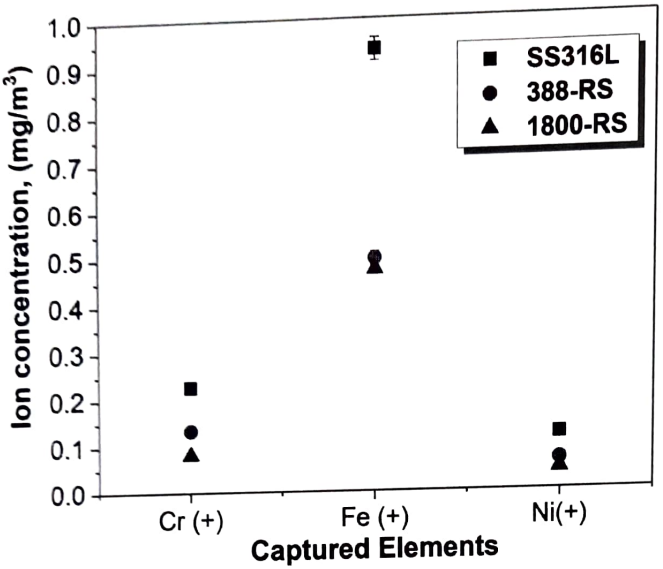

Fig. 4: Ion concentration of chromium, nickel and iron elements captured using Inductively coupled plasma mass spectrometry (ICP-MS) method for the base stainless steel SS316L, processed specimens at low rotational speed (388-RS) and high rotational speed (1800-RS) specimens that leach-out into the simulated body fluid environment. Both processed samples showed lower leaching of elements compared to the as-received alloy.

DISCUSSION

The results of the current study demonstrate that platelet adhesion was remarkably diminished in 1800-RS compared to the aggravated response for the base specimen. Platelet adhesion is a complex process & cannot be attributed to unique physico-chemical property. As per the extended DLVO (XDLVO) theory [29], the interaction of charged particle (such as platelets) with the substrate is a function of Lifshitz van der Waals, electrostatic double layer interaction and short-range polar interactions. While van der Waals energy is always positive, the electrostatic double layer interaction is attractive or repulsive depending on the substrate surface charge. Polar interactions become significantly important at short-range and basically govern the wettability state of the substrate. The platelet interactions with the substrate occur through a thin metal oxide layer that forms the outermost layer on the substrate. The nature of charge on the oxide layer plays an important role in platelet adhesion and attachment [8]. The Mott-Schottky analysis suggest lower rest potential for 1800-RS specimen compared to the flat band potential. The charge equilibrium necessitates transfer of excessive negative charge from the electrolyte to the oxide layer resulting in net negative surface charge for the 1800-RS specimen. The scenario is reversed for the base steel due to its higher rest potential than flat band, giving it a net positive charge. The short-range polar interactions which are nearly 10-100 times stronger than long-range interactions can play a more significant role [23, 30]. Both the processed samples are more hydrophilic compared to the base steel. The strong hydrogen bonding in hydrophilic surface presents a significant energy barrier for adhesion/bonding with other surfaces. Therefore, the decrease in platelet adhesion for 1800-RS specimen is likely explained by electrostatic repulsion between negatively charged substrate and the platelets as well as due to hydrophilic repulsion. In addition, processing does not affect the cellular morphology significantly. Further, the reduction in metal ion dissolution is likely attributed to more stable oxide layer on the processed specimen. Thus, the intervascular complications can be avoided by developing tailored microstructure using high strain-rate processing.

CONCLUSIONS

The microstructure of stainless steel got significantly refined by low temperature high strain-rate processing. Higher rotational speed processing resulted in nearly single-phase ultra-fine grain (UFG) structure while lower rotational speed processing resulted in dual-phase UFG structure. Single phase UFG steel showed significantly lower platelet adhesion, less toxicity and reduced metal-ion dissolution compared to base stainless steel. High resistance to platelet adhesion was attributed to negative surface charge induced by charge equilibrium at substrate-electrolyte interface and hydrophilic repulsion.

ACKNOWLEDGEMENTS

H.S. Arora thankfully acknowledge the financial assistance provided by Science and Engineering Research Board (SERB), Department of Science and Technology, under the project titled "Tailoring the Surface Properties of Crystalline and Amorphous Metals for Advanced Bio-Implants" (File no. YSS/2015/000678).

REFERENCES

[1] M. Sumita, S. Teoh, Durability of metallic implant materials, Engineering materials for biomedical applications, World Scientific 2-1-2-31, 2004.

[2] N. Eliaz, Degradation of implant materials, Springer Science & Business Media 2012.

[3] S.H. Teoh, Engineering materials for biomedical applications, World scientific 2004.

[4] M. Haidopoulos, S. Turgeon, C. Sarra-Bournet, G. Laroche, D. Mantovani, Development of an optimized electrochemical process for subsequent coating of 316 stainless steel for stent applications, Journal of Materials Science: Materials in Medicine 17(7): 647-657, 2006.

[5] G. Mani, M.D. Feldman, D. Patel, C.M. Agrawal, Coronary stents: a materials perspective, Biomaterials 28(9): 1689-1710, 2007.

[6] B. Thierry, Y. Merhi, L. Bilodeau, C. Trepanier, M. Tabrizian, Nitinol versus stainless steel stents: acute thrombogenicity study in an ex vivo porcine model, Biomaterials 23(14): 2997-3005, 2002.

[7] J. Courtney, N. Lamba, S. Sundaram, C. Forbes, Biomaterials for blood-contacting applications, Biomaterials 15(10): 737-744, 1994.

[8] V. DePalma, R. Baier, J. Ford, V. Gott, A. Furuse, Investigation of three-surface properties of several metals and their relation to blood compatibility, Journal of Biomedical Materials Research Part A 6(4): 37-75, 1972.

[9] E. Mostaed, M. Vedani, M. Hashempour, M. Bestetti, Influence of ECAP process on mechanical and corrosion properties of pure Mg and ZK60 magnesium alloy for biodegradable stent applications, Biomatter 4(1): e28283, 2014.

[10] C.S. Obayi, R. Tolouei, A. Mostavan, C. Paternoster, S. Turgeon, B.A. Okorie, D.O. Obikwelu, D. Mantovani, Effect of grain sizes on mechanical properties and biodegradation behavior of pure iron for cardiovascular stent application, Biomatter 6 (1): e959874, 2016.

[11] J. Eric Jones, M. Chen, Q. Yu, Corrosion resistance improvement for 316L stainless steel coronary artery stents by trimethylsilane plasma nanocoatings, Journal of Biomedical Materials Research Part B: Applied Biomaterials 102(7): 1363-1374, 2014.

[12] C. Hehrlein, M. Zimmermann, J. Metz, W. Ensinger, W. Kubler, Influence of surface texture and charge on the biocompatibility of endovascular stents, Coronary artery disease 6(7): 581-586, 1995.

[13] H. Zhao, J. Van Humbeeck, J. Sohier, I. De Scheerder, Electrochemical polishing of 316L stainless steel slotted tube coronary stents: an investigation of material removal and surface roughness, Progress in Biomedical Research 8: 70-81, 2003.

[14] G. Perumal, A. Ayyagari, A. Chakrabarti, D. Kannan, S. Pati, H.S. Grewal, S. Mukherjee, S. Singh, H.S. Arora, Friction Stir Processing of Stainless Steel for Ascertaining Its Superlative Performance in Bioimplant Applications, ACS applied materials & interfaces 9(42): 36615-36631, 2017.

[15] A. Di Paola, Semiconducting properties of passive films on stainless steels, Electrochimica Acta 34(2): 203-210, 1989.

[16] G. Perumal, H.S. Grewal, M. Pole, L.V.K. Reddy, S. Mukherjee, H. Singh, G. Manivasagam, H.S. Arora, Enhanced Biocorrosion Resistance and Cellular Response of a Dual-Phase High Entropy Alloy through Reduced Elemental Heterogeneity, ACS Applied Bio Materials 3(2): 1233-1244, 2020.

[17] S.V. Lale, A. Kumar, S. Prasad, A.C. Bharti, V. Koul, Folic acid and trastuzumab functionalized redox responsive polymersomes for intracellular doxorubicin delivery in breast cancer, Biomacromolecules 16(6): 1736-1752, 2015.

[18] H.M. Verheul, A.S. Jorna, K. Hoekman, H.J. Broxterman, M.F. Gebbink, H.M. Pinedo, Vascular endothelial growth factor–stimulated endothelial cells promote adhesion and activation of platelets, Blood 96(13): 4216-4221, 2000.

[19] G. Perumal, H. Grewal, H. Arora, Enhanced durability, bio-activity and corrosion resistance of stainless steel through severe surface deformation, Colloids and Surfaces B: Biointerfaces, 194: 111197, 2020.

[20] V. Muhonen, C. Fauveaux, G. Olivera, P. Vigneron, A. Danilov, M.D. Nagel, J. Tuukkanen, Fibronectin modulates osteoblast behavior on Nitinol, Journal of Biomedical Materials Research Part A, 88(3): 787-796, 2009.

[21] G. Perumal, H.S. Grewal, A. Ayyagari, S. Mukherjee, H.S. Arora, Enhancement in bio-corrosion resistance of metallic glass by severe surface deformation, Applied Surface Science 487: 1096-1103, 2019.

[22] S. Bahl, P. Shreyas, M. Trishul, S. Suwas, K. Chatterjee, Enhancing the mechanical and biological performance of a metallic biomaterial for orthopedic applications through changes in the surface oxide layer by nanocrystalline surface modification, Nanoscale 7(17): 7704-7716, 2015.

[23] G. Perumal, A. Chakrabarti, H.S. Grewal, S. Pati, S. Singh, H.S. Arora, Enhanced antibacterial properties and the cellular response of stainless steel through friction stir processing, Biofouling 35(2): 187-203,2019.

[24] N. Hakiki, S. Boudin, B. Rondot, M.D.C. Belo, The electronic structure of passive films formed on stainless steels, Corrosion Science 37(11): 1809-1822,1995.

[25] R.S. Nayak, B. Khanna, A. Pasha, K. Vinay, A. Narayan, K. Chaitra, Evaluation of nickel and chromium ion release during fixed orthodontic treatment using inductively coupled plasma-mass spectrometer: An in vivo study, Journal of International Oral Health: JIOH 7(8): 14,2015.

[26] E.K. Brooks, R.P. Brooks, M.T. Ehrensberger, Effects of simulated inflammation on the corrosion of 316L stainless steel, Materials Science and Engineering: C 71: 200-205, 2017.

[27] A. Lewis, J. Furze, S. Small, J. Robertson, B. Higgins, S. Taylor, D. Ricci, Long-erm stability of a coronary stent coating post-implantation, Journal of Biomedical Materials Research: An Official Journal of The Society for Biomaterials, The Japanese Society for Biomaterials, and The Australian Society for Biomaterials and the Korean Society for Biomaterials 63(6): 699-705, 2002.

[28] Y. Okazaki, E. Gotoh, Metal release from stainless steel, Co–Cr–Mo–Ni–Fe and Ni–Ti alloys in vascular implants, Corrosion Science 50(12: 3429-3438, 2008.

[29] C.J. van Oss, The extended DLVO theory, Interface Science and Technology, Elsevier, 31-48, 2008.

[30] C.J. Van Oss, M.K. Chaudhury, R.J. Good, Interfacial Lifshitz-van der Waals and polar interactions in macroscopic systems, Chemical Reviews 88(6): 927-941, 1988.

Journal of Metallurgy and Materials Science, Vol. 62, No. 3-4,July-December2020, pp. 49-57
Printed in India, © NML, ISSN 0972-4257

Technology glimpse of bioceramic implants developed by CSIR-CGCRI, Kolkata

BISWANATH KUNDU, VAMSI K. BALLA and K. MURALEEDHARAN*
Bioceramics & Coating Division
CSIR-Central Glass and Ceramic Research Institute, Kolkata 700032

INTRODUCTION

For the last two decades, Bioceramics Group of CSIR-Central Glass and Ceramic Research Institute (CSIR-CGCRI), Kolkata has been engaged in the development of new generation of ceramic materials for different biomedical applications. The group has developed hip joint prosthesis with ceramic heads, hydroxyapatite-based bone fillers and ocular implants which after successful animal trials have been assessed through clinical trials at different hospitals (Calcutta Medical Research Institute, Kolkata; Advanced Medical Research Institute, Kolkata; All India Institute of Medical Sciences, New Delhi and Moulana Azad Medical College, New Delhi for hip implants and bone fillers and Eye Care and Research Centre, Kolkata; All India Institute of Medical Sciences, New Delhi, Sir Gangaram Hospital, New Delhi, Moulana Azad Medical College, New Delhi, Shankara Nethralaya, Chennai, Sri Sankardeva Nethralaya, Guwahati, Sarojini Devi Eye Hospital, Hyderabad and Disha Eye Hospital, Barackpore) in the country. These technologies have been commercialized and available in Indian market through M/s IFGL Bioceramics Ltd., Kolkata since January, 2005. Thereafter, few of the technologies have been transferred to other Indian companies who are in the process of obtaining manufacturing license from DCGI before commercialization. The Institute has also developed coatings on metallic implants by plasma spraying hydroxyapatite/other calcium phosphates for cementless fixation in the human subjects. These clinical trailswere primarily carried out at Sancheti Institute of Orthopedic and Rehabilitation, Pune under the leaderships of Padmavibhushan Dr. K.H. Sancheti. Further, the Institute has also actively participated in few CSIR network programmes to develop coated implants using diamond-like nano-composite (DLN) and standardize laser engineered net shaping (LENS) process for development of patient specific prosthesis of irregular shapes.

In addition, the Institute has developed adequate expertise to develop different types of glass and glass-ceramic coatings on various metals and alloys including stainless steels, titanium and its alloys, nimonic and other super alloys for various engineering applications. Hydroxyapatite dispersed bioactive glass compositions for application as a coating on titanium and stainless steel implants have been developed and commercialized by M/s IFGL Bioceramics Limited, Kolkata. Coatings of glass-ceramics developed by this enameling technique showed desirable phases of calcium phosphates retained within a highly bioactive glass matrix which in turn improved the performance of the coating and made the coating process simpler. The Institute has already developed adequate infrastructure and network with the doctors to develop different types of devices. In the following sections, glimpse of few matured technologies emanated from the Bioceramics group of CSIR-CGCRI are being elaborated. In this article, we aim to provide overview of medical materials and implant technologies developed at CSIR-CGCRI, which have been successfully completed clinical trials and commercialized.

HYDROXYAPATITE BASED INTEGRATED ORBITAL IMPLANT

India is the dwelling place of over 70 lakhs of one eyed persons who are neither considered as handicapped, to avail the benefit offered by the Government, nor socially accepted for their repulsive appearance. Sometimes these people are treated and rehabilitated with orbital implants made of glass, stone, polymers etc. to fill-up the empty space of the orbital socket of the damaged, vision-less eye to improve their look but as these implants are static in nature the impaired conditions of the patients still remain evident and societal stigma exists.

* Corresponding author, E-mail:director@cgcri.res.in

To address this, CSIR-CGCRI developed a technology for manufacturing orbital eye-implant for damaged eye with synchronized movement of that of fellow healthy eye which was so far unavailable in our society. These novel implants occupy the empty space of the orbital socket of the damaged/ deformed eye and bring back the normal appearance of the eye to the patient. These porous (65-75% porosity) implants with pre-designed porosity are extremely light and the weak eye muscles can easily move them providing the synchronized motility mimicking the healthy eye. The porosity of the implants invites fibro-vascular tissue integration and within four to six months the implants become totally integrated with the system. The actual implant, developed by CSIR-CGCRI,is shown in Fig. 1 and their functional and other properties are summarized in Table1. The technology provides the manufacturing know-how of three different models which are suitable for evisceration (in those patients where muscles remain connected with the sclera) and enucleation (when muscles are detached from the sclera) surgery and in the latter variety, provisions are there for muscle fixation. Since these orbital implants are made of synthetically prepared bone minerals (hydroxyapatite) having excellent biocompatible and bioactive characteristics, do not cause any infection or other post-operative complications and has been proved to be clinically acceptable. These implants are economical (unit price is Rs. 1500-2000/- as against equivalent imported variety of Rs. 30,000/-) and readily affordable by the Indian patients. Considering that there are 70 lakhs people affected in our country, this technology can open-up an Indian market worth of above Rs. 1000 crore. In addition, there exists a huge export potential.Above all, by providing normal cosmetic and trouble-free long service, this product/ technology is expected to bring about a tremendous societal boon [1-7].

Earlier the technology was transferred to M/s IFGL Bioceramics Ltd., Kolkata, later this was transferred to another Chennai based company as well. The product had received ISO and CE Certification through M/s IFGL and regularly exported to many South-East Asian Countries apart from catering need by ophthalmic surgeons of different parts of India. Photographs of one of the patients with CGCRI developed and IFGL manufactured eye implant is given in Fig. 2, which demonstrate that they provide normal life to the patients with natural look and social acceptance. This initiative and development have been hailed by the medical community of the whole country and the activity was already acknowledged by awarding the prestigious awards like NRDC best Technology Award and Rangachary Award for best Ophthalmic Society Award from the Govt. of India, CSIR Best Technology Award as well as different professional medical bodies.

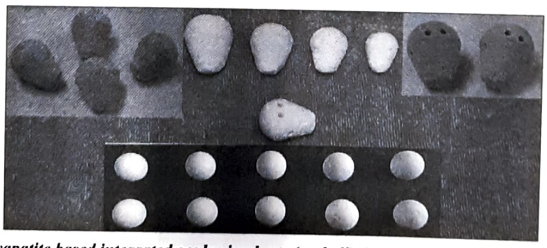

Fig. 1: Different designs of hydroxyapatite based integrated ocular implants (eyeball) developed and commercialized by CSIR-CGCRI, Kolkata.

Table 1: Properties of ocular implants

Properties	Values
Bulk density	0.6-0.8 g/c.c.
Total weight	~ 2 grams
Porosity	60-75%
Pore size	30-250 micron
Compressive strength	1-5 MPa

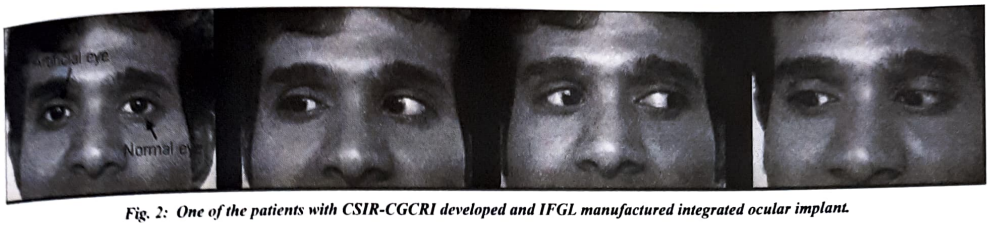

Fig. 2: One of the patients with CSIR-CGCRI developed and IFGL manufactured integrated ocular implant.

Bioactive ceramic scaffolds with controlled porosity characteristics for dental and orthopedic applications

Indian orthopaedic and prosthetic device market is valued at $450 million, and is growing at over 30% per year. High cost and affordability of devices by common people is a major concern since the industry is highly fragmented and dominated by imports with almost 80-85% of demand met through imports. Users of the products originating from this technology would be those 214 million patients suffering from different orthopaedic and dental related diseases and orthopaedic and dental market has a market of ~ 0.39 to 0.83 billion USD.

In orthopaedics, treatment of delayed union, malunion, and nonunion has been a challenge. Along with alignment-restoration and proper fixation, adjunctive measures such as bone-grafting and use of bone-graft substitutes are of great importance. Autologous bone, known to be the "gold standard" for stimulating bone regeneration, but its limited availability and the procedural complications are its main limitations. Bone-graft substitutes are known to replace autologous bone graft or expand an existing amount of autologous bone graft. Furthermore, numbers of patients with bone defects are also innumerable and most of the cases surgical procedure is the only treatment option where bone grafting is a must. This additional bone is not available from the patient and if needs an additional surgery while grafting from a donor may trigger infection or transmission of AIDS.

CSIR-CGCRI has developed process of making scaffolds based on hydroxyapatite (HAp) having different size, shape, geometry and custom shapes with high porosity for dental and bone defect filling applications [7-13]. The process provides high-purity HAp scaffolds with high crystallinity and good biological properties. Simple and economical wet chemical synthesis route was followed to synthesize HAp with calcium hydroxide and ortho-phosphoric acid as starting materials. Likewise, bi-phasic calcium phosphates (having various ratios of HAp and TCP) can also be synthesized by following a patented process [14, 15]. Fugitive materials are used for generation of highly interconnected and tailor-made porosity after firing. High-purity, crystalline and highly customized scaffolds and granules of various sizes were produced using this technology which can be used to fill bone, dental and soft tissue defects. Scaffolds and granules are having excellent tissue bonding properties and have been launched in the Indian market earlier. Technology has been transferred to one Indian company for manufacturing these scaffolds and granules intended for the above applications. Further, manufacturing of plasma spray grade spherical granules of HAp has been transferred to another Indian company. Typical properties of these scaffolds/ granules are as follows:

Composition: HAp and/ or HAp+bTCP

Bulk density = 0.5 - 2 g/c.c.

Porosity: 40 - 70%

Pore size: 100-300 micron

Scaffold/ granulessize: customized/ as per requirement

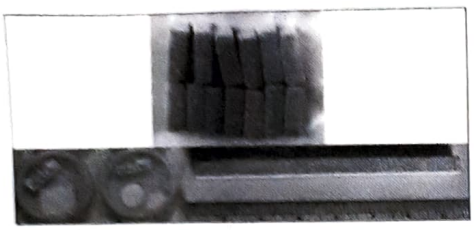

Fig. 3: Bioactive ceramic scaffolds of desired size and shape (based on HAp and/ or β-TCP)

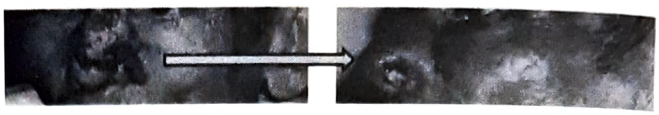

Fig. 4: Patient operated with the scaffolds for recovery of nose bone injury

Fig. 5: Calcium phosphate (based on HAp and/ or β-TCP) granules of various sizes for orthopaedic and dental filling

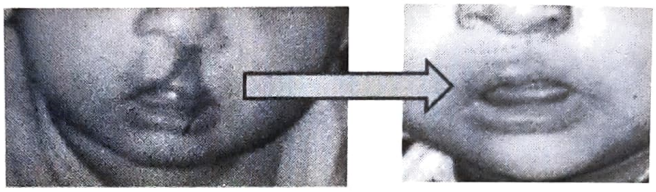

Fig. 6: Upper cleft palate recovery of child by application of bioceramic granules

Plasma spray hydroxyapatite coating on metallic biomedical implants

In orthopedic and dental application, there is a well-recognized need, of cement less fixation of metallic implants which promotes bone bonding with surrounding tissues and enables proper load transfer to prevent stress shielding. Bio-inactivity of metal surfaces, however, makes it impossible to arrive at cement-free fixation since bone tissue will not bond or grow thereon. This prevents proper load transfer and leading to a non-uniform stress distribution at the bone implant interface, which may result in an interfacial with the possible consequence of fracture in the adjacent bone. The stability of these implants require use of different polymethyl methacrylate or polymer based bone cements that may result in necrosis of surrounding tissues because of exothermic cementing reaction.

A bioactive coating with equivalent composition of a bone, offering optimum adhesion to the metal implant, bonded interfacially to the surrounding bone, is a well accepted concept to solve the problem. CSIR-CGCRI, Kolkata has developed technology for highly crystalline coating of bioactive hydroxyapatite on metallic implants using industrially popular air plasma spray system [16-20]. The coating can be deposited on variety of metallic implants for orthopedic and dental applications. CGCRI has optimized the technology with respect to the following material properties (Table 2). Recently, we have developed multi-ion doped HAp and its coating to impart osteoconductivity, improved osteogenesisand antibacterial properties. Our in vitro cell-materials interactions and antibacterial studies clearly demonstrated the potential of newly designed multi-ion HAp composition. These materials are currently under animal trials.

Table 2: Typical coating properties of plasma spray HAp coated metallic implants

Properties	Values
Coating thickness	100-200 μm
Degree of crystallinity	≥70%
Bonding/ adhesive strength	15-25 MPa
Porosity	8-12%
Roughness	7-12 μm

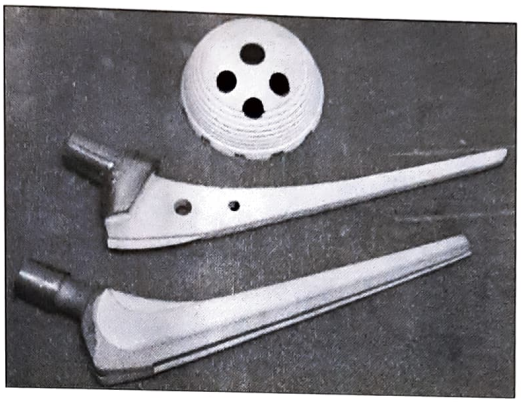

Fig. 7: Plasma sprayed hydroxyapatite coating on hip stem and acetabular shell

Alumina ceramic based femoral head and cup for total hip prosthesis (ceramic-on-PE and ceramic-on-ceramic)

Total hip replacement (arthroplasty) is one of the most common orthopaedic operations. About one lakh of patients suffer every year from the ailment of hip-joint which needs artificial joint transplantation. In India, stainless steel made prostheticsare mostly in use. The main disadvantages of these prostheses include corrosion under physiological conditions, chemical degradation and formation of wear and tear as a function of time and need periodic replacement of the implant. In other words, the patient has to undergo another operation in every five to ten years time and bear with its accompanying hazards.Indian orthopaedic and prosthetic device market is estimated to be valued at $450 million, and is growing at over 30% per year. High cost and affordability of devices by common people is a major concern since the industry is highly fragmented and dominated by imports with almost 80-85% of demand met through imports. Global market for hip replacement is: CAGR of 4.2% (2017-2024) with expected revenue ~ US$9,128.5 mn by 2024.Over 2,00,000 joint replacements operation are done in India every year.

CSIR-CGCRI, Kolkata has developed alumina ceramic-based hip joints (both ball and cup) with adequate mechanical, chemical and tribological properties as specified in ISO for similar applications. This material has been tried in animal specimens to check toxicity and biocompatibility at Bengal Immunity Research Institute, Kolkata. Tests for non-carcinogenicity and mutagenecity of the material were conducted at the University College of Medicine, University of Calcutta and the results indicated that no risk factor is involved in their implantation in human subjects. The Institute has developed hip joint prosthesis with ceramic-head as well as the cup made of high-purity alumina and fitted with the modified "Austin Moore" stainless steel stem for implantation. The later product has been clinically tried in more than 40 patients at Kolkata and Delhi initially. Thereafter, different types of hip joint implants fitted with Thomson, Charnley and Talwarkar type of stainless stems have been developed and tried in human patients. Further, alumina based ceramic heads fitted in to Ti-6Al-4V/ SS316L alloy based stems have been developed which after successful in vitro and in vivo evaluation are being implanted to human patients through many major hospitals of India which are networked with the institute. The postoperative results of all these patients have confirmed their superiority over the conventional metallic ones. Few patented stems (made of SS 316 L) having superior designs have been invented by Padmavibhushan Dr. K. H. Sancheti of Sancheti Institute for Orthopaedic Rehabilitation, Pune and these stems were also found to be suitable for the ceramic ball and cup developed by CGCRI [21-26].

The conventional hip prosthesis used presently comprises of three components: acetabular cup (made of either ultra high molecular weight polyethylene or alumina ceramic), a ceramic femoral head and a stem (either uncoated or HAp/bioactive glass coated) made out of metal. The conventional prosthesis (metal on polymer) has limited life span and is not suitable for younger patients. Other version comprises of alumina based acetabular cup and

femoral head (ceramic on ceramic) with improved mechanical properties. The use of same ceramic material in cup and head reduces friction and generates lesser amount of wear debris resulting in better performance. Above all, it increases the life of the prosthesis and minimizes the cases of revision surgeries.

The first generation (ceramic-on-PE) product launched in the Indian market in 2005 by M/s IFGL Bioceramics Ltd., Kolkata with the name of CeraHip (Fig. 8). The product had received CE and ISO certifications and regularly exported to many South-East Asian countries and few parts of Europe as well. Second generation articulation system based on ceramic-on-ceramic has been developed and single centric clinical trials have been completed (Fig. 9).Ceramic femoral head and cups were fabricated by following the process, outlined in Fig. 10. schematically. The properties of the ceramic head was closely resembled with ISO specification (6474-198L IS: 5347). A comparative chart showing the properties of ceramic head developed by CGCRI and this ISO is given in Table 3.

Following this technology, we have designed and developed new composition based on zirconia toughened alumina (ZTA) composites for total hip replacement. Different ZTA composites have been prepared, following press and sinter route, and optimized composites exhibited ~1% porosity, grain size <1μm, wear rate of 10-8mm^3/N.m, hardness of ~20GPa, and fracture toughness between 9-10 MPa root m.These femoral heads tested in hip joint simulators demonstrated gravimetric mass loss of UHMWPE cup of 0.04%. The properties of these ZTA composites indicate that they can be effectively utilized for other implant applications where toughness, strength and wear resistance are primary requirements. We have identified dental implants are one such application, which require detailed studies to establish its performance under dental related service conditions (oral environment, mastication loads and movements).

Fig. 8: Typical alumina-on-ultra high molecular weight polyethylene total hip arthroplasty (marketed as CeraHip by then M/s IFGL Bioceramics Ltd.)

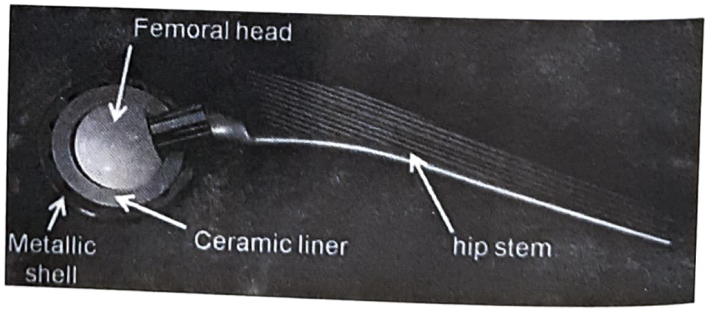

Fig. 9: Typical alumina-on-alumina total hip arthroplasty

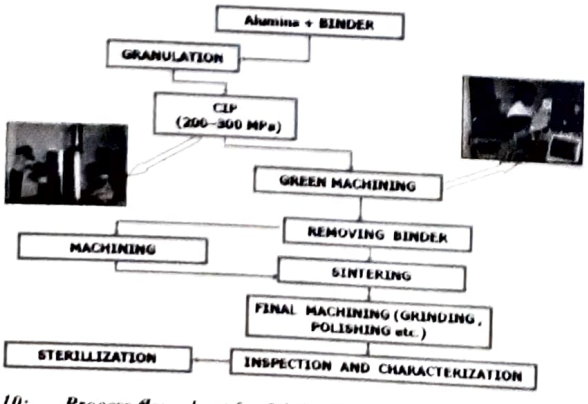

Fig. 10: Process flow chart for fabrication of ceramic head and cups

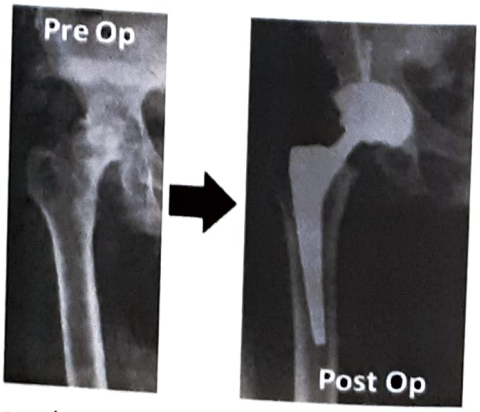

Fig. 11: Pre- and post-operative X-ray photo of the patient operated with alumina-on-alumina THR implant

Table 3: Comparison of ISO spec and CGCRI developed ceramic hip implant

Properties	ISO Spec. (6474-198L IS: 5347)	CGCRI
Density, g/c.c.	> 3.90	> 3.90
Bulk density, g/c.c.		2.70
Chem. Compⁿ	Alumina > 99.5 %	Alumina ~ 99.7 %
Micro-hardness (Vickers'), GPa	20.0	> 20.0
Comp. Stgth., MPa	4000	> 4000
Flex. Stgth., MPa	400	~ 400
Young's mod., GPa	> 350	> 350
Wear resistance [alumina pin against polished alumina disc with contact pr. of 5 MPa in distilled water medium], mm^3/hr	< 0.01	< 0.005
Coefficient of friction (Contact pr. – 5.0 MPa, Medium – Distilled water)	< 0.30	< 0.20
Corrosion resistance against Ringer's phosphate bicarbonate (p^H – 7.0 – 7.4), $mg.m^2.day^{-1}$	< 0.10	< 0.05
Surface finish (Ra), µm	< 0.05	< 0.05

An injectable biodegradable bone cement (with/ without drug)

This technology constitutes composition and preparation of self-setting, injectable bone cement with and without drug loading. Thus it refers to an artificial bone cement material which comprises at least two ceramics, one or more drugs, and at least one biodegradable polymer in the powder component. The powder component and an aqueous liquid component are mixed together to form a cement slurry that renders the paste effective for injection with a manually operated syringe and capable of hardening in vivo. The double barrier (polymer and calcium sulphatedihydrate) against the drug release from ceramic granules makes it suitable for use in the repair of infected or aseptic bone defects in a wide variety of orthopaedic and oral/maxillofacial abnormalities. The process is inexpensive and produces cement with excellent injectability, setting and biological properties.

The cement is biodegradable and self-setting at body temperature. The unique feature of this cement is "non-exothermic" reaction, which provides complete safety to tissues. Further, the cement can be used to carry drugs and deliver at site. The product can be used to fill various bone, dental and other defects [27-29].

COMPOSITION: CALCIUM SULPHATE HEMIHYDRATE

Temperature generation: 37-40°C

Liquid/ powder ratio: 0.3-0.6

Liquid: Water/ normal saline

Injectability: 88% @ 16 N

Compressive strength: 13-16 MPa

Setting time: 6 to 9 min.

CSIR-CGCRI has completed the clinical trials. Presently this cement technology is being modified with radio-opaque particles to enable post-implantation identification and evaluation of bone cement.

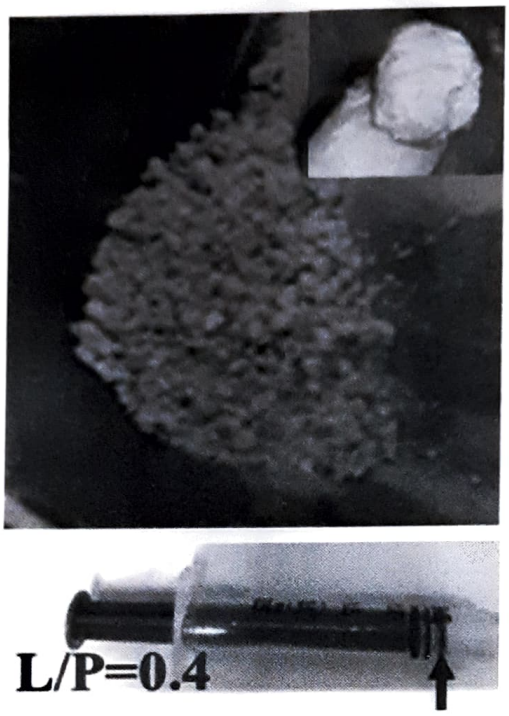

Fig. 12: Calcium sulphate hemihydrates based self-setting injectable bone cement

ACKNOWLEDGEMENTS:

Authors thank the Council of Scientific and Industrial Research (CSIR), New Delhi, India; Society for Biomedical Technology, DRDO, Bangalore, India; Indian Council of Medical Research (ICMR), New Delhi; Department of Science and Technology (DST), New Delhi, India; and Department of Biotechnology (DBT), New Delhi, India for financial support that enabled development of these indigenous medical technologies.

REFERENCES:

[1] B. Kundu, D. Sanyal, D. Basu, Physiological and elastic properties of highly porous hydroxyapatite potential for integrated eye implants: Effects of SIRC and L-929 cell lines, Ceramics International, 39: 2651-2664, 2012.

[2] B. Kundu, M.K. Sinha, D. Basu, Development of bioactive integrated ocular implant for anophthalmic human patients, Trends in Biomaterials and Artificial Organs 16: 1-4, 2002.

[3] B. Kundu, M.K. Sinha, M.K. Mitra, D. Basu, Fabrication and characterization of porous hydroxyapatite ocular implant followed by an in vivo study. Bull. Mater. Sc.27: 133-140, 2004.

[4] B. Kundu, M.K. Sinha, S. Mitra, D. Basu, Synthetic hydroxyapatite-based integrated orbital implants: A human pilot trial, Indian Journal of Ophthalmology, 53: 235-241,2005.

[5] I. Ratha, B. Kundu, Development of hydroxyapatite based modified integrated orbital implant with superior motility, J. Biotechn. Biomaterials, 5: 281,2015.

[6] D. Basu, M.K. Sinha, A process for the production of improved porous ocular implants and improved porous ocular implants produced thereby, Indian Patent, 0962DEL2001 (21/07/2006).

[7] M.K. Sinha, P.S. Sen, D. Basu, S.K. Chattopadhyay, M.K. Basu, An improved process for the synthesis of hydroxy apatite powder useful for biomedical applications, Indian Patent, 0693DEL1994 (08/01/1999).

[8] S.K. Ghosh, S.K. Nandi, B. Kundu, S. Datta, D.K. De, S.K. Roy, D. Basu, Interfacial response of hydroxyapatite and tri-calcium phosphate prepared by a novel aqueous combustion method: A comparison with bioglass in vivo implanted in goat, Journal of Biomedical Materials Research Part B: Applied Biomaterials, 86: 217-227,2008.

[9] B. Kundu, A. Lemos, C. Soundrapandian, P.S. Sen, S. Datta, J.M.F. Ferreira, D. Basu, Development of porous HAp and b-TCP scaffolds by starch consolidation with foaming method and drug-chitosan bilayered scaffold based drug delivery system, Journal of Materials Science: Materials in Medicine, 21: 2955-2969,2010.

[10] S.K. Nandi, S.K. Ghosh, B. Kundu, D.K. De, D. Basu, Evaluation of new porous b-tri-calcium phosphate ceramic as bone substitute in goat model, Small Ruminant Research, 75: 144-153,2008.

[11] S.K. Nandi, B. Kundu, S. Datta, D.K. De, D. Basu, The repair of segmental bone defects with porous bioglass: An experimental study in goat, Research in Veterinary Science, 86 : 162-173,2009.

[12] S. Mistry, D. Kundu, S. Datta, D. Basu, Effects of bioactive glass, hydroxyapatite and bioactive glass-hydroxyapatite composite graft particles in the treatment of infrabony defects, Journal of Indian Society of Periodontology, 16: 241-246,2012).

[13] M.K. Sinha, P.S. Sen, M.K. Basu, An improved process for the production of beta-tricalcium phosphate powder useful for biomedical applications, Indian Patent, 1230/DEL/94 (10/06/2000).

[14] B. Kundu, D. Banerjee, S.K. Ghosh, S. Roy, G. Banerjee, S. Nath, M.K. Sinha, D. Basu, Bioceramic materials as bone graft substitute and process for the preparation thereof, Indian Patent, 0842DEL2008 (30/10/2017).

[15] S. Datta, D. Basu, S.K. Ghosh, A process of making porous bioactive scaffolds nano sized calcium hydroxy apatite powder, Indian Patent, 0620DEL2009 (27/08/2015).

[16] A. Dey, A.K. Mukhopadhyay, S. Gangadharan, M.K. Sinha, D. Basu, Characterization of microplasma sprayed hydroxyapatite coating, Journal of thermal spray technology, 18: 578-592,2009.

[17] A. Dey, A.K. Mukhopadhyay, S. Gangadharan, M.K. Sinha, D. Basu, Weibull modulus of nano-hardness and elastic modulus of hydroxyapatite coating, Journal of Materials Science, 44: 4911-4918,2009.

[18] A. Dey, A.K. Mukhopadhyay, S. Gangadharan, M.K. Sinha, D. Basu, Development of hydroxyapatite coating by microplasma spraying, Materials and Manufacturing Processes, 24: 1321-1330,2009.

[19] A. Dey, S.K. Nandi, B. Kundu, C. Kumar, P. Mukherjee, S. Roy, A.K. Mukhopadhyay, M.K. Sinha, D. Basu, Evaluation of hydroxyapatite and b-tri calcium phosphate microplasma spray coated pin intra-medullary for bone repair in a rabbit model, Ceramics International, 37: 1377-1391,2011.

[20] S. Datta, D. Basu, A synergistic composition useful for making porous bioactive scaffold, bone filler material and bioactive coating on implants, Indian Patent, 0628DEL2009 (05/10/2016).

[21] R. Singha Roy, A. Mondal, A. Chanda, D. Basu, M.K. Mitra, Sliding wear behavior of submicron-grained alumina in biological environment, Journal of Biomedical Materials Research Part A, 83: 257-262,2007.

[22] K.K. Phani, S. Mukherjee, D. Basu, Ultrasonic characterization of zirconia-toughened alumina ceramics, Journal of the American Ceramic Society, 79: 3331-3335,1996.

[23] A. Chanda, A.K. Mukhopadhyay, D. Basu, S. Chatterjee, Wear and friction behaviour of UHMWPE-alumina combination for total hip replacement, Ceramics International, 23: 437-447,1997.

[24] R. Singha Roy, D. Basu, A. Chanda, M.K. Mitra, Distinct wear characteristics of submicrometer-grained alumina in air and distilled water: A brief analysis on experimental observation, Journal of the American Ceramic Society, 90: 2987-2991,2007.

[25] D. Basu, Fatigue behaviour of fine-grained alumina hip-joint heads under normal walking conditions, Sadhana, 28: 589-600, 2003.

[26] D. Basu, S. Chatterjee, R. Das, L.K. Naskar, D.K. Naskar, M.K. Basu, An improved hip joint prosthesis, Indian Patent, 690/ DEL/94 (15/01/2004).

[27] S. Mistry, S. Roy, N.J. Maitra, B. Kundu, A. Chanda, S. Datta, M. Joy, A novel, multi-barrier, drug eluting calcium sulfate/ biphasic calcium phosphate biodegradable composite bone cement for treatment of experimental MRSA osteomyelitis in rabbit model, Journal of Controlled Release, 239: 169-181,2016.

[28] C. Khatua, S. Sengupta, B. Kundu, D. Bhattacharya, V.K. Balla, Enhanced strength, in vitro bone cell differentiation and mineralization of injectable bone cement reinforced with multiferroic particles, Materials & Design, 167: 107628,2019.

[29] S. Mistry, S. Datta, S. Datta, B. Kundu, An injectable biodegradable bone cement composite and a process for the preparation thereof, Indian Patent, 1979DEL2015 (01/07/2015).

Journal of Metallurgy and Materials Science, Vol. 62, No. 3-4, July-December 2020, pp. 59-70
Printed in India, © NML, ISSN 0972-4257

Mg-based biodegradable alloys for orthopedic implants - A review

ANSU J KAILATH* and ARVIND SINHA
Advanced Materials and Processing Division CSIR-National Metallurgical Laboratory Jamshedpur 831007

Abstract : Traditional metallic biomaterials for orthopedic implants require materials exhibiting excellent corrosion resistance in human body. Recently, implants made of biodegradable metallic materials are thought to be potential for orthopedic implant applications as they can circumvent revision surgeries. These implants are considered as the third generation implants as they are expected to provide adequate mechanical strength to support the bone during restoration; have excellent in vivo biocompatibility and controlled degradation rate. These implants would degrade within the body after completing its mission without leaving any residues within the body. Biocompatible elements like Mg, Fe and Zn and their alloys have been considered for bone implant applications due to their biodegradability. Amongst these, Mg alloys are preferred due its high specific strength, low elastic modulus that are close to human bone and low density minimizing the risk of stress shielding. However, Mg alloys have fast degradation rate in biological fluids leading to the release of hydrogen which would lead to premature failure of implants. This paper reviews the research efforts towards the development of Mg-based biodegradable alloys for orthopedic implants. Concepts followed in designing Mg-based biodegradable alloys, the mechanical properties of developed Mg-based alloys, degradation mechanism of Mg-based alloys and the efforts to reduce the degradation rate, and status of Mg-based alloys in orthopedic applications are compiled along with the existing problems and future research directions.

Keywords: *Biodegradable alloys, Orthopedic implants, Mg-based alloys*

INTRODUCTION

Demand of orthopedic implants are dramatically increasing because of the increasing aging population and also due to the rise in accidents and injuries[1,2]. Some of the orthopedic procedures require permanent implants which need to stay within the body as they replace a body part; whereas most of the orthopedic procedures require only temporary implants to support the bone during healing and needs to be removed once the healing completes[3,4]. Partial functional substitutes of natural bones have been done by permanent implants made of titanium alloys, stainless steel and cobalt-chromium alloys[5]. However, when these alloys are used as temporary support during healing, they need to be removed through a second surgery after the patient recovers. The revision surgery would certainly burden the patients with additional expenditure and pain. Therefore, use of biodegradable implants as temporary implants can avoid revision surgeries. These implants would degrade within the body and are replaced gradually by the growing tissues[6,7]. The materials suitable for these applications should have similar or slightly higher elastic modulus, strength and hardness as compared to human bone. These materials should not induce any sort of irritation, inflammation, and toxicity within the body; on the other hand, they should be biocompatible and promote cell growth (osteogenesis)[8,9]. The degradation products produced from these materials should be non-toxic and capable of entering into the metabolic activities of the body. Biodegradable polymers viz. polylactic acid (PLA), polyglyclid acid (PGA), biodegradable bioglasses, bioceramics and biodegradable metallic materials have been developed as the third generation implant materials[10]. Biopolymers have excellent biocompatibility but their mechanical strength is not sufficient for load bearing applications[11,12]. Metallic biomaterials have better mechanical properties as compared to bioglasses and biocermaics.

Recent research efforts have been focused on developing magnesium, iron and zinc based metallic biodegradable materials[12]. Mg alloys are easy to machine and have low density, high specific strength and comparable modulus of elasticity with human bone[13,14]. Therefore, Mg-based alloys are preferred over Fe-based and Zn-based alloys for implant applications. Mg is a biocompatible element when implanted within the body which degrades to

*Corresponding Author E-mail: ansu@nmlindia.org

produce an oxide which is soluble and non-toxic. Mg^{2+} ions are one of the most abundant cations present in human body and is involved in many metabolic reactions. However, Mg being a group IIA element, is highly active and form porous oxide film on its surface with the evolution of hydrogen gas[3,15]. These films fall off in solutions containing chlorine ions thus accelerating degradation.

Efforts on the development of Mg-based biodegradable alloys for orthopedic implant applications are reviewed in this paper. Alloy design strategy, mechanical properties of the developed alloys, degradation mechanism and the methods to lower the degradation rate are reviewed. Present status of Mg-based biodegradable alloys in orthopedic applications and the unresolved problems are discussed along with the future research directions.

BIODEGRADABLE METALLIC MATERIALS

Though the medical field has been using biodegradable polymer sutures for many years, the concept of metallic implants that degrades can be considered as a novel concept. This has broken the conventional paradigm that metallic biomaterials for implant applications should be corrosion resistant[16]. Biodegradable metallic materials should have the following characteristics; (i) it should be made of metals, (ii) it should provide adequate mechanical support during the healing process, (iii) the mechanical properties of the implant material should be comparable with human bone or slightly better, (iv) it should corrode within the body by releasing corrosion products which are non-toxic, (v) it should not leave any implant residues. This restricts the biodegradable metallic materials to be made of (at least) an essential metallic element that can be metabolized by the human body[17]. The mechanical properties of conventional metallic biomaterials, Mg-based biodegradable alloys and human cortical bone are compiled in Table-1 along with their advantages and disadvantages. Last few decades have witnessed active research on the development of biodegradable Mg alloys because of the similarity in their mechanical properties with human bone. However, their applications are constrained due to the high degradation rate with hydrogen evolution. An overview of the research efforts on developing Mg-based biodegradable alloys are given in the following sections.

Mg-BASED BIODEGRADABLE ALLOYS

Mg alloys have been well investigated and established for automobile and aerospace applications; however, these alloys are not suitable for biodegradable implants due to the presence of toxic elements. Therefore, several newer Mg alloys have been developed for biodegradable implant applications as revealed by the huge number of publications dealing with microstructure studies, mechanical property evaluation, degradation characteristics and in vitro and in vivo biocompatibility studies.

Concepts of alloy design

Though pure Mg is highly biocompatible and attractive for bio-implant applications, its mechanical property is relatively low; yield strength of as-cast Mg is ~ 21 MPa which increased to ~ 105 MPa on extrusion[19]. Degradation rate of pure Mg is 2.89 mm/year in 0.9 % NaCl solution[20]. Therefore, several alloys have been developed to improve their mechanical and degradation properties. Mechanical property enhancement can be achieved through (i) solid-solution strengthening, (ii) precipitation strengthening, and (iii) grain refinement[21]. Generally, alloying elements with high solubility in Mg are chosen for strengthening. Atomic diameter of Mg is 0.320 nm and is hexagonal close packed structure with a c/a ratio 1.624[22]. It forms solid solution with a wide range of elements; the solubility limits of the main alloying elements are given in Table 2. Mg alloys, containing elements (Al, Zn, RE) having high solubility in Mg, exhibits precipitation hardening. On the other hand, the alloys made of elements having poor solubility (Si, Ca) do not exhibit strengthening by heat treatment. Grain refinement is another method to increase the mechanical properties and corrosion resistance of Mg alloys. Grain strengthening is governed by the famous Hall-Petch equation (1).

$$\sigma = \sigma_0 + kd^{-1/2} \quad ...(1)$$

where, yield strength is σ material constant is σ_0, k is the strengthening coefficient and d is the average diameter of the grain. The strengthening coefficient of Mg alloys (280-320 MPa $\mu m^{1/2}$) is several times higher than many face centered cubic (for Al, k is 68 MPa $\mu m^{1/2}$) and body centered cubic metals. Therefore, strengthening of Mg alloys by grain refinement is much more effective[23]. Studies have revealed excellent grain refinement by the addition of Zr, Ca and Si in magnesium. Plastic deformation and/or severe plastic deformation also induces grain refinement; in addition, it can create high density of dislocations and stacking faults in the material.

Table -2 : Main alloying elements in Mg and their solubility limits[6, 24-26]

Element	Solubility limit (wt.%)	Element	Solubility limit (wt.%)	Element	Solubility limit (wt.%)
Ag	15.0	Ho	28.08	Sm	~6.4
Al	12.70	In	53.2	Sn	14.5
Ca	1.34	La	0.23	Sr	0.11
Cd	100	Li	5.5	Tb	24.0
Ce	0.74	Lu	~41	Th	4.75
Dy	25.8	Mn	2.2	Tm	31.8
Er	33.8	Nd	3.6	Y	12.4
Eu	0	Pr	~0.6	Yb	8.0
Ga	8.5	Sc	~24.5	Zn	6.2
Gd	23.49	Si	~0	Zr	3.8

Therefore, selection of alloying elements for developing biodegradable Mg alloys should consider (i) the toxicity, (ii) the strengthening ability, and (iii) the influence of corrosion behavior. With regard to the toxicity level, elements are broadly classified as (a) elements (Ca, Mn, Si, Sn, Zn,) that are nutrients to humans, (b) elements (Ag, Al, Bi, Li, Sr, Zr) that are nutrients to plants and animals, (c) elements (Al, Ce, Co, Cr, Cu, La, Ni, Pr) that create allergy and liver toxicity in humans and (d) toxic elements (Ba, Be, Cd, Th, Pb)[25,27,28]. According to the strengthening ability, elements are divided as: (1) elements that can enhance both the strength and ductility (Al, Zn, Ca, Ag, Ce, Ni, Cu, Th), (2) elements that enhance the ductility reasonably with very scarce improvement in strength (Cd, Li, Tl), (3) elements that augment the strength and reduce the ductility (Bi, Pb, Sb, Sn), (4) impurities (Co, Cu, Fe, Ni)[24,22,29]. Alloying elements influence the corrosion behavior of Mg alloys; the electrochemical potential of magnesium is -2.37 V. Corrosion resistance can be improved by reducing the internal galvanic corrosion by choosing elements (Ce: -2.48 V, Nd: -2.43 V, Y: -2.37 V) with similar electrochemical potential as Mg or the elements that form intermetallic phases. A brief overview of the different Mg-alloy families developed for biodegradable application is given below:

MECHANICAL PROPERTIES OF Mg ALLOY FAMILIES

Mg-Al based alloys

Solubility of Al in Mg is very high (12.7 wt.%) and hence many Mg-Al alloys have been developed for automotive and aerospace applications. Al addition in Mg results solid solution strengthening due to the formation γ-$Mg_{17}Al_{12}$ and α-Mg phases. These alloys possess good castability, reasonable mechanical properties and good corrosion resistance[21]. Zinc and manganese are added to Mg-Al alloys to produce AZ and AM series alloys to improve the strength and ductility at room temperature[30-34]. As-cast AZ91 exhibited 145 MPa yield strength (YS), 275 MPa ultimate tensile strength (UTS) and 6% elongation. This alloy on undergoing (two-step) equal channel angular pressing (ECAP) resulted in enhancing its YS to 290 MPa, UTS to 417 MPa and elongation to 8.45 %[35]. Typical

Table-1 Mechanical properties of conventional metallic biomaterials, Mg-based biodegradable alloys and human bone with their advantages, disadvantages and applications[10,18]

Material	Mechanical Properties				Advantages	Disadvantages	Applications and Remarks
	Density gm/cm^3	Elastic Modulus (GPa)	Yield Strength (MPa)	Tensile strength (MPa)			
Stainless Steel (316L)	7.9	190	221-1213	586-1351	Cheap & readily available Good machinability High fracture toughness Biocompatible	High modulus, results in stress shielding Poor resistance to wear & corrosion Allergy around the implant	1st generation implants Bone plates, Bone screws, Bone Pins & Wires
Co-Cr alloys	7.8	210-253	448-1606	655-1896	Superior corrosion resistance, fatigue & wear High strength Long term biocompatibility	High modulus, results in stress shielding Expensive Difficult to machine Co, Cr & Ni ion toxicity	1st generation implants Popular implant material for joint bearing applications
Ti alloys	4.4	110	485	760	Low density and low modulus of elasticity High specific strength Superior corrosion resistance High biocompatibility	Poor wear resistance Poor bending ductility Expensive	2nd generation implants Fracture fixation plates, screws, rods, nails & wires Total joint replacement (TJR) arthroplasty- hips & knees
Mg-based biodegradable alloys	1.74	45	130	220	Biodegradable/Bioabsorbable Biocompatible, Density & young's modulus close to bone, no stress shielding High tissue growth	High degradation rate with evolution of Hydrogen	Categorized as 3rd generation implants
Human Cortical Bone	1.8-2.0	5-23	104.9-114.3	35-283		-	-

AM60 alloy exhibiting an ultimate tensile strength of 160 MPa and elongation 3%, on rolling (80% reduction) yielded UTS of 378 MPa and elongation of 12% [35]. Grain refinement and precipitation ($Mg_{17}Al_{12}$) strengthening are the reasons for improving the mechanical properties [35]. However, Al is neurotoxic and is not suitable for developing biodegradable alloys.

Mg-Ca and Mg-Sr based alloys

Calcium and strontium are Gr II elements with similar properties. The solubility of Ca and Sr in Mg are 1.34 wt.% and 0.11 wt.%; addition of these elements in more quantities results in the precipitation of Mg_2Ca and $Mg_{17}Sr_2$ along their grain boundaries. The mechanical properties including creep at elevated temperature improves due to the formation of thermally stable intermetallic phases. The tensile strength and elongation of Mg-Ca alloys reduced when the Ca content increased from 1 to 3 wt.%[36]. Addition of 0.6 wt.% Ca improved the bending and compressive strength in Mg-Ca alloys; further addition weakened the properties[37]. Addition of 1 wt.% Y in Mg-1Ca decreased the compressive strength but increased the ductility[38]. The incorporation of 2.31 wt.% Zn in $Mg_{.3}Ca$ alloy improved the strength and ductility[39]. In binary Mg-Sr alloys, the strength increased and elongation reduced till the Sr content increased to 3 wt.%; at higher Sr content the properties deteriorated. Investigation on as-rolled Mg-Sr alloys containing Sr 1-4 wt.%, revealed that the $Mg^{-2}Sr$ alloy has the highest UTS. Therefore, Mg-Ca alloys containing Ca < 1 wt.% and Mg-Sr alloys containing Sr < 2 wt.% are preferred for biodegradable Mg-alloy applications.

Mg-Zn based alloys

Zinc has a solubility of 6.2 wt.% in Mg and forms α-Mg matrix and γ-MgZn phase[40]. The addition of Zn (1 to 6 wt.%) results increasing yield strength (YS); however, Zn content should be limited to 4 wt.% to achieve maximum ultimate tensile strength (UTS) 216.8 MPa and elongation 15.8 %[40]. Mg-Zn alloys with less than 4 wt.% Zn are also alloyed with third alloying elements like Ca[40,41], Mn[42], Sr[43], Y[44], and Zr[45]. When the Ca content in Mg-based alloys is more than 1 wt.%, the strength and ductility of the alloys decreased with increasing Ca content[36]. In $Mg_{.4}Zn$ based alloys, the UTS and ductility decreased when the Ca content is above 0.5 wt.%[40]. Though the microstructures of $Mg^{-2}Zn$ alloys refined with the addition of Ca, Sr and Y, their mechanical properties had very little enhancement[40,41,43,44]. Zirconium is a good grain refiner in Mg-Zn alloys; addition of 0.4 to 0.6 wt.% Zr to $Mg_{.3}Zn$ and $Mg_{.6}Zn$ resulted in grain refinement effectively to produce ZK30 and ZK60 alloys respectively. ZK 30 alloy exhibited yield strength of 215 MPa, ultimate tensile strength of 300 MPa and elongation of 9%. The yield strength, ultimate tensile strength and elongation of ZK60 alloy are 235 MPa, 315 MPa and 8% respectively[45]. Addition of 0.2 wt.% Zr in $Mg^{-2}Zn$ alloy enhanced UTS from 146 MPa to 187 MPa, and elongation from 12 % to 18 %. $Mg_{97}Zn_1Y_2$ (at.%) produced by rapid solidification processing is the strongest (YS: 610 MPa & elongation: 5 %) Mg alloy produced so far[46]. $Mg_{97}Zn_1Y_2$ alloy on extrusion resulted in getting 390 MPa yield strength and 5% elongation[47]. The high strength of Mg-Zn-Y alloys is attributed to the fine grain size, dispersion of hard lamellar phase and occurrence of long-period stacking ordered (LPSO) structure[47].

Mg-Si based alloys

Solubility of Si in Mg is very low (0.003 wt.%) and it reacts with Mg forming intermetallic compound Mg_2Si. Therefore, Mg-Si alloys have initially been developed as magnesium matrix composites[48]. Mg_2Si has low density, high melting temperature, high hardness and low thermal expansion. The precipitation of Mg_2Si phase can efficiently strengthen Mg alloys. However, coarse Chinese script Mg_2Si reduce the ductility; with 0.3 to 2.3 wt.% Si addition ductility limits to < 10%. The highest YS, UTS and elongation obtained with 0.8 wt.% Si addition are 52 MPa, 152 MPa and 9.5 % respectively[49]. Though, the addition of Ca in Mg-Si alloys can refine

the grains and change the morphology of Mg_2Si precipitates, their strength and ductility could not be improved[50]. Addition of 1.5 wt.% Zn to $Mg_{0.6}Si$ alloy modified the coarse eutectic structure of Mg_2Si to dot or small bar like structure. As a result, the mechanical properties of the alloy improved.

Mg-Sn based alloys

The ultimate tensile strength and elongation of the as-cast Mg-Sn alloys increased with Sn content up to 5 wt.%, further addition of Sn deteriorated the strength and ductility[51]. Addition of Ca in Mg_5Sn alloy refined the dendritic microstructure and inhibited Mg_2Sn formation resulting in improved creep resistance and shear strength[52]. The strength and elongation of as-cast Mg1Sn alloy is higher than pure Mg[25]. Mg-Sn-Mn alloys with Sn content varying from 1 to 3 wt.% and Mn content varying from 0.5 to 1 wt.% are designed for stent applications; best combination of mechanical properties and corrosion resistance is shown by as-rolled $Mg_3Sn_{0.5}Mn$[53].

Mg-Zr based alloys

Maximum solubility limit of Zr in Mg is 3.8wt.% and is a powerful grain refiner for Mg alloys. Zr is added in Mg alloys containing zinc, rare earth elements, yttrium and thorium. However, Zr could not be used in alloys containing aluminum and manganese as it forms stable compounds with them[19]. Because of its high specific damping capacity Mg-Zr alloys have attracted research interests as it can reduce the vibrations created during movement at the interface of bone and implant[54]. Addition of 1 wt.% Zr in Mg improved the UTS to 172 MPa and elongation to 27 %[25]. Effect of the addition of Sr and Zr is investigated in Mg_xZr_ySr alloys (x and y ≤ 5 wt.%). Microstructure of the alloys revealed α-Mg matrix, $Mg_{17}Sr_2$ intermetallic phase and unalloyed Zr. The compressive yield strength and the ultimate compressive strength and the ductility obtained from the alloys are 65 to125 MPa, 200 to 290 MPa and 14 to 38 % respectively[55]. The tensile strength and the elongation of Mg-Zr-Ca alloys increased when the Zr content increased from 0.5 wt.% to 1 wt.%[56]. As cast Mg1Ca1Zr exhibited a UTS of 125 MPa and elongation of 8%. Zhou et al reported that the $Mg_{0.5}Zr_1Ca$ alloy is a single phase (α-Mg) but, $Mg_{0.5}Zr_2Ca$ and $Mg_1Zr(1,2)Ca$ alloys consist of α-Mg and Mg_2Ca phases. The strength and ductility of these alloys are ≤ 135 MPa and ≤ 8% respectively; Mg_2Ca formation along the grain boundaries deteriorates the mechanical properties[56].

Mg-Y and Mg-RE based alloys

The addition of rare earth elements to Mg helps in improving the high temperature properties, creep resistance and corrosion resistance[57-59]. Rare earth elements can be divided into two groups according to their solid solubility in Mg as (i) elements possessing high solubility in Mg (Y, Gd, Tb, Dy, Ho, Er, Tm, Yb and Lu, (ii) elements possessing limited solubility in Mg (Nd, La, Ce, Pr, Sm and Eu[1]. These elements can also be classified as light REE (La, Ce, Pr, Nd and Pm) and heavy REE (Sm, Eu, Gd, Tb, Dy, Ho, Er, Tm, Yb and Lu)[60].

Solubility of La, Ce and Nd in Mg are 0.23 wt.%, 0.74 wt.% and 3.6 wt.% respectively; addition of these elements in Mg would result in the precipitation of intermetallic phases leading to galvanic corrosion. The volume of the intermetallic precipitates increased with the REE content (0 to 5 wt.%) which results in faster degradation in 0.1 M HCl solution[61,62]. A series of Mg-Nd-Zn-Zr alloys, containing 2 – 4 wt.% Nd, 0.1 to 0.5 wt.% Zn and 0.3 to 0.6 wt.% Zr are developed for biomedical applications. These alloys after extrusion exhibited very good mechanical properties (UTS: 300 MPa and elongation 30 %)[63]. The YS, UTS and elongation of as-cast $Mg_3Nd_{0.2}Zn_{0.4}Zr$ alloy are 90 MPa, 194 MPa and 12 % respectively. On extrusion, the mechanical properties of this alloy improved due to grain refinement and dynamic precipitation of $Mg_{12}Nd$ phase[64]. Long-period stacking ordered (LPSO) structure is reported in Mg-RE based alloys (RE = Dy, Er, Gd, Ho, Tb, Tm) when Zn is added as the third alloying element[65]. This LPSO structure exhibits very high plasticity and toughness. The critical resolved shear stress (CRSS) of basal slip (0001)<11-20> of the LPSO structure is 10 to 30 times than that of pure Mg at room

temperature[66]. To cite an example, the YS and UTS of extruded $Mg_{7.25}Y_{0.31}Zn$ alloy are 149 MPa and 246 MPa respectively. The extruded $Mg_8Y_1Er_2Zn$ alloy containing LPSO exhibited much higher strength (YS: 275 MPa and UTS: 359 MPa)[67].

The elements possessing very high solubility at eutectic temperatures (Y: 11.4 wt.%, Dy: 25.3 wt.% and Gd: 23.49 wt.%) in Mg are selected for designing biomedical alloys to avoid intermetallic phase formation. Mechanical and degradation properties can be tailored over a wide range by the addition of a single (above mentioned) REEs. Since solid solubility is temperature dependent, properties of Mg-REEs can also be modified by subsequent heat treatment. In general, the strength of the alloys increased with increasing amount of Y, Dy and Gd, but ductility decreased. The degradation rate of these binary alloys depend on the concentration of each element alloyed[68-70]. The YS, UTS and elongation of the extruded $Mg_{11.3}Gd_{2.5}Zn_{0.7}Zr$ alloy are 281 MPa, 341 MPa and 13.5 %. Though this alloy has good bio-corrosion rate, it has slight cytotoxicity[71].

CORROSION

In spite of knowing the electrochemical potential and the corrosion behavior of pure Mg, the degradation behavior of multi-component Mg alloys are difficult to predict. This is due to the microgalvanic corrosion which occurs between the intermetallic phases and the matrix because of the potential difference[72]. The details of the various phases and their potential are not available in most of the newer alloys. Mg alloys undergo degradation in aqueous environment through electrochemical reactions.

$$Mg_{(s)} + 2H_2O \longrightarrow Mg(OH)_{2(s)} + H_{2(g)} \quad \text{.....(2)}$$

As seen in equation (2), magnesium hydroxide and hydrogen gas is produced[73]. This magnesium hydroxide forms a protective layer in water preventing corrosion; however this changes to $MgCl_2$ (soluble) when the concentration of chloride ions >30 $mmol^{-1}$[73]. The biggest constraint of the Mg-based alloys for orthopedic application is the evolution of hydrogen gas which accumulates around the implant[74]. Evolution of hydrogen can be minimized by improving the Mg-alloy quality; one approach is to develop Mg-based metallic glasses with high Zn content beyond the alloying threshold of Zn, second approach is to improve the corrosion resistance of the alloys which in turn minimize the evolution of hydrogen. The corrosion rate of pure Mg is very high as compared to some of the newly developed Mg-alloys. Corrosion rate can still be improved by alloy design, post processing methods viz. heat treatment, extrusion, rolling etc. and surface modification.

Corrosion resistance also depends on the processing methods followed for the development of the Mg-based alloys. Investigation of the corrosion behavior of as-cast, as-rolled and ECAPed AZ31 alloy is done in Hank's solution. It is reported that the corrosion rate of as-rolled AZ31 is much lower than that of the as-cast AZ31. Further reduction in corrosion rate is not observed in ECAPed AZ31, though the ECAPed AZ31 has much finer grain size than the as-rolled AZ31[75]. The corrosion rates of extruded Mg-Ca[36], Mg-Nd-Zn-Zr[76], and ZK60[77] alloys is lower than the corresponding as-cast alloys. Increase in (i) the density of grain boundaries, (ii) dislocation density and (iii) redistribution of the second phase contribute to the observed improvement of corrosion resistance.

Selection of proper alloying elements is very critical to improve the corrosion resistance of Mg-based alloys. Research efforts have shown that the addition of Al[31], Ca[50], Mn[74], Sn and Sr[78], Zn[41,50], Zr[55] and most REEs including Gd[68] and Nd[64] improved corrosion resistance. The majority of elements have shown a critical limit of alloying addition up to which the corrosion resistance increased and beyond which corrosion resistance deteriorated[36,41,68]. Corrosion resistance can also be controlled by adopting suitable heat treatment protocols to generate single-phase microstructure, and to produce fine and uniform distribution of precipitates[64,79]. Another approach for improving corrosion resistance is by adopting suitable surface modification[80,81]. On the other hand, excessive corrosion occurs when the protective coating develops a minor defect or failure[75].

Orthopedic applications of Mg-based biodegradable alloys

Requirement of orthopedic implants are increasing due to the increased fractures and injuries occurring worldwide. Increased quality of life demands biodegradable bone implants; thus the market for the plates, screw, nails, pins, wires and needles made of Mg-based biodegradable alloys is huge. Mg-based alloy screws made of MgCa0.8[82] MgYREZr[83], LAE442[84] and ZEK 100[85] alloys have been fabricated for animal studies and clinical trials. Osteogenic properties of Mg-based alloys are confirmed in animal trials. Hydrogen gas evolution is not reported in both $MgCa_{0.8}$ and LAE442 alloys. The bone-implant contact in MgCa0.8 alloy is better than that of LAE442 indicating the superior biocompatibility of MgCa0.8 alloy[86]. The mechanical properties of MgCa0.8 screws in the first 2-3 weeks after implantation in adult rabbits are comparable to SS316L[82]. MAGNEZIX (R) screw made of MgYREZr alloy is observed to be clinically similar to standard titanium screw used for the treating the deformities of mild hallux valgus[83]. There are no reports of any inflammatory reactions or other complications in this clinical trial.

CONCLUSIONS AND FUTURE RESEARCH DIRECTIONS

This review summarizes the progress made in the development of Mg-based biodegradable alloys for bio-implant applications. Mg-alloys for implant applications should provide adequate mechanical properties, degradation rate and biocompatibility[87,88]. Therefore, development of Mg-based alloys with superior properties is very crucial. It is known that the microstructure of the alloys depend on alloy composition, alloy preparation method, post processing techniques (heat treatment, mechanical working) and the amount of impurities present in it. Studies so far has shown that Mg-RE- based alloys have exhibited sufficient mechanical properties and reasonable corrosion resistance. As a result, stents and screws made of these materials have passed animal trial and are in clinical trials. Mg-Zn-based alloys are also potential alloys for bio-implant applications because of their mechanical properties. Therefore, future research directions towards development of Mg-based alloys should focus on the following aspects: (i) to develop Mg-based alloys possessing suitable mechanical properties and degradation rate by alloy design (element selection & controlling impurities), method of alloy preparation, post processing techniques (heat treatment, mechanical working), (ii) to develop functional Mg-based alloys using the nutritional elements of the human body viz. Ca, Mn, Sn, Sr, (iii) to understand the biological degradation of the implant especially at the implant / tissue interface.

REFERENCES

[1] Feyerabend, F.; Fischer, J.; Holtz, J.; Witte, F.; Willumeit, R.; Dru¨cker, H.; Vogt, C. and Hort, N., Evaluation of short-term effects of rare earth and other elements used in magnesium alloys on primary cells and cell lines, Acta Biomater. 6: 1834–1842, 2010.

[2] Tian, P. and Liu, X., Thermodynamic analysis of phase stability of nanocrystalline titania, Regener. Biomater. 2: 135–151,2015.

[3] Tan, L.; Yu, X.; Wan, P. and Yang, K., Biodegradable Materials for Bone Repairs: A Review, J. Mater. Sci. Technol. 29: 503–513, 2013.

[4] Levy, G. and Aghion, E., Effect of diffusion coating of Nd on the corrosion resistance of biodegradable Mg implants in simulated physiological electrolyte, Acta Biomater. 98624–8630, 2013.

[5] Wu, S.; Liu, X.; Yeung, K.W.K.; Guo, H.; Li, P.; Hu, T.; Chung, C.Y. and Chu, P.K. , Surface nano-architectures and their effects on the mechanical properties and corrosion behavior of Ti-based orthopedic implants, Surf. Coat. Technol. 233: 13–26, 2013.

[6] Zheng, Y.F.; Gu, X.N. and Witte, F. Biodegradable metals, Mater. Sci. Eng. R. 77: 1–34, 2014

[7] Cheng, J.; Liu, B.; Wu, Y.H. and Zheng Y.F., Comparative in vitro Study on Pure Metals (Fe, Mn, Mg, Zn and W) as Biodegradable Metals, J. Mater. Sci. Technol. 29: 619–627, 2013.

[8] Elrahman, S.S., Neuropathology of aluminum toxicity in rats (glutamate and GABA impairment), Pharmacol. Res. 47: 189–194, 2003.

[9] Nakamura,Y.; Tsumura, Y.; Tonogai, Y. and Shibata T., J. Health Sci. 45: 15–18, 2008.

[10] Chen, Q. and Thouas, G.A., Metallic implant biomaterials, Mater. Sci. Eng. R. 87: 1-57, 2015.

[11] Zhao, D.; Witte, F.; Lu, F.; Wang, J.; Li, J. and Qin L, Current status on clinical applications of Magnesium-based orthopaedic implants: A review from clinical translational perspective, Biomaterials 112: 287–302, 2017.

[12] Heiden, M.; Walker, E. and Stanciu, L Magnesium, iron and zinc alloys, the trifecta of bioresorbable orthopaedic and vascular implantation-a review, J. Biotechnol. Biomater. 5:2:1-9,2015, doi:https://dx.doi.org/10.4172/biotechnology-biomaterials.1000178

[13] Persaud-Sharma, D. and McGoron, A., Biodegradable magnesium alloys: A review of material development and applications. J. Biomim. Biomater. Tissue Eng. 12:25–39. doi: 10.4028/www.scientific.net/JBBTE.12.25, 2012.

[14] Shih, T.S.; Liu, W.S. and Chen Y.J., Fatigue of as-extruded AZ61 magnesium alloy, Mater. Sci. Eng. A. 325: 152–162, 2002.

[15] Seal, C.; Vince, K. and Hodgson, M. A., IOP Conf. Ser.: Mater. Sci. Eng. 4, 012011:1, 2009.

[16] Hermawan, H., Biodegradable Metals: State of the Art. In: Biodegradable Metals, Springer, Briefs in Materials. Springer, Berlin, Heidelberg. https://doi.org/10.1007/978- 3-642-31170-3-2, 2012.

[17] Zheng,Y.F.; Gu, X.N. and Witte F., Biodegradable Metals, Mater. Sci. Eng. R. Rep. 77: 1-34, 2014.

[18] Witte, F.; Kaese, V.; Haferkamp, H.; Switzer, E.; Meyer-Lindenberg, A; Wirth, C.J. and Windhagen, H., In vivo corrosion of four magnesium alloys and the associated bone response, Biomaterials 26: 3557-3563, 2005.

[19] Friedrich, H.E. and Mordike, B.L., Magnesium Technology—Metallurgy, Design Date, Applications, Springer, Berlin/ Heidelberg/New York.

[20] Chen, Y.; Xu, Z.; Smith, C. and Sankar, J., Recent advances on the development of magnesium alloys for biodegradable implants, Acta Biomater. 10:4561-4573, 2014.

[21] Bamberger, M. and Dehm, G. Trends in the development of new Mg alloys, Annu. Rev.Mater. Res. 38: 505-533, 2008.

[22] Raynor GV., The physical metallurgy of magnesium and its alloys: Pergamon Press 1959.

[23] St John, D.H.; Qian, M.; Easton, M.A.; Cao, P. and Hildebrand, Z., Grain refinement of magnesium alloys, Metall. Mater. Trans. A 36A: 1669-1679, 2005.

[24] Polmear, I.J., Grades and Alloys. In: Avedesian MM, Baker H, editors. Magnesium and magnesium alloys, Materials Park, OH: ASM International Handbook Committee:12-25, 1999.

[25] Gu, X.N.; Zheng, Y.F.; Cheng, Y.; Zhong, S.P. and Xi, T.F. In vitro corrosion and biocompatibility of binary magnesium alloys, Biomaterials 30: 484-498, 2009.

[26] Mg (Magnesium) Binary Alloy Phase Diagrams in ASM Handbook, Volume 3, Alloy Phase Diagrams Ohio, USA: ASM international, 2016.

[27] Chen, Y.J.; Li, Y.J.; Walmsley, J.C.; Dumoulin, S; Skaret, P.C. and Roven, H.J., Microstructure evolution of commercial pure titanium during equal channel angular pressing, Mater. Sci. Eng. A 527: 789-796, 2010.

[28] Nakamura, Y.; Tsumura, Y.; Tonogai, Y.; Shibata, T. and Ito, Y., Differences in Behavior among the Chlorides of Seven Rare Earth Elements Administered Intravenously to Rats,Toxicol. Sci. 37(2): 106-116, 1997.

[29] Yang, Z.; Li, J.P.; Zhang, J.X.; Lorimer, G.W. and Robson, J. Review on Research and Development of Magnesium Alloys, Acta Metall. Sin. 21: 313-328, 2008.

[30] Kannan, M.B. and Raman, R.K.S. In vitro degradation and mechanical integrity of calcium-containing magnesium alloys in modified-simulated body fluid, Biomaterials 29: 2306-2314, 2008.

[31] Wen, Z.H.; Wu C.J.; Dai, C.S. and Yang, F.X. Corrosion behaviors of Mg and its alloys with different Al contents in a modified simulated body fluid, J. Alloys Compd. 488: 392- 399, 2009.

[32] Lu, S.K.; Yeh, H.I.; Tian, T.Y. and Lee, W.H. Degradation of Magnesium Alloys in Biological Solutions and Reduced Phenotypic Expression of Endothelial Cell Grown on These Alloys. In: Ibrahim F, Osman N, Usman J, Kadri N, editors. 3rd Kuala Lumpur International Conference on Biomedical Engineering 2006, Springer, Berlin Heidelberg: 98-101, 2007.

[33] Gu, X.N.; Li N.; Zheng, Y.F.; Kang, F.; Wang, J.T. and Ruan, L.Q. In vitro study on equal channel angular pressing AZ31 magnesium alloy with and without back pressure, Mater. Sci. Eng. B 176: 1802-1806, 2011.

[34] Gray-Munro, J.E.; Seguin, C. and Strong, M. Influence of surface modification on the in vitro corrosion rate of magnesium alloy AZ31, J. Biomed. Mater. Res. A 91A : 221-230, 2009.

[35] Chen, B.; Lin, D.L.; Jin, L.; Zeng, X.Q. and Lu, C. Equal-channel angular pressing of magnesium alloy AZ91 and its effects on microstructure and mechanical properties, Mater. Sci. Eng. A 483-84: 113-116, 2008.

[36] Li, Z.J.; Gu, X.N.; Lou, S.Q. and Zheng, Y.F. The development of binary Mg-Ca alloys for use as biodegradable materials within bone, Biomaterials 29:1329-1344, 2008.

[37] Wan, Y.; Xiong, G.; Luo, H.; He, F.; Huang, Y. and Zhou, X. Preparation and characterization of a new biomedical magnesium–calcium alloy, Mater. Des. 29: 2034– 2037, 2008.

[38] Li, Y.; Hodgson, P. and Wen, C.E. The effects of calcium and yttrium additions on the microstructure, mechanical properties and biocompatibility of biodegradable magnesium alloys, J. Mater. Sci. 46, 365–371, 2011.

[39] Du, H.; Wei, Z.; Liu, X. and Zhang, E. Effects of Zn on the microstructure, mechanical property and bio-corrosion property of Mg–3Ca alloys for biomedical application, Mater. Chem. Phys. 125:568–575, 2011.

[40] Zhang, B.P.; Wang, Y. and Geng, L. Research on Mg-Zn-Ca Alloy as Degradable Biomaterial, In : Pignatello R, editor. Biomaterials-Physics and Chemistry : In Tech. :183-204, 2011.

[41] Zhang, B.; Hou, Y.; Wang, X.; Wang, Y. and Geng, L. Mechanical properties, degradation performance and cytotoxicity of Mg–Zn–Ca biomedical alloys with different compositions, Mater. Sci.Eng. C 31:1667–1673, 2011.

[42] Zhang, E.; Yin, D.; Xu, L.; Yang, L. and Yang, K.Microstructure, mechanical and corrosion properties and biocompatibility of Mg–Zn–Mn alloys for biomedical application, Mater. Sci. Eng. C 29: 987–993, 2009.

[43] Brar, H.S.; Wong, J. and Manuel, M.V.: Investigation of the mechanical and degradation properties of Mg–Sr and Mg–Zn–Sr alloys for use as potential biodegradable implant materials, J. Mech. Behav. Biomed. Mater. 7: 87–95, 2012.

[44] Zhang, E.; He, W.; Du, H. and Yang, K.: Microstructure, mechanical properties and corrosion properties of Mg–Zn–Y alloys with low Zn content, Mater. Sci. Eng. A 488: 102–111, 2008.

[45] Huan, Z.G.; Leeflang, M.A.; Zhou, J.; Fratila-Apachitei, L.E. and Duszczyk, J.: In vitro degradation behavior and cytocompatibility of Mg-Zn-Zr alloys, J. Mater. Sci. ater. Med. 21: 2623-2635, 2010.

[46] Kawamura, Y.; Hayashi, K.; Inoue, A. and Masumoto, T.: Rapidly solidified powder metallurgy Mg(97)Zn(1)Y(2)Alloys with excellent tensile yield strength above 600 MPa, Mater. Trans. 42: 1172-1176, 2001.

[47] Yoshimoto, S.; Yamasaki, M. and Kawamura, Y.: Microstructure and mechanical properties of extruded Mg-Zn-Y alloys with 14H long period ordered structure, Mater.Trans. 47, 959-965, 2006.

[48] Mabuchi, M. and Higashi, K.: Strengthening mechanisms of Mg-Si alloys, Acta Mater. 44: 4611-4618, 1996.

[49] Hu, X.S.; Wu, K.; Zheng, M.Y.; Gan, W.M. and Wang, X.J.: Low frequency damping capacities and mechanical properties of Mg-Si alloys, Mater. Sci. Eng. A 452: 374-379, 2007.

[50] Zhang, E.L.; Yang, L.; Xu, J.W. and Chen, H.Y.: Microstructure, mechanical properties and bio-corrosion properties of Mg-Si(-Ca, Zn) alloy for biomedical application, Acta Biomater. 6: 1756-1762, 2010.

[51] Liu, H.; Chen, Y.; Tang, Y.; Wei, S. and Niu, G.: The microstructure, tensile properties, and creep behavior of as-cast Mg–(1–10)%Sn alloys, J. Alloys Compd. 440: 122–126, 2011

[52] Nayyeri, G. and Mahmudi, R.: Effects of Ca additions on the microstructural stability and mechanical properties of Mg–5%Sn alloy, Mater. Des. 32: 1571–1576, 2011.

[53] Yang, X.: Study on microstructure and properties of biomedical Mg–Sn–Mn alloy, (Master Thesis), Harbin Engineering University, 2011.

[54] Tsai, M.H.; Chen, M.S.; Lin, L.H.; Lin, M.H.; Wu, C.Z.; Ou, K.L. and Yu, C.H.: Effect of heat treatment on the microstructures and damping properties of biomedical Mg–Zr alloy, J. Alloys Compd. 509: 813–819, 2011.

[55] Li, Y.C.; Wen, C.; Mushahary, D.; Sravanthi, R.; Harishankar, N.; Pande, G. and Hodgon, P.: Mg-Zr-Sr alloys as biodegradable implant materials, Acta Biomater. 8: 3177-3188, 2012.

[56] Zhou, Y.L.; An, J.; Luo, D.M.; Hu, W.Y.; Li, Y.C.; Hodgson, P. and Wen, C.E.: Microstructures and mechanical properties of as cast Mg-Zr-Ca alloys for biomedical applications, Mater. Technol. 27: 52-54, 2012.

[57] He, S.M.; Zeng, X.Q.; Peng, L.M.; Gao, X.; Nie, J.F. and Ding, W.J.: Precipitation ina Mg-10Gd-3Y-0.4Zr (wt.%) alloy during isothermal ageing at 250 degrees C, J. Alloy Compd. 421: 309-313, 2006.

[58] Zheng, J.; Wang, Q.D.; Jin, Z.L. and Peng, T.: Effect of Sm on the microstructure, mechanical properties and creep behavior of Mg-0.5Zn-0.4Zr based alloys, Mat. Sci. Eng. A 527: 1677-1685, 2010.

[59] Mert, F.; Blawert, C.; Kainer, K.U. and Hort, N.: Influence of cerium additions on the corrosion behaviour of high pressure die cast AM50 alloy, Corros. Sci. 65: 145-151., 2012.

[60] Gerold, B.: Implant made of a biodegradable magnesium alloy. US Patent, 8,915,953 B2. 2014

[61] Razychon, T.; Michalska, J. and Kielbus, A.: Effect of heat treatment on corrosion resistance of WE54 alloy, J. Achiev. Mater. Manuf. Eng. 20: 191–194, 2007.

[62] Walter, R. and Kannan, M.B.: In-vitro degradation behaviour of WE54 magnesium alloy in simulated body fluid, Mater. Lett. 65: 748–750, 2011.

[63] Zhang, X.; Yuan, G. and Wang Z.: Mechanical properties and biocorrosion resistance of Mg-Nd-Zn-Zr alloy improved by cyclic extrusion and compression, Mater. Lett. 74: 128-131, 2012.

[64] Zhang, X.B.; Yuan, G.Y.; Mao, L.; Niu, J.L.; Fu, P.H. and Ding, W.J. Effects of extrusion and heat treatment on the mechanical properties and biocorrosion behaviors of a Mg-Nd-Zn-Zr alloy, J. Mech. Beha. Biomed. Mater. 7: 77-86, 2012.

[65] Leng, Z.; Zhang, J.H.; Zhang, M.L.; Liu, X.H.; Zhan, H.B. and Wu, R.Z. Microstructure\and high mechanical properties of Mg-9RY-4Zn (RY: Y-rich misch metal) alloy with long period stacking ordered phase, Mater. Sci. Eng. A 540: 38-45, 2012.

[66] Hagihara, K.; Yokotani, N. and Umakoshi, Y.: Plastic deformation behavior of Mg12YZn with 18R long-period stacking ordered structure, Intermetallics 18: 267-276, 2010.

[67] Leng, Z.; Zhang, J.; Yin, T.; Zhang, L.; Guo, X. and Peng, Q., et al. Influence of biocorrosion on microstructure and mechanical properties of deformed Mg–Y–Er–Zn biomaterial containing 18R-LPSO phase, J. Mech. Beha. Biomed. Mater. 28: 332-339, 2013.

[68] Hort, N.; Huang, Y.; Fechner, D.; Sto¨rmer, M.; Blawert, C.; Witte, F.; Vogt, C.; Dru¨ cker, H.; Willumeit, R.; Kainer, K.U. and Feyerabend, F. Magnesium alloys as implant materials – Principles of property design for Mg–RE alloys, Acta Biomater. 6: 1714–1725, 2010.

[69] Liu, M.; Schmutz, P.; Uggowitzer, P.J.; Song, G. and Atrens, A. The influence of yttrium (Y) on the corrosion of Mg–Y binary alloys, Corros. Sci. 52:3687–3701, 2010.

[70] Yang, L.; Huang, Y. ;Peng, Q.; Feyerabend, F.; Kainer, K.U.; Willumeit, R. and Hort, N. Mechanical and corrosion properties of binary Mg–Dy alloys for medical applications, Mater. Sci. Eng. B 176: 1827–1834, 2011.

[71] Zhang, X.B.; Wu, Y.J.; Xue, Y.J.; Wang, Z.Z. and Yang, L. Biocorrosion behavior and cytotoxicity of a Mg-Gd-Zn-Zr alloy with long period stacking ordered structure, Mater. Lett. 86: 42-45, 2012.

[72] Brar, H.S.; Keselowsky, BG.; Sarntinoranont, M. and Manuel,Design Considerations for Developing Biodegradable and Bioabsorbable Magnesium Implants, JOM. 63: 100-104, 2011.

[73] Witte, F.; Hort, N.; Vogt, C.; Cohen, S.; Kainer, KU. and Willumeit, R. Degradable biomaterials based on magnesium corrosion, Curr. Opin. Solid State Mater. Sci. 12: 63-72, 2008.

[74] Persaud-Sharma, D. and McGoron, A. Biodegradable Magnesium Alloys: A Review of Material Development and Applications, J Biomim. Biomater. Tissue Eng. 12: 25-39, 2011.

[75] Wang, H.; Estrin, Y. and Zuberova, Z. (2008), Bio-corrosion of a magnesium alloy with different processing histories, Mater. Lett. 62, pp. 2476-2479.

[76] Zhang, X.B.; Yuan, G.Y.; Niu, J.L.; Fu, P.H. and Ding, W.J.: Microstructure, mechanical properties, biocorrosion behavior and cytotoxicity of as-extruded Mg-Nd-Zn-Zr alloy with different extrusion ratios, J Mech. Behav. Biomed. Mater. 9: 153-162, 2012.

[77] Gu, X.N.; Li, N.; Zheng, Y.F. and Ruan, L.: In vitro degradation performance and biological response of a Mg–Zn–Zr alloy, Mater. Sci. Eng. B 176: 1778-1784, 2011.

[78] Zhang, W.; Li, M.; Chen, Q.; Hu, W.; Zhang, W. and Xin, W.: Effects of Sr and Sn on microstructure and corrosion resistance of Mg–Zr–Ca magnesium alloy for biomedical applications, Mater. Des. 39: 379-383, 2012.

[79] Yang, L.; Huang, Y.D.; Feyerabend, F.; Willumeit, R.; Kainer, K.U. and Hort, N.: Influence of ageing treatment on microstructure, mechanical and bio-corrosion properties of Mg-Dy alloys, J Mech. Behav. Biomed. Mater.13: 36-44, 2012.

[80] Wu, G.; Ibrahim, J.M. and Chu, P.K. Surface design of biodegradable magnesium alloys — A review, Surf. Coat. Technol. 233: 2-12, 2013.

[81] Shadanbaz, S. and Dias, G.J.: Calcium phosphate coatings on magnesium alloys for biomedical applications: A review, Acta Biomater. 8:20-30, 2013.

[82] Erdmann, N.; Angrisani, N.; Reifenrath, J.; Lucas, A.; Thorey, F. and Bormann, D.: Biomechanical testing and degradation analysis of MgCa0.8 alloy screws: A comparative in vivo study in rabbits, Acta Biomater. 7: 1421-1428, 2011.

[83] Windhagen, H.; Radtke, K.; Weizbauer, A.; Diekmann, J.; Noll, Y. and Kreimeyer, U.: Biodegradable magnesium-based screw clinically equivalent to titanium screw in hallux valgus surgery: short term results of the first prospective, randomized, controlled clinical pilot study, Biomed. Eng. Online. 12: 62, 2013.

[84] Wolters, L.; Angrisani, N.; Seitz, J.; Helmecke, P.; Weizbauer, A. and Reifenrath, J.: Applicability of degradable magnesium LAE442 alloy plate-screw-systems in a rabbit model, Biomed Tech. 58, (Suppl. 1): 4015-4016, 2013.

[85] Reifenrath, J.; Angrisani, N.; Erdmann, N.; Lucas, A.; Waizy, H.; Seitz, J.M., Bondarenko, A. and Meyer-Lindenberg, A.: Degrading magnesium screws ZEK100: biomechanical testing, degradation analysis and soft-tissue biocompatibility in a rabbit model. Biomed. Mater. 8(4): 045012(1)-045012(10), 2013.

[86] Thomann, M.; Krause, C.; Bormann, D.; von der Hoh N.; Windhagen, H. and Meyer-Lindenberg, A. Comparison of the resorbable magnesium alloys LAE442 und MgCa0.8 concerning their mechanical properties, their progress of degradation and the boneimplant- contact after 12 months implantation duration in a rabbit model, Mat.-wiss. u. Werkstofftech. 40:82-87, 2009.

[87] Narayan, R.J.: The next generation of biomaterial development, Phil. Trans. R. Soc. A 368: 1831–1837, 2010.

[88] Hench, L.L. and Polak, J.M.: Third-generation biomedical materials, Science. 295, 1014-1017, 2002.

Journal of Metallurgy and Materials Science, Vol. 62, No. 3-4, July-December 2020, pp. 71-80
Printed in India. © NML, ISSN 0972-4257

Tuning surface resistivity and thermal conductivity of water resistant fly ash waste based polymer composite via tailoring the interfacial polarization

SANDHYA SINGH TRIPALIYA[1], MANOJ KUMAR GUPTA[1,2*], RIYA SAHU[1], ASOKAN PAPPU[1,2], CHARU SHARMA[2], ASHISH KUMAR CHATURVEDI[2], and AVANISH KUMAR SRIVASTAVA[1,2]
[1]Advanced Materials and Processes Research Institute Bhopal, [2]Academy of Scientific and Innovative Research (AcSIR), Bhopal, Madhya Pradesh, India-462026

Abstract: High performance environment friendly industrial inorganic waste (fly ash) waste based water resistant electrical insulating hybrid composites are fabricated with very high surface and volume resistivity. Dielectric constant of hybrid composite was decreased significantly from 10900 to 4.98, 5.25, 5.00, 5.81, and 6.69 for filler concentrations of 10, 20, 30, 50 and 60% in epoxy matrix, respectively. Very high surface resistivity of 10^{13} Ohms/sq. and volume resistivity of 10^{14} to 10^{15} Ohms-cm with ultra-low water absorption of 0.14 % were achieved . Thermal conductivity analysis shows a slight increase in the thermal conductivity of the composite sheet and reaches the value of 0.4387 W/mK. Such high resistivity is attributed due to low dielectric constant and interfacial polarization and low water absorption in the samples. Our approach presents new, adaptable and cost-effective means for effectively utilizing waste as eco-friendly electrical and thermal insulating sheet and lowering the thermal loss in microelectronics.

INTRODUCTION

Fabrication of electrical insulator with high resistance to electric current has gained huge interest for separating electrical conductors and building electrical insulating panels. Previously, many materials e.g. wood, glass, fabrics, mineral oil, and ceramics are used for electrical insulating purposes [1,2]. With the growth of electrical/electronics industry, there is high need for an alternative material that possessed the desired electrical, thermal, and mechanical properties. New high performance engineering polymeric materials with additional properties such as ease of fabrication, lighter weight, low cost and excellent insulation properties are the most desirable and demanding materials for electrical applications[1-6]. In addition, the interface between filler and matrix has long been a critical problem that affects the thermal conductivity and electric properties of the polymer composites. Industrial waste from thermal power plant especially fly ash of about 150 millions of tons generated across the world every year[7]. Moreover, enviro-friendly utilization of fly ash become global challenge as dumping the fly ash into the open environment creates air, land and water pollutions. Heavy metal presented in fly ash are most important sorts of contaminant in the environment that produced severe diseases such as lung cancer, anemia, dermatitis and skin cancer as their small sizes penetrate into different organs of the human system and also create permanent respiratory disorder [8-9]. In addition, dumping of fly ash into the environment creates air, land and water pollutions. Presently, fly ash are utilized in to cement manufacturing, filling of low lying area, construction of road and embankment, making fly ash brick, ash pond dyke raising and also in agriculture area with certain conditions [10] Various researches have been carried out across the world to find an economical and suitable way to use fly ash, the industrial waste for some application[7]. However, fly ash solidification in cement and disposal at landfills is not an optimized solution due to variation of fly ash characteristics. Fly ash as basement material for road construction is also limited to 5 % in the United States and Japan, due to releasing of heavy metals from solidification matrix. Moreover, to preserve the toxic element including fly ash numerous thermoplastics and thermosets are used [11]. Quan et al. have studied the role of fly ash in the performance of fly ash concrete [12]. Lingling et. al have also studied fired bricks with replacing clay by fly ash in high volume ratio and shown that fired fly ash bricks has high compressive strength, low water absorption, no cracking due to lime, no frost and high resistance to frost melting. The properties of fired bricks were improved by pulverized fly ash [13]. However, the sintering temperature of bricks with high

* Corresponding author E-mail: mkgupta@ampri.res.in, manojampri@gmail.com

volume of fly ash was about 1050^{0}C, which is very high and energy consuming. PVC resin and fly ash based polymer composite and fly ash/ polyurea (FA/PU) composites have been also reported by Nidal H. et al and Jing Qiao et al, respectively [14-15]. They have reported thermal properties and loss of moduli and compared with those of neat polymer. However, dielectric properties, surface resistivity and ac conductivity are still not reported for fly ash based polymer composites. H. Khan et al. have shown that SiR (Silicone Rubber) composites with addition of fillers are used as high voltage (HV) electrical and non electrical application, [16] and Masahiro Kozako et. al. have improved both thermal and electrical insulation properties of epoxy based composites using nanocomposite technique [17]. In addition, the rapid development of micro-electronic technology, and highly integration of the electric component cause the high heat flux and release of high heat from electronic component creates severe problem to electronic devices. Moreover, the heat dissipation is also an important issue for electronic devices and controlling them by tuning the thermal conductivity and dielectric loss tangent is very important. However, to the best of our knowledge investigation of fly ash based polymer composite with epoxy system as electrical insulation with superior dielectric and high surface/volume resistivity through lowering the interfacial polarization and water absorption are not reported till date.

In this work, water resistant fly ash-based polymer-based composites are prepared in epoxy matrix. Dielectric constant, dissipation factor, electrical conductivity, surface and volume resistivity and water absorption of the fly ash waste polymer composite with variation of filler concentration have studied in details. Physical, chemical and dielectric properties of fly ash industrial waste powder was also investigated.

EXPERIMENTAL SECTION

Fabrication of electrical insulating sheet using fly ash waste.

The inorganic fly ash waste powder is collected from Sarni, district of Madhya Pradesh state of India. Physiochemical properties such as pH, density, porosity and electrical conductivity of fly ash waste powder were measured. The synthesis of polymer composites were carried out using hand operated compressive moulding machine at room temperature. The prepared solution was poured in specific mould frame and then allowed to cure for 6 hours at room temperature.

Characterization and measurements.

Elemental analysis was performed using S8 Tiger X-Ray fluorescence spectrometer (XRF). Morphology of the fly ash powder was identified using scanning electron microscope (SEM) using JEOL, Model :NeoScope, JCM6000. Dielectric constant and dissipation factor of fly ash waste powder and their polymer composites were measured using Keysight LCR meter (E4980A) in the frequency range 20Hz–2MHz at room temperature. Surface and volume resistivity are measured using Tektronix Electrometer Model 8009 Resistivity Test Fixture as per ASTM D-257 standard. Water absorption study of fly ash waste epoxy composites was performed as per ASTM D 570-98 method.

RESULTS AND DISCUSSIONS

Physicochemical analysis of fly ash powder.

The physio-chemical analysis through various parameters such as pH value, bulk density, specific gravity, conductivity and porosity of fly ash waste powder were measured and calculated as per standard procedures. Bulk density of the fly ash sample was calculated using IS: 2386-1963 method and the calculated value is found to be 1.04 g/cm^3. Specific gravity of fly ash was calculated using the IS CODE 2720 Part 3 and found to be 1.39. The pH of fly ash sample of 7.04 and conductivity of 2.06 µS/cm were obtained using ASTM standard. The detail results are shown in Table No. 1.The porosity was calculated using the known value of bulk density and specific gravity and porosity of fly ash waste sample was found to be 25.68 %.

Table 1: Physicochemical properties of fly ash waste powder

S No.	Parameter	Value
1	pH	7.04
2	Bulk Density	1.04 g/cm^3
3	Specific Gravity	1.39
4	Electrical Conductivity	2.06 µS/cm
5	Porosity	25.68 %

Scanning electron microscopy (SEM) of fly ash sample.

The morphology of the fly ash powder sample is recorded using scanning electron microscope studies and results are shown in the shown in Fig.1 (A-C). It is evident that the fly ash sample has cenospheres morphology and size in the range of 3 -12 µm. The morphological results was well correlated with the characteristic morphologies of coal fly ash sample [18-20].

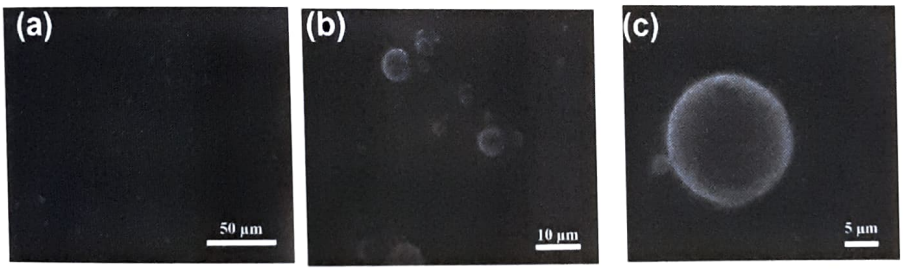

Fig.1. (a) low (b) mid and (c) high magnification of the SEM images of the fly ash waste powder sample

X-Ray Florescence (XRF) studies.

Wavelength dispersive X-ray fluorescence (WD-XRF) is a well-known technique for fast, and accurate quantitative determinations of matrix elements over a wide concentration range. To perform the elemental analysis of the fly ash sample, a pellet is prepared using the 5g fly ash and 5 gm boric acid.[21] The results obtained by using WD-XRF analysis is shown in Fig 2A and Table 2. It is clearly visible that fly ash has SiO_2 (57.3 %), CaO (1.12 %), Fe_2O_3 (3.73 %), Al_2O_3 (27.8 %), MgO (0.967 %), SO_3 (0.243 %) , Na_2O, (0.210 %), K_2O (3.00 %) TiO_2 (1.92 %), P_2O_5 (0.232 %) and various elements including heavy elements such as Zn, Mn, Cu, Ni, Pb, and Zr concentration in ppm range are also detected. The results are displayed in Fig 2B.

Table 2: XRF of fly ash waste powder showing elemental composition of the fly ash particulates

S. No.	Oxides	% in fly ash
1.	SiO_2	57.3 %
2.	CaO	1.12 %
3.	Al_2O_3	27.8 %
4.	Fe_2O_3	3.73 %
4.	MgO	0.967 %
5.	SO_3	0.243 %
6.	Na_2O	0.210 %
7.	K_2O	3.00 %
8.	TiO_2	1.92 %
9.	P_2O_5	0.232 %

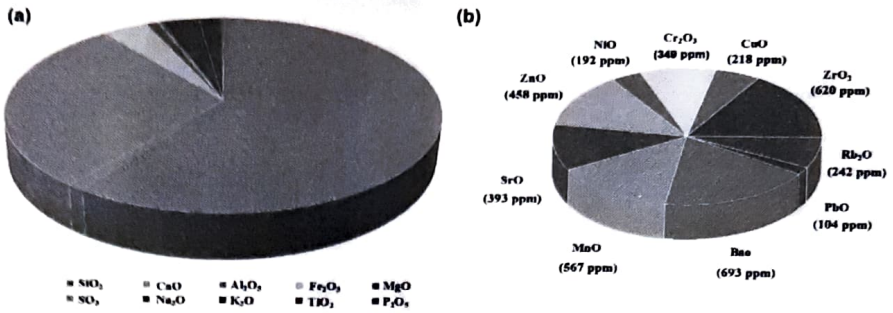

Fig. 2. (a)WD- XRF results of the fly ash waste powder showing elemental composition (b) heavy element presented in the fly ash samples

Water absorption of Fly ash polymer composite sheet.

Electrical insulating sheet prepared from fly ash with various content (10, 20, 30, 50 and 60 wt %) is shown in the Fig 3. Calculation of water absorption of fly ash polymer composite was carried out through initial and final weight of fly ash polymer composite samples before and after fully immersion in distill water bath for 24 hours are measured and calculated.

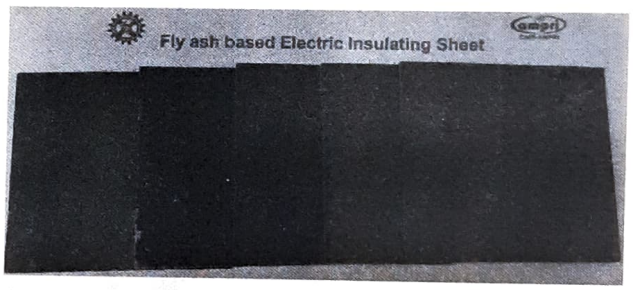

Fig. 3. Original image of fly ash waste based polymer composite (FAPC) samples with various filler concentration

Samples are conditioned at 50°C for 24 hours before testing the water absorption of samples. Water absorption measured for 10, 20, 30, 50 and 60 wt% fly ash waste based polymer composite samples is shown in Fig 4 a and b.

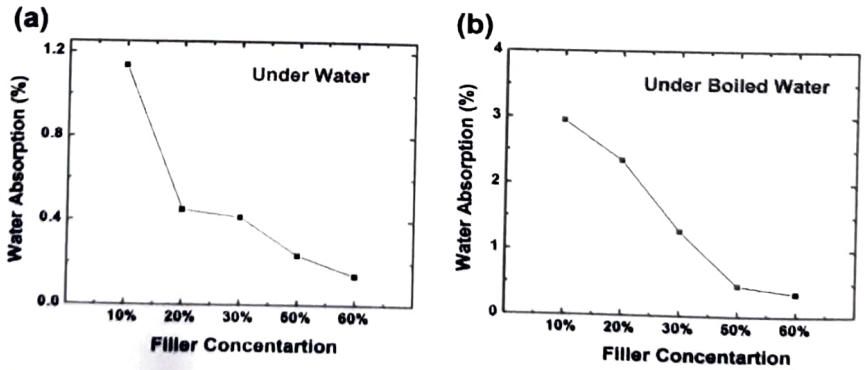

Fig. 4 (a) Water absorption (b) Water absorption under boiled water of fly ash waste hybrid polymer composites.

It is clearly seen that as the weight amount of the fly ash waste powder in epoxy matrix system increases as the water absorption decreases. The water absorption of value 1.13, 0.44, 0.416, 0.84 and 0.14 % were obtained for fly ash polymer composite sheet containing 10, 20, 30, 50 and 60% of filler amount (fly ash) for 24 hour water immersion test. Similar procedure was repeated for boiling water absorption test and fly ash composite samples was immersed in boiling distill water for 2 hours. Boiling water absorption test shows that water absorption of 2.94, 2.34, 1.27, 0.45 and 0.34 % were obtained for fly ash polymer composite samples of filler concentration 10, 20, 30, 50 and 60 % of fly ash. It has been observed that very low water absorption upto 0.14 % and 0.34 % was obtained for sample containing 60 % wt of fly ash in water absorption and boiling water absorption

test, respectively. The results show that the prepared polymer fly ash polymer composites are water resistant and suitable for high end application towards fabrication of electrical insulations sheet and other construction materials.

Scanning electron microscopy (SEM) of fly ash polymer composite.

The morphology of fly ash based polymer composites are analysed using SEM technique. Figure 5 (a-d) depict the SEM micrographs of industrial fly ash polymer composites samples. SEM technique is a strong method to see the interfacial bonding of inorganic particulates with the polymer. To investigate the interfacial bonding of prepared polymer composite sample, SEM of fracture sample has been used. Fig 5 clearly indicate that fly ash are randomly distributed with the epoxy system and no leakage or weak bonding with polymer is observed[3].

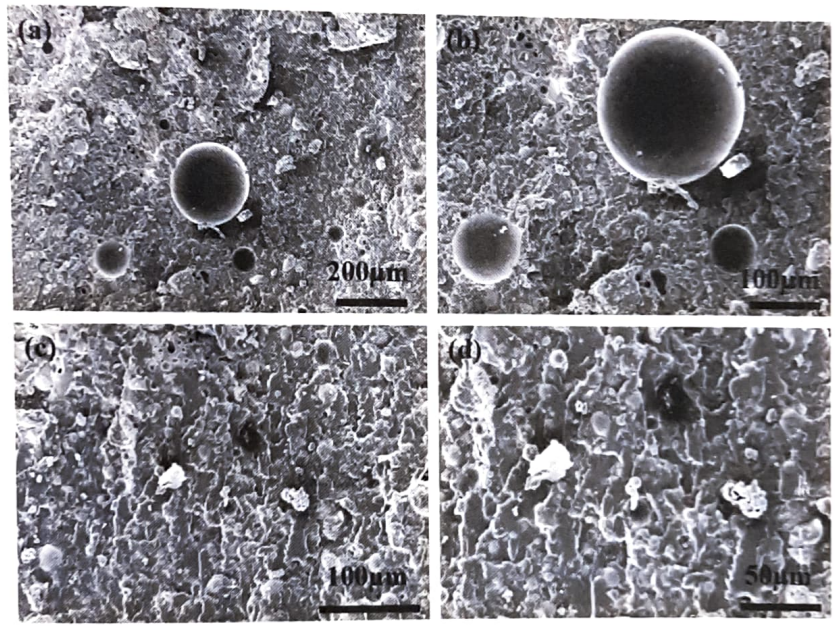

Fig. 5.(a) low and (b-d) high magnified SEM images of the fly ash based hybrid polymer composite.

Dielectric and Electrical Analysis.

Dielectric constant is important parameter to design the electrical insulating sheet and it the ratio of the capacitance formed by two plates with a material between them to the capacitance of the same plates with air as the dielectric. Dissipation factor has also important role to fabricate high performance electrical insulating sheet and electronic components and it is equivalent to the ratio of current dissipated into heat to the current transmitted. Dielectric constant (ε′) and dissipation factor (tan δ) for fly ash powder was measured in the wide frequencies range of 20 Hz –2 MHz at RT and the obtained results are shown in Fig. 6(a) and (b), respectively.

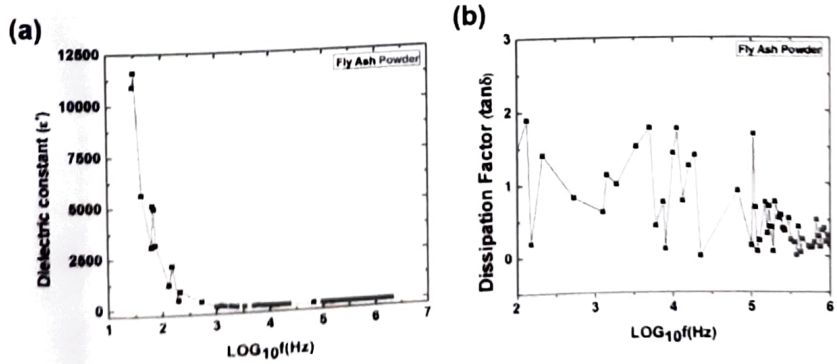

Fig. 6 Variation of (a) Dielectric constant and (b) dissipation factor with frequency for fly ash sample

Fly ash waste powder sample exhibited a very high dielectric constant of about ~10900 at RT at lower frequency region (29 Hz) which attains a low constant value of 6.16 at higher frequencies side (2 MHz) (Fig. 6 (a)). The observed dielectric constant showed that fly ash may be used as capacitor for energy storage, however to fabricate the electrical insulating sheet such high value may add capacitance effect which is not desirable for fabricating electrical insulating sheet. S. C. Raghavendra et. al. have reported that fly ash has a dielectric constant of order 10^4.[22] The dielectric constant (ε') of the materials was calculated by the relation

$$\varepsilon' = \frac{C_p \, x \, t}{\varepsilon_0 \, x \, A} \qquad (1)$$

Where, ε_0 is permittivity of free space, A is the cross sectional area, t is the thickness, and C_p is the capacitance of the sample [3]. Dissipation factor (tan δ) is given by

$$\text{Tan } \delta = \frac{\varepsilon''}{\varepsilon'} \qquad (2)$$

Where, ε'' is the imaginary part of dielectric constant [23-26]. Fig 6(b) present the variation of dissipation factor of fly ash with applied frequency and a tan d of ~ 1.8 was detected at low frequency side. Dielectric constant, dissipation factor and ac conductivity of the fabricated fly ash polymer composite samples consisting filler concentration varying from 10-60 wt % fly ash powder were measured under same condition in range of 20 Hz to 2 MHz at RT.

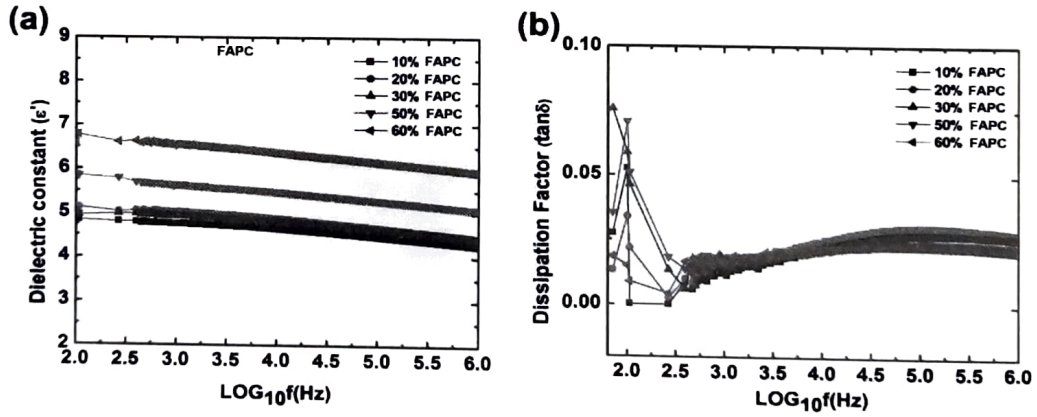

Fig. 7. Variation of (a) dielectric constant and (b) dissipation factor with frequency for fly ash waste polymer composite with various filler concentration.

Fig 7a and 7b show the variation of dielectric constant and tangent loss with applied frequencies of polymer composite samples. As the frequency increases the dielectric constant of all composite sample found to be decreases. It is interesting to note that dielectric constant of fly ash polymer composite samples dramatically decreases from 10900 to 6.69 for 60 % fly ash filler concentration sample. Dielectric constant of fly ash polymer composite with 10, 20, 30, 50 and 60 % fly ash content shows dielectric constant of 4.98, 5.25, 5.00, 5.81, and 6.69 respectively. It is clearly visible that as the fly ash concentration increases in the epoxy resin, the value of dielectric constant increases. However, very minute decrease is detected for 30 % fly ash content polymer composite sample comparative to 20 % fly ash content sample. Such remarkable decrease in the fly ash based composite is due to the low dielectric constant of epoxy resin. Dielectric loss of the polymer composite with various filler concentration was also measured in the same frequency range of 20 Hz to 2MHz. Dielectric loss were also found to be decreases with increase of frequency and found to be very small of about 0.002 for 60 % fly ash based polymer composite sample. The calculated ac conductivity of all fabricated samples and variation of ac conductivity with applied frequency is shown in the Fig 8.

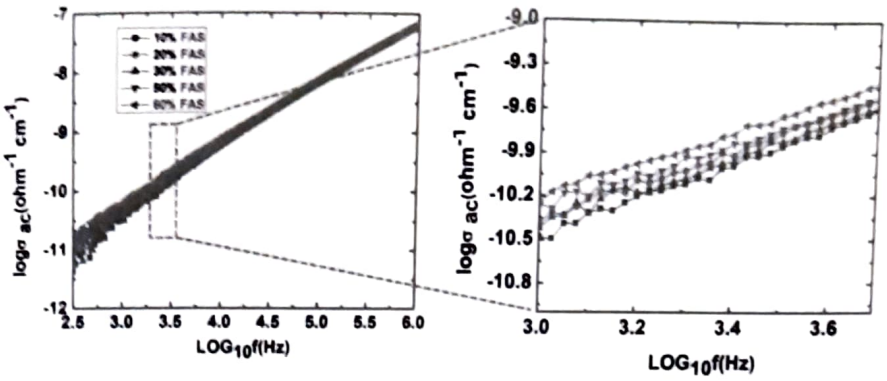

Fig. 8. Variation of ac conductivity with frequency for fly ash waste polymer composite with various filler concentration (right side shows enlarge view of ac conductivity).

AC conductivity increases with increase of the fly ash waste concentration in the polymer composites and ac conductivity has low value of 1.27 x $10^{-14}\Omega^{-1}$ cm^{-1} in low frequency region and high 2.96 x $10^{-10}\Omega^{-1}$ cm^{-1} at higher frequency side (2 MHz) for 60 % fly ash hybrid polymer composite sample.

Surface and Volume Resistivity Studies

Surface and Volume resistivity of the fabricated fly ash based polymer composite samples are measured as per ASTM D257 standard. The samples are prepared in square shape of 100 mm dimension to measure both surface/ volume resistivity. Surface resistivity of the fly ash based polymer composite samples was found to in range of 10^{13} ohms/sq (Fig 9a).

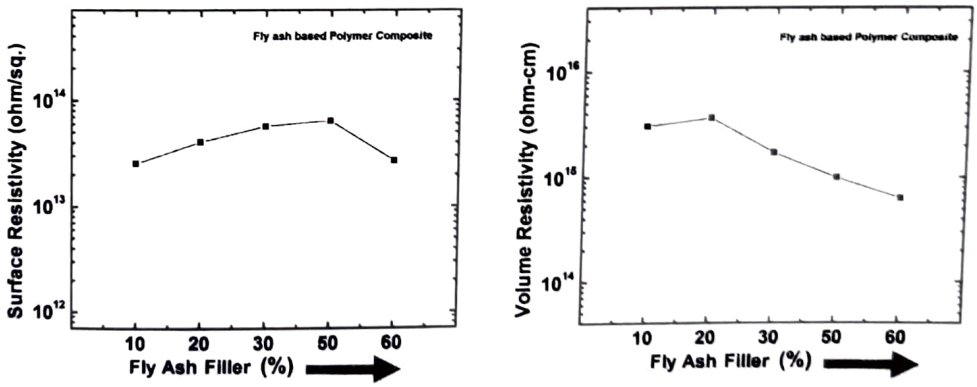

Fig.9 (a) Variation of surface and (b) volume resistivity of fly ash waste polymer composite with various filler concentration.

The results indicate that surface resistivity increases with increase of filler concentration till 50 % filler content and decrease to 10^{13} for 60 % fly ash amount. Further, volume resistivity of the fly ash polymer composite samples was found in range of 10^{14} to 10^{15} ohms-cm for the filer concentration of fly ash from 10, 20, 30, 50 and 60% in polymer composites (Fig 9b). It is observed that volume resistivity slightly decreases with increase of filler concentration (Figure 8b). The observed high value of surface and volume resistivity of fabricated polymer composite samples shows their suitability for electrical insulation application. Roy E. Bickelhaupt et al has reported that ash producing by plants may have resistivity greater than 10^{12} ohm-cm [27]. Osarenmwinda J.O. et al. have observed that composite materials prepared using sawdust:palm kernel shell has insulation resistance of 490MΩ [28].To the best of our knowledge such polymer composite with high value of surface and volume resistivity are not reported till date. The higher resistivity is basically attributed due to low water absorption and weak interfacial polarization between polymer and fly ash particles.

THERMAL CONDUCTIVITY ANALYSIS

Thermal conductivity of the developed composites sheet with fly ash filler loading up to 60 % were evaluated and measured. Thermal conductivity set up based on hot wire method using KEM QTM-710, Japan is used. The obtained thermal conductivity of the polymer composites samples having filler concentration of 10, 20, 30, 50 and 60 % fly ash exhibited thermal conductivity of 0.1765, 0.278, 0.3164, 0.3925 and 0.4387 W/mK (Fig 10).

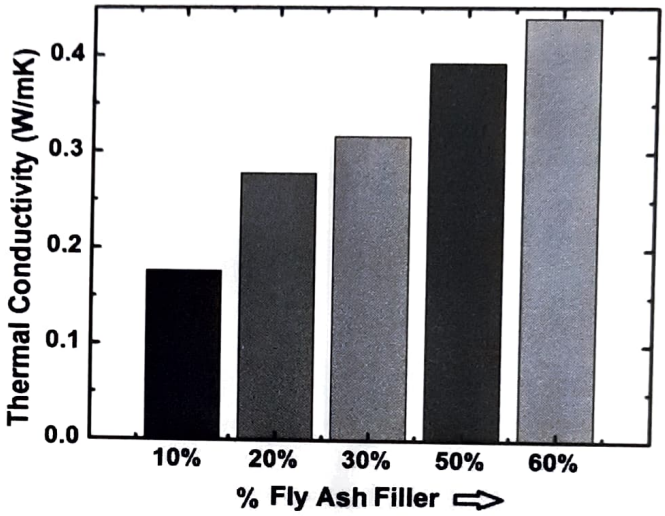

Fig. 10. Thermal conductivity of the fly ash polymer composite sample.

As the filler increases in the epoxy resin, the thermal conductivity increases and reached a maximum value of 0.4387 for 60 % filler condition. We found the spherical shape of fly ash create a path way in epoxy resin matrix, resulting slight enhancement of the thermal conductivity polymer composites. The low value of thermal conductivity enable the product to use in thermal insulating materials specially it reduces the high heat flux and release of high heat from electronic component in micro-electronic technology cause by the integration of the electronic components.

CONCLUSIONS

In summary, this study disclose a facile method for developing environmentally friendly industrial inorganics fly ash based moisture resistant electrical insulating hybrid polymer composite using compressive moulding techniques. Very high dielectric constant of 10900 at low frequency and high dissipation loss factor at RT were measured of fly ash waste powder. Various fly ash polymer composite with filler concentration of 10, 20, 30, 50 and 60 % wt ratio were fabricated. Very low water absorption of 0.14 % was observed from developed sheet. Effect of filler concentration on density, water absorption, dielectric constant, surface/volume resistivity were analyzed in details. Dielectric constant of fly ash based hybrid polymer composites were found to be decreased with respect to applied frequency and increases with fly ash waste powder. Surface resistivity about 10^{13} ohms/sq and volume resistivity in the range of 10^{14} to 10^{15} ohms-cm were measured from the fly ash based polymer composite samples. Low thermal conductivity of the fabricated composite was obtained and slight increase in the thermal conductivity was observed with increase in the filler loading. The high resistivity is discussed in the light of low water absorption and interfacial polarization between polymer and fly ash particles. Our work not just only demonstrates a promising way to utilize industrial waste to fabricate electrical insulating sheet but also greatly broadens the eco-friendly recycling method of industrial waste.

ACKNOWLEDGEMENTS

Authors are very thankful to the Dr. A. K. Srivastava, Director, CSIR-AMPRI, Bhopal for giving permission to publish the work. Authors are thankful to Mr. Ravi Patidar, Mr. Ashwin and Mr. Deepak Kashyap for collecting the raw materials and SEM measurements. Dr. M. K Gupta is grateful to CSIR, India for granting MLP -116 and MLP-115 projects.

REFERENCES

[1] Y. Yang, J. He, Q. Li , L. Gao, J. Hu, R. Zeng, J. Qin, S.X. Wang and Q. Wang: Self-healing of electrical damage in polymers using super paramagnetic nanoparticles. Nature Nanotech 14: 151–155, 2019

[2] G. Shimoga and S.Y. Kim: High k polymer nanocomposite materials for technological applications. Appl. Sci. 10(12): 4249, 2020

[3] Sahu, R., Gupta, M.K., Chaturvedi, R. Tripaliya, S.S., Pappu, A.: Moisure resistant stones waste based polymer composites with enhanced dielectric constant and flexural strength. Composite Part B: Engineering 182: 107656. 2020.

[4] D.K. Mahla, M. Rahman and Khastgir: Composition-dependent electrical and dielectric properties of polyaniline/graphene composites produced by in situ polymerization technique. Polymer Composites 36: 445-453, 2015.

[5] D. Chung: Composite materials for dielectric app lications. Composite Materials: 73–89, 2003.

[6] A. Rybak and J.Nieroda: Aluminosilicate-epoxy resin composite as novel material for electrical insulation with enhanced mechanical properties and improved thermal conductivity. Polymer Composites 40(8): 3182-3188, 2019.

[7] B.K Singh and P. Nema: Characterization of various flyash fractions for adsorption processes. Res. J. Material Sci. 3 (3): 7-16, 2015

[8] S Anandhan: Recent trends in fly ash utilization in polymer composites. International Journal of Waste resources 4: 1000149, 2014.

[9] R. Setsuda, I. Fukumoto and Y. Kanda.: Effects of fly ash in composites fabricated by injection molding. Polymer Composites 33: 1351-1359 2012.

[10] Surabhi: Fly ash in india:generation vis-avis utilization and global perspective. International Journal of Applied Chemistry 13(1): 29-52, 2017.

[11] J.D. Chow, W.N. Chai, C.M. Yeh and F.S. Chuang: Recycling and application characteristics of fly ash from municipal solid waste incinerator blended with polyurethane foam. Environmental Engineering Science 25(10): 461-471. 2008

[12] H Quan and H. Kasami.:Experimental study on durability improvement of fly ash concrete with durability improving admixture. The Scientific World Jr. 81810311, 2014

[13] X Lingling,., G Wei, W. Tao and Y. Nanru: Study on fired bricks with replacing clay by fly ash in high volume ratio. Construction and Building Materials. 19: 243-247, 2005.

[14] H Nidal, A.P. Khoshnoud, M. Jamel and S. Gunashekar: Enhanced thermal properties of rigid PVC foams using fly ash. World Academy of Science, Engineering and Technology International Journal of Materials and Metallurgical Engineering 9(1): 18-24, 2015.

[15] J Qiao, A.V. Amirkhizi, K. Schaaf and S.N. Nasser: Dynamic mechanical analysis of fly ash filled polyurea elastomer. Journal of Engineering Materials and Technology 133(1): 011016-1, 2011.

[16] H Khan, M. Amin and A. Ahmad:Characteristics of silicone composites for high voltage insulations. Rev. Adv. Mater Sci. 56 (1): 91-123. 2018.

[17] M. Kozako, Y. Okazaki, M. Hikita and T. Tanaka:Preparation and evaluation of epoxy composite insulating materials toward high thermal conductivity. International Conference on Solid Dielectrics, Potsdam, Germany. 2010.

[18] S. Vassilev and C. Vassileva: Methods for Characterization of Composition of Fly Ashes from Coal-Fired Power Stations: A Critical Overview. Energy & Fuels 19 (3): 2005.

[19] Barbara Kutchko, Kim and Ann: Fly ash characterization by SEM–EDS. Fuel.85 (17-18): 2537-2544. 2006.

[20] G. Raghavendra., S. Ojha, S.K. Acharya and S.K. Pal: A comparative analysis of woven jute/glass hybrid polymer composite with and without reinforcing of fly ash particles. Poymer Composites 37 (3): 658-665, 2016.

[21] Malik, M., N.K. Soni, K.V. Kanagasabapathy, M.V.R. Prasad and K.K. Satpathy: Characterisation of Fly Ash from Coal Fired Thermal Power Plants Using Energy Dispersive X-Ray Fluorescence Spectrometry. Scientific Reviews & Chemical Communications, Sci. Revs. Commun. 6(4): 91-101, 2016.

[22] Raghavendra, S.C. Raibagkar, R.L. and Kulkarni, A.B.: Dielectric properties of fly ash. Bull Mater Sci 25 (1): 37–39, 2002.

[23] Eroglu, A. Tataroglu, A. and Altindal, S.: On the temperature dependent dielectric properties, conductivity and resistivity of MIS structures at 1MHz. Microelectronic Engineering 91:154-158. 2012.

[24] Supriya, S., Kumar, L. and Kar, M.: Optimization of dielectric Properties of PVDF-CFO nanocomposites. Polymer Composites, 40: 1239-1250, 2019.

[25] Malki, M. and Echegut, P.: Electrical Conductivity of the CaO-SiO_2 system in the solid and the molten states. Journal of Non-Crystalline Solids 323(1-3): 131-136, 2003.

[26] Bharti, D.K., Gupta, M.K. and Srivastava, A.K.:Temperature dependent dielectric and electric properties of zinc silicate nanorods. Nano-Structures & Nano Objects 17: 123–128, 2019.

[27] Bickelhaupt, R.E: Surface Resistivity and the Chemical Composition of Fly Ash. Journal of the Air Pollution Control Association 25(2): 148-152, 1975 doi.org/10.1080/00022470.1975.10470063.

[28] Osarenmwinda, J.O and Nwachukwu, J.C. : Electrical Insulating Properties of Developed Composite Material from Palm Kernel/ Sawdust. Proceeding of the World Congress on Engineering I., 2011.

Journal of Metallurgy and Materials Science, Vol. 62, No. 3-4, July-December 2020, pp. 81-88
Printed in India, © NML, ISSN 0972-4257

Rapidly quenched magnetic materials for functional and sensor applications

ASHIS K. PANDA*, RAJAT K. ROY, PREMKUMAR MURUGAIYAN, SOMNATH DAS, TARUN K. DAS and AMITAVA MITRA**
CSIR-National Metallurgical Laboratory, Jamshedpur, India

Abstract : Rapidly quenched (RQ) amorphous / nanostructured materials have been addressed in relation to their properties targeted towards potential applications. Quenching techniques like melt spinning and in-water quenching for production of these materials in the form of ribbons and microwires production respectively have been addressed. CoFe-based microwires exhibited interesting giant magneto-impedance (GMI) behviour and was used in development of GMI sensor for detection of carburization in austenitic stainless steel. Efforts have been laid on the production of Fe-based magnetostrictive amorphous ribbons and their potential use in magnetostrictive sensor (MsS) for generation of guided waves for detection of defects in pipes. Compositional tailoring has also been carried out in amorphous / nanostructured ribbons to raise the saturation magnetization beyond 1.6 Tesla. Some of these ribbons have also been found to manifest interesting electromagnetic interference shielding effectiveness (EMI SE) properties.

Keywords: *Rapid quenching, magnetic, amorphous, nanostructured, giant magneto-impedance (GMI), electromagnetic interference shielding effectiveness (EMI SE).*

INTRODUCTION

In recent years, there has been a paradigm shift in the materials development strategies. Such approaches circumscribe not only the aspects of fundamental studies but also their potentiality towards applications. Amongst such materials, the advanced magnetic alloys have drawn special attention due to emerging synergy between properties and application requirements. The properties of these ferromagnetic materials can be tailored through different non-conventional processing routes. Amongst different processing methodologies, the rapid solidification is a potential route to get amorphous / nanostructured metallic precursors directly from the melt [1] and thereby reducing magnetic anisotropy energy in a greater extent than the crystalline counterpart. In this route, melt spinning to get ribbons /foils [2] or in-water quenching to get microwires [3,4] are some of the prevalent techniques. These techniques for getting metastable materials have an edge over the others in view of their efficiency in producing materials in large scale. The property of as-prepared precursors can be modified through control of alloy chemistry, rapid solidification parameters and heat treatment schedule. The modification in the processing conditions can deliver desired intrinsic and extrinsic magnetic properties. Bench marked properties pertaining to saturation magnetisation, saturation magnetostriction, Curie temperature, coercivity, permeability and coreloss are some of the targeted ones. Till the advent of metastable materials, these properties were catered by conventional crystalline materials. The metastable amorphous/nanostructured magnetic alloys find applications in distribution transformers [5], electrical components for electric vehicles (EVs)[6] etc. In these applications, the amorphous / nanostructured materials exhibit excellent performance due to their low coreloss and high permeability [7]. In the application areas of distribution transformer, these new materials are competing against conventionally known silicon steels like cold rolled grain oriented (CRGO) and non-oriented (CRNO) ones due to their reduced coreloss. However, the limiting scope of amorphous materials due to their lower induction values has been taken as a challenge worldwide to push their restricting limits of saturation magnetisation through appropriate tailoring of compositions [8,9].

The scope of metastable magnetic materials is further widened due to their potentiality as elements in sensors for structural health monitoring (SHM) of industrial components which are predominantly made of ferromagnetic

* Corresponding Author Email: akpanda@nmlindia.org
** Presently at Indian Institute of Technology, Jodhpur, Rajasthan, India.

steel. The typical magnetic sensing devices for SHM have been developed on the principle of magnetostrictive sensors (MsS)[10,11], giant magnetoimpedance sensors (GMI) [12], fluxgate magnetometer [13] etc. The low driving field requirements for magnetostriction in amorphous materials is an appealing parameter in sensor and transducer design concepts. The amorphous / nanostructured based MsS sensors are under current research priority in our laboratory for their scope in SHM through generation of ultrasonic guided waves and consequent detection of defects in components like pipes [14] and plates. Apart from magnetostriction, the amorphous materials also display sensitive change in magneto-impedance (MI) even at feeble external magnetising field. In view of sensitivity in very low magnetic field, the GMI based materials [15] and sensors are being explored for detection of phase transformation in steels. With increasing application of amorphous and nanostructured magnetic materials for sensors, attempts have been made in recent years of using these materials for electromagnetic interference (EMI) shielding elements. The EMI shielding or absorption materials are key to avoid the signal/noise interference, device malfunctioning and electromagnetic pollution to humans. The EMI shielding materials are typically composite structures using dielectric and/or magnetic filler materials to attenuate the incoming electromagnetic waves [16]. Recently, shielding through absorption is highly desirable for their stealth and environmental benefits.

The present investigation is focussed on development of various metastable magnetic materials and their desirable functional properties for different applications. The issues related to compositional tailoring, process control and sensing applications have been addressed in this paper.

RAPID QUENCHING OF MAGNETIC ALLOYS

The alloys in the form of ribbons / foils and wires that have been used in the present study have been developed in our laboratory through rapid quenching techniques. Prior to quenching, the master alloys are prepared through arc melting of pure elements under inert atmosphere. A series of Fe-, CoFe- and Co-based alloys have been prepared with different stoichiometric variation.

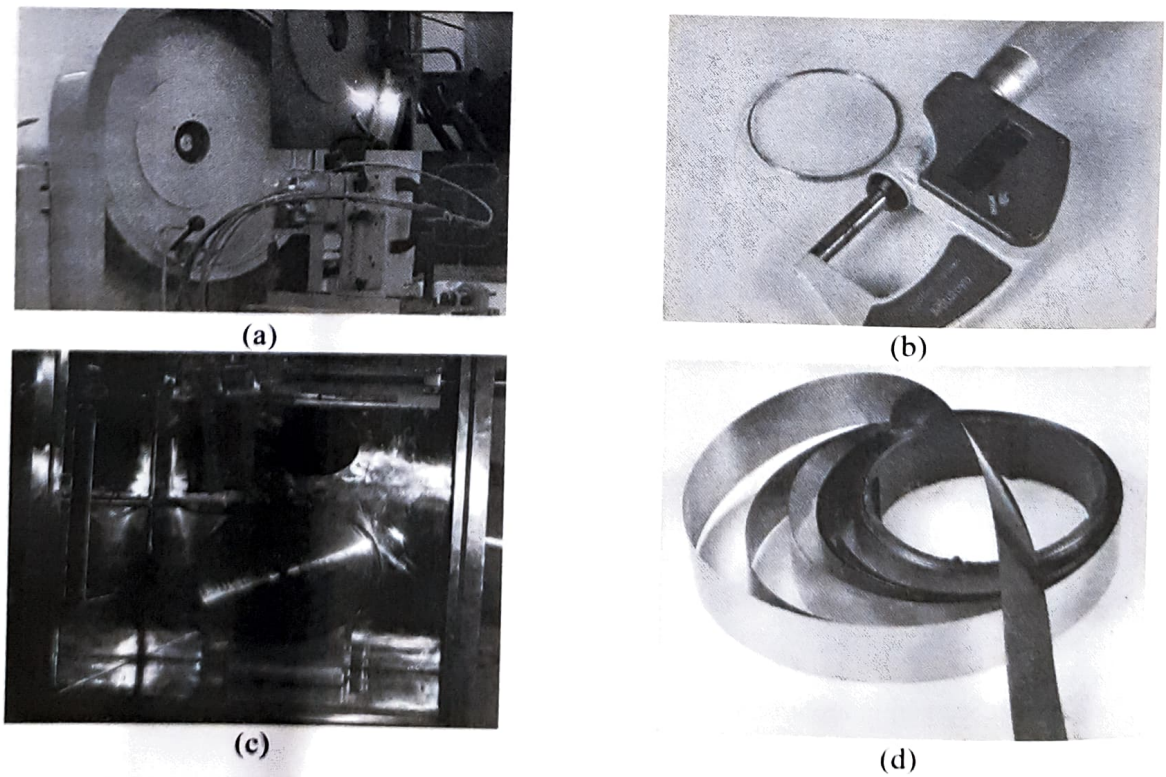

Fig. 1. Photographs of (a) In-water quenching system (inset: melt ejection) and (b) amorphous wires, (c) melt spinning system and (d) melt spun ribbon.

In these wires, the ferromagnetic elements of Co, Fe contribute towards magnetic components while the metalloids (Si, B) are the stabilizers for the glassy phase. The thermally stable refractory element Nb acts as a grain growth retarder to inhibit nucleation and growth phenomena of crystallites. The amorphous / nanostructured metallic microwires have been processed through in-water quenching apparatus (Fig-1a). The alloy was re-melted and ejected (Fig-1b) through quartz crucible orifice into the rotating water drum of this apparatus to get continuous microwires with diameter in the range of 80 to 120 microns. Argon pressure of 3-4 bar was maintained for ejection of alloy melt into drum rotating at speed of 300 – 350 rpm. Similarly, the amorphous / nanostructured ribbons have been prepared using a melt spinning system (Fig-1c) with a quenching wheel made of oxygen free copper. The master alloy is induction melted and ejected through a slit orifice in the bottom of the quartz crucible to get ribbons (Fig-1d) upto 25mm width and thickness of around 25 to 35 microns.

GIANT MAGNETO-IMPEDANCE BEHAVIOR IN MICROWIRES AND SENSOR APPLICATION

The giant magneto-impedance is a phenomenon wherein the amorphous wires / ribbons reveal a large change in ac complex impedance with applied dc magnetic field in the presence of a small alternative current applied on the material[17]. The property is evaluated in terms of percentage change in magneto-impedance with respect to a maximum applied dc magnetizing field. The magneto-impedance of the prepared microwires was measured using an impedance analyser (Agilent 4294A) through four probe technique wherein the applied ac current and frequency are optimized to achieve maximum GMI ratio. Typical GMI plots of representative amorphous microwires are shown in Fig-2. It is observed that the incorporation of thermally stable Nb in

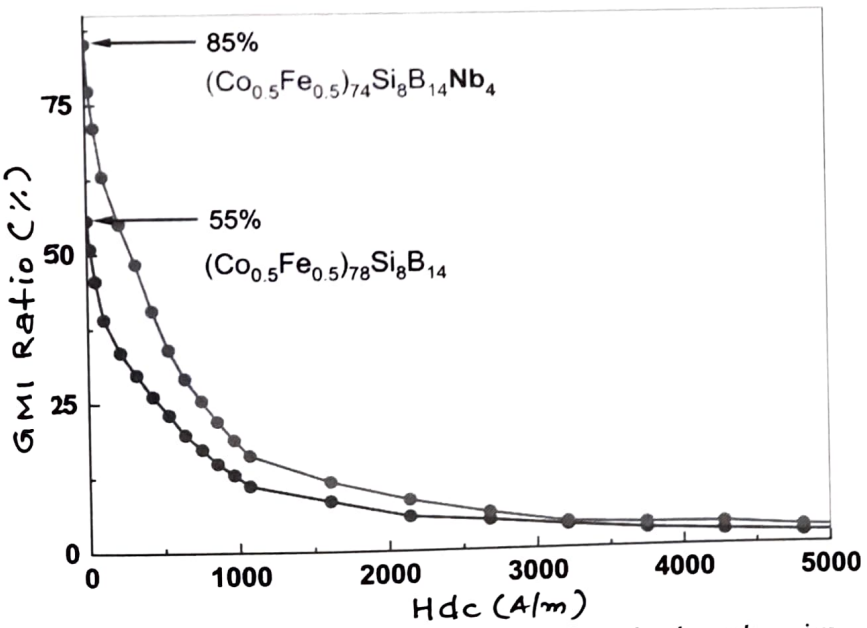

Fig.2. Giant magneto-impedance plots of as-quenched CoFe-based amorphous wires

CoFeSiB system (with Co:Fe :: 50:50) enhanced the GMI_{max} value from 55% to 85%. GMI values were obtained (Table-1) for a series of microwires with incorporation of Cr and also with stoichiometric variation of Co / Fe ratio. It was observed that optimal content of Cr along with appropriate tailoring of ferromagnetic constituents like Co and Fe further improved the GMI properties. The microwire with high GMI_{max} values was used as a sensing core element inside the probe of a Giant magneto-impedance based device. The sensing device (Fig-3a) developed in the laboratory using above mentioned microwires was able to detect the effects of carburization in a Ti-stabilized austenitic stainless steel (SS321). This type of problem is faced by petroleum refining industry where cracking of hydrocarbon takes place in a reactor unit made of SS321. The sensor output voltage for

three samples with varied carburization level (industrially carburized and heat treated) are shown in Fig-3b. AR represents the sample which was not carburized. Other samples were and subsequently heat treated at 800°C for one hour (Carb-1) and 12 hours (Carb-1) for carbide precipitation. The carburized sample also showed increase in mechanical hardness with soaking time.

Table-1 : GMI_{max} (%) values for CoFe-based amorphous microwires

Alloy Composition (at%)	GMI_{max} (%)
$(Co_{0.5}Fe_{0.5})_{78}Si_8B_{14}$	55
$(Co_{0.5}Fe_{0.5})_{74}Si_8B_{14}Nb_4$	85
$(Co_{0.5}Fe_{0.5})_{72}Si_8B_{14}Nb_4Cr_2$	121
$(Co_{0.5}Fe_{0.5})_{74}Si_8B_{14}Cr_4$	135

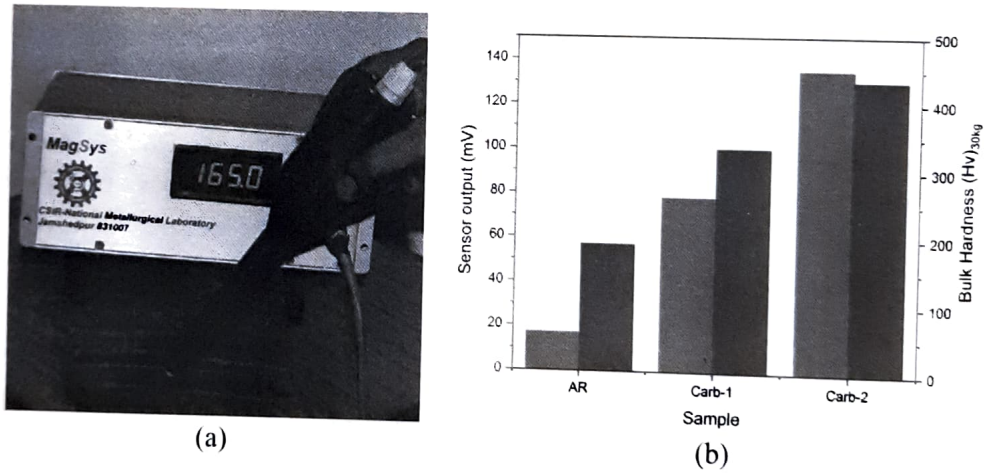

(a) (b)

Fig. 3. (a) Giant magneto-impedance sensor and (b) sensor output for different carburized samples along with hardness data.

The optical micrographs of as-received and carburized sample (Carb-1) are shown in Fig-4a and 4b respectively. The as-received sample with granular morphology converted to one with carbide precipitation in the grain boundaries. With depletion of chromium to form carbides, there is enhancement in ferromagnetic components in the matrix leading to rise in magnetic signal. The developed GMI based sensing device can be used for detection of carburization in reactor units of petrochemical industries.

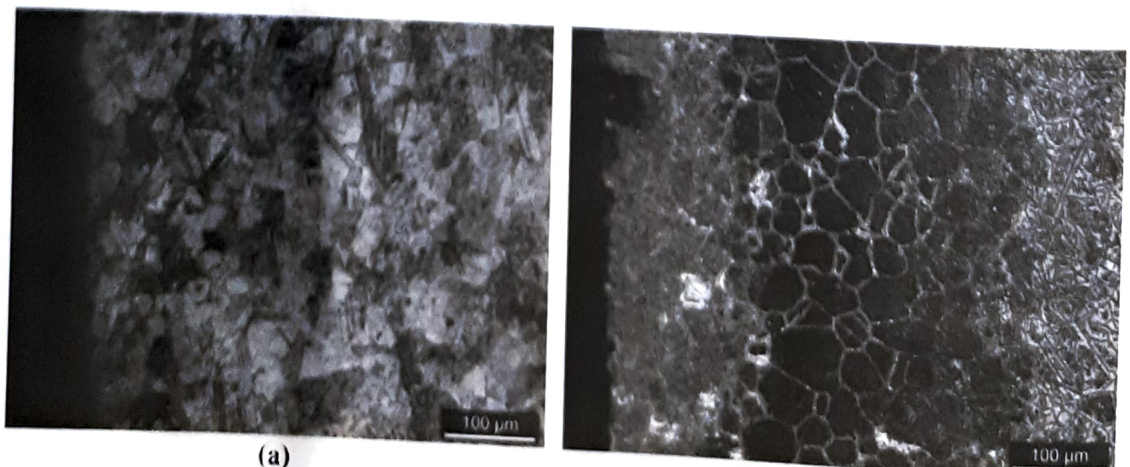

(a) (b)

Fig.4. Optical micrograph of (a) as-received and (b) Carb-1 sample.

RAPIDLY QUENCHED MAGNETOSTRICTIVE AND HIGH INDUCTION ALLOYS

Magnetostrictive materials for sensor application

In the laboratory, amorphous FeSiB based alloy ribbon having magnetostriction in the range of 25 to 30 ppm, have been used for generation of ultrasonic guided waves for detection of defects in pipes. The advantages of these soft magnetic ribbons are that they exhibit saturation magnetostriction constant in low magnetizing field and thereby high magnetizing field sources like either permanent magnets or bulky biasing coils can be eliminated. The melt Spun ribbons are pasted on one end of the pipe. Transmitting (T_c), Biasing (B_c) and Receiving (R_c) coils are placed over the magnetostrictive ribbons. The AC and DC current was sent through T_c and B_c coils. The laboratory based MsS measurement system is shown in Fig-5a. The MsS sensor output obtained as a variation of backwall (BW) echoes, and those obtained from hole as function of hole diameters are explained in Fig-5b. The magnetostrictive ribbon induces mechanical waves and transmitted through the pipe, while the reflected mechanical waves change permeability of stress sensitive ribbons due to Villari effect [18]. The change in permeability induces a secondary voltage picked up by R_c. It is observed that with increase in hole diameter, the MsS signal increases distinctly beyond one mm while the BWs correspondingly decreases.

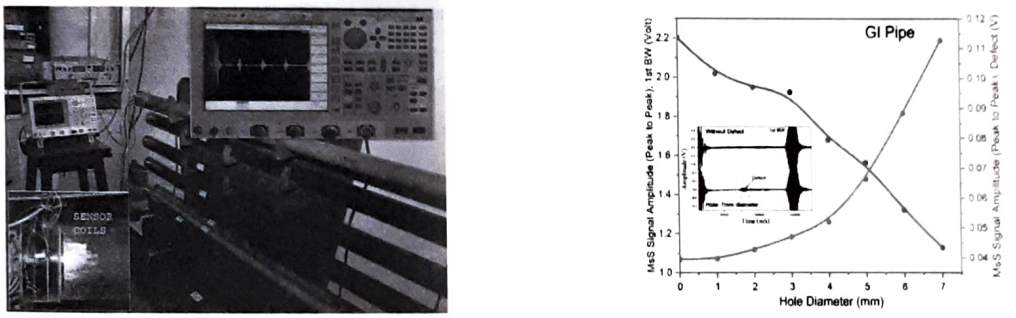

(a) (b)

Fig.5. Photograph of (a) MsS sensor system and (b) variation of MsS signals from backwall (BWs) and those obtained from hole in the galvanized iron (GI) pipe.

Tailoring metastable alloy compositions for high induction

The proper alloy design is the basis for high saturation magnetization and Curie point, fundamentally governed by Slater-Pauling curve [19]. It describes that magnetization of Fe-Co alloys become maximum at a fixed compositional ratio than any other stoichiometric ratio for same elements even for any other ferromagnetic elements. Accordingly, the crystalline alloys with nominal composition of $Fe_{65\text{-}70}Co_{35\text{-}30}$ have been reported a maximum values of M_s (2.4 T) and T_c (1000°C)[20]. These magnetic parameters of similar type Fe-Co basic composition are deviated in amorphous alloys owing to the addition of necessary metalloids. However, the controlled annealing treatment for same amorphous alloy results in the nanocomposites with a distribution of nanocrystallites in amorphous precursor, and the M_s values of annealed alloys are superior than pre-annealed amorphous alloys. On the view point of alloy design, the amorphous and nanostructutred soft magnetic alloy consist of four different categories elements, e.g., ferromagnetic, metalloid, grain growth inhibitors and nucleating agents with different compositional ratio to achieve necessary magnetic properties. The elemental percentage affects material properties, discussed here for the alloys of nominal compositions $(Fe_{1\text{-}b}Co_b)\ 100_{\text{-}w\text{-}x\text{-}y\text{-}z}\ B_wSi_xNb_yCu_z$ (where $0.05 \le b \le 0.5$ at%, $8 \le w \le 13$ at%, $0 \le x \le 8$ at%, $0 \le y \le 3$ at%, $0 \le z \le 1$at %). Fig.6 explains the effect of ferromagnetic (Fe/(Fe+Co)) and non-magnetic (B/Nb(B+Si)) elements on saturation magnetization and coercivity. The saturation magnetization (M_s) becomes greater than 1.6 T while Fe/ (Fe+Co) and B/Nb(B+Si) vary within 0.5-0.65 and 0.3 -0.5, respectively (Figs. 6a and 6b). It is also noteworthy that the similar low range (0.5-0.65) of Fe/ (Fe+Co) ratio is also responsible for maintaining coercivity below 250 mOe (Fig. 6c). Similarly, the B/Nb(B+Si) ratio with lower range (0.15 -0.27) also leads to alloys with coercivity below 250 mOe (Fig. 6d).

Therefore, the amorphous and nanocrystalline alloys achieve high saturation magnetization and low coercivity with the optimization of alloy composition by varying ferromagnetic and non-magnetic elemental ratios.

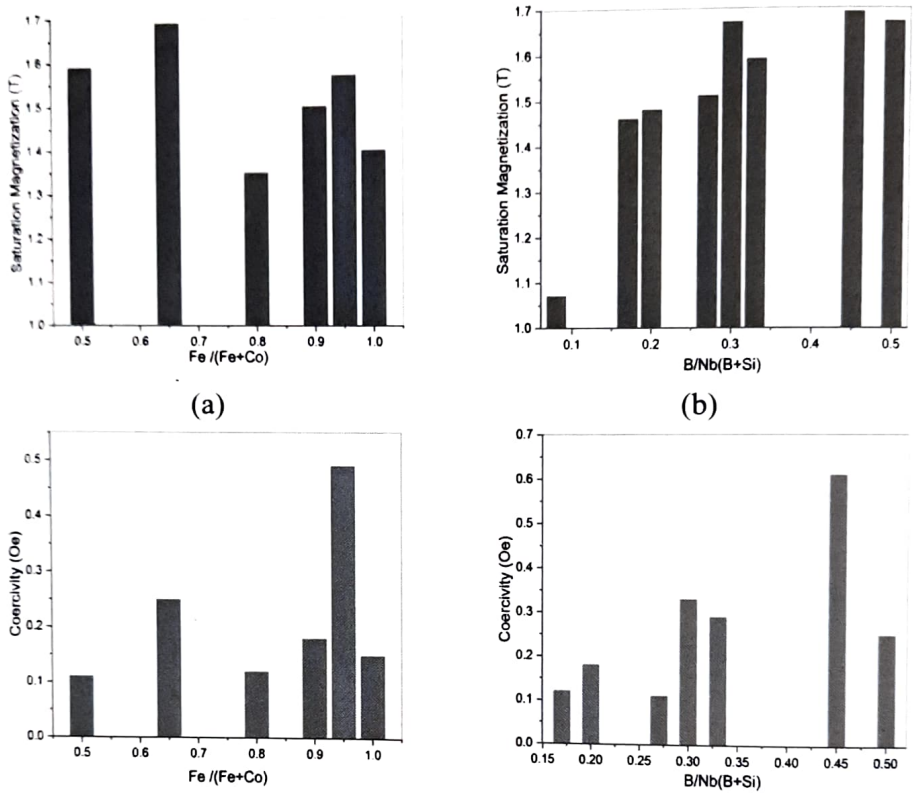

Fig. 6. Variation of saturation magnetization with the ratios of (a) Fe/(Fe+Co)), (b) B/Nb(B+Si) and coercivity with that of (c) Fe/(Fe+Co)), (d) B/Nb(B+Si)

PERSPECTIVE APPLICATION FOR EMI SHIELDING

The electromagnetic interference shielding effectiveness (EMI SE) of soft magnetic amorphous ribbons of typical composition $Co_{72.5}(SiB)_{22.5}$, $Fe_{80}(SiB)_{20}$, $Fe_{83}(SiB)_{15}Nb_2$ and $(FeCo)_{83}(SiB)_{13}Nb_3Cu_1$ were studied in the 0-8 GHz microwave frequency range. The EMI SE mechanism of typical soft-magnetic melt-spun ribbons has been described schematically (Fig. 7). The total shielding of incoming EM waves is done through attenuation by shields through surface reflection, matrix absorption and multiple internal reflection.

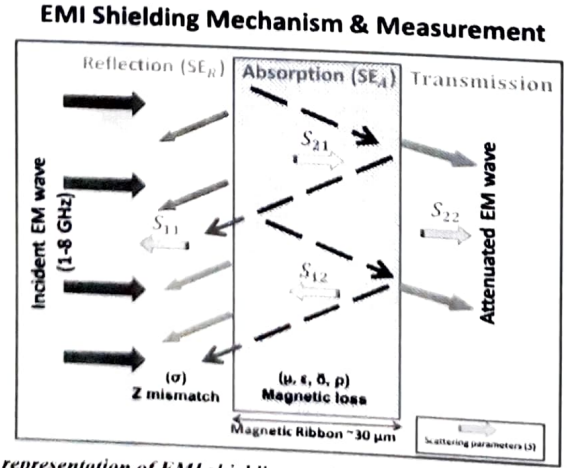

Fig. 7. Schematic representation of EMI shielding mechanism in amorphous soft magnetic ribbons.

The material parameters like complex permittivity (ε', ε''), complex permeability (μ', μ'') and scattering parameters (S_{11}, S_{12}, S_{22}, S_{21}) obtained from VNA were used to calculate the reflection(SER) and absorption(SE_A) contribution from the total shielding effectiveness(SE_T) using equations 1-4 [21].

EMI $SE_T(dB) = SE_R + SE_A + SE_M$ (1) (SE_M neglected for SE_T>10dB)

$$SE_T = SE_R + SE_A \quad (2)$$

$$SE_R = 10\log_{10}\left(\frac{1}{1-|S_{11}|^2}\right) \quad (3)$$

$$SE_A = 10\log_{10}\left(1-\frac{|S_{11}|^2}{|S_{12}|^2}\right) \quad (4)$$

The complex parameters (ε', ε'', μ', μ'') spectrum, decreases from 0-5 GHz and remains constant till 8 GHz for all alloy ribbons. Further, the real part of complex permittivity (ε') and permeability (μ') representing energy storage part does not show difference based on alloy composition. Whereas, the imaginary or lossy part (ε'', μ'') show significant variation among the ribbons based on alloy composition, decreasing in the order of CoSiB, FeSiB, FeCoSiBNbCu and FeSiBNb. The total EMI SE and material properties of amorphous ribbons are given in Table. 2.

Table. 2. Summary of electromagnetic shielding and soft magnetic properties of amorphous ribbons

S.No	Alloy	SE_T (dB)	SE_A	SE_R	H_c (A/m)	M_s (T)	μ_i
1	$Co_{72.5}(SiB)_{22.5}$	>35	33	<3	3 ± 0.5	0.7	10^{4-5}
2	$Fe_{80}(SiB)_{20}$	>30	27	<3	8 ±0.5	1.5	10^{3-4}
3	$(FeCo)_{83}(SiB)_{13}Nb_3Cu1$	>33-26.5	21-30	<5	18 ±1	1.6	10^3
4	$Fe_{83}(SiB)_{15}Nb_2$	32 -12	10-20	<8	24 ±1.5	1.45	10^2

The as-quenched amorphous ribbons irrespective of composition, show good EMI shielding properties (> 10 dB) in the entire 0-8 GHz microwave frequency range. Particularly, CoSiB and FeSiB alloys show exceptional total shielding characteristics (SET >30 dB) in the entire frequency range, attenuating 99.99% of incident EM waves. Interestingly, the absorption is a main shielding mechanism in magnetic ribbons. The reflection (SE_R) contribution lies less than 5 dB, signifying, the entire EM waves enters into ribbon matrix and undergoes attenuation through absorption mechanism (SE_A). Further, the compositional dependent variation among the ribbons can be observed (Table.2). The variation is mainly attributed to the effective skin depth, in turn depends on the magnetic permeability and electrical resistivity of the alloy ribbons [22]. The present study substantiates the excellent shielding properties of soft magnetic ribbons, particularly as magnetic absorbers in 0-8 GHz frequency range. The soft magnetic ribbons can be effectively pulverized and used as magnetic filler agents in composites for broadband shields/absorbers.

CONCLUSION

The rapidly quenched materials in the form of amorphous / nanostructured wires and foils were prepared by in-water quenching and melt spinning techniques. The CoFe-based microwires reveal excellent giant magneto-impedance properties and were used as core element of a GMI based sensing device for detection of carburization in austenitic steel. The magnetostrictive sensing (MsS) device was developed with amorphous magnetostrictive ribbons as sensing element for detection of defects in pipes. The dimension change of pipe defect (e.g., hole)

displayed corresponding evidence in MsS signals. Other than sensor applications, the properties of rapidly quenched ribbons where also tailored for achieving high saturation induction. For this, compositional control was carried out on metalloids (Si, B), refractory element like Nb and ferromagnetic constituents (Fe,Co) to achieve saturation induction greater than 1.6 Tesla. The rapidly quenched amorphous ribbons also manifested potential electromagnetic shielding properties. Amongst different alloy ribbons, the CoSiB and FeSiB based ribbons showed exceptional total shielding characteristics with SE_T >30 dB.

REFERENCES

[1]. Y. Yoshizawa, S. Oguma, K. Yamauchi : New Fe-based soft magnetic alloys composed of ultrafine grain structure. J. Appl. Phys 64: 6044, 1988.

[2]. Nicholas de Christofaro : Amorphous Metals in Electric-Power distribution applications.MRS Bulletin 23: 50-56, 1998.

[3]. AO. Olofinjana, J.H. Kern, H.A. Davies : Effects of process variables on the multi-strand casting of high strength sub-millimeter metallic glass wire. J. Mater. Process. Technol 155–156:1344, 2004.

[4]. P. Sarkar, R. K. Roy, A. K. Panda, A. Mitra : Optimization of process parameters for developing FeCoSiB amorphous microwires through in-rotating-water quenching technique. App. Phys A: Mater. Sc. and Proces 111: 575-580, 2013.

[5]. V.R.V. Ramanan : Metallic Glasses in Distribution Transformer Applications: An Update. J. Mater. Eng 13: 119-127, 1991.

[6]. K. Souma, S. Tanigawa, I. Moue, H. Kikuchi, T. Iwasaki : High-performance Materials for Electric Drive Solutions. Hitachi Review 60: 54-62, 2011.

[7]. M.E. McHenry, M.A. Willard, D.E. Laughlin : Amorphous and nanocrystalline materials for applications as soft magnets. Prog. Mater. Sci 44: 291, 1999.

[8]. R.K. Roy, A. K. Panda, A. Mitra : Effect of Co content on structure and magnetic behaviors of high induction Fe-based amorphous alloys. J. Magn. Mag. Mater 418: 236–241, 2016.

[9]. R.K. Roy, S. J. Kernion, S. Shen, and M. E. McHenry : Crystallization behavior and high temperature magnetic phase transitions of Nb-substituted FeCoSiBCu nanocomposites. Applied Physics Letters 99: 192506, 2011.

[10]. H. Kwun and K.A. Bartels : Magnetostrictive sensor technology and its applications Ultrasonics 36: 171–8: 1998.

[11]. A.K. Panda, P K Sharan, R. K. Roy, G.V.S. Murthy, A. Mitra : Generation and detection of guided waves in a defective pipe using rapidly quenched magnetostrictive ribbons.Smart Materials and Structures 21: 045015, 2012.

[12]. V. Zhukova, M. Ipatov, A. Zhukov : Thin magnetically soft wires for magnetic microsensors. Sensors 9: 9216–9240, 2009.

[13]. P. Ripka : Review of fluxgate sensors. Sensors & Actuators A 33: 129-141, 1992.

[14]. A.K.Panda, A.P. James, A. Mohan, S. Dey, R.K.Roy, A.Mitra : Investigation on transverse defect and cavitation depth in ferrous pipe using melt spun FeSiB ribbon as magnetostrictive sensing element. NDT&E International 80: 15-22, 2016.

[15]. T.K. Das, A. Mitra, S.K. Mandal, R.K. Roy, P. Banerji, A.K. Panda : Parametric controls on giant magnetoimpedance (GMI) behaviour of CoFeSiBCr amorphous wires for prospective sensor applications. Sens. & Actuators A 220: 382-387, 2014.

[16] V.M. Petrov, V.V. Gagulin : Microwave absorbing materials. Inorg. Mater 37:93-98, 2001.

[17]. M. Vazquez : Giant magneto-impedance in soft magnetic wires. J. Magn. Magn.Mater. 226–230: 693-699, 2001.

[18]. E. Villari : Change of magnetization by tension and by electric current Annal. Phys. Chem., Lpz. 128:1865.

[19]. J.C. Slater : The Ferromagnetism of Nickel. II. Temperature Effects. Phys. Rev. 49: 931, 1936.

[20]. F. Pfeifer, C.J. Radelo : Soft magnetic Ni-Fe and Co-Fe alloys - some physical and metallurgical aspects. J. Magn. Magn. Mater 19:190, 1980.

[21]. R. Panigrahi, S.K. Srivastava, J. Pionteck : Fabrication of elastomer blends involving core (Polystyrene)@shell (Polyaniline) approach, their characterization and applications in electromagnetic shielding. Rubber Chem. Technol 91: 97–119, 2018.

[22]. P. Murugaiyan, A. Mitra, A.K. Panda, A.S. Kumar, R.K. Roy, S. Kumar : Electromagnetic interference shielding effectiveness of soft magnetic amorphous. Physica B: Condensed Matter 568: 13-17, 2019.

Journal of Metallurgy and Materials Science, Vol. 62, No. 3-4, July-December 2020, pp. 89-93
Printed in India, © NML, ISSN 0972-4257

Spectroscopic changes in conventional magnetorheological fluid and graphene oxide based magnetorheological fluid with combustion method

KUNAL SINGH BISHT[1] and KAVERI SAH[2]
[1] Chemical Engineer of RI Nanotech India, Plot No. 92, Sector- IIDC, SIDCUL, Pantnagar, Rudrapur, Uttarakhand-263153, India
[2] Lab Scientist of RI Nanotech India, Plot No. 92, Sector- IIDC, SIDCUL, Pantnagar, Rudrapur, Uttarakhand-263153, India

Abstract: A comparative spectroscopic analysis of conventional Magnetorheological fluid and Graphene Oxide based Magnetorheological fluid. Raman spectra have been recorded using 532 nm laser excitation. The down shifted G-band of Graphene Oxide observed at 1576.42 cm^{-1} due to the doubly degenerate zone center E2g mode and 2D band at 2702.58 cm^{-1} confirms the presence of Graphene Oxide. UV - VIS Absorption spectrum of GO based MR fluid has been recorded of π-π plasmon peak at 233.82 cm^{-1} while a broad band is displayed in conventional Magnetorheological fluid. Here, Graphene Oxide used in Magnetorheological fluid is prepared by combustion method of separating Graphene layers by controlled oxidation. This analysis shows highly efficient, unequivocal, non-destructive identification of Graphene Oxide in Magnetorheological fluid.

INTRODUCTION

Graphene Oxide based Magnetorheological fluid is a controllable active smart material which can respond precisely to external magnetic field by aligning along the lines of magnetic flux, forming a chain like microstructure which opposes the flow. It consists of polarizable particles suspended in a nonmagnetic carrier medium. In the absence of magnetic field, Graphene oxide occupies the interspaces between the magnetic particles to restrain the direct contact of these particles, consequently sustaining the stability of MR fluid, due to its structurally supportive amphiphilic nature. Furthermore, stabilizing polarizable particles in the base fluid. In the presence of magnetic field, these dispersed particles polarizes, forming assembled chain-like micro-structure along with Graphene oxide filled in the space of body-centered pentagonal structure of iron particles under van der Waals interparticle interactions.

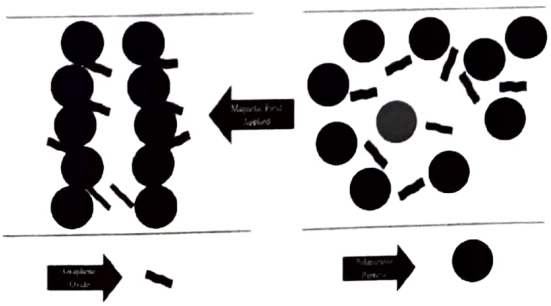

Fig.1. Schematic diagram of GO based MR fluid

EXPERIMENTAL PROCEDURE

Raman spectroscopy

Raman spectra were recorded using RIRM Direct Coupled Raman Spectrometer, an excitation laser source at 532 nm, dual sample holder (Vertical and Horizontal), and a charge-coupled device (CCD) detector. Analysis of samples with a microscopic laser spot using high quality lens and filters with 10x long working distance, a 200mW tunable laser power, a spectral range from 120 to 4500 cm^{-1} with an optical resolution of 1 to 3 cm^{-1}, a precise stage height movement, a direct coupled air free optics. The acquisition time was of 2 scans with 4500ms exposure time.

UV-Visible spectroscopy

UV-Visible absorption spectra was recorded using RI2AS spectrometer, a balanced deuterium halogen composite light source (deuterium lamp emitting a continuous spectrum of light ranging from 190-400 nm in the UV range to 400-800 nm in visible light, tungsten halogen lamp emitting light ranging from 360-2000 nm), a spectral range from 190-2500 nm, an optical resolution of 0.03-8.4 nm, sensitivity of 161000 counts/μW per millisecond integration time, focal length of 110 mm, 6:1 round to linear fiber, detector collecting lens and order sorting filter. The acquisition time was 51 scans with 2ms exposure time.

RI software features

Instrument control and data collection parameters are user definable, such as exposure time, dark correction, signal averaging, spectral smoothing, and automatic saved spectra. Graphics saved in .txt format and can be opened in any third-party software e.g. Origin, Excel and other data processing software.

Comparative analysis

Graphene oxide based Magnetorheological fluid fingerprint is quite different from conventional Magnetorheological fluid and it can be easily identified by the Raman spectra.

Through Raman spectroscopy it is possible to monitor the changes in the morphology of different Magnetorheological fluids since C-C and C=C symmetric vibrations of the aromatic rings have a strong change of polarizability of their electronic cloud inducing a strong Raman Effect. Absence of less intense D peak indicates absence of significant number of defects. It was only observed in the sample of Graphene Oxide.

Magnetorheological fluid has several characteristic sharp bands at about 488.50 cm^{-1} representing Fe-CO stretching [2], 1069.88 cm^{-1} corresponding to Si–O–C stretching, asymmetric deformation vibration of the CH_3 group at 1413.94 cm^{-1}, characteristic sharp band at 1260 cm^{-1} due to the symmetric deformation of methyl groups, asymmetric and symmetric stretching vibration of C-H at 2800-3000 cm^{-1} [1]. Graphene oxide based Magnetorheological fluid has same characteristic bands including two more bands at 1576.42 cm^{-1} representing in plane vibration of c-c bond corresponding to the E2g symmetry and an evolved broad band at 2702.58 cm^{-1} [3].

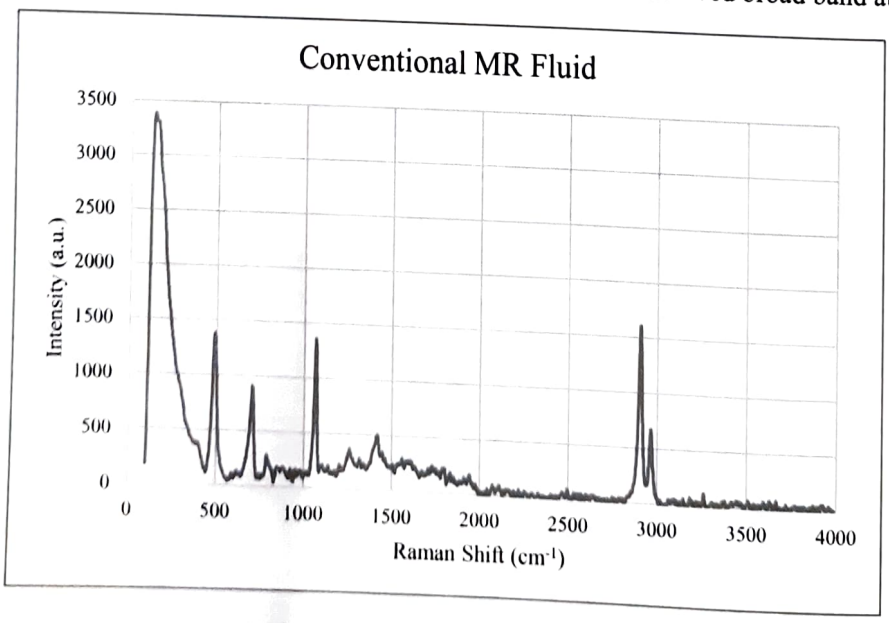

Fig.2. Raman spectrum of Conventional MR fluid

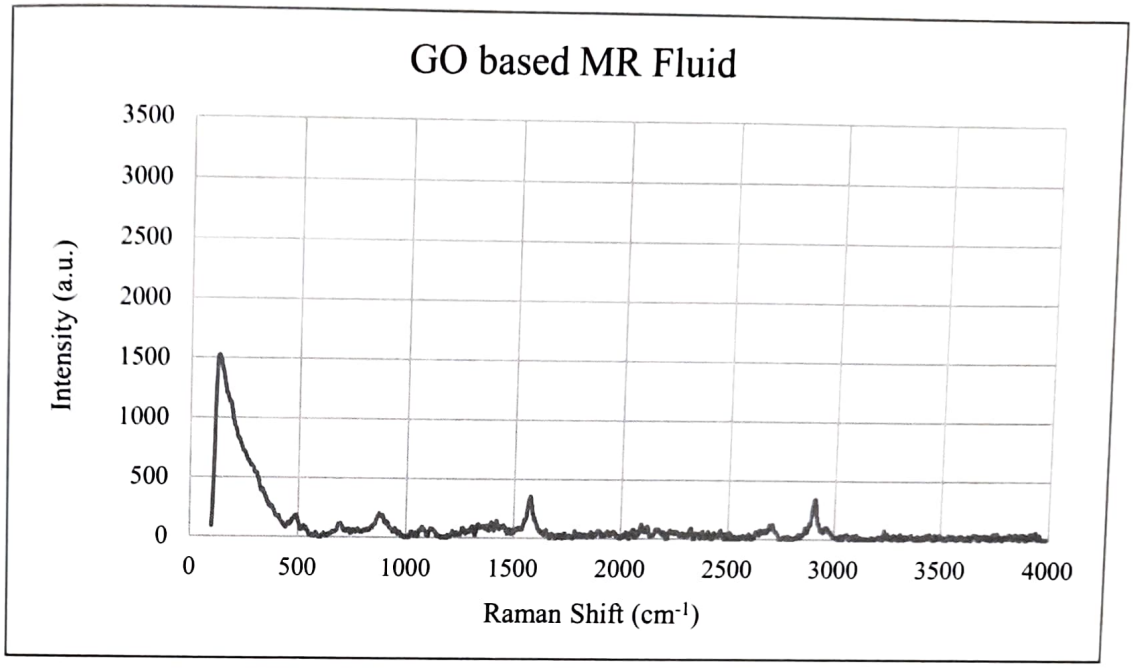

Fig.3. Raman spectrum of GO based MR fluid

In UV-VIS Absorption spectra, it can be inferred that optical absorption of Graphene Oxide in Magnetorheological fluid is dominated by the π-π plasmon peak near 233.82 nm depending on nanometer-scale sp2 clusters and linking of chromophore units like C=C, C-C, C=O bonds while in absorption spectrum of Conventional Magnetorheological fluid, this peak is absent [4].

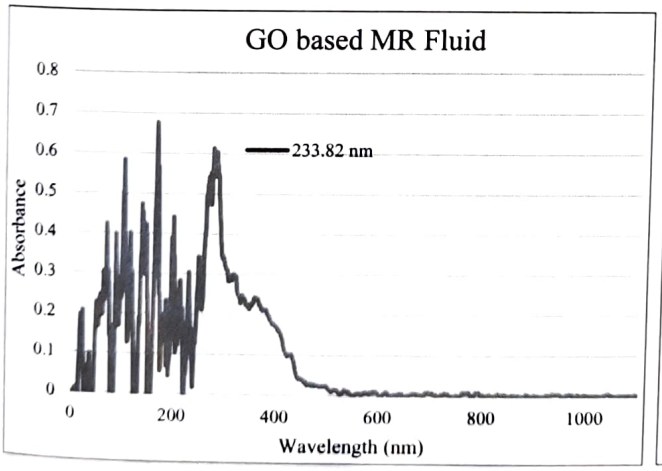

Fig.4. Absorption spectrum of GO based MR fluid

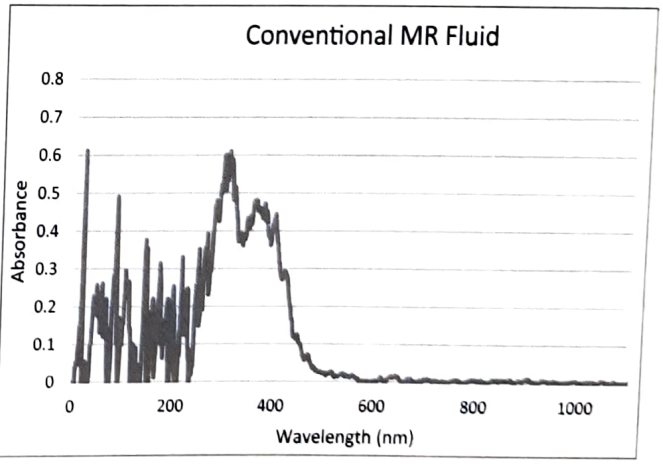

Fig.5. Absorption spectrum of Conventional MR fluid

Stability of Graphene Oxide based Magnetorheological Fluid as compared to Conventional Magnetorheological fluid

Because of the large density mismatch between dispersing (0.967 gm/ml) and dispersed phase (7.8 gm/ml), magnetic particles tends to settle down at the bottom. For the quantitative analysis of sedimentation rate, a simple experiment was performed [5]. Two falcon tubes of 50 ml were taken and filled with conventional and GO based Magnetorheological fluid. The phase boundary separating Magnetorheological fluid from the supernatant was observed over a period of time.

Following equation was used for sedimentation rate calculation:

Sedimentation Ratio = Volume of supernatant fluid / Total volume of Magneto rheological fluid × 100

Fig.6. represents the sedimentation ratios of the two Magnetorheological fluids. Conventional Magnetorheological fluid has the sedimentation ratio of 34.61% and Graphene Oxide based Magnetorheological fluid has sedimentation ratio of 0.02%.

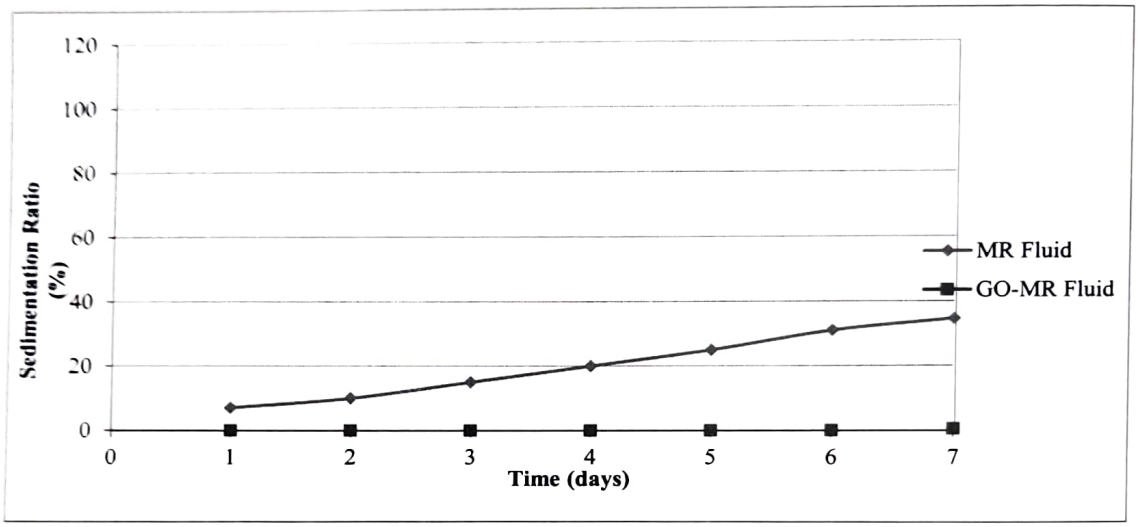

Fig.6. Sedimentation rate of MR fluids

It was observed that GO based Magnetorheological fluid was well dispersed and stable for a period of 7 days. Thus, in terms of sedimentation ratio, Graphene Oxide based Magnetorheological fluid is more suitable for real-time torque transmission applications.

This test reveals that Graphene Oxide based Magnetorheological fluid is one the best candidate for overcoming the problem of high sedimentation rates.

Stability of the fluid is crucial in every torque transmission industrial application including shear, valve and squeeze mode operations. Thus, optimum concentration of Graphene Oxide is desirable for stability enhancement of Magnetorheological fluid. Graphene oxide based Magnetorheological fluid shows no sedimentation after qualitative observation of over two months. The samples were kept under observation and photographed before and after 7 days.

Fig.7. (a) MR fluid on the left hand side & GO Based MR Fluid on the right

Fig.7. (b) After 7 days sedimentation of MR fluid on the left hand side & GO Based MR Fluid on the right hand side

CONCLUSION

A new approach to directly capture Graphene Oxide based Magnetorheological fluid in Raman Spectrum which is clearly different from the Spectrum of Conventional Magnetorheological fluid. Presence of Graphene Oxide in Magnetorheological fluid increased sedimentation stability, directly increasing the shelf life of Magnetorheological fluid. The Raman Spectra of both Magnetorheological fluids reflect changes in the electronic structure and electron-phonon interactions allowing unequivocal, highly efficient, non-destructive identification of Graphene Oxide in Magnetorheological fluid.

ACKNOWLEDGMENT

The authors gratefully acknowledge Dr. R.P. Joshi sir, for his invaluable guidance during this work and the entire RI Group for continuous encouragement and support.

REFERENCES

[1] W. Osterle, A. Giovannozzi, T. Gradt, I.Häusler, A. Rossi , B. Wetzel, G. Zhang, A.I. Dmitriev. Exploring the potential of Raman spectroscopy for the identification of silicone oil residue and wear scar characterization for the assessment of tribofilm functionality.Tribol Int; 90: 481–490, 2015.

[2] Bogdan M. Leu, Nathan J. Silvernail, Marek Z. Zgierski, Graeme R. A. Wyllie, Mary K. Ellison, W. Robert Scheidt, Jiyong Zhao, Wolfgang Sturhahn, E. Ercan Alp, and J.Timothy Sage. Quantitative Vibrational Dynamics of Iron in Carbonyl, Porphyrins, Biophys. J. 92: 3764–3783,2007.

[3] A.C. Ferrari, J.C. Meyer, V. Scardaci, C. Casiraghi, M. Lazzeri, F. Mauri, S. Piscanec, D. Jiang, K. S. Novoselov, S. Roth and A. K. Geim. Raman Spectrum of Graphene and Graphene Layers. Phys. Rev. 97: 187401,2006.

[4] Qi Lai, Shifu Zhu, Xueping Luo, Min Zou, and Shuanghua Huang. Ultraviolet-visible spectroscopy of graphene oxides, AIP Advances 2: 032146,2012.

[5] Muhammad Taha Manzoor, Ji Eun Kim, Jung Hwan Jung, Chulhee Han, Seung BokChoi & Il-Kwon Oh. Scientific reports, 8:12672,2018..

Journal of Metallurgy and Materials Science, Vol. 62, No. 3-4, July-December 2020, pp. 95-102
Printed in India, © NML, ISSN 0972-4257

Electrochemical application of shape and phase dependant copper sulphide for cost-effective next generation supercapacitive energy storage: A review

ARYA DAS, MAMATA MOHAPATRA and SUDDHASATWA BASU*
CSIR-Institute of Minerals and Materials Technology, Bhubaneswar, Odisha, INDIA-751013

Abstract : Copper sulphides ($Cu_{2-x}S$) based chalcogenide materials have received voluminous consideration for supercapacitive energy storage with unique semiconducting properties, nontoxicity and extensive earth abudancy. The existence of $Cu_{2-x}S$ in discrete crystal geometries and morphology liberalizes opportunities to tune them for desired performances. Consequently, the understanding of the phase and morphology dependency on performances can be pivotal in building novel designs for enhanced power and energy delivery. Herein an in-depth recent literature investigation into the synthesis of diverse phases and morphologies of $Cu_{2-x}S$ nano/microstructures and their super capacitive behaviours has been reported. Given the potent of $Cu_{2-x}S$ as highly efficient supercapacitive electrode as low cost material and their extensive deployment it is imperative to profoundly highlight the recent advances in $Cu_{2-x}S$ based electrode materials directed towards supercapacitive energy storage.

Keyword: *$Cu_{2-x}S$, electrode material, synthesis, energy storage*

INTRODUCTION

Search of low-cost materials as supercapacitors for sustainable energy storing devices is one of the current pivotal R&D area, because of their application in wide range of commercial electronics starting from minute memory caches, portable electronics to vast transportation and military technologies [1, 2]. The potent of supercapacitor as rapid power delivery devices is realised through its fast charge discharge mechanisms enabling rapid energy delivery and extensive lifespan of performance. Supercapacitors store electrical energy either through charge accumulation at the electrode/electrolyte (Electric double layer capacitance) interface or via near to surface reversible redox reactions (Pseudo capacitance) [3, 4] (Fig 1(a)). The design of novel electrode materials in terms of sustainability and cost effective for efficient energy storage has been the forefront of energy research and a wide range of materials have been constantly evaluated for the same. Transition metal sulphides (TMS) have made a commendable stand in terms of impending electrode material due to their inherent high electrical conductivity and high theoretical capacitance [5, 6].Thus reasonable R&D efforts are given on rationally designed novel sulphide materials to tune the surface area and short diffusion paths to attain optimum specific capacitance [7, 8] for feasible commercial implication. Among them, earth abundant copper sulphides ($Cu_{2-x}S$) (Fig 1(b)) suits more convenient electrode materials due to their high electrical conductivity assisted with enhanced redox electrochemical activity at an affordable cost[9-12] and existence in different stoichiometry form copper rich to sulphur rich valence states. Though these materials have electronic conductivity of $10^{-3}S \cdot cm^{-1}$and theoretical specific capacity of 561 $mA \cdot h \cdot g^{-1}$, it is desired to tune their semiconducting and low conductivity properties for a favourable SC applications[13]. Diverse semiconductor micro/nanostructured copper sulphides ($Cu_{2-x}S$) electrodes with varied crystal engagements can result better electrical features for enhanced energy storage performance [14]. The crystal structure of copper sulphides ($Cu_{2-x}S$) is assigned on the basis of sulphur packing in the lattice structure. Anilite and digenite exist as cubic packing, djurleite and chalcocite exist in hexagonalclose packing and covellite results due to integration ofhexagonal close packing and sulfur atoms covalent bonding [15]. The different reported crystal structures with varying compositions ranging from smaller value from $x < 1$ to larger value of $x=1$ in $Cu_{2-x}S$ exist as covellite (CuS), yarrowite($Cu_{1.12}S$), spionkopite ($Cu_{1.40}S$), geerite ($Cu_{1.60}S$), anilite ($Cu_{1.75}S$, or Cu_7S_4), digenite ($Cu_{1.80}S$djurleite ($Cu_{1.96}S$) and chalcocite (Cu_2S). The crystal structures of various forms of copper sulphides shown in Fig 2 [16, 17] are reported.

*Corresponding Author Email - sbasu@immt.res.in, #mamata@immt.res.in

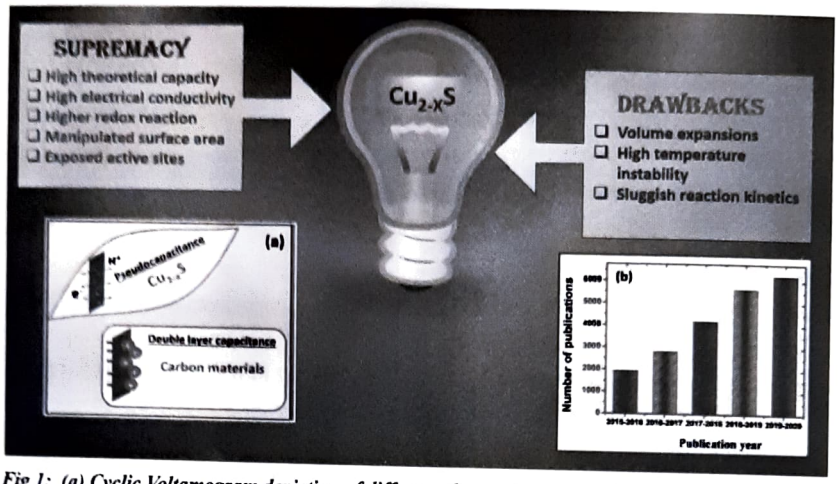

Fig 1: (a) Cyclic Voltamogram depiction of different charge storage mechanisms of supercapacitor (b) the increasing research publications on copper sulphides based energy storage.

However, investigation of size-controlled and composition-optimized $Cu_{2-x}S$ nano/microstructures stands incomplete without underlining the morphology-dependent properties for effective energy storage. Therefore, the design and study of novel $Cu_{2-x}S$ micro- /nanostructures assisted with governable crystalline building block and composition is necessary for basic fundamental understanding and technological implementation. Thus, with the basic understanding of tuneable intrinsic properties of $Cu_{2-x}S$ micro-/nanostructures leading to great expediency of supercapacitive storage, in this review we highlight the recent advancements in prevalent pure phases of $Cu_{2-x}S$ micro-/nanostructures as electrode materials.

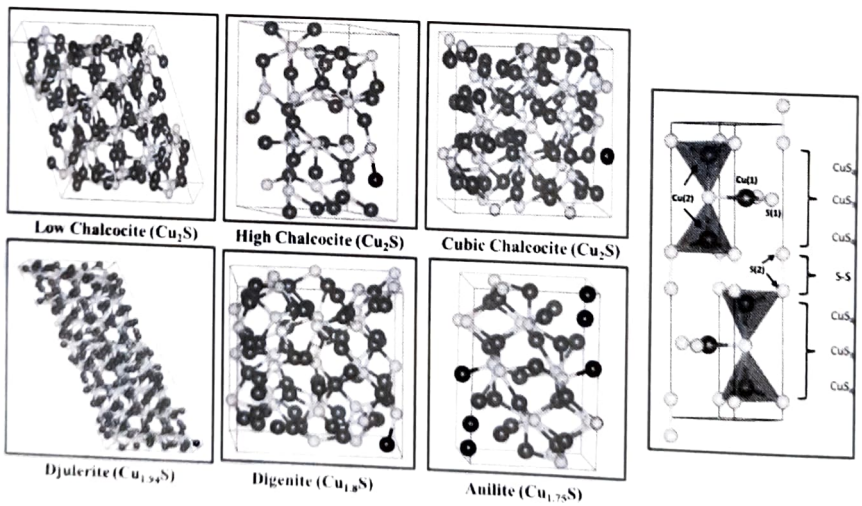

Fig 2: Different crystal structures of Copper sulphide existence. Reprinted with permission from Ref[10] and Ref[17].

VARIOUS MORPHOLOGIES OF PURE $CU_{2-X}S$ NANO/MICRO-STRUCTURES ELECTRODE MATERIALS

From the electrochemical performance point of view, tailored/designed material structures can be conducive to a large surface area which creates sufficient sites for ionic adsorption. Thus, notable efforts have been made in the last few years in the area of development of super capacitors based on different structure, morphology and composition of the $Cu_{2-x}S$. For this purpose, the different phases endowing atypical 0D, 1D, 2D, 3D morphologies and their subsequent impact on the energy storage will be explicated. Particularly, 1-D and 2-D materials are of much interest because of facile intercalate and de-intercalation enhances charge-discharge phenomenon. Again 3D

materials provides more reaction sites using three dimensional interconnection and hence helpful for increasing both energy and power densities. Various synthesis methods have been proposed involving hydrothermal [18], microwave [19], solvothermal [20], chemical vapour deposition [21], to obtain diversified dimensional morphologies such as zero dimensional 0D [22-24], one dimensional 1D [25-27], two dimensional 2D [28-30], three dimensional 3D [31-33] micro/nanostructures obtained by specific to get specific applications (Fig 3). A systematic study on specific phase synthesis mechanism of $Cu_{2-x}S$ micro-/nanostructures with desired intrinsic properties for enhanced energy storage is expected to provide an in-depth insight for developing novel $Cu_{2-x}S$ based supercapacitive electrode materials.

Zero dimensional (0D) $Cu_{2-x}S$ nano/micro-structures

Three dimension constrained 0D nano/micro-structures possess high available surface area for electrode/ electrolyte interfaces, which has led to immense investigation for their application as supercapacitor electrodes [34,35]. In this regard 0D $Cu_{2-x}S$ nano/micro-structures have also been explored. Recently Zhao et al.

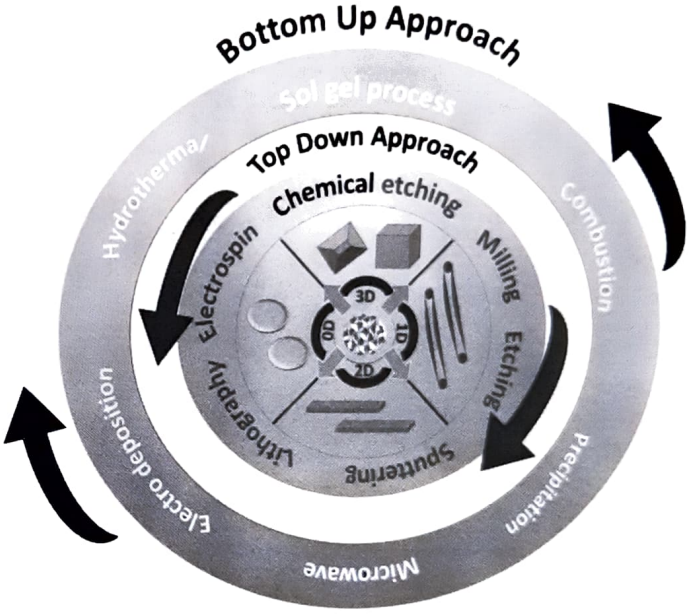

Fig 3: Various Synthesis approaches undertaken for shape and crystal structure desired synthesis of copper sulphide $Cu_{2-x}S$ nano/micro-structures.

reported hydrothermal synthesis CuS microspheres with specific capacitance of 131.7 Fg^{-1} at 10 mV/s in 3M KOH electrolyte. Further when modified with carbon dots on carbon nanotubes a high specific capacitance of 736.1 Fg^{-1}at 1 $Ag^{-1}$was achieved. The electrodes also reflected a high cycling retention of 92% retention over 5000 cycles at current density of 3Ag^{-1} [36].

In another recent study by the same group CuS microspheres were synthesized in room temperature within 2 hours using a novel facile one pot synthesis technique. The CuS microspheres in the range of 1.5 to 3 μm with 1:1.5 feeded copper to sulphur molar ratio exhibits a superior capacitance of 444.2 Fg^{-1} at 1 Ag^{-1}. Additionally an asymmetric device assembled using reduced graphene oxide as negative electrode could achieve energy density and power density as high as 18.6 $Whkg^{-1}$ 681.2 Wkg^{-1} with cyclic stability of 89% after 4000 cycles at 6 Ag^{-1} [37].

One dimensional (1D) $Cu_{2-x}S$ nano/micro-structures

1D are nano/micro-structures singular structures such as nanotubes, nanorods, nanowires etcare apprehended to provide ample contact area, high flexibility and shorter diffusion pathways between electrode and electrolyte.

A lot of studies have been directed towards this direction by several methods [38, 39]. Lately, vertical binder free growth of active material conductive substrateshas served as one of the most encouraging electrode design tactics owing to enhanced quick ion transport capability [40]. Javed et al reported highly flexible Cu_7S_4 nanowires – Carbon Fibre Fabric exhibited a high capacitance of 400 Fg^{-1} at the scan rate of 10 m Vs^{-1} achieving energy density of 35 Wh kg^{-1} at power density of 200 W kg^{-1} which could light 6 LEDs effectively [41]. In another work Hou et al designed hierarchical grown 1D architecture CuS nano-needles using a template based conversion route. The electrode materials delivered a high capacitance of 566.4 Fg^{-1} realising an energy density of 29.9 kW kg^{-1} even at high power density of 1.1 kW kg^{-1} [42]. In a very recent study by authors could grow 1D single crystalline Cu_2S nanorods on conducting Cu substrate in a very short time using a novel solution based direct synthesis method. The Cu_2S nanorods reflected superior specific of 750 mF cm^{-2} at a current density of 2 $mAcm^{-2}$ with extremely good cycling stability of 82.3% at a high current density of 40 $mAcm^2$ after 20 000 cycles, respectively. When assembled into an asymmetric using activated carbon the AC//SC-Cu_2S device(shown in Fig.4) a higher energy density of 2.69 mW h cm^{-3} and power density ranging from 10.9 to 218.4 mW cm^{-3} in a wide potential window 1.6 V [43].

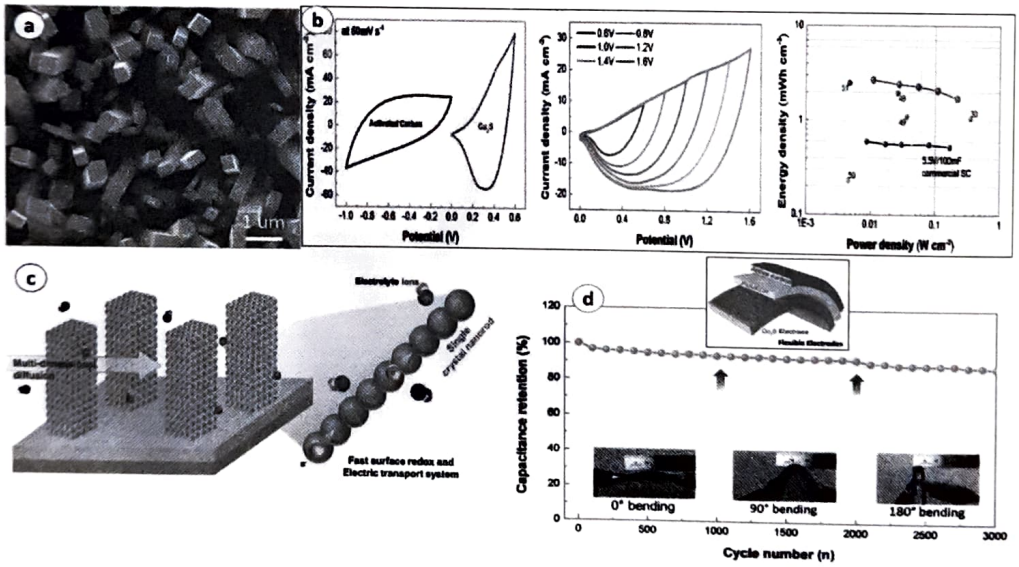

Fig 4: (a) SEM of SC-Cu_2S nanoarrays, (b) Comparative CV curves of the AC and Cu_2S electrodes at 50 mV/s, CV curves of the AC//Cu_2S asymmetric supercapacitor (ASC) over at different potential windows 0.6 to 1.6 V along with comparative Ragone plots for the AC//Cu_2S ASC, (c) the superior performance plausible mechanism illustration of SC-Cu_2S nanoarrays, (d) capacitive retention of assembled AC//Cu_2S ASCAC//Cu_2S ASC (inset) with performance at different bending angles. Reprinted with permission form Ref[43].

Two dimensional (2D) $Cu_{2-x}S$ nano/micro-structures

The enhanced surface area with facets for ample interaction of electrode/electrolyte has augmented their use for design of novel electrochemically active 2D materials as supercapacitor electrodes. 2D materials additionally exhibit superior mechanical and chemical stability, flexibility, transparency which envisions them to be widely deployed in electrochemical Supercapacitors [44-46]. Xu et al reported clusters of 2D CuS materials from dealloying of $Ti_{70}Cu_{30}$ amorphous alloy. The CuS spherical clusters made of amalgamation of 2D CuS could achieve a high specific capacitance of ~276 F g^{-1} at 5 mVs^{-1} with cyclic retention of 73% at 2 A g^{-1} [47]. In a contemporary kind of study 2D mesoporous nanosheets were prepared with pore diameter 2.2-2.5 nm using a simple rapid microwave synthesis. The as synthesized mesoporous nanosheets when assembled into a practical asymmetric hybrid device along with Activated carbon reflecting a high capacitance of 177 Fg^{-1} at 0.5Ag^{-1} accompanied with high energy density of 63.2 $Whkg^{-1}$ at power density of 400 Wkg^{-1} as well as outstanding cycling retention

of 88% after 10000 cycles at $10Ag^{-1}$ [48]. In a recent quite interesting study by Raj et al. synthesized 2D CuS nanoplates patterned directly on FTO to assemble a planar supercapacitor.The planar supercapacitor imitated a high areal capacitance of 4.88 mF cm^{-2} at 0.05 mA cm^{-2} in PVA/LiCl gel polymer electrolyte. The energy density range alters from 5.5×10^{-9} to 4×10^{-7} W h cm^{-2} with decrement in power density decreases from 2×10^{-3} to 2.1×10^{-5} W cm^{-2} respectively [49].

Three dimensional (3D) $Cu_{2-x}S$ nano/micro-structures

3D active materials with porous structures deliver large surface area, distinct pathways for interfacial electrode/electrolyte access and for effectual supercapacitor electrodes. 3D electrodes have no dimension constraints and usually constructed either using conducting metal foam substrates as templates or selective 3D active material synthesis [50, 51]. Tian et al reported CuS hierarchical structures embedded on 3D graphene (3DG)with specific capacitance of 249 Fig^{-1} at current density of 4 Ag^{-1}. A flexible symmetric supercapacitor assembled using CuS/3DG active material possessed 5 Wh kg^{-1} at power density of 450Wkg^{-1} [52]. In another look alike study 3D erythrocyte-like ordered CuS superstructures wrapped in rGO were synthesized using a simple solvothermalstatergy exhibiting a superior energy density of 16.7 Wh kg^{-1} at a power density of 681 W kg^{-1} when assembled into a asymmetric device using activated carbon in organic electrolyte [53]. In a recent study by Quan et al reported carbon quantum doped CuS nanoflowers (CuS@CQDs) like uniform hollow structures. The nano-assembly could own specific capacitance as high as 920.5 F g^{-1} at a current density of 0.5 Ag^{-1}. Further CuS@CQDs//AC ASC device fabricated displayed optimum energy density of 44.19 W h kg^{-1} is obtained at a power density of 397.75 W kg^{-1} with cyclic retention of 92.8% even after 10,000 cycles at $5Ag^{-1}$ [54]. In another very recent study 3D hierarchical CuS micro-flowers as binder free electrodes were loaded on copper powders filled nickel foam. The high surface area of Ni foam assisted with superior electrical conductivity of copper powder along with CuS pathways for efficient electrolyte interaction yielded ultrahigh area capacitance of 11.4 F cm^{-2} at a high current density of 90mAcm^{-2}. The as prepared electrode also displayed a reliable stability with cyclic retention of 106% (4.01 F cm^{-2}) even after 3000 cycles [55]. As shown in Fig.5, besides specific capacitance, both energy densities and power densities are not much comparable on the basis of dimensions. However, cost effective synthesis methods and fabrication engineering of various dimensional copper sulphide materials may lead the future market for specific application as supercapacoitor electrode.

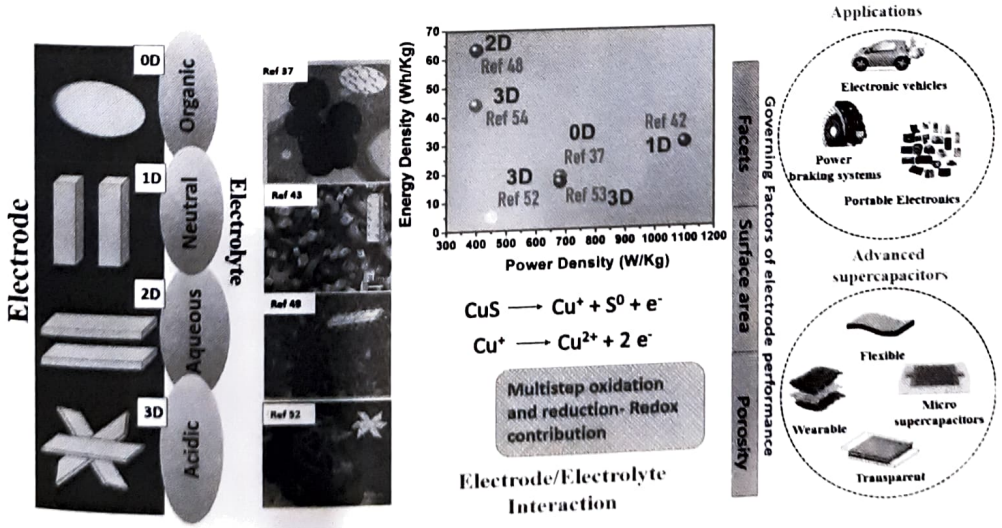

Fig 5: (a) Schematic presentation of the preparation of various dimensional CuS electrode materials along with comparative Ragone plots for the for $Cu_{2-x}S$ electrodes, plausible mechanism illustration and their possible application.

CONCLUSION

Diversified $Cu_{2-x}S$ nano/micro-structures have been of keen interest and aptly implemented for supercapacitive energy storage that offers numerous benefits. The ability of copper sulphide to provide unique crystalline phases with sundry and highly tunability morphologies can be of great potential to enhance the energy storing properties. Although more works are still necessary for practical applications in economic-benign routes. Though the variation of experimental conditions and considerations make it quite ambiguous for comparative evaluation of materials but nonetheless the clear rewards of individual phases and dimensionalities of $Cu_{2-x}S$ nano/micro-structures can be clearly inferred. However, the synthesis processes need further investigations in-deep to precisely control, to achieve the highly scalable, cost-effective production to get tunable pure materials having long-term stability during charge–discharge cycle along with the improvement in their conductivity. Empathetically, this review provides a basic understanding for rational design of different morphological and compositional $Cu_{2-x}S$ nano/micro-structures for enhanced supercapacitive performances.

REFERENCES

[1] Wang, F., Wu, X., Yuan, X., Liu, Z., Zhang, Y., Fu, L., Huang, W.: Latest advances in supercapacitors: from new electrode materials to novel device designs. Chemical Society Reviews, 46(22): 6816-6854, 2017.

[2] Dubal, D. P., Chodankar, N. R., Kim, D. H., Gomez-Romero, P.: Towards flexible solidstate supercapacitors for smart and wearable electronics. Chemical Society Reviews, 47(6): 2065-2129, 2018..

[3] Simon, P., Gogotsi, Y.: Materials for electrochemical capacitors. In Nanoscience and technology: a collection of reviews from Nature journals 320-329, 2010.

[4] Xiong, G., He, P., Lyu, Z., Chen, T., Huang, B., Chen, L., Fisher, T. S.: Bioinspired leaveson-branchlet hybrid carbon nanostructure for supercapacitors. Nature communications, 9(1): 1-11, 2018.

[5] Rui, X., Tan, H., Yan, Q.: Nanostructured metal sulfides for energy storage. Nanoscale, 6(17): 9889-9924, 2014.

[6] Yu, X. Y., Lou, X. W.: Mixed metal sulfides for electrochemical energy storage and conversion. Advanced Energy Materials, 8(3):1701592, 2018.

[7] Lalwani, S., Sharma, R. K., Singh, G., Kim, H.: Vanadium, Incorporated Metallic (1-T)Molybdenum Sulfide Nanoroses for High-Energy-Density Asymmetric Supercapacitors. ChemSusChem, 13(1): 221-229, 2020.

[8] Bhardwaj, R., Jha, R., Bhushan, M., Sharma, R.: Enhanced electrocatalytic activity of the solvothermally synthesized MesoporousRhombohedral nickel sulphide. Materials Science in Semiconductor Processing, 118: 105194,2020.

[9] J. Zhang, H. Feng, J. Yang, Q. Qin, H. Fan, C. Wei, W. Zheng, SolvothermalSynthesis of Three-Dimensional Hierarchical CuS Microspheres from a Cu-Based Ionic Liquid Precursor for High-Performance Asymmetric Supercapacitors, ACS ApplMater Interfaces, 7: 21735-21744, 2015.

[10] Shamraiz, U., Hussain, R. A., Badshah, A. Fabrication and applications of copper sulfide (CuS) nanostructures. Journal of solid state chemistry, 238: 25-40, 2016.

[11] H. Heydari, S.E. Moosavifard, S. Elyasi, M. Shahraki, NanoporousCuSnanohollow Spheres as advanced material for high-performance supercapacitors, Appl. Surf. Sci. 394 : 425e430, 2017.

[12] Pranav Kulkarni, S.K. Nataraj, R. GeethaBalakrishna, D.H. Nagaraju, M.V. Reddy, Nanostructured binary and ternary metal sulfides: synthesis methods and their application in energy conversion and storage devices, J. Mater. Chem. A 5:22040–22094, https://doi.org/10.1039/C7TA07329A, 2017.

[13] Huang, K.-J.; Zhang, J.-Z.; Liu, Y.; Liu, Y.-M. Synthesis of reduced graphene oxide wrapped-copper sulfidehollow spheres as electrode material for supercapacitor.Int. J. Hydrogen Energy 40: 10158–10167, 2015.

[14] S. Sun, P. Li, S. Liang, Z. Yang, Diversified copper sulfide (Cu2-XS) micro-/ nanostructures: A comprehensive review on synthesis, modifications and applications, Nanoscale 9: 11357–11404, 2019. https://doi.org/10.1039/c7nr03828c.

[15] Pattrick, R. A. D., Mosselmans, J. F. W., Charnock, J. M., England, K. E. R., Helz, G. R., Garner, C. D., Vaughan, D. J.: The structure of amorphous copper sulfide precipitates: An X-ray absorption study. Geochimicaet Cosmochimica Acta, 61(10): 2023-2036, 1997.

[16] Morales-García, A., SoaresJr, A. L., Dos Santos, E. C., de Abreu, H. A., Duarte, H. A. First-principles calculations and electron density topological analysis of covellite (CuS). The Journal of Physical Chemistry A, 118(31): 5823-5831, 2014.

[17] Xu, Q., Huang, B., Zhao, Y., Yan, Y., Noufi, R., Wei, S. H. Crystal and electronic structures of Cu x S solar cell absorbers. Applied Physics Letters, 100(6): 061906, 2012.

[18] C.J. Raj, B.C. Kim, W.-J. Cho, W.-G. Lee, Y.Seo, K.-H. Yu: Electrochemical capacitor behavior of copper sulfide (CuS) nanoplatelets, J. Alloy. Comp. 586: 191e196, 2014..

[19] H. Hu, J. Wang, C. Deng, C. Niu, H. Le: Microwave-assisted controllable synthesis of hierarchical CuSnanospheres displaying fast and efficient photocatalytic activities, J. Mater. Sci. 53: 14250–14261, 2018. https://doi.org/10.1007/s10853- 018-2669-6.

[20] K.-J. Huang, J.-Z. Zhang, Y. Liu, Y.-M. Liu: Synthesis of reduced graphene oxide wrapped-copper sulfide hollow spheres as electrode material for supercapacitor, Int. J. Hydrogen Energy 40:10158e10167, 2015.

[21] M.D. Khan, M.A. Malik, J. Akhtar, S. Mlowe, N. Revaprasadu: Phase pure deposition of flower-like thin films by aerosol assisted chemical vapor deposition and solvent mediated structural transformation in copper sulfide nanostructures, Thin Solid Films 638: 338–344, 2017.

[22] Zhou, M., Li, J., Liang, S., Sood, A. K., Liang, D., Li, C.: CuS nanodots with ultrahigh efficient renal clearance for positron emission tomography imaging and image-guided photothermal therapy. ACS nano, 9(7): 7085-7096, 2015.

[23] M. Tanveer, C. Cao, Z. Ali, I. Aslam, F. Idrees, W.S. Khan, F.K. But, M. Tahir, N. Mahmood, Template free synthesis of CuSnanosheet-based hierarchical microspheres: an efficient natural light driven photocatalyst, Cryst. Eng. Comm. 16:5290e5300, 2014.

[24] Zhou, D., Liu, D., Xu, W., Yin, Z., Chen, X., Zhou, P., ...& Song, H. Observation of considerable upconversion enhancement induced by $Cu_{2-x}S$ plasmon nanoparticles. ACS nano, 10(5): 5169-5179, 2016.

[25] Zhou, L., Li, W., Chen, Z., Ju, E., Ren, J., Qu, X.: Growth of Hydrophilic CuS Nanowires via DNA-Mediated Self-Assembly Process and Their Use in Fabricating Smart Hybrid Films for Adjustable Chemical Release. Chemistry–A European Journal, 21(7), 2930-2935, 2015.

[26] J. Liu, D. Xue: Rapid and scalable route to CuS biosensors: a microwave-assisted Cu-complex transformation into CuS nanotubes for ultrasensitive nonenzymaticglucose sensor, J. Mater. Chem. 21:223–228, 2011. https://doi.org/10.1039/c0jm01714k.

[27] Y.-K. Hsu, Y.-C. Chen, Y.-G. Lin: Synthesis of copper sulfide nanowire arrays for high-performance supercapacitors, Electrochim. Acta 139:401e407, 2014.

[28] Liu, P., Huang, Y., Yan, J., Yang, Y., Zhao, Y.: Construction of Cu Snanoflakes vertically aligned on magnetically decorated graphene and their enhanced microwave absorption properties. ACS applied materials & interfaces, 8(8): 5536-5546, 2016.

[29] Y. Xie, A. Riedinger, M. Prato, A. Casu, A. Genovese, P. Guardia, S. Sottini, C. Sangregorio, K. Miszta, S. Ghosh, T. Pellegrino, L. Manna: Copper sulphide nanocrystals with tunablecomposition by reduction of covellitenanocrystals with Cuþ ions, J. Am. Chem. Soc. 135:17630–17637, 2013, https://doi.org/10.1021/ja409754v.

[30] Savariraj, A. D., Viswanathan, K. K., Prabakar, K.: Influence of Cu vacancy on knit coir mat structured CuS as counter electrode for quantum dot sensitized solar cells. ACS applied materials & interfaces, 6(22): 19702-19709, 2014.

[31] Ghosh, D., Halder, G., Sahasrabudhe, A., and Bhattacharyya, S. A: microwave synthesized Cu_xS and graphene oxide nanoribbon composite as a highly efficient counter electrode for quantum dot sensitized solar cells. Nanoscale, 8(20): 10632-10641, 2016.

[32] F. Tao, Y. Zhang, S. Cao, K. Yin, X. Chang, Y. Lei, R. Fan, L. Dong, Y. Yin, X. Chen, CuSnanoflowers/semipermeable collodion membrane composite for highefficiencysolar vapor generation, Mater. Today Energy 9: 285–294, 2018, https:// doi.org/10.1016/j.mtener.2018.06.003.

[33] C.F. Mu, Q.Z. Yao, X.F. Qu, G.T. Zhou, M.L. Li, S.Q. Fu, Controlled synthesis of various hierarchical nanostructures of copper sulfide by a facile microwave irradiation method, Colloids Surf. A: Physicochem. Eng. Aspects 371: 14–21,2010, https://doi.org/10.1016/j.colsurfa.2010.08.049.

[34] Gamby, J., Taberna, P.L., Simon, P., Fauvarque, J.F., Chesneau, M.: Studies characterisations of various activated carbons used for carbon/carbon supercapacitors. Journal of power sources, 101(1): 109-116, 2001.

[35] Gamby, J., Taberna, P.L., Simon, P., Fauvarque, J.F.: Chesneau, M.: Studies and characterisations of various activated carbons used for carbon/carbon supercapacitors. Journal of power sources, 101(1): 109-116, 2001 .

[36] Zhao, T., Peng, X., Zhao, X., Hu, J., Jiang, T., Lu, X., Ahmad, I.: Preparation and performance of carbon dot decorated copper sulphide/carbon nanotubes hybrid composite as supercapacitor electrode materials. J. Alloys and Compounds, 817: 153057, 2020.

[37] Zhao, T., Peng, X., Zhao, X., Hu, J., Yang, W., Li, T., Ahmad, I.: Facile preparation and high capacitance performance of copper sulfide microspheres as supercapacitor electrode material. Composites Part B: Engineering, 163: 26-35, 2019.

[38] Wei, T. Y., Chen, C. H., Chien, H. C., Lu, S. Y., Hu, C. C.: A cost effective supercapacitor material of ultrahigh specific capacitances: spinel nickel cobaltite aerogels from an epoxide-driven sol–gel process. Advanced materials, 22(3): 347-351, 2010.

[39] Yu, Z., Li, C., Abbitt, D., & Thomas, J.:. Flexible, sandwich-like Ag-nanowire/PEDOT: PSS-nanopillar/MnO_2 high performance supercapacitors. Journal of Materials Chemistry A, 2(28): 10923-10929, 2014.

[40] Ye, H., Wang, K., Zhou, J., Song, L., Gu, L., Cao, X. A: true cable assembly with a carbon nanotube sheath and nickel wire core: a fully flexible electrode integrating energy storage and electrical conduction. Journal of Materials Chemistry A, 6(3): 1109-1118, 2018.

[41] Javed, M. S., Dai, S., Wang, M., Xi, Y., Lang, Q., Guo, D., and Hu, C. Faradic redox active material of Cu_7S_4 nanowires with a high conductance for flexible solid state supercapacitors. Nanoscale, 7(32): 13610-13618, 2015.

[42] Hou, X., Liu, X., Lu, Y., Cheng, J., Luo, R., Yu, Q., and Luo, Y. : Copper sulfidenanoneedles on CNT backbone composite electrodes for high-performance supercapacitors and Li-S batteries. Journal of Solid State Electrochemistry, 21(2): 349-359, 2017.

[43] Hong, J., Kim, B. S., Yang, S., Jang, A. R., Lee, Y. W., Pak, S., Hong, J. P. Chalcogenide solution-mediated activation protocol for scalable and ultrafast synthesis of single-crystalline 1-D copper sulfide for supercapacitors. Journal of Materials Chemistry A, 7(6): 2529-2535, 2019.

[44] Mas-Balleste, R., Gomez-Navarro, C., Gomez-Herrero, J.,and Zamora, F.: 2D materials: to graphene and beyond. Nanoscale, 3(1), 20-30, 2011

.[45] Naguib, M., Mochalin, V. N., Barsoum, M. W., and Gogotsi, Y. 25th anniversary article: MXenes: a new family of two-dimensional materials. Advanced materials, 26(7): 992-1005, 2011.

[46] Gao, W., Singh, N., Song, L., Liu, Z., Reddy, A. L. M., Ci, L., Ajayan, P. M. Direct laser writing of micro-supercapacitors on hydrated graphite oxide films. Nature nanotechnology, 6(8): 496-500, 2011.

[47] Xu, W., Liang, Y., Su, Y., Zhu, S., Cui, Z., Yang, X., Liang, C. Synthesis and properties of morphology controllable copper sulphide nanosheets for supercapacitor application. ElectrochimicaActa, 211: 91-899, 2016.

[48] Naveed, M., Younas, W., Zhu, Y., Rafai, S., Zhao, Q., Tahir, M., Cao, C. Template free and facile microwave-assisted synthesis method to prepare mesoporous copper sulfidenanosheets for high-performance hybrid supercapacitor. Electrochimica Acta, 319: 49-60, 2019.

[49] Raj, C.J., Rajesh, M., Manikandan, R., Lee, W. G., Yu, K. H., Kim, B.C.: Direct fabrication of two-dimensional copper sulfide nanoplates on transparent conducting glass for planar supercapacitor. Journal of Alloys and Compounds, 735: 2378-2383, 2018.

[50] Sahoo, S., Shim, J. J. Facile synthesis of three-dimensional ternary $ZnCo_2O_4$/reduced graphene oxide/NiO composite film on nickel foam for next generation supercapacitor electrodes. ACS Sustainable Chemistry & Engineering, 5(1):2 41-251, 2017.

[51] Li, J., Ji, B., Jiang, R., Zhang, P., Chen, N., Zhang, G., Qu, L.: Hierarchical hole enhanced 3D graphene assembly for highly efficient capacitive deionization. Carbon, 129: 95-103,2018.

[52] Tian, Z., Dou, H., Zhang, B., Fan, W., Wang, X. Three-dimensional graphene combined with hierarchical CuS for the design of flexible solid-state supercapacitors. ElectrochimicaActa, 237: 109-118, 2017.

[53] Cui, Y., Zhang, J., Li, G., Sun, Y., Zhang, G., & Zheng, W. Ionic liquid-assisted synthesis of rGO wrapped three-dimensional CuS ordered nanoerythrocytes with enhanced performance for asymmetric supercapacitors. Chemical Engineering Journal, 325: 424-432, 2017.

[54] Quan, Y., Wang, G., Lu, L., Wang, Z., Xu, H., Liu, S., Wang, D. High-performance Pseudo-capacitor Energy Storage Device Based on a Hollow-structured Copper SulfideNanoflower and Carbon Quantum Dot Nanocomposite. ElectrochimicaActa, 136606, 2020.

[55] Ying, Z., Zhao, S., Yue, J., Ju, T., Zhang, Y., Xie, J., Wang, Q. 3D hierarchical CuSmicroflowers constructed on copper powders-filled nickel foam as advanced binder-free electrodes. Journal of Alloys and Compounds, 821: 153437, 2020.

Journal of Metallurgy and Materials Science, Vol. 62, No. 3-4, July-December 2020, pp. 103-126
Printed in India, © NML, ISSN 0972-4257

Recent advances in photodetection applications of two dimensional MoS_2 nanostructures

BISHNU PADA MAJEE and ASHISH KUMAR MISHRA*
School of Materials Science and Technology,
Indian Institute of Technology (Banaras Hindu University), Varanasi-221005, India

Abstract : Two-dimensional transition metal dichalcogenides (TMDs) with unique properties have received a great attention of scientific community in recent years. Among the TMDs family, MoS_2 has been already established as an intriguing building block for the next generation optoelectronics, such as photodetectors. The optoelectronic device performance of TMDs are known to be layer dependent. The MoS_2 shows excellent light absorption and is found stable in natural environment, which make it suitable for optoelectronic devices. In the present review article, we discuss different synthesis processes for 2D-MoS_2 and have summarized few important studies on the photodetection application of different morphologies of MoS_2 nanostructures. Here, we discuss the different MoS_2 based photodetectors comprising of p-n junction photodiode and the metal-semiconductor-metal (MSM) junction.

Keywords: *Transition metal dichalcogenides, MoS_2, Top down approach, Bottom up approach, Photodetector, p-n junction device, MSM device.*

INTRODUCTION

Two-dimensional (2D) transition metal dichalcogenides (TMDs) have attracted huge attention of scientific community in the field of optoelectronics due to their different properties such as tunable bandgaps, strong interaction with light and the presence of weak van der Waals force between the layers[1-3]. The 2D-TMDs have enormous advantages in various photonic and optoelectronic applications due to the energy bandgaps covering the visible and near infrared spectral region, which is suitable for ultra-broadband photodetectors. Graphene and TMDs are the earth-abundant and have emerged as 2D materials of choice due to multiple advantages such as their low-cost production, easy synthesis and these materials can be easily transferred on required substrate with precise thickness i.e. the layer number. The general formula for TMDs is MX2, where M is the transition metal (= Mo, W from the group 4, 5, or 6 of the periodic table) and X stand for a chalcogen atom (S, Se and Te). These TMDs material having energy bandgaps (1.0-2.1 eV), covering the visible and the near infrared spectral region leading to the various photonic and optoelectronic applications. The most interesting properties in TMDs structures are layer dependent bandgaps and quantum efficiency. The 2D monolayer Molybdenum disulfide (MoS_2) shows high carrier mobility and optical transparency compared to conventional semiconductors, which make it suitable for developing ultra-broadband photodetectors for use in different areas such as surveillance and sensors in real life applications. MoS_2 shows an indirect-to-direct bandgap transition, when it transforms from bulk to monolayer. The direct bandgap nature of MoS_2 makes it ideal for photonic and optoelectronic applications[4-10]. Each 2D material has its own advantages and disadvantages. As an example, black phosphorus (BP) shows higher carrier mobility as compared to TMDs, but layered TMDs have relatively higher light absorption in visible range as compared to BP. In another example, graphene-based photodetector is used in ultrafast and broadband technologies, whereas MoS_2 based device is having advantage of strong electroluminescence [11-12]. The presence of direct electronic transitions in monolayer MoS_2 increases the probability for excitons (electron-hole pairs) generation [13,14]. The structure of MoS_2 shows three different phases, 1T (tetragonal symmetry, octahedral coordination), 2H (hexagonal symmetry, trigonal prismatic coordination) and 3R (rhombohedral symmetry, trigonal prismatic coordination). Among three phases, 2H-MoS_2 is found most stable while 3R phase is found unstable. The 1T MoS_2 is also found stable however at high temperatures it turns into 2H phase. The stacking sequence in 2H phase of MoS_2 is AbA

*Corresponding Author, E-mail: akmishra.mst@iitbhu.ac.in

BaB where the upper case and lower-case letters represent the S atom and Mo atom, respectively. The staking sequence in 3R phase of MoS_2 is AbA CaC BcB. In 2H and 3R phase of MoS_2 the metal coordinate is trigonal prismatic. The staking sequence in 1T phase of MoS_2 is AbC AbC[15-18].

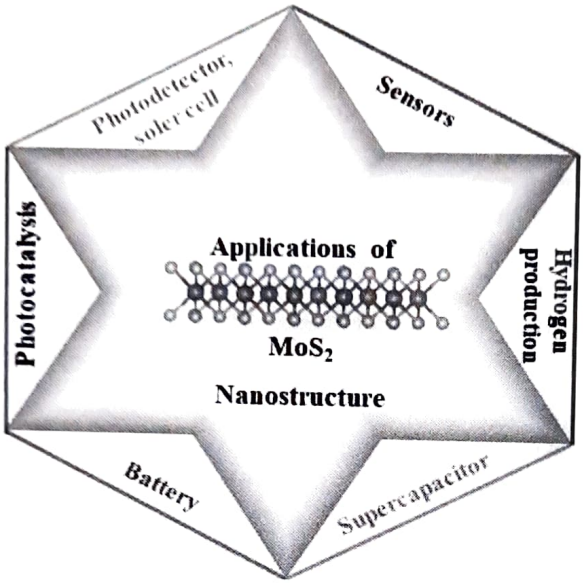

Figure 1. Schematic diagram of applications of MoS_2 nanostructure.

Different TMDs nanostructures along with graphene have been investigated in wide range of electronics and optoelectronic devices [19–29]. The 2D-MoS_2 has been extensively demonstrated for different applications such as photodetectors, solar cells, field-effect transistors (FETs), sensors, supercapacitors, batteries and other photonic applications, as shown schematically in figure 1 [30-36]. Among electronic and optoelectronic devices, photodetectors are becoming a key component of optoelectronic technology due to their wide range of applications for surveillance, robotics, sensors, night vision, security, motion detection and other optical communications [23]. In literature, there have been wide range of studies on MoS_2 based photodetectors, however, a comprehensive review via summarizing the recent trend on the developments in MoS_2 based photodetectors is still needed. Here, we summarize different synthesis processes for MoS_2 via top down and bottom up approaches. We discuss recent advances in MoS_2 based photodetector devices with two different configurations i.e. p-n junction and metal-semiconductor-metal junction diodes.

Synthesis of MoS_2 nanosheets

In order to use in optoelectronic applications such as photodetectors, growth of high quality and large area 2D-TMDs nanostructures remains a challenge. To achieve high efficiency of such systems, defect free 2D-TMDs nanostructures are needed which can improve the exciton generation and separation. A large area growth of these nanomaterials is required for the successful realization of commercial optoelectronic devices. The 2D materials can be synthesized by two general paths such as top-down and bottom-up approaches. The widely used top-down approach incudes mechanical exfoliation, liquid phase exfoliation and Lithium ion intercalation methods [37-40]. These exfoliation processes are suitable for synthesis of 2D materials due to the weak van der Walls force between the layers, that allows individual 2D layers to be separated from its bulk counterpart bulk. On the other hand, bottom-up approaches include the physical vapor deposition (PVD), chemical vapor deposition (CVD) and solution chemical (hydrothermal/solvothermal) process. In this section we have discussed these processes separately [41].

TOP-DOWN APPROACH FOR MoS_2 SYNTHESIS

Mechanical exfoliation

It is based on the peeling process of layered materials by application of mechanical force to result in one or few monolayers. In 2004, this method was first used to synthesize Graphene [39]. The scotch assisted mechanical peeling is still a widespread approach for making a top-quality 2D sheets of Graphene and TMDs materials. High quality MoS_2 can be synthesized via this method quickly as the mechanical force can overcome the van der Waal interaction between layers. Bulk MoS_2 crystal can be used as starting material for synthesis of monolayer/few-layer MoS_2 via scotch tape assisted mechanical peeling, as shown schematically in figure 2. The quality of the film prepared by this technique is known to be highest, which enables the properties study of pristine MoS_2. Oriol et. al. used this exfoliation method to synthesis MoS_2 monolayer and showed its suitability for ultrasensitive photodetection [37]. However, the main demerits of this method are the low yield and the small flake size, which are crucial part for scalable production of such photodetectors. Therefore, MoS_2 synthesis via this process is limited to the fundamental study at laboratory level.

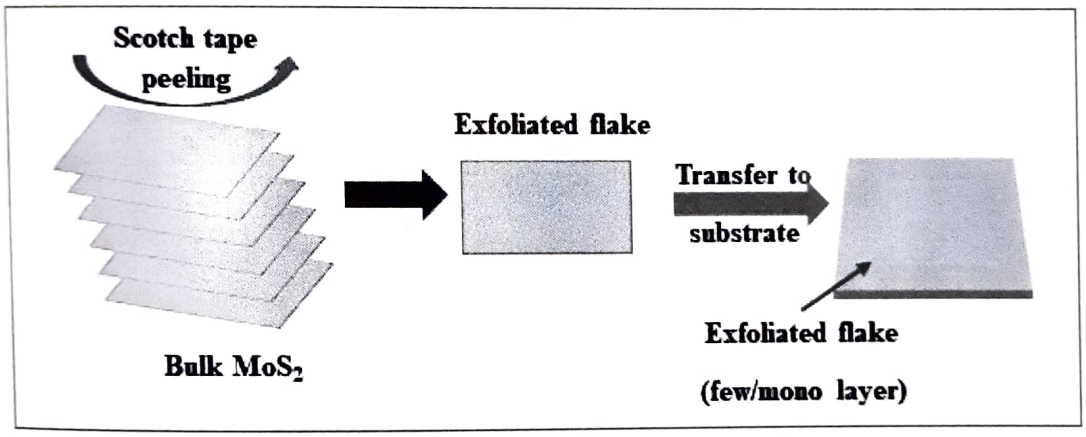

Figure 2. Schematic diagram for mechanical exfoliation method.

Liquid exfoliation

The another important and widely used top-down method is liquid exfoliation process. In this method, bulk MoS_2 powder is used as starting material and common organic solvents and/or functionalization is used to exfoliate the bulk materials. The exfoliation of the bulk materials can be done by various mechanical processes like sonication, shearing, stirring, grinding and bubbling methods. The direct sonication process depends on the solvent and/or surfactant to defeat the cohesion between adjacent layers. Thus, the solvent must be chosen to have surface tension close to the surface energy of the material [42]. In this method, the materials shape, size and layer numbers vary randomly. The quantity of the flakes is much larger than the mechanical exfoliation but the quality is lower as compared to mechanical exfoliation. In one of the works, synthesis of few layer MoS_2 and WS_2 was demonstrated via sonication of their bulk powders using soapy water as solvent [40]. Figure 3 shows the schematic diagram of synthesis of MoS_2 by liquid exfoliation methods. The re-aggregation of 2D-nanosheets is removed via steric and electrostatic repulsion. The yield of liquid exfoliation method can be increased by surfactants and sonication. The yield of liquid exfoliation is drastically improved from the mechanical exfoliation technique, but the quality of the flake is still low. This method is suitable in different applications, where a vast amount of nanoflakes are required such as energy production and storage applications. This process is a cost effective and simple technology for large scale production of 2D nanosheets.

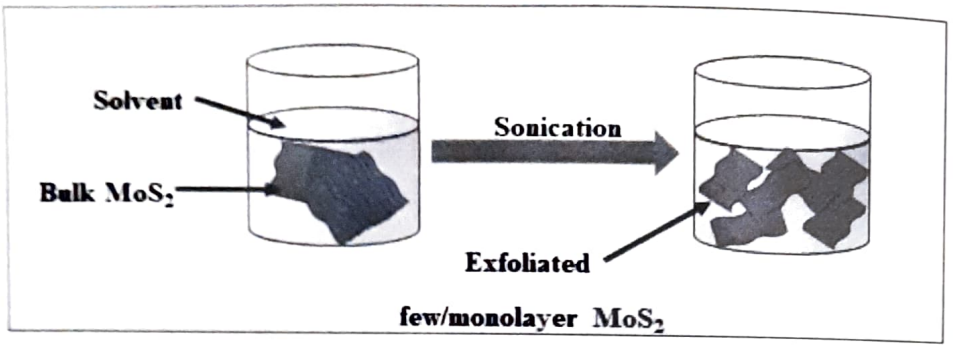

Figure 3. Schematic diagram of synthesis of MoS2 via liquid exfoliation.

Lithium ion intercalation methods:

In this method, the small radii ions are intercalated into the adjacent layers in bulk layered materials. Generally, Lithium ion is used to intercalate between the different layers of MoS_2 to expand the interlayer spacing. This increase of interlayer spacing facilitates the exfoliation process by mechanical treatment, as shown schematically in Figure 4. Generally, N-butyl lithium is used for Li intercalation between layers of TMD material [43]. The single layer MoS_2 was demonstrated by Joensen and co-workers using n-butyl lithium dissolved in hexane. During the intercalation the formation of Li_xMoS_2 compound occurs which controls the yield of monolayer MoS_2 [44]. The main problem with this method is that, during the synthesis/intercalation process, Li atoms intercalate in the layer of MoS_2 and during that time the semiconducting 2H of MoS_2 transforms into its metallic 1T phase. However, after annealing at 300°C, semiconducting 2H-MoS_2 phase can be obtained [45]. This method is likely to be better suited for applications in energy storage and generation, sensing or as filler materials for composites where large quantity of materials are required.

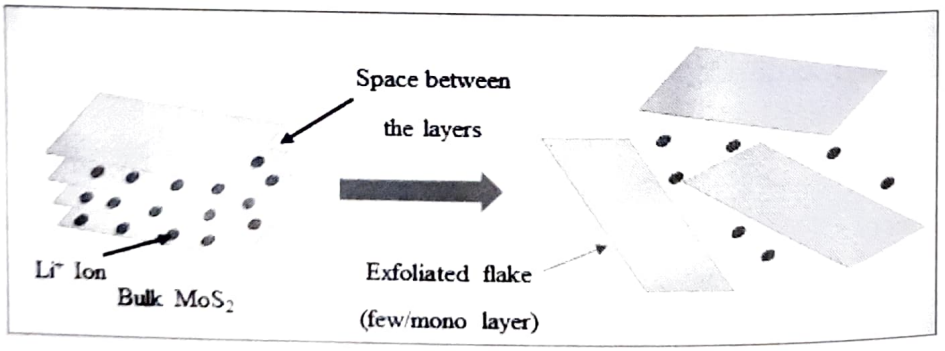

Figure 4. Schematic diagram of Li ion intercalation method to obtain MoS_2 nanosheets.

BOTTOM-UP APPROACH FOR MoS_2 SYNTHESIS

Physical Vapor Deposition (PVD)

The molecular beam epitaxy (MBE) is a cutting-edge automation for synthesis of single crystal semiconducting film; however, this method is not suitable for the synthesis of 2D materials due to the smaller grain [46]. The 2D-MoS_2 can be synthesized by this method. Muratore et. al. reported the synthesis of ultra-thin MoS_2 films at low-temperature by physical vapor deposition method [47]. This synthesis process is based on magnetron sputtering.

Chemical Vapor Deposition (CVD):

CVD technique is known as the best technique to synthesize high quality and large area monolayer TMDs nanosheets. In this process, chemical reaction occurs among different precursors in vapour state and solid-state

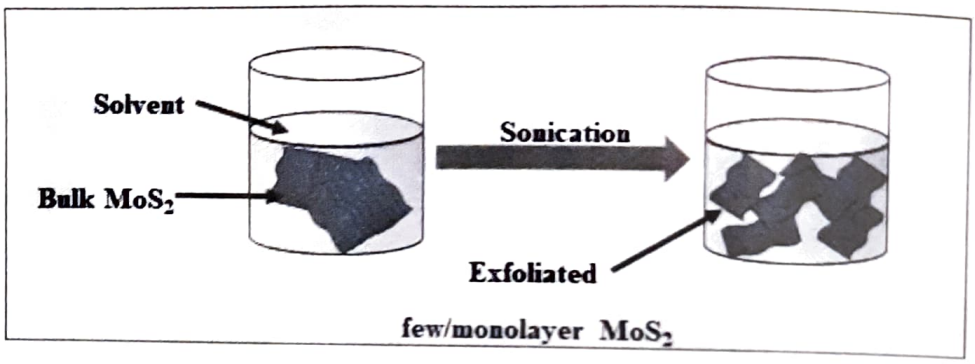

Figure 3. Schematic diagram of synthesis of MoS2 via liquid exfoliation.

Lithium ion intercalation methods:

In this method, the small radii ions are intercalated into the adjacent layers in bulk layered materials. Generally, Lithium ion is used to intercalate between the different layers of MoS_2 to expand the interlayer spacing. This increase of interlayer spacing facilitates the exfoliation process by mechanical treatment, as shown schematically in Figure 4. Generally, N-butyl lithium is used for Li intercalation between layers of TMD material [43]. The single layer MoS_2 was demonstrated by Joensen and co-workers using n-butyl lithium dissolved in hexane. During the intercalation the formation of Li_xMoS_2 compound occurs which controls the yield of monolayer MoS_2 [44]. The main problem with this method is that, during the synthesis/intercalation process, Li atoms intercalate in the layer of MoS_2 and during that time the semiconducting 2H of MoS_2 transforms into its metallic 1T phase. However, after annealing at 300°C, semiconducting 2H-MoS_2 phase can be obtained [45]. This method is likely to be better suited for applications in energy storage and generation, sensing or as filler materials for composites where large quantity of materials are required.

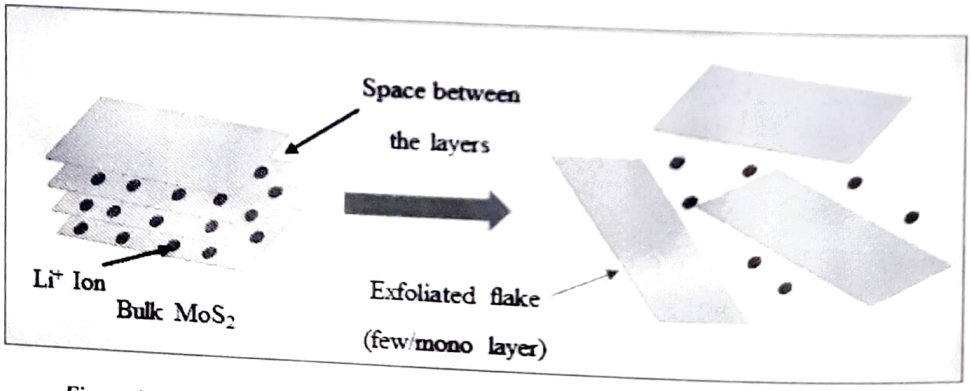

Figure 4. Schematic diagram of Li ion intercalation method to obtain MoS_2 nanosheets.

BOTTOM-UP APPROACH FOR MoS_2 SYNTHESIS

Physical Vapor Deposition (PVD)

The molecular beam epitaxy (MBE) is a cutting-edge automation for synthesis of single crystal semiconducting film; however, this method is not suitable for the synthesis of 2D materials due to the smaller grain [46]. The 2D-MoS_2 can be synthesized by this method. Muratore et. al. reported the synthesis of ultra-thin MoS_2 films at low-temperature by physical vapor deposition method [47]. This synthesis process is based on magnetron sputtering.

Chemical Vapor Deposition (CVD):

CVD technique is known as the best technique to synthesize high quality and large area monolayer TMDs nanosheets. In this process, chemical reaction occurs among different precursors in vapour state and solid-state

thin film is deposited as a desired product. The schematic diagram for MoS_2 synthesis via CVD method is shown in Figure 5. Generally, Mo compounds like Molybdenum tri-oxide, Molybdenum chloride, Ammonium molybdate etc. are used as Mo precursors while sulfur powder and H_2S gas are used as reducing agents and sulfur source [33,48,49]. Generally, the reaction temperature for MoS_2 synthesis is in the range 600-1000°C in CVD process [50]. As an example following chemical reactions take place in CVD process during the growth of MoS_2.

$$MoO_3 + x/2\ S \rightarrow MoO_{3-x} + x/2\ SO_2 \quad (1)$$

$$MoO_3{-}x + (7{-}x)/2\ S \rightarrow MoS_2 + (3\text{-}x)/2\ SO_2 \quad (2)$$

where MoO_2 is intermediate phase formed when x = 1, during the reaction. [10, 38] The growth of MoS_2 has been demonstrated on different substrates like Si, SiO_2/Si and quartz. The large area monolayer MoS_2 via CVD method was synthesized by Lee et. al. on Si/SiO_2 substrate at 650°C and ambient pressure using MoO_3 and S powders as precursors [38]. In one of our study, we showed the growth of few-layer MoS_2 nanosheets over large area of Si substrates treating same precursors (MoO_3 and S) at 690°C for 5 minutes in nitrogen atmosphere [51]. Further by modifying the reaction time (10 minutes), temperature (750°C) and precursors amount, we have successfully demonstrated the large area growth of vertically aligned few-layer MoS_2 nanosheets [41].

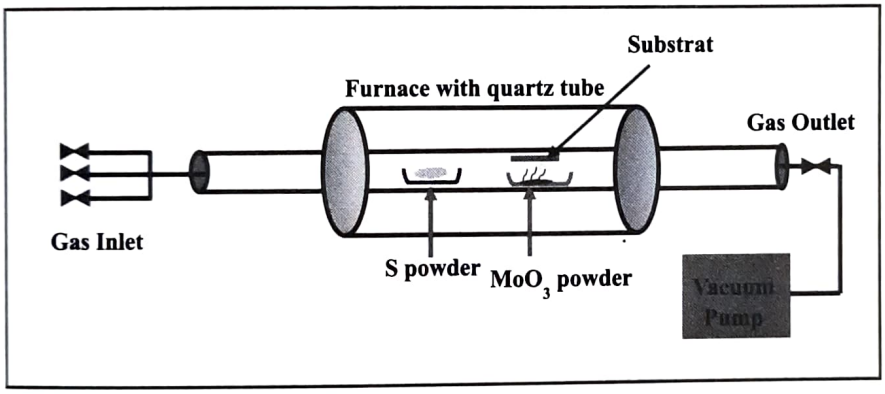

Figure 5. Schematic diagram of MoS_2 growth via CVD methods.

Solution chemical process

There are two different methods for synthesis of MoS_2 nanosheets by this process, hydrothermal and solvothermal processes [52-54]. The schematic diagram of synthesis of MoS_2 via solution chemical process is shown in figure 6. During the synthesis process, sodium molybdate react with sulfide compounds or sulfur at temperature range 150 to 240°C and the autoclave is kept at that temperature for several hours for completing the synthesis process. In this method, synthesized MoS_2 is in powder form of different shapes and size. Just after the synthesis the powder is treated with temperature, to increase their crystalline nature and freshness. The main dissimilarity between these two methods are that the precursor solution in the solvothermal is usually non-aqueous, however in hydrothermal method it is aqueous.

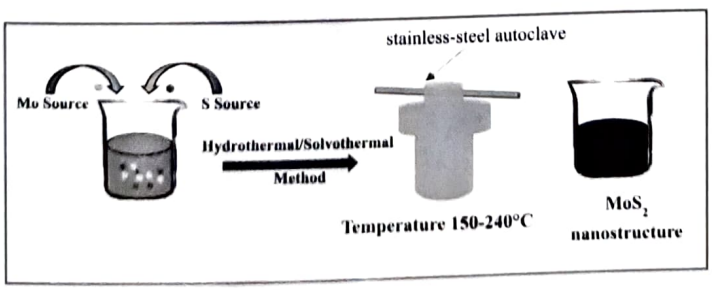

Figure 6. Schematic diagram of MoS_2 growth via hydrothermal/solvothermal methods.

Photodetection Process

Photodetector is a device, which can convert the light into electrical signals. MoS_2 makes good junctions with other materials like Si and other 2D materials, hence different junction formations have been investigated for optoelectronic applications. In this section, we will discuss about the main mechanisms that are involved in photodetectors. The two main mechanisms, (a) photoconductive and (b) photovoltaic effect are used for the photodetection purpose, which are briefed as follows [14,55].

(a) Photoconductive Effect

The electron-holes are generated in the semiconductor system when the energy of the incident light (photon) is higher than the band gap of a materials. In this effect, photogenerated charge carriers (electron–hole pairs) drift in opposite directions by built-in electric field and the applied external field. It greatly reduces the possibility of recombination of generated charge carriers. Under the reverse bias condition across the junction, the photogenerated charge carriers are separated, which result in photocurrent of the device.

(b) Photovoltaic Effect

In this effect, photogenerated charge carriers are decoupled by intrinsic built-in electric field rather than the applied bias voltage. The open circuit voltage can be developed by the accumulation of the carriers of opposite polarities, which leads to the separation of charge carriers resulting in large photocurrent.

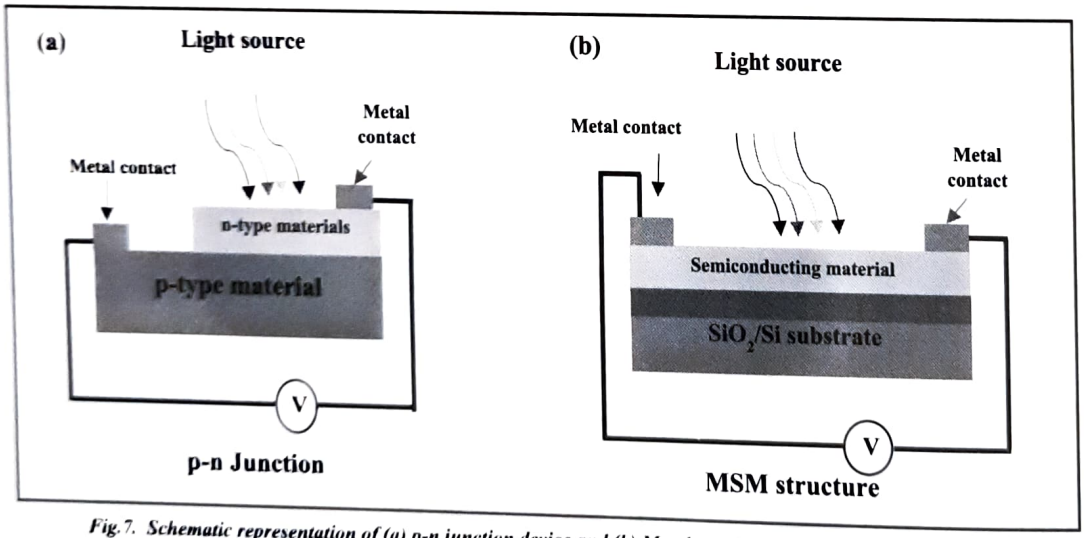

Fig. 7. Schematic representation of (a) p-n junction device and (b) Metal-semiconductor-metal (MSM) device.

The photodetector devices can be made in two different ways- p-n junction device and metal-semiconductor-metal (MSM) device. The schematic representations of a p-n junction device and MSM device are shown in Figure 7a, and 7b, respectively [51,56].

MoS_2 Photodetectors

Last few years the many scientific articles have been published based on Graphene and TMDs in the field of optoelectronics. Few-layer TMDs based photodetectors shows relatively higher photoresponsivity as compared to graphene-based photodetectors due to the presence of finite direct band gap. Among semiconducting TMDs, MoS_2 is having direct bandgap of around 1.8 eV in monolayer form with high mobility [26,51,53,55,57-58]. The electromagnetic spectrum covered by two dimensional TMDs is marked in the schematic diagram of

Figure 8. Most of the TMDs show emission in visible and near-infrared region of the spectrum [4]. Monolayer and few-layer MoS_2 show emission in the red region of the visible light, as marked in Figure 8. The MoS_2 shows high quality of interface with other semiconductive materials such as Si. The monolayer MoS_2 has some unique properties like direct band gap, high absorption coefficient and the flexibility, which makes it suitable for photodetector application. Beside monolayer MoS_2, multilayer MoS_2 shows band gap reduction which leads to the extension of detection range and higher absorption due to the larger number of layers. However, the responsivity of the multilayer film is low as compared to monolayer due to the presence of indirect band gap. In the following section, we will discuss the recent studies on monolayer and few-layer MoS_2 based photodetectors with p-n junction and MSM device structures.

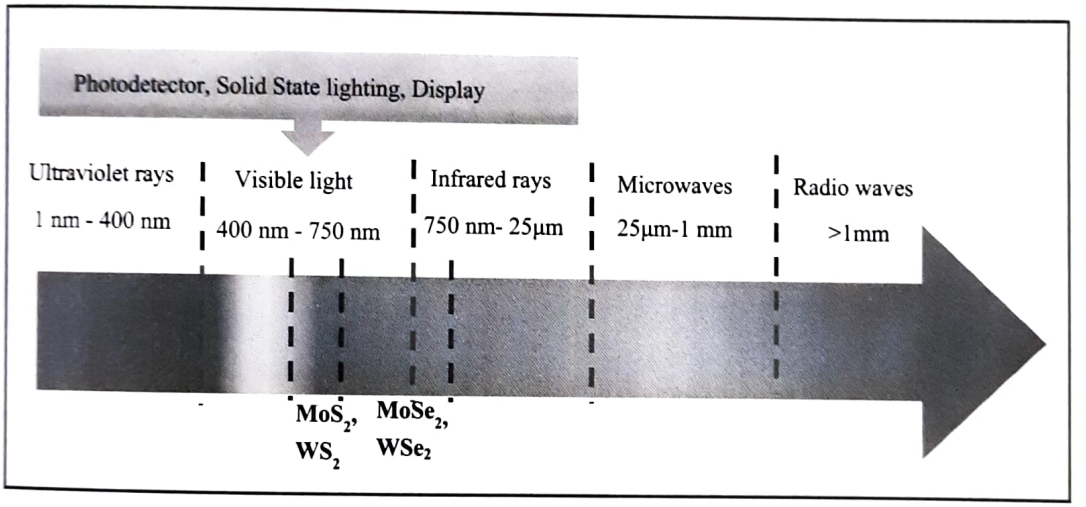

Fig. 8. The electromagnetic spectrum of 2D TMDs.

In one of the recent studies, we demonstrated the growth of n-type bulk and few-layer MoS_2 by CVD over p-type Si substrate. In this study, we showed that the bulk MoS_2 did not show the photoemission hence could not be used for photodetection application. The grown few-layer and interconnected MoS_2 nanosheets possessed suitable properties to be used for photodetection. The SEM image of prepared few-layer MoS_2 film (Figure 9a) indicates the interconnected network of MoS_2. Raman study (Figure 9b) showed the 2H phase of prepared MoS_2 film in both bulk and few-layer form. The inset image shows the two vibrational modes of MoS_2, where E12g represents the in-plane vibration of Mo and S atoms in opposite directions and A1g peak shows the only vibration of S atom in outward direction. In order to examine the suitability of prepared bulk and few-layer MoS_2 for photodetection, we performed the photoluminescence (PL) study. Figure 9c shows the PL spectra of bulk and few-layer MoS_2 film where only few-layer MoS_2 shows emission peaks indicating the presence of direct bandgap while absence of PL peaks in bulk MoS_2 indicates the indirect bandgap. These characterization studies confirmed the semiconducting nature of prepared MoS_2 and suitability of few-layer MoS_2 for photodetection application [51].

Further photodetection behaviour of prepared MoS_2 film was examined by performing current-voltage (I-V) characteristic study with and without illumination, as shown in Figure 9d. It shows current response to the applied voltage under dark and two different illumination conditions (0.05 and 0.15 mW cm^{-2} of a white light using neon lamp source). Under illumination condition the revers bias photocurrent gradually increased and the forward bias photocurrent remained nearly constant. High asymmetry in I-V characteristic suggests the formation of good quality p-n junction between n-type MoS_2 and p-type Si substrate. The reverse bias photocurrent increases with increased intensity of incident light as larger number of photogenerated charge carriers are resulted. In this study, conduction mechanisms of MoS_2 based p-n junction photodiode was discussed on the basis of band diagram,

shown in figure 9e. Under reverse bias, the photogenerated charge carriers are separated by built-in electric field and are collected by electrodes to result in increase in photocurrent.

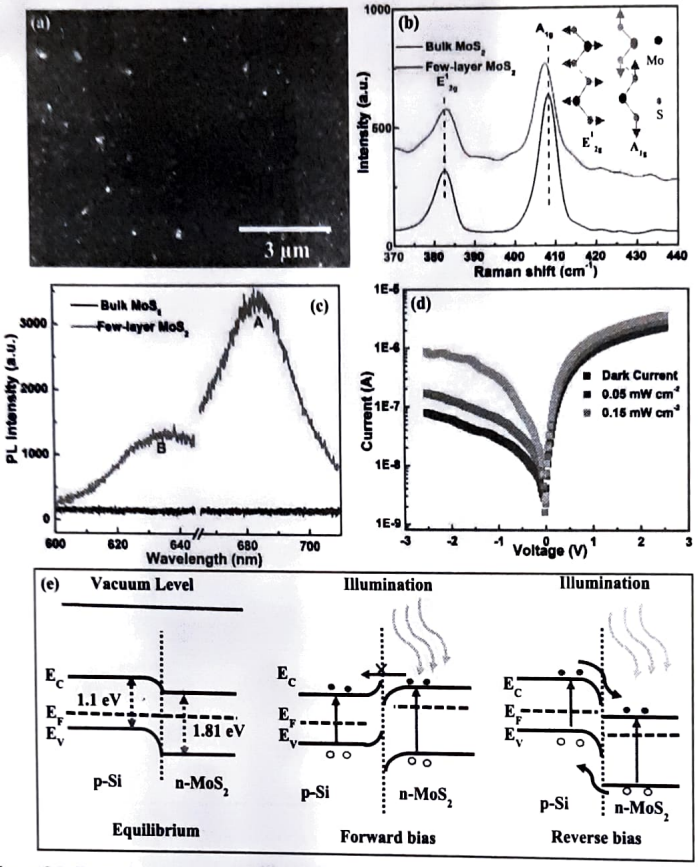

Fig. 9. (a) SEM images of few-layer MoS_2 (b) Raman spectra of both MoS_2 and inset is the vibrational modes. (c) PL spectra of both MoS_2 (d) I-V characteristics under dark and illumination condition, (e) A schematic band diagram for Si/MoS_2 heterojunction. (Adapted with permission from [51]. Copyright 2019 American Chemical Society)

In forward bias condition, the photogenerated electro-hole cannot move due to the unfavourable band bending and hence, insignificant change in photocurrent is observed. The photoresponsivity (R) of this device was examined using following equation 3.

$$R = \frac{I_{ph}}{P_{inch} S} \qquad (3)$$

where Pinc is the incident power density, S is illuminated area of the few-layer MoS_2 and I_{ph} is the photocurrent. The R~ 0.1413 A W^{-1} at -2V was obtained under white light of power density 0.15 mW cm^{-2} for few-layer MoS_2/ Si heterojunction device.

Recently in another work, we demonstrated the photodetection application of thermal conducting vertically oriented few-layer (VFL) MoS_2, synthesized directly on p-type Si substrate [41]. As shown in figure 10a, SEM image of synthesized film suggests the interconnected network of vertically grown few-layer MoS_2 with respect to the substrate. The VFL-MoS_2 were found to be 5 nm thick and 500 nm of height. Raman spectrum (Figure 10b) shows separation around 25 cm^{-1} between characteristic peaks of 2H MoS_2 (E12g ~ 383 cm^{-1} and A1g ~ 408 cm^{-1}), indicating presence of few-layers. The semiconducting nature of VFL-MoS_2 was confirmed by PL study, which indicates two peaks around 681 and 635 nm for direct A and B excitons, respectively, as shown in Figure 10c. The photodetection study of VFL-MoS_2 using I-V characteristics in this study is shown in figure 10d indicating high degree of asymmetry in the I-V curve in dark condition, which suggests formation of high-quality p-n junction at interface. The photodetection properties of the device was observed under green light (532 nm). As expected,

it was found that under reverse bias, the photocurrent increases with laser power density because of increased photogenerated electron-hole pairs. The photogenerated charge carriers were separated by the built-in electric field across p-n junction and applied bias before recombination. The photoresponsivity (R) of the device, under illumination power density of 0.15 mW cm^{-2} at −2 V was found around 7.37 A W^{-1} using equation 3. The reverse bias photocurrent depends upon the incident laser power density (Figure 10e) and it can follow the below equation 4.

$$I_{ph} = CP^{\alpha}_{in} \quad (4)$$

Where C is constant and α is the exponent parameter. The calculated α for the photodiode was around 0.92 indicating small photocurrent loss. Figure 10f shows the switching ability of the device under laser illumination of 0.15 mW cm^{-2} and applied voltage of -3V. Based on above two studies, we found that vertically oriented few-layer MoS_2/Si based photodetector is more efficient than horizontal few-layer MoS_2/Si, which can be ascribed to the enhanced light absorption due to vertical morphology of the film that enhances the light trapping by multiple reflections. An efficient electron-hole separation due to built-in electric field at heterojunction junction also improves the photodetection capability of prepared MoS_2.

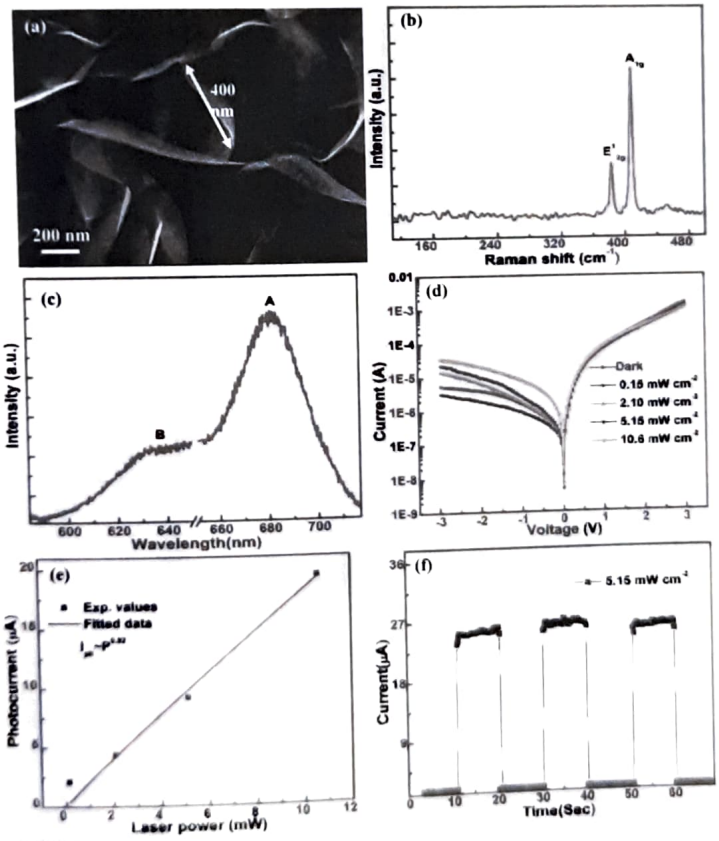

Fig. 10. (a) HRSEM image of VFL-MoS_2 (b) Raman and (c) PL spectrum of synthesized MoS_2 (d) I-V curves of heterojunction device under dark and different illumination intensities. (e) Variation of photocurrent with laser intensities at -2V. (f) Switching behavior of device at -3V. (Adapted with permission from [61]. Copyright 2020 American Chemical Society)

In another work, Liu et. al. synthesized monolayer MoS_2 via CVD technique and transferred it over p-type Si substrate to make heterojunction photodetector[59]. In this process, they deposited Al_2O_3 on Si- substrate to create electrode. Two different electrodes Cr/Au/Cr (6 nm/3 nm/6 nm) and Pd were created over Al_2O_3 via thermal deposition and hence asymmetric electrodes were used for photodetection in this study. The schematic diagram of the final device is given in Figure 11a. The SEM image (figure 11b) shows the prepared heterojunction photodetector with Cr/Au/Cr (6 nm/3 nm/6 nm) and Pd electrode. Figure 11c shows the I-V characteristics curve of fabricated device under 532 nm laser intensities at 0.95, 3.27 and 5.60 mW. The I-V characteristics show

nonlinear behaviour due to Schottky barrier at junction between MoS_2 and electrodes and rise in photocurrent was observed with illumination intensity.

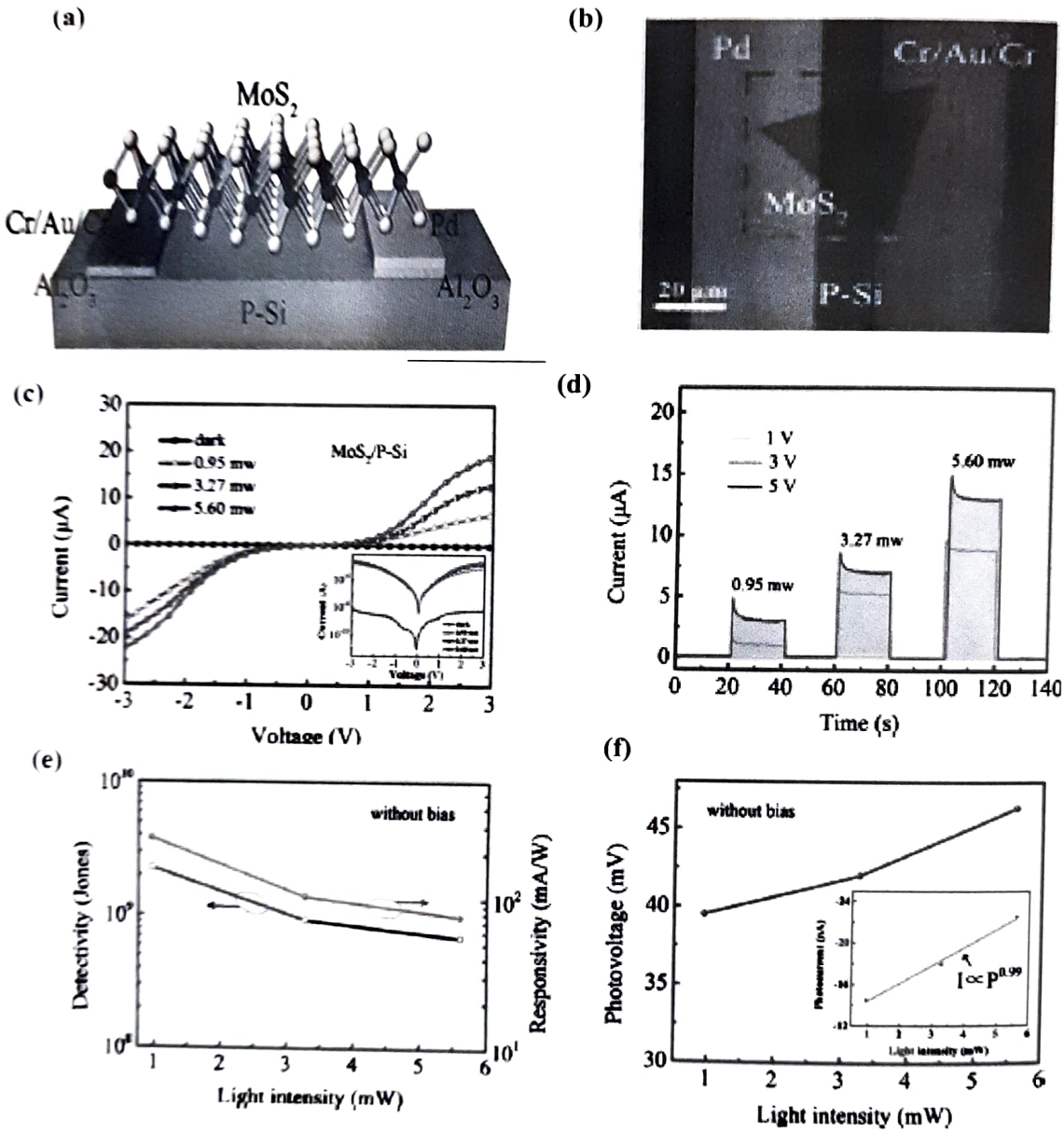

Fig.11 (a). Schematic representation of the fabricated device. (b) SEM image of the fabricated device. (c) I-V characteristics of the device under dark and illumination condition with different laser power intensity. (d) Time dependent photocurrent of the device at different applied voltage. (e) Variation of detectivity and responsivity with light intensity. (f) Variation of photovoltage with light intensity. Inset is the variation of photocurrent with light intensity.

(Adapted with permission from[59]. Copyright 2018 American Chemical Society)

Figure 11d shows the time-dependent photoresponse of device at different bias voltage with different intensities. They calculated the response time and found rise and fall time of 74 ms and 115 ms at 3V bias, respectively. They calculated the photoresponsivity of 117 A W^{-1} at 3 V bias for the device under incident light intensity of 0.95 mW. They further investigated the self-photodetection behaviour of the device by measuring responsivity (~0.253 A W^{-1}) and detectivity (~10^9 jones) at zero bias. Figure 11e shows the variation of detectivity and responsivity of

the fabricated device without bias with different incident laser power intensities. They found that both detectivity and responsivity decreased with increasing incident laser power intensity and suggested that this reduction was observed due to capture of photogenerated charge carriers in trap states. Figure 11f shows the dependence of photovoltage on light intensity, which suggests that the photovoltage gradually enhanced from 37 to 48 mV when light intensity varied from 0.95 to 5.60 mW. Inset of Figure 11f shows the variation of photocurrent of the device with light intensity at zero bias. This curve follows the power law with exponent value around 0.99, attributing less trap states at interface. Mostly MoS_2 based photodetectors with 2D-2D or 2D-Bulk heterojunctions have been studied. In a different kind of study, Um et. al. demonstrated a high-performance 2D-1D photodiode based on MoS_2 nanosheets/CuO nanowire (NW) heterojunction[5] They prepared CuO NWs on Cu foil via thermal oxidation at 500°C and exfoliated MoS_2 nanosheets from bulk MoS_2 via mechanical exfoliation technique. They fabricated the 2D-1D heterojunction device over SiO_2/Si surface by transfer processing of MoS_2 nanosheets over CuO NWs and made electrical contacts of Cr (5 nm)/Au (70 nm) on MoS_2 nanosheets and CuO NWs via thermal evaporator. The measured thickness of 50 nm for MoS_2 nanosheets and 150 nm of diameter for CuO NWs was found. The schematic diagram of the prepared 2D-1D heterojunction photodiode is given in Figure 12a and SEM image of the final device is shown in figure 12b. The I-V characteristics under dark condition of the heterojunction diode (n-type MoS_2 nanosheet and p-type CuO NW) is shown in Figure 12c. The observed high rectification was attributed to the formation of good junction between MoS_2 nanosheets and CuO NWs. The I-V characteristics can be expressed by following equation – 5

$$I = I_s \left[\exp\left(\frac{qV}{\eta KT}\right) - 1\right] \qquad (5)$$

Where $\eta = \frac{q}{kT}\left(\frac{\partial V}{\partial \ln I}\right)$

Terms I_s, K, T, q and η represent reverse saturation current, Boltzmann's constant, temperature, electronic charge and ideality factor, respectively. They value of ideality factor was found to be around 1.37 i.e. higher than 1 suggesting presence of some defects or impurities at the junction resulting in recombination current. Figure 12d represents the I-V characteristics under dark and different wavelengths (560, 600, 700, and 760 nm) illumination at 1 mW incident laser power. The photocurrent clearly depends upon the incident wavelength and the applied reverse bias voltage and device shows the maximum photocurrent under illumination of 600 nm light. They found that the responsivity decreases with increased incident power, however, photocurrent increases, as shown in Figure 12e. In order to suggest the high-performance activity of prepared 2D-1D heterojunction device, they compared the ON/OFF ratio with CuO NW MSM device and MoS_2 nanosheets MSM device under 570 nm illumination at 1 mW. The examined ON/OFF ratio at different potentials is shown in figure 12f, indicating highest value of 3500 of ON/OFF ratio for the MoS_2/CuO heterojunction device at -1V.

Shin et. al. also reported the vertical p-type Si/n-type MoS_2 heterojunction photodetector prepared by mechanically exfoliated n-type MoS_2 flakes [60]. They studied the effect of the thickness of MoS_2 on photodetection behaviour of the prepared device. The schematic diagram of the photodetector device used in this study is shown in Figure 13a. They used Ti/Au (10 nm/40 nm) electrical contacts created using thermal evaporation technique and device was illuminated by the laser light with spot size of 10 μm.

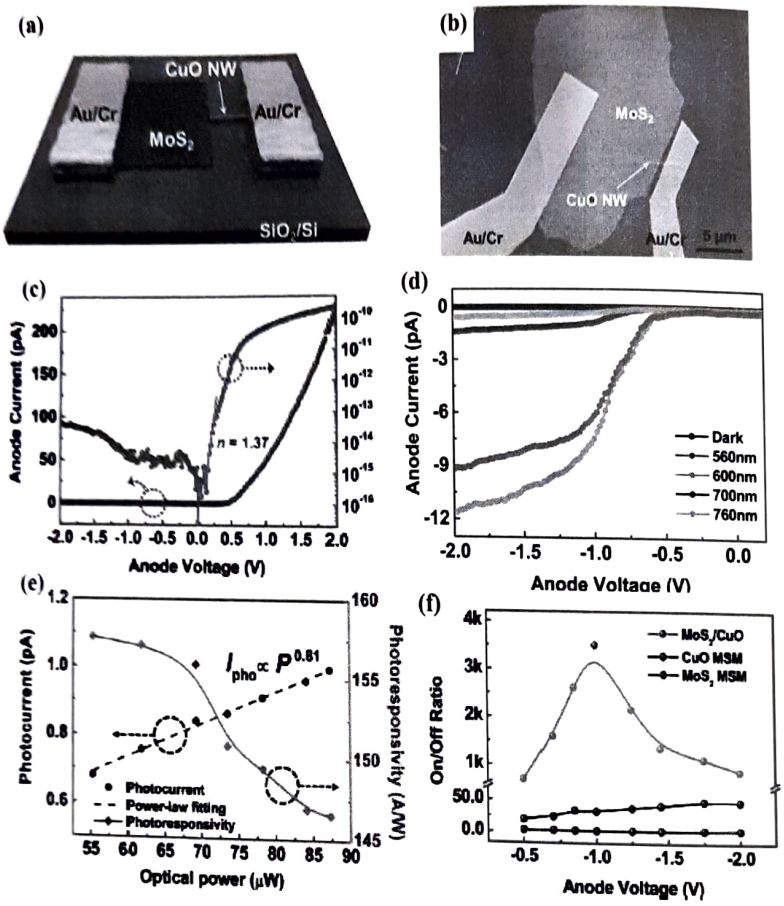

Fig. 12. (a) Schematic representation of p-n heterojunction photodetector. (b) SEM image of the fabricated device. (c) I-V carve of heterojunction under dark condition. (d) Photocurrent of the prepared heterojunction under different light of wavelength (560, 600, 700, and 760 nm). (e) Variation of photocurrent and photoresponsivity at different optical power. (f) Variation of ON/OFF ratio of MoS_2/CuO heterojunction, CuO NW MSM and MoS_2 sheet MSM under green light. (Adapted with permission from [5]. Copyright 2016 American Chemical Society)

Figure 13b shows the cross-sectional TEM image of prepared Si-MoS_2 heterojunction indicating presence of multilayer MoS_2. The photoresponse of the heterojunction was studied under the excitation of different wavelengths of the light (405, 520 and 660 nm) at same intensity at 0.16 W cm^{-2} and corresponding I-V characteristic is given in Figure 13c. The p-n junction showed the rectifying diode behaviour in dark current and the obtained ideal factor for this device was found around 1.49 suggesting good quality of junction diode. The photoresponsivity of the device was found maximum at 660 nm wavelength. The varying laser power intensity in the range 5 μW to 12 nW for 660 nm laser was used to study the photoresponse behaviour of the device. The value of photoresponsivity was 76 A W^{-1} under excitation of 12 nW at reverse voltage of 5 V. Figure 13d shows the increase in responsivity with increasing reverse bias voltage at different laser power. They explained it by considering that the photocurrent at below 1V reverse bias passes through native oxide (SiOx), while it goes over the oxide barrier at above 1V reverse bias. They found the power law exponent around 0.89 at 1V reverse bias indicating nearly linear variation in photocurrent with light intensity. Figure 13e and 13f show the variation of responsivity and detectivity with varying thickness of MoS_2. The best performance of the device was observed for 48 nm thick MoS_2 based photodetector. They also showed the good switching behaviour of the device with On/Off ratio of 10 for the photoresponse having dark current of 0.3 μA. They observed an open-circuit voltage of 0.5 V and short-circuit current density of 161 mA cm^{-2} with the wavelength of 660 nm and intensity of 50 μW of laser. They suggested the trapping mechanism along with high-electric field in the p-n junction for good performance of the photodetector device.

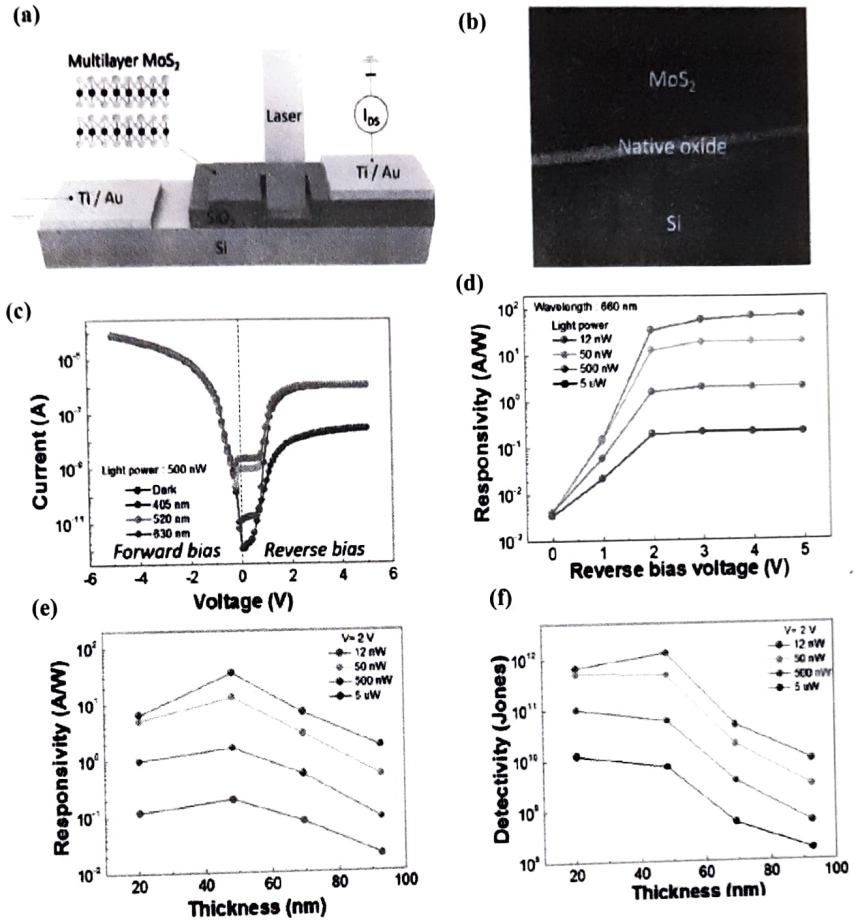

Fig. 13. (a) Schematic diagram of the fabricated device (b) TEM image of Si–MoS_2 heterojunction (Cross-sectional) (c) I–V characteristics of the Si-MoS_2 p-n heterojunction at dark condition and different wavelengths. (d) Variation of photoresponsivity for different bias voltages of the heterojunction device. The variation of (e) Responsivity and (f) Detectivity of the device for different MoS_2 thicknesses. (Adapted with permission from [60]. Copyright 2019 American Chemical Society)

Zhang et. al. reported the different type of MoS_2/GaN 2D heterostructure for photodetection application [61]. In this work, 2D n-type GaN flake was synthesized via liquid metal printing and surface-confined nitridation reaction process. In this process, liquid Ga was pushed to slide on poly-dimethylsiloxane (PDMS) film to form 2D Ga_2O_3 over PDMS film. The prepared 2D Ga_2O_3 was further transferred from PDMS to SiO_2/Si substrate and was treated in NH_3 environment at 800°C for 10 min to grow 2D-GaN flakes. The synthesis process of 2D-GaN flakes is shown schematically in figure 14a. Further, mechanically exfoliated MoS_2 was transferred over 2D-GaN flakes to form heterostructure and conventional photolithography with lift-off process was used to create Ti/Au (5/30 nm) electrical contacts. Figure 14b shows the optical image of prepared MoS_2/GaN heterostructure based photodetector device. A schematic representation of photogeneration of charge carriers in prepared heterostructure and their separation upon illumination is shown in Figure 14c. Interestingly, in this work authors showed that n-type GaN and p-type MoS_2 had different band gaps hence photogeneration of charge carriers was achieved by illumination of both ultraviolet and visible light.

The I-V characteristics were studied under ultraviolet (365 nm) and visible (532 nm) lights as shown in Figure 14d, indicating excellent rectification characteristics and a low threshold voltage ~1.5 V. They found the high rectification ratio of 3.4×10^2 under ±2.5 V bias with ideality factor to be ~2.95. The ideality factor is expected to have value between 1 and 2 and the deviation in this case can be attributed to the possible electron-hole

recombination due to surface states at the heterostructure interface. The photoresponsivity of the device were found to be 328 and 27.1 A W^{-1} under visible and UV light illumination, respectively. They also calculated two other important parameter of nanoscale photodetectors, external quantum efficiency (EQE) and specific detectivity (D).

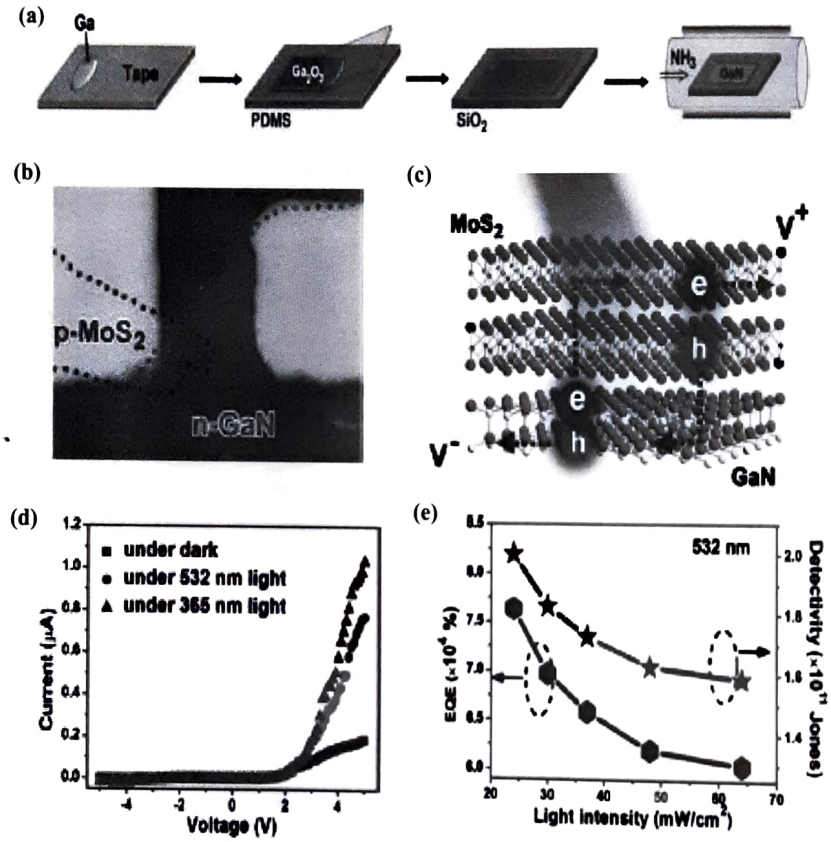

Fig. 14. (a) Schematic diagram for the fabrication of 2D-GaN flake. (b) Optical image of the device. (c) Schematic representation of electron-hole pair generation and their separation. (d) I–V characteristics of the heterojunction under dark conditions and with different wavelengths. (e) Variation of EQE, and detectivity of the heterojunction with light intensity. (Adapted with permission from [61]. Copyright 2020 American Chemical Society)

Figure 14e shows that EQE and detectivity of the photodetector device decreases with increasing visible light intensity. They observed similar trend with variation in ultraviolet light intensity. The calculated values of EQE and D for heterojunction device under 532 nm illumination were obtained around 764% and 2×10^{11} Jones, respectively. However, under 365 nm light illumination, maximum values of EQE and D were achieved to be 92% and 1.7×10^{10} Jones, respectively. The reduction of photoresponsivity, EQE and the detectivity at high power density can be associated with the screening of the internal field by the excited carriers and presence of trap states.

Mukherjee *et. al.* synthesized MoS_2 nanocrystals with varying dimensions by controlled sonication and centrifugation process [56]. They prepared different size of nanocrystals in the range 4 nm to 40 nm and designed MSM photodetectors using different nanocrystals. They found that the crystal size decreases with increasing rotation speed of centrifugation. The average diameter of the nanocrystal is around ~4, ~7, ~12, and ~18 nm. TEM images of 4 nm and 18 nm MoS_2 nanocrystals are shown in figure 15a and 15b, respectively. Figure 15c shows the photoluminescence spectra for synthesized MoS_2 nanocrystals suggesting strong emission with particle size up to 26 nm, while emission peak was found negligible for 40 nm nanocrystal (inset of figure 15c). The prepared MoS_2

nanocrystals exhibited the emission peaks between 500 and 550 nm and hence authors performed photocurrent measurement under 514 nm laser. In this work,

Au electrode was used for the fabrication of MSM device and measured symmetric I-V characteristics (Figure 15d) suggests formation of MSM device. The photo-to-dark current ratio of 10^2 under 514 nm laser illumination with 0.15 mW cm^{-2} power at −2 V bias. The photocurrent increased due to the photogeneration of minority carriers upon illumination and it saturated at higher bias voltage due to the equilibrium state of carrier generation and collection rate. Figure 15e shows the photocurrent vs voltage graph for prepared MoS_2 nanocrystals (7, 12, 18, 26 and 40 nm) based photodetector devices. As observed, photocurrent increased with increasing size of MoS_2 up to 18 nm and decreased beyond this size. The poor photoresponse of smaller size nanocrystals can be attributed to the presence of trap states and recombination centres because of amorphous fraction of MoS_2 nanocrystals. As far as higher particle size than 18 nm is concerned, reduced photodetection efficiency can be attributed to the decrease in probability of direct transitions. The maximum photoresponsivity of the device was found around 0.133 A W^{-1} at -2V under 514 nm laser excitation for 18 nm MoS_2 nanocrystal. They also demonstrated the switching response of 18 nm MoS_2 nanocrystal based MSM device at -5V (figure 15f) with ON/ OFF ratio of the device to be around 5.0.

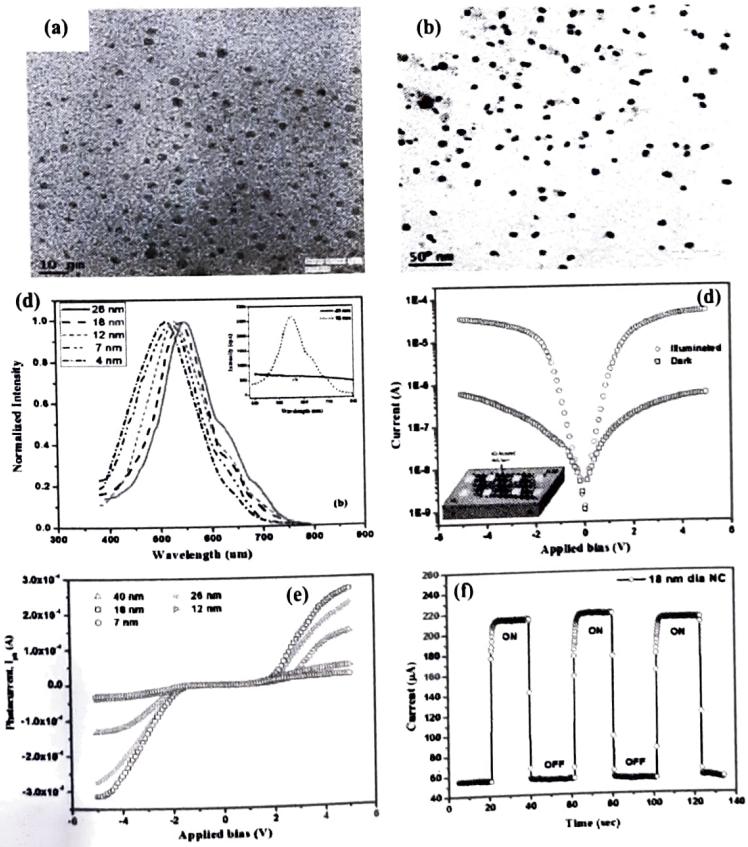

Fig. 15 TEM image of MoS_2 nanocrystal of size (a) 4 nm and (b) 18 nm. (c) Normalized PL emission spectra from different size MoS_2 samples. Inset is the compares PL intensity of sizes 18 and 40 nm MoS_2. (d) I−V curve of the fabricated MSM (Au−MoS_2−Au) device particle size 18 nm. (e) Photocurrent as a function of voltage for different MoS_2 nanocrystal devices. (d) ON/OFF current of MSM device. (Adapted with permission from [56]. Copyright 2015 American Chemical Society)

Lu *et. al.* studied the photoresponse behaviour of multilayer/monolayer MoS_2 junction [62]. The uniform large area multilayer MoS_2 was synthesized via self-limiting growth approach in CVD process. The prepared multilayer MoS_2 was further transferred on prepatterned electrode for device fabrication as shown in Figure 16a. The top left corner shows the optical image of the pristine device with multilayer MoS_2 and Au electrodes with gap of 10

μm. Photoresponse characteristics of pristine device was observed under 532 nm laser light. The power dependent photoresponse at different laser powers and 3V bias is shown in Figure 16b. The laser light at 100 mW cm^{-2} gives the ON/OFF current ratio of about 20 with photoresponsivity around 0.12 A W^{-1}. A post synthesis treatment with laser beam was subjected to create micropatterns to make multilayer/monolayer MoS_2 junction device (inset of figure 16c). The monolayer region surrounded by multilayer film was made by high laser power 50 mW, at scan rate 50 μm s^{-1}. The I-V characteristics for pristine and laser modified devices are shown in Figure 16c. The photoresponse behaviour was studied using 532 nm laser at different power density. The pristine device showed symmetric behaviour while laser modified device indicated certain amount of asymmetry in I-V characteristic with increased current. The asymmetry in modified device was observed due to increased defect concentration because of laser treatment. The bandgap engineering and modified built-in potential barrier in multilayer/monolayer junction device result in its better photodetection behaviour than pristine device. The switching characteristic of modified device at 3V bias is shown in Figure 16d. The photocurrent of modified device was increased up to 4-5 times compared to the pristine one under same illumination condition. The improved photoresponsivity (~0.55 A W^{-1}) of the modified device was obtained due to the created defects via laser modification approach leading to the increase in conductivity. In this work authors could demonstrate the precise control over the thickness of MoS_2 resulting in different bandgaps in the same film, which can be used for tuning the optoelectronic response of the device.

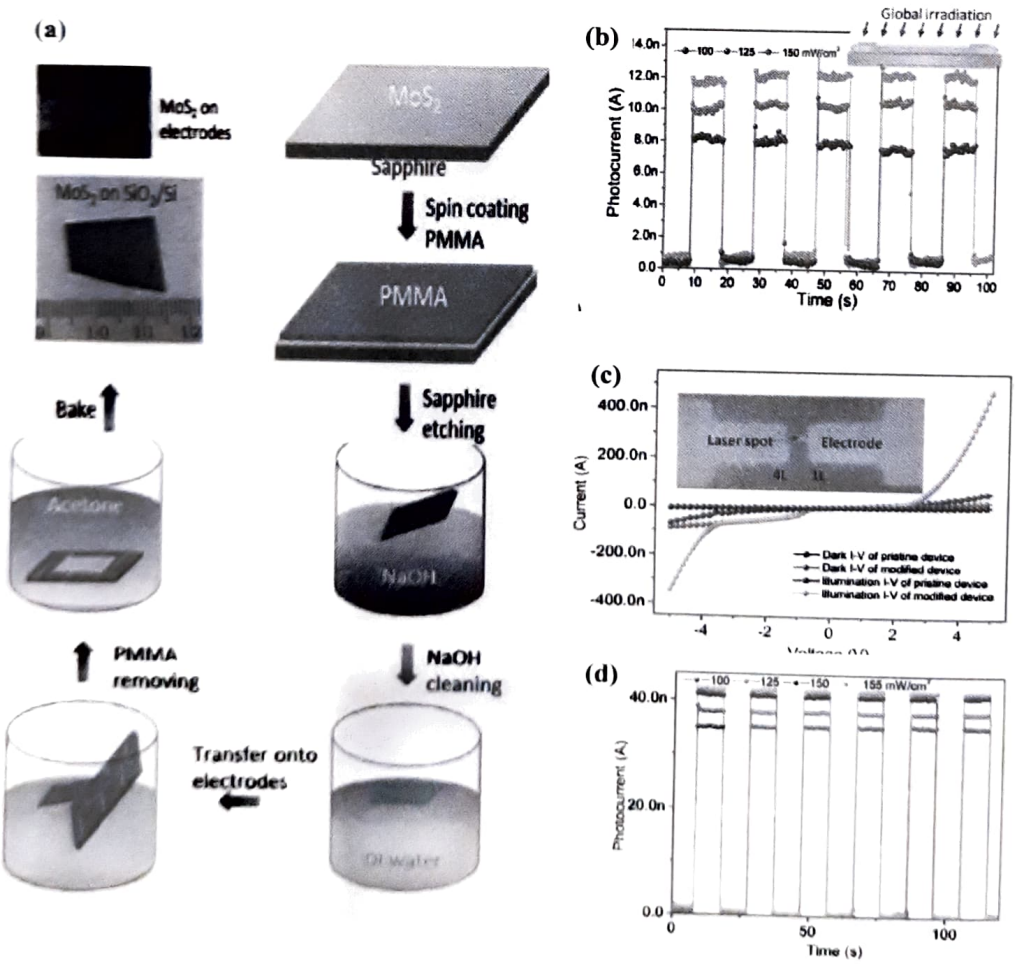

Fig. 16 (a) The schematic diagram of film transfer of MoS_2 and the device. (b) ON/OFF current of pristine device under irradiation. (c) The I-V curves of pristine and modified devices under dark and light. (d) ON/OFF current of laser modified device under irradiation. (Adapted with permission from[63]. Copyright 2014 American Chemical Society)

Tsai *et. al.* reported few-layered MoS_2 based Schottky MSM photodetector with high broadband photogain for use in harsh environments [63]. They prepared the large-area MoS_2 layers with high degree of crystallinity by two-step thermolysis process. Figure 17a shows the AFM image with the height profile of the MoS_2 film indicating thickness around 1.9 nm corresponding to three layers of MoS_2. They made the Schottky contacts using 100 nm thick Au electrode deposited over MoS_2 via electron beam deposition. Figure 17b shows the schematic diagram of the prepared MoS_2 MSM photodetector device, which was examined under 532 nm laser light. The photocurrent of MoS_2 MSM device as a function of time is shown in figure 17c.

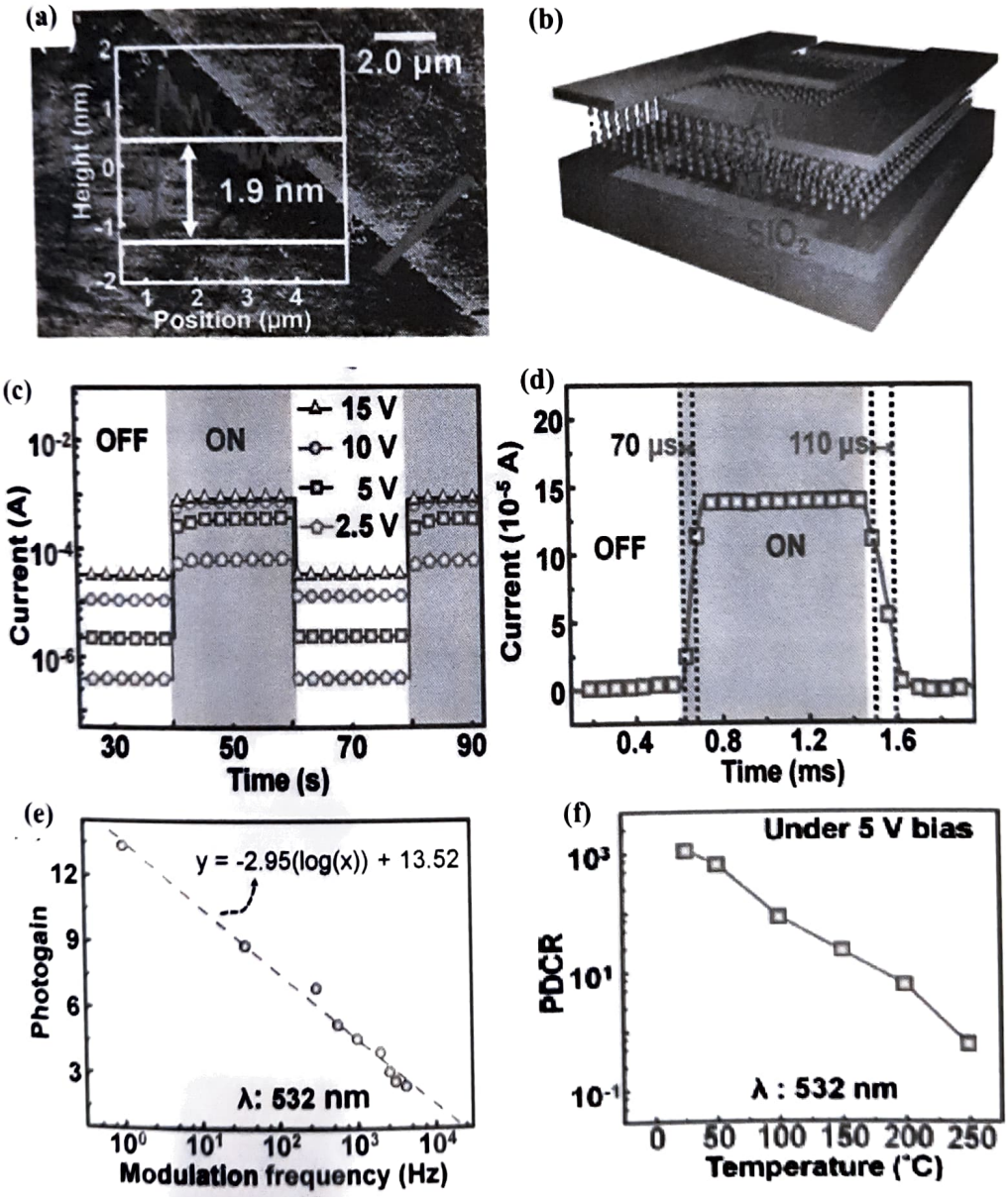

Fig. 17 (a) AFM image of few-layer MoS_2 (b) Schematic diagram of the device. (c) ON/OFF current under dark and under 532 nm laser illumination. (d) High-resolution time response of fabricated device at bias voltage 5 V. (e) Frequency dependent photogain. (f) PDCR of MSM device is a function of temperature. (Adapted with permission from [63]. Copyright 2013 American Chemical Society)

The photocurrent rose to a high value (ON state) upon illumination and returned to a low value (OFF state) when the light was off. The photocurrent saturated beyond 10 V suggesting the build-up of full depletion of the few-layer MoS_2 between two Au electrodes. They found the rise time (10% to 90%) and fall time (90% to 10%) of the

MSM device to be 70 and 110 μs, respectively (Figure 17d). They obtained the photo responsivity of 0.57 A W^{-1} under the excitation of green laser of wavelength of 532 nm. The photogain of the device was estimated using the following equation 6-

$$R = \frac{I_P}{P} = \eta_{ext} G q / h\nu \quad (6)$$

Where R and Ip are the responsivity and photocurrent of the fabricated device, while P is the illumination power. The ηext, G and q represent external quantum efficiency, photogain, and electronic charge, respectively, while hν is the energy of the incident photon. They obtained the high value of photogain (~13.3) for the device due to the high responsivity of 0.57 A W^{-1} and detectivity around 10^{10} Jones. In order to investigate the dynamics of the photogenerated carriers modulated frequency response was studied at 10 V bias. Photogain was gradually reducing with the modulation frequency as shown in Figure 17e. Thermal stability of the fabricated MSM device was measured in respect of photocurrent to dark current ratio (PDCR). Where PDCR is given by following equation 7-

$$PDCR = \frac{(I_{ph} - I_d)}{I_d} \quad (7)$$

Where Iph and Id are the photocurrent and dark current, respectively. They studied the variation of PDCR with temperature and found that it decreases gradually decrease with temperature as shown in Figure 17f. They found PDCR to be ~10^3 at room temperature which remained up to ~10 at 200°C. This few-layer MoS_2 based MSM photodetector device with broadband high photogain and fast optical switching paves the way for the development of optoelectronic devices for harsh environments.

Xie *et. al.* recently reported the room-temperature terahertz photodetection using MoS_2 [64]. They synthesized multilayer MoS_2 by pulsed laser deposition (PLD) technique and observed that the MoS_2 bandgap changed with the defect of Mo and S vacancies. Theoretical calculation showed that the band gap of MoS_2 reduces with increasing S-deficiency and Mo-deficiency.

Figure 18a shows the modulated bandgap of MoS_x ($1.72 \leq x \leq 2.21$) at different defect concentrations. Experimentally, they varied the defect concentrations by tuning the deposition parameter and found that under higher pulse number, thickness of the MoS_x gradually increases. They prepared a metal-semiconductor-metal (MSM) structure using the prepared MoS_x thin film and two electrodes of Au with thickness of 80 nm as shown in SEM image of Figure 18b. They used a 2.52 Terahertz (THz) illumination source for photodetection studies. The time dependent photocurrent of the fabricated MSM device under different light intensities is shown in figure 18c, indicating increase in photocurrent with increased light illumination power. They found the response time ~5.12 sec and the decay time 6.33 sec at 10 mW illumination power. Figure 18d shows the variation of photocurrent with the incident power at two different applied voltages of 10V and 1V. These photocurrents follow the power law with exponent values 0.86 for 1V bias and 0.9 for 10V bias. They calculated the change in carrier concentrations (Δn) increases with the incident light power and reached to maximum value of around 6.96 × 104 cm^{-3} at 19 mW illumination. The device shows the photoresponsivity of 0.12 × 10^{-3} A W-1 at 1V bias. Figure 18f shows the variation of photocurrent and responsivity of MSM device with applied voltage under illumination power 10 mW. The photoresponsivity shows the peak value of 10 × 10^{-3} A W^{-1} at 20 V. Photocurrent also reached its maximum value at bias voltage of 20 V.

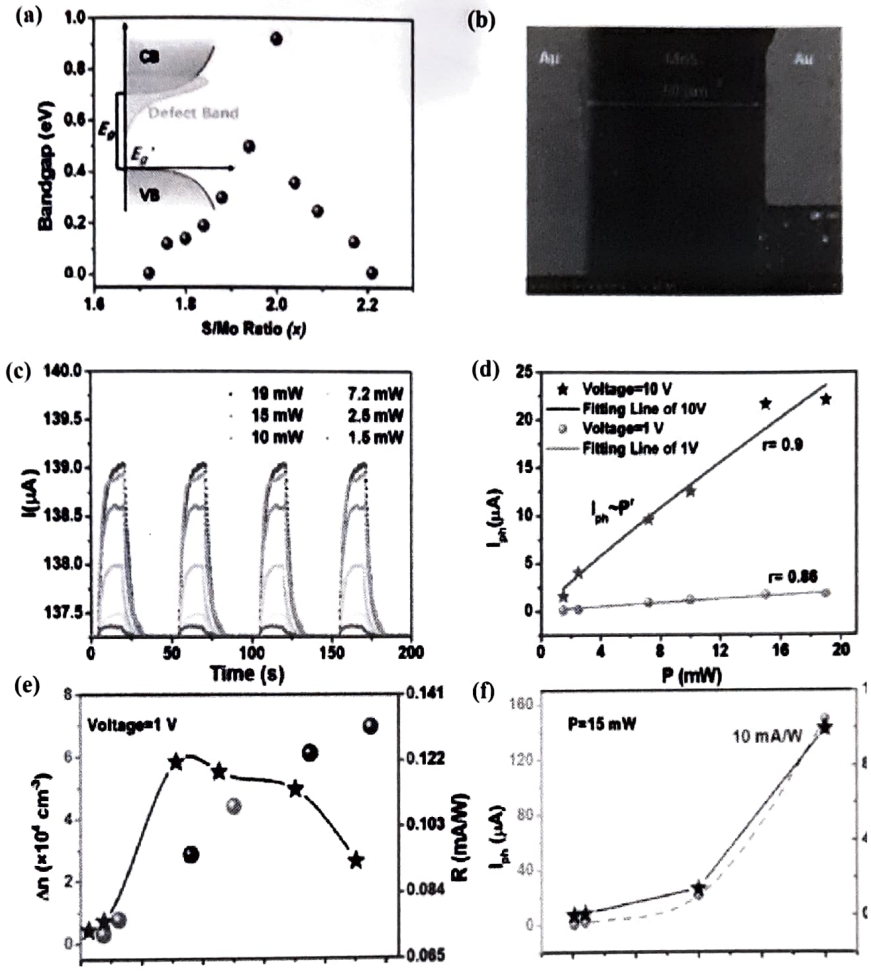

Fig. 18. (a) Variation of bandgap with the Mo/S ratio x. (b) SEM images of the fabricated device. (c) Time dependent photocurrent of the MSM detector with different power. (d) Variation of photocurrent at different incident power at applied voltage 1V and 10V. (e) Variation of calculated Δn and photoresponsivity with incident power at applied voltage 1 V. (f) Variation of photocurrent and photoresponsivity with applied voltage. (Adapted with permission from [64]. Copyright 2020 American Chemical Society)

Dhyani and Das reported the few-layer MoS_2 for photodetection using Si/MoS_2 (p-n) heterojunction and Au/MoS_2/Au MSM devices[65]. They prepared 10 nm thick MoO_3 on the SiO_2/Si substrates by reactive sputtering and reduced it with sulfur in N_2 atmosphere at 500°C for 20 min. They patterned the device by lithography process and created the metal contacts of Cr/Au. The schematic diagram of the fabricated device is shown in Figure 19a. Figure 19b shows the I–V characteristic of prepared Si/MoS_2 p-n heterojunction device under dark and illumination condition. They observed the dark current ~1.8×10^{-7} at reverse bias of 3 V and photocurrent enhances by 127 times upon illumination of 560 nm light at 5mW cm^{-2}. The ideality factor of 2.4 was achieved due to the presence of interface defect states.

The Figure 19c shows the I-V characteristics of the Au/MoS_2/Au MSM photodetector, which shows photo-to-dark current ratio ~72. They also calculated the photoresponsivity of both the devices within the wavelength range 350-1050 nm at a bias of 3 V (Figure 19d). Two prominent peaks were observed around 580 nm and 860 nm for Si/MoS_2 heterojunction, however, only a single peak was observed at 580 nm for MoS_2 MSM photodetector. The peak around 580 is observed due to the absorption of the MoS_2 film in the visible region, while 860 nm peak appears due to silicon substrate. Photoresponsivity was found lower for MSM device (~ 6.8 A W^{-1}) compared to Si/MoS_2 (p-n) heterojunction (~ 8.75 A W^{-1}) due to the absence of charge carriers of p-type silicon substrate in MSM device.

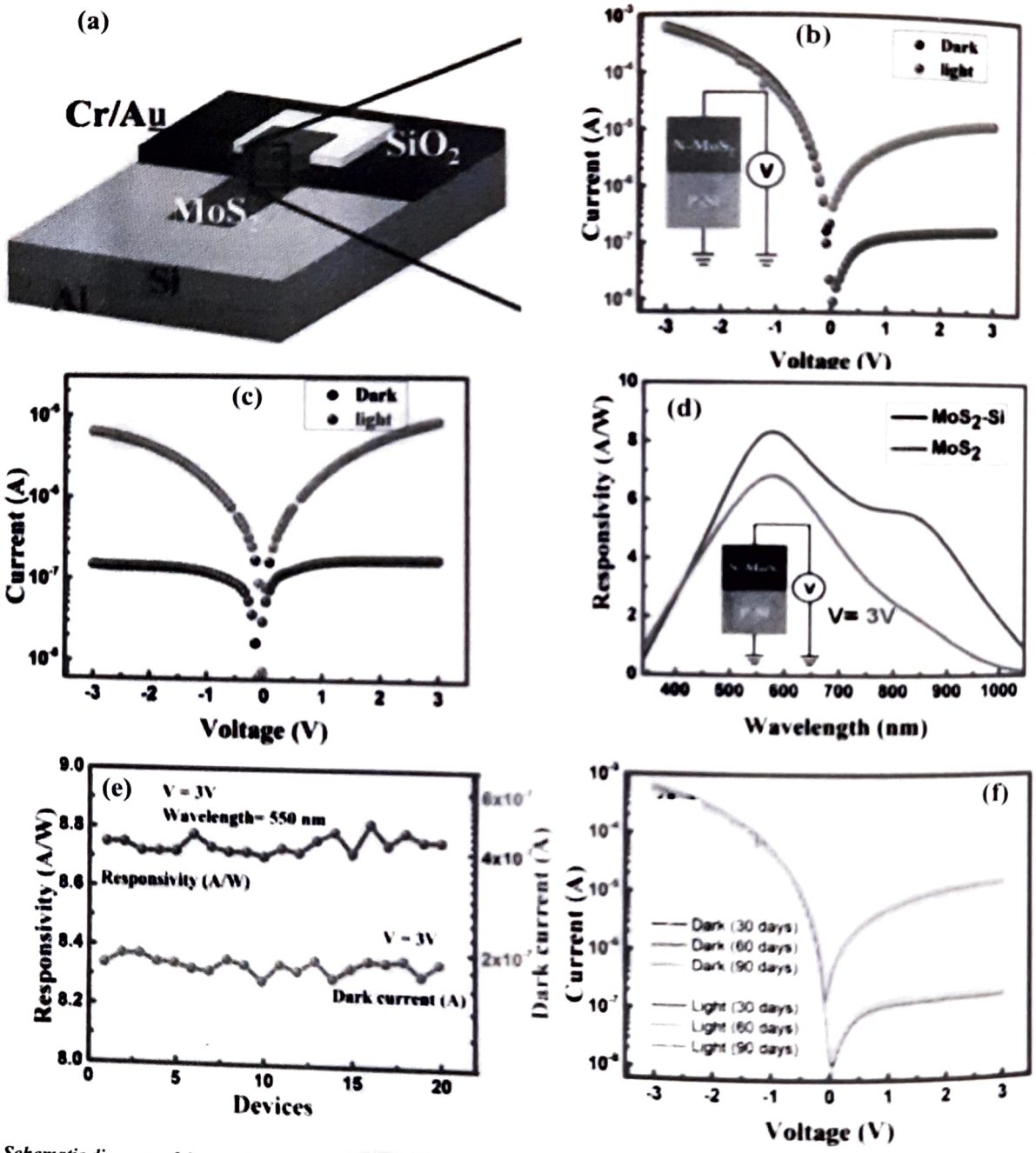

Fig. 19 (a) Schematic diagram of the Si/MoS_2 p-n junction. I-V characteristics of (b) Si-MoS_2 heterojunction and (c) Au/MoS_2/Au MSM photodetector. (d) photoresponsivity of both the device with wavelength. Inset shows the biasing condition for heterojunction. (e) photoresponsivity and dark current of 20 devices (f) I-V curve of Si/MoS_2 heterojunction device for different time period. (Adapted with permission from [65]. Copyright 2017 Nature)

The high built-in electric field in Si/MoS_2 p-n junction also enhances its photoresponsivity. In order to test the scalability of p-n junction device, they prepared 20 devices on same substrate and measured the photoresponsivity and dark current of those devices (Figure 19e). They found stable performance from different devices. Further, they investigated the air stability of the Si/MoS_2 p-n junction photodetector and observed it for 90 days in air. Figure 19f clearly shows the stable nature of prepared p-n junction device. Apart from above discussed studies, there have been multiple studies on MoS_2 based photodetectors, performance summary of some of them have been summarized below in Table 1 [66-75].

Table 1 The comparison of figure of merit parameter of different MoS_2 based photodetectors.

Photodetector	Source wavelength (nm)	Applied voltage (V)	Incident power ($mW\ cm^{-2}$)	Photo-responsivity ($A\ W^{-1}$)	Ref.
2D MoS_2/1D CuO heterojunction	LED 570	-2	–	157.6	5
Few-layer V-MoS_2/Si heterojunction	laser 532	-2	0.15	7.37	41
Few-layer MoS_2/Si heterojunction	Neon lamp white light	-2	0.15	0.1413	51
MoS_2 nanocrystal MSM	laser 532	-2	–	0.133	56
MoS_2 /P-Si heterojunction	laser 532	3	–	117	59
MoS_2/Si heterojunction	laser 660	–	12×10^{-6}	76.1	60
MoS_2/GaN heterojunction	532	5	–	328	61
Few-layer MoS_2 (MSM)	laser 532	3	100	0.12	62
Three-layer MoS_2 MSM	laser 532	10	–	0.57	63
Multilayer MoS_2 MSM	laser (2.52 THz frequency)	20	–	10×10^{-3}	64
Multi-layer MoS_2/Si heterojunction	580	3	–	8.50	65
MoS_2 /a-Si heterojunction	550	1	–	0.21	66
Multilayer MoS_2/Si heterojunction	laser 808	–	1	0.21	67
Multi-layer MoS_2/Si heterojunction	laser 808	-2	5	0.746	68
Multi-layer MoS_2/Si heterojunction	laser 780	-5	45×10^{-3}	23.1	69
p-MoS_2/n-ZnO heterojunction	365	5	5.7	24.36	70
MoS_2/Si nanowire heterojunction	650	0	6.3×10^{-3}	53.5	71
Multi-layer MoS_2/GaN heterojunction	laser 405	–	2	17.2	72
FL MoS_2/CdSe heterojunction	laser 405	–	8.52×10^{-3}	2.5×10^{5}	73
MoS_2/GaAs heterojunction	laser 635	-1	–	0.247	74
MoS_2/PbS heterojunction	laser 800	–	0.15	4.5×10^{4}	75

CONCLUSION

Two dimensional materials like MoS_2 is chemically and environmentally stable in air and hence it can be used for practical electronic and optoelectronic applications. In this review, we have particularly summarized synthesis processes for different morphologies of MoS_2 nanostructures along with fabrication and design of photodetectors. Recent studies on MoS_2 based p-n junction and MSM devices for photodetection application have been discussed. These studies clearly suggest that monolayer to few-layer MoS_2 can be used efficiently for photodetection purposes. Performances of such devices depends upon the quality and thickness of the film, electrical contacts and light source. The band engineering in MoS_2 can be applied to tune the suitability of such devices for varying applications like sensors, night vision devices, surveillance, optical communications etc.

REFERENCES

[1] B. Radisavljevic et.al.: Single-layer MoS_2 transistors. Nat. Nanotechnol. 6: 147-150, 2011.

[2] K.F. Mak et.al.: Atomically thin MoS_2: a new direct-gap semiconductor. Phys. Rev. Lett.105: 136805-4, 2010.

[3] Q.H. Wang et.al.: Electronics and optoelectronics of two-dimensional transition metal dichalcogenides. Nat. Nanotechnol. 7: 699-712, 2012.

[4] H.S. Nalwa: A review of molybdenum disulfide (MoS_2) based photodetectors: from ultra-broadband, self-powered to flexible devices. RSC Adv., 10: 30529–30602, 2020.

[5] D.S. Um et.al.: High-performance MoS_2/CuO nanosheet-on-one-dimensional heterojunction photodetectors, ACS Appl. Mater. Interfaces. 8: 33955–33962, 2016.

[6] A.K. Geim, K. S. Novoselov: The rise of graphene. Nat. Mater. 6: 183–191, 2007.

[7] H. Castro Neto et.al. :The electronic properties of graphene. Rev. Mod. Phys. 81: 109–162, 2009.

[8] H. Li et.al. Preparation and applications of mechanically exfoliated single-layer and multilayer MoS_2 and WSe_2 nanosheets. Acc. Chem. Res. 47:1067–1075, 2014.

[9] V. Nicolosi et.al.: Liquid exfoliation of layered materials. Science. 340: 1226419-18, 2013.

[10] M. Chhowalla et.al.: The chemistry of two-dimensional layered transition metal dichalcogenide nanosheets. Nat. Chem. 5: 263–275, 2013.

[11] L. Song et.al.: Large scale growth and characterization of atomic hexagonal boron nitride layers, Nano Lett.10: 3209–3215, 2010.

[12] F. Xia et.al.: Ultrafast graphene photodetector. 4: 839–843, 2009.

[13] M.L. Tsai et.al.: Monolayer MoS_2 heterojunction solar cells. ACS Nano 8: 8317–8322, 2014.

[14] X. Wei et.al.: Photodetectors based on junctions of two-dimensional transition metal dichalcogenides. Chin. Phys. B, 26: 038504–038515, 2017.

[15] J.A. Wilson, A.D. Yoffe: The transition metal dichalcogenides discussion and interpretation of optical, electrical and structural properties. Adv. Phys. 18: 193–335, 1969.

[16] R. Bissessur et.al.: Encapsulation of polymers into MoS_2 and metal to insulator transition in metastable MoS_2. Chem. Commun. 1993: 1582–1585, 1993.

[17] R. F. Frindt and A. D. Yoffe: Physical properties of layer structures: Optical properties and photoconductivity of thin crystals of molybdenum disulphide. Proc. R. Soc. Lond. A. 273: 69–83, 1963.

[18] Y. Yu et.al.: High phase-purity 1T′-MoS_2- and 1T′-$MoSe_2$- layered crystals, 10: 638-643, 2018.

[19] S. Das, et.al.: High performance multilayer MoS_2 transistors with scandium contacts. Nano Lett. 13: 100–105, 2013.

[20] W. J. Zhang et.al.: Ultrahigh-gain photodetectors based on atomically thin graphene-MoS_2 heterostructures. Sci. Rep., 4: 3826, 2014.

[21] S. J. Park et.al.: Ultrasensitive flexible graphene based field-effect transistor (FET)-type bioelectronic nose, Nano Lett. 12: 5082–5090, 2012.

[22] N. Liu, et.al.: Large-area, transparent, and flexible infrared photodetector fabricated using p-n junctions formed by n-doping chemical vapor deposition grown graphene, Nano Lett. 14:3702–3708, 2014

[23] R. Singh, E. Singh, H.S. Nalwa: Inkjet printed nanomaterial based flexible radio frequency identication (rfid) tag sensors for the internet of nano things, RSC Adv. 7: 48597–48630, 2017.

[24] S. K. Krishnan et.al.: A review on graphene-based nanocomposites for electrochemical and fluorescent biosensors, RSC Adv. 9: 8778–8881, 2019.

[25] W. K. Chee et. al.: Flexible graphene-based supercapacitors: a review, J. Phys. Chem. C, 120:4153–4172, 2016.

[26] K. Ruan et.al.: Flexible graphene/silicon heterojunction solar cells, J. Mater. Chem. A, 3: 14370–14377, 2015.

[27] W. J. Yu et.al.: Highly efficient gate-tunable photocurrent generation in vertical heterostructures of layered materials, Nat. Nanotechnol. 8: 952–958, 2013.

[28] Y. Gong et.al.: Two-step growth of two-dimensional WSe_2/ $MoSe_2$ heterostructures, Nano Lett. 15: 6135–6141, 2015.

[29] R. Cheng et. al.: Electroluminescence and photocurrent generation from atomically sharp WSe_2/MoS_2 heterojunction p–n diodes. Nano Lett. 14: 5590–5597, 2014.

[30] Y. Li et.al.: Photodiode-like behavior and excellent photo-response of vertical Si/Monolayer MoS_2 heterostructures. Sci. Rep., 4: 7186–7194, 2014.

[31] A. Midya et.al.: Hydrothermal growth of few layer 2H-MoS_2 for heterojunction photodetector and visible light induced photocatalytic 2020 applications. J. Mater. Chem. A, 4: 4534–4543, 2016.

[32] C. Li et. al.: Constructing 3d and flexible plasmonic structure for high-performance SERS application. Adv. Mater. Technol. 3: 1800174–1800185, 2018.

[33] B. P. Majee, V. Shrivastava and A. K. Mishra: Surface-enhanced Raman scattering detection based on an interconnected network of vertically oriented semiconducting few-layer MoS_2 nanosheets. ACS Appl. Nano Mater. 3: 4851–4858, 2020.

[34] F. C. Feng et.al.: Synthesis of molybdenum disulfide (MoS_2) for lithium ion battery applications. Mater. Res. Bull. 44: 1811–1815, 2009.

[35] Q. Xiang, J. Yu, M. Jaroniec: Synergetic effect of MoS_2 and graphene as cocatalysts for enhanced photocatalytic H_2 production activity of TiO_2 nanoparticles. J. Am. Chem. Soc. 134: 6575–6578, 2012.

[36] S. Mishra, P. K. Maurya, A. K. Mishra: 2H-MoS_2 nanoflowers with exposed edges for hydrogen producing electrochemical cell. Mater. Today. Commun. 25: 101270, 2020.

[37] O. L. Sanchez et.al.: Nat. Nanotechno. Ultrasensitive photodetectors based on monolayer MoS_2. 8: 497-501, 2013.

[38] Y. H. Lee et.al.: Synthesis of large-area mos_2 atomic layers with chemical vapor deposition. Adv. Mater. 24: 2320–2325, 2012.

[39] K. S. Novoselov et.al.: Electric field effect in atomically thin carbon film. Science 306: 666–669, 2004.

[40] A. K. Mishra, K V Lakshmi, L. Huang: Eco-friendly synthesis of metal dichalcogenides nanosheets and their environmental remediation potential driven by visible light. Sci. Rep. 5: 15718–15726, 2015.

[41] B.P. Majee et.al.: Large area vertically oriented few-layer MoS_2 for efficient thermal conduction and optoelectronic applications. J. Phys. Chem. Lett. 11: 1268–1275, 2020.

[42] R.J. Smith et.al.: Large-scale exfoliation of inorganic layered compounds in aqueous surfactant solutions. Adv. Mater. 23: 3944–3948, 2011.

[43] S. Bertolazzi, J. Brivio, A. Kis: Stretching and breaking of ultrathin MoS_2. ACS Nano 5: 9703–9709, 2011.

[44] P. Joensen et.al.: Single-layer MoS_2. Mater. Res. Bull. 21: 457–461, 1986.

[45] G. Eda et. al.: Photoluminescence from chemically exfoliated MoS_2. Nano Lett 11:5111–5116, 2011.

[46] S. Vishwanath et.al.: Comprehensive structural and optical characterization of MBE grown $MoSe_2$ on graphite, CaF_2 and graphene. 2D Mater. 2: 024007, 2015.

[47] C. Muratore et.al.: Continuous ultra-thin MoS_2 films grown by low-temperature physical vapor deposition, 104: 261604, 2014.

[48] Y. Gong B. Li, G. Ye: Direct growth of MoS_2 single crystals on polyimide substrates, 2D Mater. 4: 021028-6, 2017.

[49] K. M. McCreary, A. T. Hanbicki, J.T. Robinson: Large-area synthesis of continuous and uniform MoS_2 monolayer films on graphene. Adv. Funct. Mater. 24: 6449–6454, 2014.

[50] J. Sun et. al.: Synthesis methods of two-dimensional MoS_2: A brief review crystals, 7: 198, 2017.

[51] B. P. Majee et. al. Multifunctional few-layer MoS_2 for photodetection and surface enhanced Raman spectroscopy application with ultrasensitive and repeatable detectability. J. Phys. Chem. C, 123: 18071–18078, 2019.

[52] X. Zhou et. al. Hydrothermal synthesis of flower-like MoS_2 nanospheres for electrochemical supercapacitors. J. Nanosci. Nanotechnol. 14: 7250–7254, 2014.

[53] X. Feng, et. al. Novel mixed–solvothermal synthesis of MoS_2 nanosheets with controllable morphologies. Cryst. Res. Technol., 48: 363–368, 2013.

[54] S. Mishra, P. K. Maurya, A. K. Mishra: 2H–MoS_2 nanoflowers based high energy density solid state supercapacitor, 2020 doi. org/10.1016/j.matchemphys.2020.123551.

[55] L. Zheng, L. Zhongzhu, and S. Guozhen: Photodetectors based on two dimensional materials: J. Semicond. 37: 091001-11, 2016.

[56] S. Mukherjee et. al.: Tunable direct bandgap optical transitions in MoS_2 nanocrystals for photonic devices. ACS Photonics, 2: 760–768, 2015.

[57] A. Ayari et. al.: Realization and electrical characterization of ultrathin crystals of layered transition metal dichalcogenides. J. Appl. Phys. 101(1): 14507, 2007.

[58] A. Splendiani et.al.: Emerging photoluminescence in monolayer MoS_2. Nano Lett. 10: 1271-1275, 2010.

[59] X. Liu et. al.: high response, self-powered photodetector based on the monolayer MoS_2/P–Si heterojunction with asymmetric electrodes. Langmuir, 34: 14151–14157, 2018.

[60] G.H. Shin et.al.: Si–MoS_2 vertical heterojunction for a photodetector with high responsivity & low noise equivalent power, ACS Appl. Mater. Interfaces. 11: 7626–7634, 2019.

[61] X. Zhang et.al.: Design and Integration of a layered MoS_2/GaN van der Waals Heterostructure for Wide Spectral Detection and Enhanced Photoresponse, 2020, ACS Appl. Mater. Interfaces. https://dx.doi.org/10.1021/acsami.0c11021

[62] J. Lu et. al. Improved photoelectrical properties of MoS_2 films after laser micromachining. ACS Nano. 8: 6334-6443, 2014.

[63] D.S Tsai et.al. Few-layer MoS_2 with high broadband photogain and fast optical switching for use in harsh environments, ACS Nano. 7: 3905–3911, 2013.

[64] Y. Xie et.al.: Defect engineering of MoS_2 for room-temperature terahertz photodetection ACS Appl. Mater. Interfaces. 12: 7351–7357, 2020.

[65] V. Dhyani and S. Das: High-Speed Scalable Silicon-MoS_2 P-N Heterojunction Photodetectors, Scr. Rep. 7: 44243-9, 2017.

[66] M. R. E. Rad and S. Sala huddin: High performance molybdenum disulfide amorphous silicon heterojunction photodetector, Sci. Rep. 3: 2345-6, 2013

[67] L. Wang et. al. MoS_2 /Si Heterojunction with vertically standing layered structure for ultrafast, high-detectivity, self-driven visible–near infrared photodetectors. Adv. Funct. Mater. 25: 2910–2919, 2015.

[68] J. Guo et.al. Broadband photodetector based on vertically stage-liked MoS_2/Si heterostructure with ultra-high sensitivity and fast response speed, Scripta Mater. 176: 1–6, 2020.

[69] Z. Lou et.al.: High-performance MoS_2/Si heterojunction broadband photodetectors from deep ultraviolet to near infrared. Optics Lett. 42: 3337-4,2017.

[70] J. Zhang et.al. High-Performance Ultraviolet-Visible Light-Sensitive 2D-MoS_2/1D-ZnO Heterostructure Photodetectors. Chem. Select. 5: 3438–3444, 2020.

[71] D. Wu et.al.: Photovoltaic high-performance broadband photodetector based on MoS_2/Si nanowire array heterojunction, Sol. Energy Mater. Sol. Cells 182: 272–280, 2018.

[72] X. Liu et.al.: Nearly lattice-matched molybdenum disulfide/gallium nitride heterostructure enabling high-performance phototransistors. Photonics Res. 7: 311–317, 2019.

[73] H.-S. Ra, D.-H. Kwak and J.-S. Lee: A Hybrid MoS_2 nanosheet–CdSe nanocrystal phototransistor with a fast photoresponse. Nanoscale 8:17223–17230, 2016.

[74] Z. Xu et.al.: MoS_2/GaAs Heterostructure self-driven photodetector with extremely high detectivity. Nano Energy. 23: 89–96, 2016.

[75] Y. Wen et.al.: Integrated high-performance infrared phototransistor arrays composed of nonlayered Pbs– MoS_2 heterostructures with edge contacts. Nano Lett. 16: 6437–6444, 2016.

Journal of Metallurgy and Materials Science, Vol. 62, No. 3-4, July-December 2020, pp. 127-133
Printed in India, © NML, ISSN 0972-4257

Weakly coupled metal-semiconductor plasmonic nanoparticles in solution

BHASKAR SAHA[1], SALIL S. VAIDYA[2], KAUSTAV BHATTACHARJEE[3], BHAGAVATULA L. V. PRASAD[*3,4]
[1]Indian Institute of Science Education and Research, Pune 411008, India
[2]Department of Chemical Engineering, Vishwakarma Institute of Technology, Pune 411037, India
[3]Physical and Material Chemistry Division, National Chemical Laboratory, Pune 411008, India
[4]Academy of Science and Innovation Research (AcSIR), Ghaziabad, 201002, India.

Abstract: The optical properties of binary metal-semiconductor (gold-copper sulphide, both of which are plasmonic in nature) nanoparticle system has been investigated in solution, demonstrating a clear plasmonic coupling between them, due to proximity effect. Monodisperse nanoparticles of gold and copper sulphide were first synthesized using reported methods and then characterized using advanced instrumental techniques. Upon gradual addition of copper sulphide nanoparticle dispersion to that of gold nanoparticles, the intensity of the characteristic localized surface plasmon resonance (LSPR) peak of gold nanoparticles gets reduced, while that of the copper sulphide increases and an 'isosbestic point' could be observed. However, the reduction and the increase in the intensities do not follow the trends as expected from simple dilution/increase in the concentrations indicating a plasmonic coupling between them. The same coupling in the mixed state could be seen with respect to the shift in binding energies of the core-level orbitals of the both the materials, from the XPS spectra. Thus, the present study exemplifies a facile solution method to tune the LSPR bands in plasmonic nanomaterials for any potential device application.

Keywords: *Localized surface plasmon resonance, nanoparticle, Fermi energy, weak coupling*

INTRODUCTION

Boundary between a metal and semiconductor plays a vital role in various interfacial charge transfer processes for electronic device applications[1]. Moreover, light-induced energy transfer in metal-semiconductor hybrid nanostructures is also the central issue for the photovoltaic[2,3], and photocatalytic applications[4,5]. Investigation on binary nanoparticle assembly of two different sizes and their compactness is important for various metallurgical purposes[6,7]. In the nano regime, the 'dielectric confinement' in the metal leads to highly polarizable localized surface plasmons, and the 'quantum confinement' in the semiconductor leads to excitonic electron-hole pair generation[8]. Localized surface plasmon resonance (LSPR) is an optical phenomenon manifested in a geometrically confined electrically conducting structure in which free charge carriers (free electrons or holes) can collectively oscillate in resonance with incoming light[9]. Though LSPR is mostly seen in noble metal nanoparticle, semiconductor nanocrystals with appreciable free carrier concentrations can also display LSPR. This has been excellently demonstrated by Luther et al. in $Cu_{2-x}S$ system[10]. Copper-deficient copper chalcogenides are p-type semiconductors in which the highest energy states in the valence band are empty. The free holes associated with these unoccupied states are responsible for LSPR.[9] Interestingly, the spectral position of this LSPR peak can be tuned by variation in copper vacancies; the greater the vacancy concentration, the higher the LSPR frequency. The LSPR arising from such semiconductors relative to noble metals is distinguished by their absorption position in the NIR spectral region (proportional to free carrier concentration, varies 10^{16}-10^{21} /cm^3)[10] which can be tuned with composition and crystal structure of the material, while that is fixed in the visible region (free electron density in the range 10^{22}-10^{23} /cm^3) [10] for the metal and can only be tuned by changing the size- and morphology. The low carrier density in semiconductor compared to metal makes it sensitive to local electron density fluctuation[11].

*Corresponding Author Email :pl.bhagavatula@ncl.res.in

Earlier studies have demonstrated that an electron donor or acceptor molecule can modulate the position and intensity of the LSPR[12,13]. Therefore, in this work we wanted to see when such a plasmonic semiconductor nanoparticle comes in proximity to a plasmonic metal nanoparticle by simple solution phase mixing, whether the photoexcitation could modulate their respective LSPR properties. Such kind of study can leverage the basic understanding of the underlying photophysical processes for next-generation plasmonic applications. Addressing this, we have separately prepared monodisperse dodecylamine coated gold nanoparticles by digestive ripening process[14] and oleylamine coated $Cu_{2-x}S$ nanoparticles by a hot-injection method.[15] Subsequently, the organic dispersion of metal nanoparticles was titrated against incremental addition of semiconductor nanoparticles dispersion in the same solvent and monitored the change in their absorption spectra in the entire UV-VIS-NIR region. The mixture was also analyzed by XPS spectra to see whether the modifications seen in the LSPR spectra are also reflected in the changes in binding energies or not.

EXPERIMENTAL SECTION

Materials

Gold chloride ($AuCl_3$, 99%), didodecyldimethylammonium bromide (DDAB, 98%), 1-dodecylamine (DDT, 99%), sodium borohydride ($NaBH_4$), oleylamine (99%), carbon disulphide (CS_2), 1-octadecene (ODE), cadmium acetate ($Cd(CH_3COO)_2$), sodium diethyldithiocarbamate trihydrate ($(C_2H5)_2NCS_2Na{\cdot}3H_2O$), silver nitrate ($AgNO_3$), copper iodide (CuI), were procured from Sigma-Aldrich. Methanol, acetone, and toluene were procured from Thomas Bakar, India. All reagents were used without further purification. Extra pure Mili-Q water was used in all aqueous preparation.

Preparation of DDA capped gold nanoparticles

45 mg of $AuCl_3$ (0.14 mmol), 150 mg of DDAB (0.32 mmol), 15 µL of toluene was loaded in an RB flask. 170 mg of $NaBH_4$ was dissolved in 500 µL milli-Q water. This was followed by the addition of 126 µL of $NaBH_4$ solution to the Au-toluene solution. The stirring was continued for 1 h at room temperature. 5 µL of the as-prepared solution, 360 µL of DDA were loaded in a 50 µL RB and stirred for 15 minutes. This was followed by the addition of 18 µL of ethanol to the reaction mixture and keeping it aside/idle for 2 h. After the supernatant was decanted and the precipitate was dried under N_2 gas. This precipitate was re-dispersed in 5 µL toluene, and an excess amount of DDA (360 µL) was added to this dispersion. After that, it was refluxed under N_2 atmosphere for 1 h at 110°C.

Preparation of OlAm/OlAc capped nonstoichiometric copper sulphide nanoparticle

0.38 g copper iodide (CuI) (2 mmol), 1.5 mL of oleic acid and 6 mL of 1-octadecene (ODE) was loaded in a three-necked 100 mL RB and heated to 110°C for 1-2 h under vacuum to obtain a clear or pale orange colour solution. The temperature was adjusted to the desired injection temperature (140 -180°C) followed by a fast injection of the sulphur solution (32 mg of elemental sulphur + 3 mL of oleylamine + 10 mL of ODE) at 180°C. Immediately after injection, the heating mantle was removed, and the solution cooled naturally after the injection till room temperature. When the reaction solution cooled to room temperature (~30°C), the NCs were purified twice using methanol, centrifuged at 5000 rpm for 3 min and re-dispersed in toluene.

Sample preparation for UV-VIS-NIR absorption analysis

For absorbance study, the as prepared gold solution was diluted 40 times and the as prepared copper sulphide solution was diluted 100 times, with toluene. All the absorption spectra were recorded in the UV-VIS-NIR region with a Cary 300 Conc UV-Visible spectrophotometer. For solution phase interaction study between two different nanoparticles, we start measuring the absorbance of pure gold solution and on to that we add calculated volume

of copper sulphide solution in a sequential manner, and measured the change in the absorption spectra after each addition. The final binary nanoparticle dispersion sample was isolated and used for TEM and XPS studies.

Sample preparation for transmission electron microscopy (TEM) analysis

For TEM analyses, we used the diluted gold nanoparticle dispersion (40 times to the stock solution) and the diluted copper sulphide dispersion (100 times to the stock solution), similar to the procedure used for the absorption study. The binary nanoparticle mixture was collected from the cuvette after performing the absorption measurements. TEM analyses were performed using Tecnai-G220S-Twin instrument with an acceleration voltage of 200 kV. 5 μL of each nanofluid droplet is cast on a TEM grid at ambient conditions. The droplet readily evaporates in a constant area mode within couple of minutes. Subsequent to this, a thin film of solvent remains (resembling a completely wetting surface) which then dried overnight at the same ambient condition.

Sample preparation for X-ray photoelectron spectroscopy (XPS) analysis:

In this case, we drop-cast the same solutions used for the absorption studies (diluted gold and copper sulphide dispersion and their mixture), on a properly cleaned silicon wafer and dried at RT before placed it for XPS measurement on an M/s Thermo Fisher Scientific Instruments (UK) model K α+ instrument.

RESULTS AND DISCUSSION

Absorption spectroscopy analysis

Figure 1a) shows the absorption spectra for DDA capped gold nanoparticles and OlAm/OlAc capped copper sulphide nanoparticles, where the typical metal LSPR peaks at 526 nm and semiconductor LSPR peak at 1160 nm, respectively could be clearly seen. The onset of absorption band around 680 nm for copper sulphide nanoparticles corresponds to the bandgap transition (Eg = 1.82 eV). Powder x-ray diffraction (PXRD) measurement indicates the composition of the semiconductor nanocrystals to be cubic-phase digenite $Cu_{7.2}S_4$ (JCPDS no.: 72-1966) (see inset of figure 1a)). The bulk band-gap of $Cu_{2-x}S$ system is calculated to be around ~1.2-1.5 eV, depending on stoichiometry[10]. The broad absorption band in the NIR region with a maximum around 1160 nm arises from the LSPR in copper-deficient $Cu_{2-x}S$ nanoparticles[10]. The position of this peak is highly sensitive to the concentration of copper vacancy in the material.

To investigate the nature of the interaction between the two types of nanoparticles, we performed an experiment where the metal nanoparticles dispersion was titrated with the dispersion of semiconductor nanoparticles and systematically measured the change in their absorption spectra. Figure 1b) shows the variation in the absorption characteristics of the two systems in thermal equilibrium. A number of interesting features emerged from this result. 1) The semiconductor LSPR peak appeared considerably blue shifted (around 1060 nm) at the very first dose of addition in the metallic dispersion, compared to the pure solvent. This can be explained by the change in the local refractive index of the medium at the vicinity of the semiconductor nanoparticles due to the additional presence of gold nanoparticles. The LSPR band in this heavily doped semiconductor system is more sensitive towards the perturbation in the local environment than the metallic counterpart. 2) With increasing semiconductor nanoparticle concentration, the intensity of the characteristic LSPR band gradually increases while the position is red-shifted from 1060 nm to 1100 nm. This implies the decrease in free carrier density in the semiconductor nanoparticle, in the close vicinity of gold nanoparticles, as the change in refractive index in the new solution is expected to be very small. 3) There is a decrease in gold LSPR intensity with no change in absorption maxima. The decrease in intensity of gold LSPR is more than what is expected from a simple dilution indicating that the surface plasmons of gold nanoparticles are indeed coupled with those of copper sulphide system. The absence

of any shift in gold nanoparticle LSPR position could be attributed to the fact that these metal nanoparticles have high free carrier density than semiconductor, therefore the position of its LSPR maxima is less sensitive to its carrier concentration. Nevertheless, the decrease in the gold LSPR intensity and the concomitant redshift in copper sulphide LSPR maxima, upon each incremental addition of the latter to the former, clearly support the contention that there is some kind of interaction between the plasmonic levels between these two types of nanoparticles through which the two systems attain a Fermi charge equilibrium state, as characterize by an isosbestic point in between the two peaks.

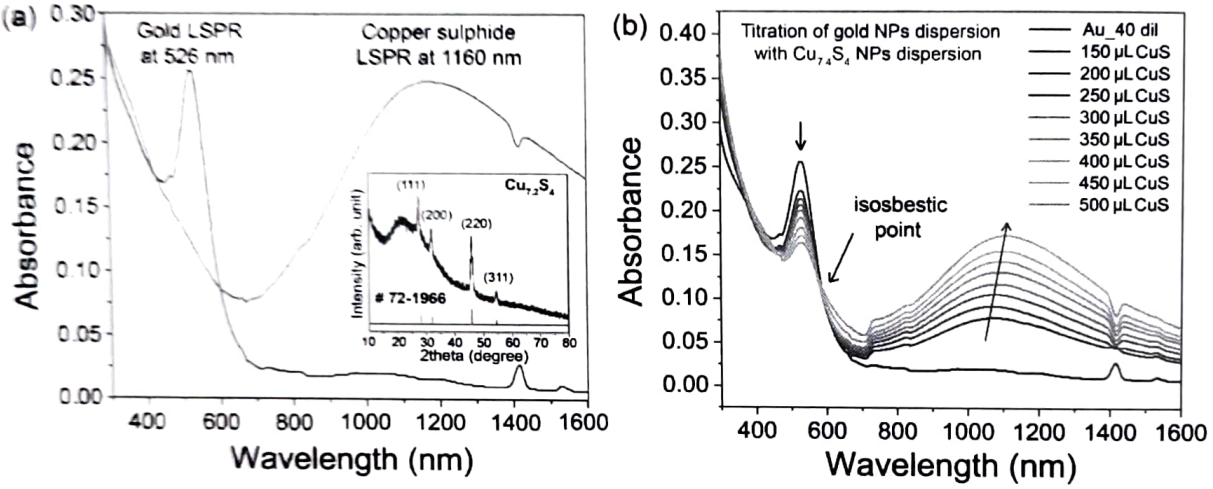

Fig. 1: a) Comparison of the absorption spectrum of DDA coated gold nanoparticles and OlAm/OlAc coated copper sulphide nanoparticles. PXRD pattern of the as synthesized copper sulphide nanoparticle is shown in the inset. b) Change in absorption spectra upon sequential addition (150 µL at first then 50 µL each time) of copper sulphide nanoparticle dispersion to gold nanoparticle dispersion.

TEM analysis

Figure 2 shows the bright field TEM analyses of the as-synthesized nanoparticles as well as their mixture. The grayscale images were further processed using an automated image processing tool, namely, Materials Image Processing and Automated Reconstruction (MIPAR) which could be customized as desired.[16] A series of image processing steps, collectively known as the recipe, have been utilized to identify and extract valuable information about our features of interest from the respective images. The average size for the DDA capper gold nanoparticles was calculated to be around 8(±3) nm, while that is for OlAm/OlAc coated copper sulphide nanoparticles is found to be little higher, around 13(±4) nm. It can also be noted that the particles are essentially round in shape. Any two particles are always separated by a layer of organic ligands, though remain invisible under TEM, attached to their respective surfaces and therefore, they are not truly in contact with each other. In mixture, the two types of nanoparticles (metal and semiconductor) appear differently in contrast under TEM due to the difference in their electron densities.

A gray level histogram of the image (as shown in the inset) help us to understand the intensity distribution of the pixels in the image, which was subsequently utilize to cluster each pixel to one of the specified classes (we specified to three, for metal, semiconductor, and background), using k-means clustering. This is a powerful way of segmenting an image and isolate the features into separate layers[17]. We noted that the gold nanoparticles lay on top of the copper sulphide nanoparticles. After clustering, it becomes easier to calculate individual feature properties (such as area fraction and perimeter fraction, which was difficult to calculate from the original grayscale image) from each layer (corresponding to each type of nanoparticle system), and the results are listed in the figure (Figure 2, bottom right corner image).

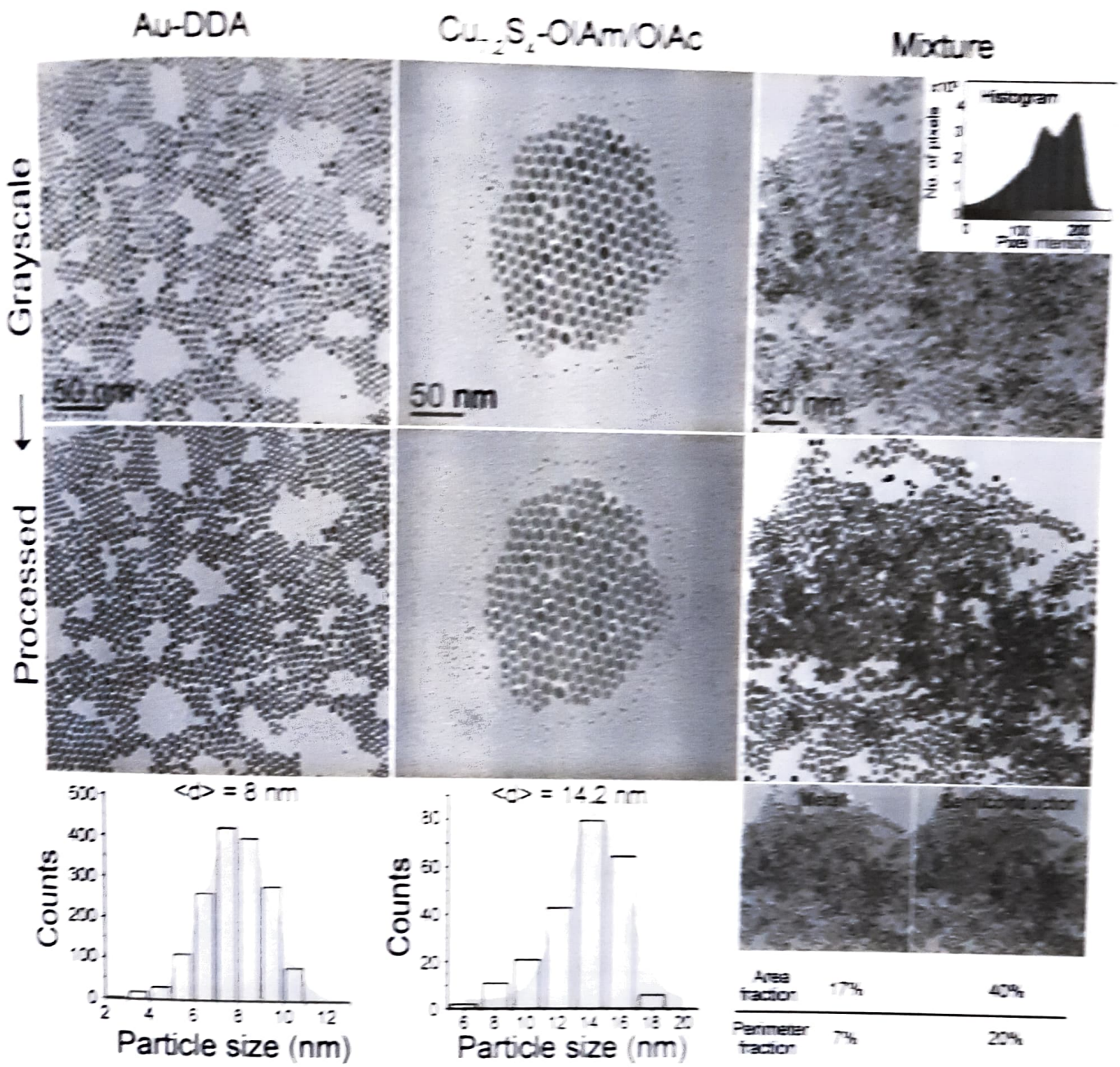

Fig. 2: ***TEM image analyses of DDA coated gold nanoparticles, OLAm/OLAc coated copper sulphide nanoparticles, and their mixture. Each grayscale image was processed by creating a customized recipe using the software MIPAR. A histogram shown in the inset of the grayscale image of the mixture was used to segment the two different constituents in the image. Feature measurements (such as particle size, area fraction, and perimeter fraction) were performed for each of the image and the results are shown at the bottom.***

XPS analysis

The intimate contact between the metal and semiconductor at the particle surface in the mixed nanoparticle solution was established further by XPS analyses. Figure 3a) and b) show the high-resolution scan for the Au 4f and Cu 2p core orbitals, respectively, before and after the mixing. In the Au 4f region, we have observed two major peaks at 84.2 eV and 87.8 eV (with an energy gap of ~3.6 eV) arising due to the spin-orbit coupling corresponding to Au $4f_{7/2}$ and Au $4f_{5/2}$ respectively. Interestingly, a small shift in the peak position Au $4f_{7/2}$ by 0.3 eV and Au $4f_{5/2}$ by 0.4 eV towards the higher binding energy were observed in the mixture.

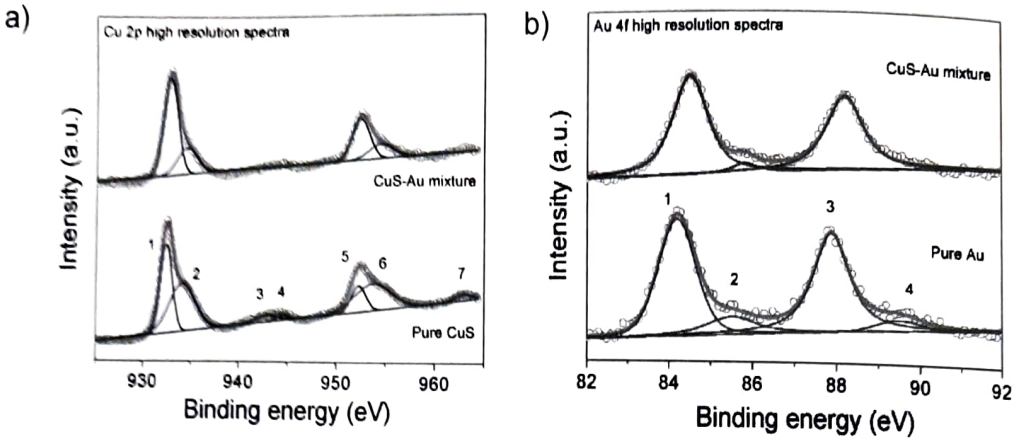

Fig. 3: High resolution XPS scan of a) Au 4f orbital and b) Cu 2p orbital, for individual nanoparticles in comparison with their mixture (for assignment of peaks denoted by different numbers please refer to Table 1).

Table 1: List of deconvoluted peaks for Cu-2p and Au-4f orbitals, before and after mixing.

System	Before mixing		After mixing	
	Binding energy	Orbital (valency)	Binding energy	Orbital (valency)
$Cu_{2-x}S_4$-OlAm/OlAc	932	Cu^{+} ($2p_{3/2}$)	932	Cu^{+} ($2p_{3/2}$)
	934	Cu^{2+} ($2p_{3/2}$)	934	Cu^{2+} ($2p_{3/2}$)
	942	Cu^{2+} ($2p_{3/2}$)	--	
	944	Cu^{2+} ($2p_{3/2}$)	--	
	952	Cu^{+} ($2p_{1/2}$)	952	Cu^{+} ($2p_{1/2}$)
	953	Cu^{2+} ($2p_{1/2}$)	954	Cu^{2+} ($2p_{1/2}$)
	963	Cu^{2+} ($2p_{1/2}$)	--	
Au-DDA	84.2	Au ($4f_{7/2}$)	84.5	Au ($4f_{7/2}$)
	85.5		85.9	
	87.8	Au ($4f_{5/2}$)	88.2	Au ($4f_{5/2}$)
	89.7		--	

This shift indicates some transfer of the electron density from the gold core. On the other hand, the Cu 2p orbitals also showed some significant difference before and after mixing. Upon deconvolution the spectrum of pure copper sulphide sample we found seven peaks for Cu^{+} and Cu^{2+}. Whereas, few of them were found to be significantly suppressed upon mixing with gold nanoparticles, and the details are listed in Table 1 and 2. A significant increase in Cu^{+} concentration was observed upon mixing, which could be due to the transfer of electron density from gold nanoparticle to nearby copper sulphide nanoparticles, leading to a decrease in free hole concentration. Since the valence band maxima of $Cu_{2-x}S$ is at a relatively lower energy than the Fermi level energy of gold nanoparticle (relative to NHE), electron transfer could be expected to take place from metal to semiconductor.[18] Thus, the XPS results nicely corroborate with the absorption study.

CONCLUSION

In conclusion, we have successfully synthesized NCs of metallic and semiconducting systems using different solution chemistry routes. The morphology and phase of the as-prepared NCs were characterized using TEM and PXRD respectively. Based on the UV-Vis-NIR study, we conclude that there is some interaction occurring between the metallic (Au) and semiconductor ($Cu_{7.2}S_4$) plasmonic levels upon simple solution-phase mixing. This finding was further corroborated by XPS measurements which suggests the shifting of electron density occur from metal to semiconductor owing to coupling between the two energy levels.

ACKNOWLEDGMENTS

B. Saha wants to thank IISER Pune for financial support, and would also like to thank Mr. Jayesh Shimpi, Mr. Abhijit Bera, Dr. Vijay Chaudhari, andMr. D. Mandal for their constant support and guidance. K. Bhattacharjee want to thank the 'Council for Scientific and Industrial Research, India', for financial support during his research associateship (31/11 (1094)/2019-EMR-I). The authors are grateful to the whole members of Central Instrumental Facility, National Chemical Laboratory, India, for their continuous instrumental support. The authors declare no competing financial interest.

REFERENCES

[1] M. T. Sheldon, P. E. Trudeau, L. W. Wang, A. P. Alivisatos: Enhanced semiconductor nanocrystal conductance via solution grown contacts. Nano Lett 9: 3676–3682, 2009.

[2] P. V. Kamat: Quantum Dot Solar Cells. Semiconductor nanocrystals as light harvesters. J Phys Chem C 112: 18737–18753, 2008.

[3] R. Costi, A. E. Saunders, U. Banin: Colloidal hybrid nanostructures: A new type of functional materials. Angew Chem Int Ed 49: 4878–4897, 2010.

[4] V. Subramanian, E. E. Wolf, P. V. Kamat: Catalysis with TiO_2/gold nanocomposites. effect of metal particle size on the fermi level equilibration. J Am Chem Soc 126:4943–4950, 2004.

[5] Y. Shemesh, J.E. Macdonald, G. Menagen, U. Banin: Synthesis and photocatalytic properties of a family of CdS-PdX hybrid nanoparticles. Ang Chem Int Ed 50: 1185–1189, 2011.

[6] M. Ibanez, Z. Luo, A. Genc¸, L. Piveteau, S. Ortega, D. Cadavid, O. Dobrozhan, Y. Liu, M. Nachtegaal, M. Zebarjadi, J. Arbiol, M. V. Kovalenko, A. Cabot: High-performance thermoelectric nanocomposites from nanocrystal building blocks. Nat Commun 7: 10766, 2016.

[7] S. Ortega, M. Ibanez, Y. Liu, Y. Zhang, M. V. Kovalenko, D. Cadavid, A. Cabot: Bottom-up engineering of thermoelectric nanomaterials and devices from solution processed nanoparticle building blocks. Chem. Soc. Rev., 46: 3510-3528, 2017.

[8] E. Shaviv, O. Schubert, M. Alves-Santos, G. Goldoni, R. Di-Felice, F. Vallee, N. D. Fatti, U. Banin, C. Sonnichesen: Absorption properties of metal-semiconductor hybrid nanoparticles. ACS Nano, 5: 4712-4719, 2011.

[9] Y. Liu, M. Liu, and M.T. Swihart: Plasmonic copper sulfide-based materials - A brief introduction to their synthesis, doping, alloying, and applications. J Phys Chem C 121: 13435−13447, 2017.

[10] J.M. Luther, P.K. Jain, T. Ewers, and A.P. Alivisatos: Localized surface plasmon resonances arising from free carriers in doped quantum dots. Nature Material 10: 361−366, 2011.

[11] R. Alam, M. Labine, C.J. Karwacki, and P. V. Kamat: Modulation of $Cu_{2-x}S$ nanocrystal plasmon resonance through reversible photoinduced electron transfer. ACS Nano 10: 2880−2886, 2016.

[12] A.M. Schimpf, K.E. Knowles, G.M. Carroll, D.R. Gamelin: Electronic doping and redox-potential tuning in colloidal semiconductor nanocrystals. Acc Chem Res 48: 1929−1937, 2015.

[13] O.K. Jain, K. Manthiram, J.H. Engel, S.L. White, J. A. Faucheaux, A. P. Alivisators: Doped nanocrystals as plasmonic probes of redox chemistry. Angew Chem Int Ed 52: 13671−13675, 2013.

[14] J. R. Shimpi, D. S. Sidhaye, B. L.V. Prasad: Digestive ripening: a fine chemical machining process on the nanoscale. Langmuir 33:9491, 2007.

[15] A. Bera, B. Busupalli, B.L.V. Prasad: Solvent-less solid-state synthesis of dispersible metal and semiconducting metal sulfide nanocrystals, ACS Sustain Chem Eng., 6: 12006−12016, 2018.

[16] J. M. Sosa, D.E. Huber, B. Welk, H.L. Fraser: Development and application of MIPAR™: a novel software package for two- and three-dimensional microstructural characterization. Integr Mater Manuf Innov 3:1, 2014.

[17] A. David, S. Vassilvitskii: K-means++: The advantages of careful seeding. SODA '07: Proceedings of the Eighteenth Annual ACM-SIAM Symposium on Discrete Algorithms. 1027–1035,2007.

[18] P.V. Kamat, B. Shanghavi: Interparticle electron transfer in metal/semiconductor composites. Picosecond dynamics of CdS-capped gold nanoclusters J Phys Chem B 101: 7675–7679, 1997.

Journal of Metallurgy and Materials Science, Vol. 62, No. 3-4, July-December 2020, pp. 135-146
Printed in India, © NML, ISSN 0972-4257

Prospective of titania based photocatalyst for environmental reduction reactions

TRILOCHAN MISHRA*
Functional Material Group, AMP Division, CSIR-National Metallurgical Laboratory, Jamshedpur-831007, India

Abstract : In the last two decade photocatalysis is widely studied so as to evolve a green chemical rout to deal with the environmental and energy problem faced by the mankind. Among all the studied photocatalysts anatase TiO_2 is most attractive even today though limited to UV light absorption in pure form. However, easy availability, high aqueous stability and nontoxic nature attracted the researchers to go for different possible modifications. Effort has been made by number of researcher to modify titania through metal, nonmetal doping and mixing with other oxides and sulphides to engineer the band gap, band potential and delay the charge separation through Z-scheme and hetero-junction formation so as to achieve the goal of producing stable and highly active photocatalyst for energy and environmental application. In recent past, various strategies have been tried to extend the solar light absorption from visible to NIR range by using appropriate material so as to ultimately promote the solar photocatalytic performance of TiO_2 based composites. Keeping these in view, present review will discuss the past and present development in the area of material modification to deal with band gap engineering, heterojunction formation, required porosity, powder catalyst separation and better charge separation with special objective of improved environmental reduction reactions. In addition future prospect of these materials has been discussed in details for new generation researchers. In particular material based on MOFs, two dimensional materials and metal halide *perovskites* based titania composites are emphasized for future evaluation to address both air and water pollution.

Key wards: *Titania, doped oxide, heterojunction, band potential, Z-scheme, photocatalyst, environmental, reduction reaction.*

INTRODUCTION

Report on photo-induced water splitting by Fujishima and Honda on titania in presence of UV light [1] opened the area of photocatalysis for future environmental and energy application. Till date though a lots of semiconductrs are available but TiO_2 is considered as the most promising photocatalyst for large scale application due to its appropriate electronic band potential, better chemical inertness, high photo-stability and easy market availability [2]. In general TiO_2 acts as an n-type semiconductor because of the presence of oxygen vacancies. For the photocatalytic reaction semiconductor is required with proper band gap and band potential for appropriate light absorption. In TiO_2 valency band and conduction band are constituted by the overlapping of the O 2p and Ti 3d orbitals, respectively. In general titania found in the form of anatase, brookite and rutile[3-4] having distorted octahedral structure (TiO_6) with different symmetries [5]. The band gap of pure rutile, anatase and brookite are 3.0, 3.2 and 3.3 eV, respectively. Though brookite is reported to be a better photocatalyst than anatase but the stability is questionable [6]. However anatase form is well studied as photocatalyst because of easy of synthesis, better thermal stability at least up to 500°C and photocatalytically active than other polymorphs [7]. Due to the revival of more interest on the TiO_2 photocatalyst Fujishima again reviewed [8] the subject in 2012 with new prospective for future application highlighting the importance of different forms including 0D, 1D and 2D titania.

To make TiO_2 photocatalyst more attractive for larger application number of researchers extensively investigated surface characteristics by various techniques in the last few years so as to provide important insights to the TiO_2 photocatalyst in molecular level [9]. All these discussion in recent years revives the importance of the traditional material. As per the basic principle a semiconductor produces electron and hole in presence of light which can facilitates both oxidation and reduction reaction to address both air and water pollution as schematically presented in Fig-1.

* Corresponding Author Email :tmishra@nmlindia.org

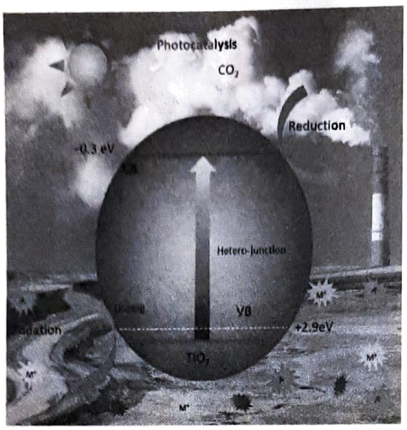

Fig-1: Schematic presentation of TiO_2 based photocatalyst for environmental remediation.

TiO_2 with conduction band (CB) potential level of -0.3 eV is more negative and hence suitable for the redox reaction H^+/H_2 (0 eV). On the other hand valency band (VB) potential of +2.9eV which is more positive with respect to O_2/H_2O (1.23 eV) standard redox potential, makes it suitable for oxidation reactions. Due to its favourable CB and VB potential level TiO_2 is capable of splitting water, oxidation of organics and converting CO_2 to fuel[10]. However it suffers with the main disadvantage of absorbing in UV light region thus making it inactive for much desired solar photocatalysis. Moreover, TiO_2 suffers with the large band gap (3.2 eV) with limited utilization of solar light (2%) and fast recombination of photoinduced charges which significantly limits the practical applications. In addition, phase change of anatase to rutile at moderate temperature (500–600°C) resulting in the drastic decrease in photocatalytic activities limits the large scale application of pure anatase as photocatalyst [11]. Therefore anatase based mixed oxides and hetero-junctions were explored by number of researchers to extend the thermal stability and visible light absorption[12]. In this context size and shape of the nanoparticles also plays an important role in modifying the electronic properties of different semiconductor oxides [13]. This recent review highlights the importance of pure oxide semiconductors, solid solution, heterostructures including Z-scheme catalyst fabrication for prospective photocatalytic applications. However, if one will look at the solar light, it is clear that around 46% is contributed by NIR region and hence for proper utilization of solar radiation we requires materials to absorb in the broad spectrum of visible to NIR so as to improve the efficiency. In this regard important strategies (Fig 2) include metal/ nonmetal doping, noble metal deposition, structural modification, heterostructure/ heterojunction formation with other semiconductor oxides and sulphides and dye sensitization with a primary objective of increasing the practical efficiency under solar light through better light absorption and charge separation. Here we will concentrate on the applicability of different modified catalysts for environmental reduction reactions so as to deal with the different waste water containing toxic metal ions and other anions.

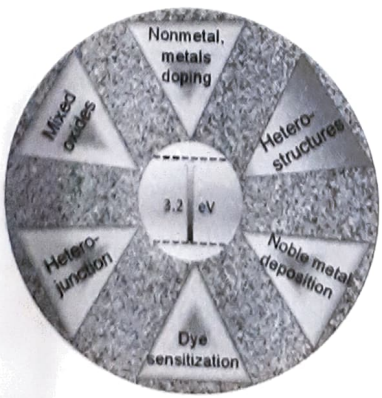

Fig 2: Important strategies to improve photocatalytic activity of titania based photocatalyst.

MODIFICATION OF TiO_2

TiO_2 based mixed oxides

Initially titania based mixed oxides are well studied with a objective of anatase phase stabilization and visible light absorption so as to project titania as a potential solar photocatalysts. Recently a number of critical reviews are published [11, 12] with different objectives and applications. Subsequently new innovative approaches are explored to improve the solar light absorption, charge separation and photo-stability of several composites, core shell structures involving Z-scheme and heterojunctions. In our lab we have demonstrated different titania based mixed oxides with attractive shape and surface morphology (Fig 3) for enhanced photo-induced catalytic activity under visible light. Shape and surface morphology control the much required porosity as demonstrated in spherical to nodular shaped materials. Titania and silica mixed oxide has attracted the researchers due to the extensive application as both catalyst support and active catalyst [14-15]. Due to the similar oxidation state (+4) of both Ti and Si with similar oxidation state are compactable to each other in the lattice and can easily interlink through oxygen bridge [16]. Silica lattice at the interface confined the TiO_2 species in nanoscale preventing from further growth. In addition, Si^{4+} with smaller ionic radius (0.042 nm) can easily enter into the lattice of TiO_2 and substitute the Ti^{4+}. Possibly this is one of the cause of high thermal stability of anatase phase in SiO_2 mixed titania[17]. Moreover, formation of Ti–O–Si hetero bridges gives rise to the Brønsted acidity as silica tetrahedra is chemically coordinated with the titania octahedral. Ultimately, this also contributes towards enhanced photocatalytic activity of silica-titania mixed oxides.

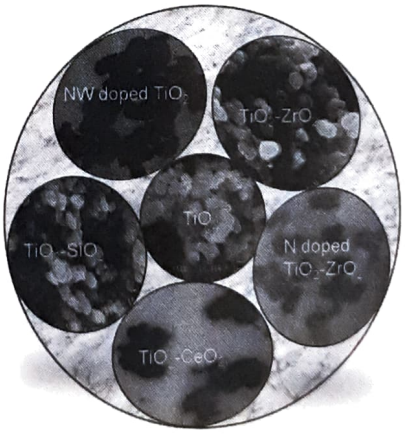

Fig-3: Different mixed oxides of titania as photocatalysts. Some of the figures are reproduced from ref (18, 47 & 53) with copyright permission.

For photocatalytic activity crystallinity of particular titania phase is a critical factor. In general addition of silica to titania enhances anatase phase stability at higher temperature by suppressing phase transformation to rutile and thereby maintains the high surface area and surface acidity. Addition of 10-20 wt% silica resulted in the stabilization of anatase phase [18] up to 900°C with high surface area. Interestingly the spherical shape of the titania and the mixed oxides are retained in a controlled sol-gel synthesis. Surprisingly presence of silica mostly facilitates the formation of Ti-O-Si bonds thus stabilizing the anatase phase and porous structures [19] even at high temperature. On the other hand pure titania easily transforms to nonporous rutile phase even at 600°C calcination thereby decreasing the photocatalytic activity. Similarly, in the periodic table zirconium and titanium belong to the IVB group of elements. Moreover, both TiO_2 and ZrO_2 come under n-type semiconductors having band gap of 3.2eV and 5.0eV respectively and exhibit close physicochemical properties. Wide band gap ZrO_2 with sufficient conduction band and valence band potential of -1.0 V and 4.0 V vs NHE, respectively emerges as a promising photocatalyst particularly for the pollutants degradation. Therefore ZrO_2 works better in a composite system where photoinduced electron can transfer from other semiconductor to facilitates the required reactions. Due to

this importance TiO_2-ZrO_2 materials are synthesized by several methods which include sol-gel [18, 20-21] and co-precipitation [22-23]. In sol-gel processes, typical problem arises due to the different hydrolysis and condensation rates of Zr and Ti alkoxides which gives rise to separate domain formation. In co-precipitation technique homogeneous colloids are formed where zirconia is mostly segregated within the titania matrix. On the other hand, ZrO_2 is distributed on the titania surface in case of heterogeneous colloids formation [24, 25]. Recently effect of other semiconductors oxides with TiO_2 for solar photocatalysis has been reviewed in details [19]. Mostly interfaces of other oxides like WO_3, Cu_2O, CeO_2 or Fe_2O_3 with anatase controls the electronic properties and hence influence the photocatalytic properties. Therefore it is essential to understand the change in electronic properties of a mixed oxides system.

Among all the mixed oxides TiO_2-WO_3 [26] and TiO_2-CeO_2 [27] system is well studied due to some inherent interesting properties of WO_3 and CeO_2. In particular these oxides when combined with titania exhibit improved photocatalytic properties under solar light. It is observed that nanosized WO_3 crystallizes in the form of orthorhombic or monoclinic phases with TiO_2. Presence of different oxidation states, oxygen vacancies and different surface phases on TiO_2 creates the variable surface properties [26]. Moreover monoclinic phase of WO_3 exhibits band gap of 2.7-2.8eV which is ideal for solar light absorption and hence can be used as solar photocatalyst [28]. In addition defect chemistry of WO_3 and CeO_2 [11] make these materials more interesting. Mixed oxides systems are explored with a objective of better photocatalytic activity because of fast charge recombination on pure WO_3 and CeO_2. Recently WO_3 based photocatalysts are reviewed [29] particularly in relation to doping and composites formation for various solar photocatalytic application. In case of TiO_2-WO_3 system surface acidity and size in nanoscale plays a decisive role for enhanced sunlight absorption and photocatalytic activity. In addition, Schumuki group reported on unidirectional Ti-W oxide nanotubes grown on TiW alloy through controlled anodization process[30]. Ti-W mixed oxide nanotubes with as low as 0.2wt% WO_3 showed improved ion insertion and photocatalytic activity in comparison to the pure TiO_2 nanotubes. Similarly doping of lanthanides can significantly enhance the photocatalytic activity of TiO_2 [31-32]. In a reported result high photocatalytic activity is noticed for 5wt% cerium oxide mixed titania material calcined at 600°C towards selenium reduction. Photocatalytic activity is found to be mainly dependant on the variable oxidation states like Ce^{4+}/ Ce^{3+} rather than only visible light absorption. Moreover, an important role is also played by oxygen vacancy created by the presence of mixed oxidation states [27]. Among the lanthanides ceria and lanthanum oxide mixed titania is well studied due to some interesting properties like variable oxidation states and easy formation of labile oxygen vacancy. Interestingly, pure ceria nanomaterial also acts as good photocatalyst [33]. In addition $SrTiO_3$ with band gap of 3.4 eV is also studied as photocatalyst in combination with TiO_2 [34-35] having improved photocatalytic activity due to better charge separation in $SrTiO_3$-TiO_2 heterojunction. Similarly, photocatalytic activities of TiO_2 [36-37] can be substantially improved due to the coupling of SnO_2 through better charge separation. On the other hand hematite having narrow band gap (~2.1 eV) has attracted the attention of researchers due to its advantages of natural abundance, low-cost, high stability towards visible light active photocatalytic and photo-electrochemical (PEC) [38, 39] applications. Coupling of Fe_2O_3 to TiO_2 has been studied by number of researchers for different applications. Branch shaped Fe_2O_3-TiO_2 nanocomposites synthesized by a combination of electrospinning and hydrothermal techniques were reported recently [40]. Even Bi_2O_3 with titania [41] can improve the photocatalytic activity under visible light with improved H_2 evolution efficiency. Therefore scope of designing an inovative mixed oxides with controlled heterostructure and porosity is enormous at present in exploration of new photocatalyst.

Doping with metals and nonmetals

Since the report of Ashi et al [42] several researcher investigated the doping of nonmetals like S, C, N and B so as to extend the light absorption by titania to visible region. Due to close atomic diameter these elements can easily substitute the O atoms of titania lattice. Typically, these types of doping results in decreased band gap and

changed electronic properties due to the contribution of p-orbitals [43-44]. In some cases surface doping takes place resulting in the surface functionalisation thereby altering the photocatalytic properties. Sometimes it is difficult to distinguish the surface and lattice doping of the materials. XPS is the most important tool used to identify the types of nonmetal doping in oxide semiconductors. Typically C1s, N1s spectra [45-46] is used to see the type of doping. Recently O1s spectra also showed the indication of doping and oxygen vacancy resulted from doping and partial Ti^{4+} reduction [47].

In this effort new strategies like plasmonic metals (Au, Ag etc) deposition on TiO_2 [48, 49], dye sensitisation and combination of low band gap semiconductor with TiO_2 making a heterojunction are extensively tried in last few years [50]. Recently graphitic carbon doping of semiconductor oxides are reported with tuneable band gape using coordination polymers. Amount of graphitic carbon in the interface of the oxide controls the band gap [51]. Titania based nanotubes synthesized by anodisation process is an interesting 1D material as presented in Fig 4. Obtained tubes are uniform in size and the length can be controlled with anodisation time and choice of electrolyte. Transition metal doped TiO_2 nanotubes also attracted the attention of researchers with increased photo-current and photocatalytic activity [52]. In situ chromium doping through anodisation of Ti-Cr alloy increases the crystalinity and electronic conductivity of the oxide tubes. Non-metal (N) doping on TiO_2-ZrO_2 mixed oxide improved the photocatalytic activity due to the creation of oxygen vacancy [47]. Formation of Ti^{3+} and oxygen vacancy with increased porosity is possible when reducing agents like hydrazine is used as nitrogen source. Similarly N and W doped titania is reported to be highly active for photocatalytic nitrate reduction reaction under visible light [53]. This indicates the beneficial effect of simultaneous doping of metal and nonmetal for different applications.

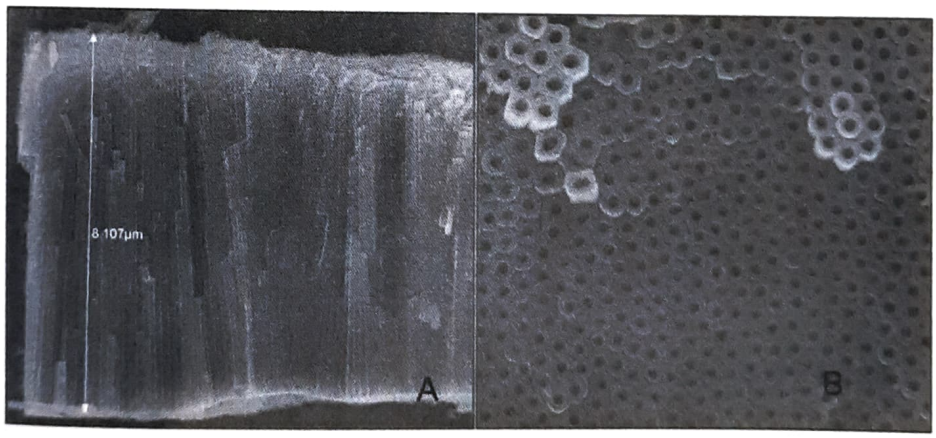

Fig 4: Anodized titania nanotubes (A) side view and (B) top view

Different hetero-junctions

In the recent years a lot of hetrojunction based photocatalysts are studied based on Z-scheme [54] and P-N junctions so as to improve the solar photocatalytic activity. Titania based heterojunction with more positive valence band and conduction band potential than TiO_2 exhibit better charge separation and photocatalytic activity [55]. Typically low band gap semiconductors like Fe_2O_3, WO_3, Ag_3PO_4, $BiVO_4$ and Bi_2WO_6, have been used by number of researchers to create a better heterojunction system for different photocatalytic applications [55-57]. However, most of these efforts are targeted for increased visible light absorption only. On the other hand copper hydroxy phosphate $Cu_2(OH)PO_4$ with libethenite structure is reported to extend the solar light absorption up to NIR range [58] thus increasing the photocatalytic activity. $Cu_2(OH)PO_4$ acts as an n-type semiconductor as reported from photo-eletrochemical study with optical band gap in the range of 3.4 to 1.52 eV [59]. Heterojunction based on TiO_2-$Cu_2(OH)PO_4$ reports the efficient photoreduction of Cr(VI) under solar light through better charge separation [60]. CdS with narrow band gap (2.4 eV) and sufficient negative conduction band potential become a well studied

solar photocatalyst for practical applications in the field of water splitting and CO_2 reduction. However, the poor aqueous stability and high charge recombination rates are the main bottle neck for photocatalytic solar water splitting application [61]. In a recent report [62] one dimensional CdS-TiO_2 having core shell structure synthesized via solvo-thermal method showed improved chromium (VI) reduction under visible light. Therefore, hetreojunction formation with other stable semiconductors is well studied with increased stability [63-65]. In particular heterojunction with metal chalcogenides and 2D C_3N_4 [64] are well reported in recent times due to their improved performance under solar light for variety of phtocatalytic reactions. Efficiency of a catalyst also depends on the shape and size of the material and the type of heterojunction formation which is well controlled by different synthetic techniques.

Environmental reduction reactions

Initially the photocatalysis process is mostly investigated for organic dye decomposition resulting in colour removal, purification and decontamination of indoor air, decontamination of soil and destruction of other hazardous organics such as through oxidation process. In this context photodecomposition of chlorinated organic like chlorophenol, tricloroethylene in contaminated water has been investigated at different pH by several researchers using titania based materials like TiO_2 [66], SiO_2-TiO_2 [67], ZrO_2-TiO_2 [68] and CdS-TiO_2 [69] with increased efficiency. Subsequently researchers extended the applications to environmental reduction reaction.

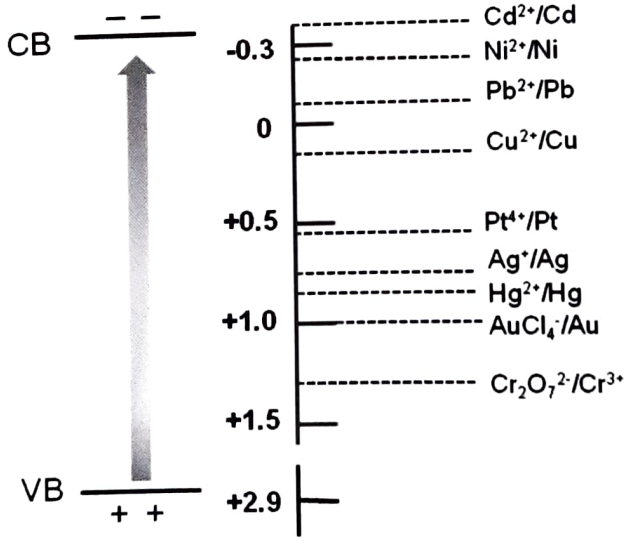

Fig 5: Positions of the redox potentials of metallic couples with respect to TiO_2 at pH = 0.

For efficient photoreduction of any metal ion to metallic form, the energy of the CB electron should be more negative than the E0 (Mn+/M couple). It is well known that these metallic couples are controlled by the pH of the solution. Thus pH is important for better reduction reaction efficiency. Reduction possibility of different cations is presented with respect to CB and VB of TiO_2 in Fig-5. It is understood that [70] metal ions having redox potential more than 0.4 V can possibly be reduced on anatase titania. Accordingly, the photo-induced reduction of dofferent inorganic cations and anions are investigated with a objective of recovery or removal application has been discussed. Even dye sensitized TiO_2 is also used for chromium ion reduction [71] under visible light. Fabrication of triphenylamine [72] and tetramethylpiperidin [73] based organic dyes with TiO_2 composites improves the photocatalytic efficiency to many fold under visible light.

Lead and cadmium are most commonly used toxic metal ions usually found in the waste and drinking water. Therefore, removal of these ions is important and mostly adsorption process is used for the same. However based on their reduction potentials (Pb: 0.126 V, Cd: -0.403 V) it is very difficult to reduce these applying

titania based photocatalyst. Efficient photoreduction of Pb(II) using Pt–TiO_2 suspensions [74] was reported. Mostly reduction process is enhanced in presence of a hole scavenger like organic molecules. Simultaneous oxidation of nitrobenzene and reduction of Pb^{2+} at pH-6 was demonstrated with the deposition of PbO_2 [75]. Whereas, cadmium reduction is only possible in presence of selective organics as hole scavengers. Importance of the hole scavenger is well noticed as presence of methanol is not capable of reducing Cd to metallic form whereas formate can do the same [76]. In one of our work importance of mixed oxides for lead and cadmium ions reduction were demonstrated using SiO_2-TiO_2 and ZrO_2-TiO_2 materials. In particular mixing of 10wt% silica and zironia with TiO_2 increases the surface area of the material which ultimately helps in increasing photoreduction activity in presence of formate under UV light [15, 18]. Similarly mercury is considered as a serious pollutant (0.005 mg/l) due to its biological or chemical non-degradability. Presence of other metal ions such as Cr(VI) [77], Fe(III) [78] etc. inhibits the photocatalytic reduction of Hg(II). In addition presence of hole scavengers increases the Hg(II) photoreduction activity. Among the hole scavengers presence of EDTA [78] enhances the photoreduction of mercury in comparison to the methanol, 4-nitrophenol, and salicylic acid.

In wastewater most common selenium species are selenate, selenite and their protonated forms. The toxicity of Se species is related to their mobile nature and oxidation states. So among the selenate and selinite Se(VI) is more stable towards reduction and more toxic than Se(IV). Efficient selenium reduction to red Se(0) on N doped TiO_2-ZrO_2 was reported under visible light [47]. Improved efficiency was credited to the synergistic effect of partial Ti^{3+} formation, oxygen vacancy and high surface area. Amal et al also reported the comparative study on the role of hole scavengers towards photo-reduction of Se ions [79]. However presence of hole scavenger is essential. Photo-reductions of different aqueous oxyanions which includes nitrate, chromate, nitrite, bromate, selenate and perchlorate in waste water is reported on TiO_2 based photocatalyst [80]. At the same time photocatalytic reduction of copper ion is only possible in presence of hole scavenger like EDTA, sodium formate, sodium oxalate or alcohols [81] and organic dyes [82]. Complete reduction of nitrate to nitrogen gas with 94.6% selectivity was reported with Wand N co-doped TiO_2 material under visible light [53]. Improved nitrate reduction with formic acid as hole scavenger is credited to the $CO_2^{\bullet-}$ free radical formation with high reduction potential. Simultaneous photocatalytic reduction of Cu(II) and Se(IV) using spherical binary oxide materials was first time reported by Aman et al [83]. Only formic acid and EDTA are found to be better hole scavengers for the reduction process among other organics. A comparative study is reported using both the hole scavengers varying reaction time, concentration, pH etc. In independent reaction formic acid is found to better hole scavenger for Se(IV) reduction while EDTA is the best for Cu(II) reduction. However, in a mixture solution both EDTA and formate performs equally in presence of visible light.

Similarly chromium (VI) is carcinogenic and a lot of catalysts are tried with improved photoreduction in UV [66, 70] as well as visible light [60, 62, 69]. In presence of hole scavenger Cr(VI) is reduced to less toxic Cr(III) which is easily removed through precipitation or adsorption. TiO_2-$Cu_2(OH)PO_4$ based hetero-junction[60] improves the photo reduction of Cr(VI) under solar light as $Cu_2(OH)PO_4$ extend the light absorption from visible to NIR range. In addition various new types of catalysts like MOFs [84] and halide pervoskite [85] based titania composites are tried for the photocatalytic reduction reactions. Possibly these materials will emerge as prospective catalyst in the future if the aqueous stability and other problems will be solved through modifications. These new catalysts are good for the CO_2 reduction reaction which is the one of the most critical environmental problem. CO_2 reduction to fuel has been well studied in recent time with a objective of improved efficiency to deal with the practical problem [69]. Among the oxyanions arsenate and arsenites are important due to their high toxicity and availability in the drinking water of eastern India. Recently total arsenic removal of 3 ppm using an innovative $BiVO_4$/TiO_2 system under LED light irradiation from aqueous solution was reported [86]. In this context titania based photocatalysis as an effective and green method is reviewed by Litter highlighting the mechanism and practical applicability [87].

Efficient arsenic reduction within two hours of reaction offers the possibility of practical application. Moreover, titania composites with two dimensional materials like metal chalcogenides [88] are important and need proper evaluation for various photocatalytic applications. In addition to catalysts materials development reactor designing is also important for practical application. Recent progress on continuous flow based slurry reactors attracted a lot of researchers towards flow reactor designing [89]. In this regard a plug flow reactor was designed where hematite nanomaterials as photocatalysts were used in the suspension [90].

FUTURE PROSPECTS

Presently, designing of modified titania based photocatalyst is mainly concentrated on doping, mixed oxides and hetero-structure formation with one dimensional, two dimensional semiconductors. Possible approaches to enhance solar photocatalytic activity and separation of photocatalysts from reaction mixture are discussed to provide a future direction in highly efficient photocatalyst design. The TiO_2 based heterostructure materials is an important and attractive subject for future development in the area of photocatalysis and photo-electrocatalysis. However, a breakthrough research is essential for material designing based on z-scheme and heterojunctions maintaining the required band potential to solve the renewable energy based environmental problems at the earliest. One need to emphasize on the stability of materials, porosity, sufficient solar light absorption and better charge separation in heterostructure designing based on binary and tertiary system. This review focused on the future scope of development and use of low-cost TiO_2 based material for different reduction reaction in particular. Photocatalytic removal of different toxic oxyanions needs more investigation with respect to efficiency and catalytic material deigning. In addition designing of continuous flow reactor is emphasized for practical application with increased photon and mass transfer. Flow type photoreactors reduces the safety hazards and simplify the process in large scale in comparison to batch reactors. As far as material is concerned MOFs and metal halides pervoskite titania composites are emerging photocatalyst which need in depth study with respect to aqueous stability and appropriate application. In addition titania and two dimensional material composites are versatile photocatalyst and need extensive research in fine tuning the heterojunction formation for improved solar photocatalysis towards toxic metal ions, oxyanions and CO_2 reduction to address both air and water pollution.

ACKNOWLEDGMENT

Author is thankful to the director of CSIR-NML for giving encouragement and permission to publish this review paper in the special edition of this journal. Author also acknowledge the contribution of past students whose work is included in this manuscript.

REFERENCES

[1] Fujishima, A. and Honda, K. Electrochemical photolysis of water at a semiconductor electrode. Nature, 238: 37-38, 1972.

[2] Kabra, K.; Chaudhary, R. and Sawhney, R.L. Treatment of hazardous organic and inorganic compounds through aqueous-phase photocatalysis: a review. Ind. Eng. Chem. Res. 43: 7683-7696, 2004.

[3] Zhang, H. and Banfield, J.F. Thermodynamic analysis of phase stability of nanocrystalline titania, J. Mater. Chem. 8: 2073-2076, 1998.

[4] H. Zhang, J.F. Banfield: Understanding polymorphic phase transformation behavior during growth of nanocrystalline aggregates: insights from TiO_2, J. Phys. Chem. B 104: 3481-3487, 2000.

[5] A. Beltran, L. Gracia, J. Andres: Density functional theory study of the brookite surfaces and phase transitions between natural titania polymorphs, J. Phys. Chem. B 110: 23417-23423, 2006.

[6] TA. Kandiel, L Robben, A Alkaim, D Bahnemann: Photochem. Photobiol. Sci., 12: 602-609, 2013

[7] A.L. Linsebigler, G. Lu, J.J. Yates Jr.: Photocatalysis on TiO_2 surfaces: principles, mechanisms, and selected results. Chem. Rev. 95: 735-758, 1995.

[8] K Nakata, A Fujishima: TiO_2 photocatalysis: Design and applications. J Photochem. Photobiol. C: Photochem. Rev. 13: 169-189, 2012

[9] Q Guo, C Zhou, Z Ma, X Yang: Fundamentals of TiO_2 photocatalysis: concepts, mechanisms, and challenges. Adv. Mater. 31: 1901997, 2019

[10] J Schneider, M Matsuoka, M Takeuchi, J Zhang, Y Horiuchi, M Anpo, D.W. Bahnemann: Understanding TiO_2 photocatalysis: mechanisms and materials. Chem. Rev. 114: 9919–9986, 2014

[11] N Aman, T Mishra: Recent development on titania based mixed oxide photocatalysts for environmental application under visible light. Mater. Sci. Forum 734: 186-214, 2013.

[12] M. Humayun, F. Raziq, A. Khan & W. Luo: Modification strategies of TiO_2 for potential applications in photocatalysis: a critical review. Green Chem Lett. Rev 11: 86-102, 2018.

[13] C Xu, P R Anusuyadevi, C. Aymonier, R Luque, S. Marre: Nanostructured materials for photocatalysis. Chem. Soc. Rev. 48: 3868-3902, 2019

[14] R.J. Davis, Z. Liu: Titania-silica: A model binary oxide catalyst system, Chem. Mater. 9: 2311-2324, 1997.

[15] T. Mishra, J. Hait, Noor Aman, R.K.Jana, S. Chakravarty: Effect of UV and visible light on photocatalytic reduction of lead and cadmium over titania based binary oxide materials, J. Colloid Interface Sci. 316: 80-84, 2007.

[16] Z. Ding, G. Q. Lu, P.F. Greenfield: Role of the crystallite phase of TiO_2 in heterogeneous photocatalysis for phenol oxidation in water. J. Phys. Chem. B 104: 4815-4820, 2000.

[17] K.V. Baiju, P. Periyat, P. Krishna Pillai, P. Mukundan, K.G.K. Warrier, W. Wunderlich: Enhanced photoactivity and anatasethermal stability of silica-alumina mixed oxide additives on sot-gel nanocrystalline titania. Mater. Lett. 61: 1751-1755, 2007.

[18] T. Mishra, J. Hait, Noor Aman, M. Gunjan, B. Mahahto and R.K. Jana: Surfactant mediated synthesis of spherical binary oxides photocatalysts with enhanced activity in visible light, J. Colloid Interface Sci. 327: 377-383, 2008.

[19] A. Kubacka, M. Fernandez-Garcia, G. Colon: Advanced nanoarchitectures for solar photocatalytic applications, Chem Rev. 112: 1555-1614, 2012.

[20] B. Gao, T. M. Lim, D.P. Subagio, T.T. Lim: Zr-doped TiO_2 for enhanced photocatalytic degradation of bisphenol A, Appl. Catal. A 375: 107-115, 2010.

[21] M.D.H. Alonso, I.T. Tejedor, J.M. Coronado, J. Soria, M.A. Anderson: Sol-gel preparation of TiO_2-ZrO_2 thin films supported on glass rings: Influence of phase composition on photocatalytic activity. Thin Solid Films 502: 125-131, 2006.

[22] J. Lukac, M. Klementova, P. Bezdicka, S. Bekardjieva, J. Subrt, L. Szatmary, Z. Bastl, J.Jirkowsky: Influence of Zr as TiO_2 doing ion on photocatalytic degradation of 4-chlorophenol. Appl. Catal. B 74: 83-91, 2007.

[23] A. Mattsson, C. Lejon, V. Stengl, S. Bakardjieva, F. Oplustil, P. O. Andersson, L.Osturlund: Photodegradation of DMMP and CEES on zirconium doped titania nanoparticles, Appl. Catal. B 92: 401-410, 2009.

[24] J.R. Bartlett, D. Gazeau, Th. Zemb, J.L. Woolfrey: Structure of multicomponent (titania/zirconia) colloids, Langmuir 14: 3538-3544, 1998.

[25] B. Wu, R. Yuan, X. Fu: Structural characterization and photocatalytic activity of hollow binary ZrO_2/TiO_2 oxide fibers, J. Solid State Chem. 182: 560-565, 2009.

[26] M. Boulora, G. Lucazeau: Crystallite nanosize effect on the structural transitions of WO_3 studied by raman spectroscopy, J. Solid. State. Chem. 167: 425-434, 2000.

[27] N. Aman, P. K. Satapathy, T. Mishra, M. Mahato, N.N. Das: Synthesis and photocatalytic activity of mesoporous cerium doped TiO_2 as visible light sensitive photocatalyst. Mater. Res. Bull. 37: 179-183, 2012.

[28] T.T. Nguyen, S-N. Nam, J. Son, J. Oh: Tungsten Trioxide (WO_3)-assisted Photocatalytic Degradation of Amoxicillin by Simulated Solar Irradiation. Scientific Reports, 9: 9349, 2019.

[29] H. Quan, Y. Gao, W. Wang: Tungsten oxide-based visible light-driven photocatalysts: crystal and electronic structures and strategies for photocatalytic efficiency enhancement. Inorg. Chem. Front. 7: 817-838, 2020.

[30] Y-C. Nah, A. Ghicov, D. Kim, S. Berger, P. Schmuki: TiO_2-WO_3 composite nanotubes by alloy anodization: Growth and enhanced electrochromic properties, J. Am. Chem. Soc. 130: 16154–16155, 2008.

[31] V.O. Ndabankulu, S. Maddila, and S.B. Jonnalagadda: Synthesis of lanthanide-doped TiO_2 nanoparticles and their photocatalytic activity under visible light. Can. J. Chem. 97: 672–681, 2019.

[32] C.P. Sibu, R.S. Kumar, P. Mukundan, K.G.K. Warrier: Structural modifications and associated properties of lanthanum oxide doped sol-gel nanosized titanium oxide, Chem. Mater. 14: 2876–2881, 2002.

[33] Y.S. Chaudhary, S. Panigrahi, S. Nayak, B. Satpati, S. Bhattacharjee, N. Kulkarni: Facile synthesis of monodisperse ultra-small ceria nanocrystals at room temperature and their catalytic activity under visible light, J. Mater. Chem. 20: 2381–2385, 2010.

[34] F. Zhu, C. Li, M.N. Ha, Z. Liu, Q. Guo, Z. Zhao: Molten-salt synthesis of Cu–$SrTiO_3$/TiO_2 nanotube heterostructures for photocatalytic water splitting. J. Mater. Sci., 51: 4639-4649, 2016.

[35] J. Zhang, J.H. Bang, C. Tang, P.V. Kamat: Tailored TiO_2–$SrTiO_3$ heterostructure nanotube arrays for improved photoelectrochemical performance. ACS Nano. 4: 387-395, 2010.

[36] Z. Zhang, Y. Ma, X. Bu, Q. Wu, Z. Hang, Z. Dong, X. Wu: Facile one-step synthesis of TiO_2/ Ag/SnO_2 ternary heterostructures with enhanced visible light photocatalytic activity. Sci Reports 8: 10532, 2018.

[37] B. Zhou, S. Yang, W. Wu, L. Sun, M. Lei, J. Pan, X. Xiong: Self-assemble SnO_2@TiO_2 porous nanowire-nanosheet heterostructures for enhanced photocatalytic property. Cryst. Eng. Comm. 16: 10863-10869, 2014.

[38] R. Zhang, M. Sun, G. Zhao, G. Yin, B. Liu: Hierarchical Fe_2O_3 nanorods/TiO_2 nanosheets heterostructure: Growth mechanism, enhanced visible-light photocatalytic and photoelectrochemical performances. Appl. Surface Sci. 475: 380-388, 2019.

[39] Q. Mei, F Zhang, N. Wang, Y. Yang, R. Wu, W. Wang: TiO_2/Fe_2O_3 heterostructures with enhanced photocatalytic reduction of Cr(VI) under visible light irradiation. RSC Adv. 9: 22764-22771, 2019.

[40] X. Li, H. Lin, X. Chen, H. Niu, J. Liu, T. Zhang, F. Qu: Dendritic α-Fe_2O_3/TiO_2 nanocomposites with improved visible light photocatalytic activity. Phys. Chem. Chem. Phys. 18: 9176-9185, 2016.

[41] N. L Reddy, S. Emin , M. Valant, M.V. Shankar: Nanostructured Bi_2O_3@TiO_2 photocatalyst for enhanced hydrogen production. Int. J. Hydrog. Energy 42: 6627-6636, 2017.

[42] R. Asahi, T. Morikawa, T. Ohwaki, K. Aoki, Y. Taga: Visible-light photocatalysis in nitrogen-doped titanium oxides. Science 293: 269-271, 2001.

[43] G. Zhang, Y.C. Zhang, M. Nadagouda, C. Han, K. O'Shea, S.M. El-Sheikh, A.A. Ismail, D.D. Dionysiou: Visible light-sensitized S, N and C co-doped polymorphic TiO_2 for photocatalytic destruction of microcystin-LR. Appl. Catal. B: Environ. 144, 614-621, 2014.

[44] G.G. Bessegato, J.C. Cardoso, M.V.B. Zanoni: Enhanced photoelectrocatalytic degradation of an acid dye with boron-doped TiO_2 nanotube anodes. Catal. Today 240: 100-106, 2015.

[45] P.A.O. Rodríguez, T. B. Benzaquén, G.A. Pecchi, S. G. Casuscelli, V.R. Elías, G.A. Eimer: Novel route to obtain carbon self-doped TiO_2 mesoporous nanoparticles as efficient photocatalysts for environmental remediation processes under visible light. Materials 12: 3349, 2019.

[46] X Cheng, X Yu, Z Xing, L Yang: Synthesis and characterization of N-doped TiO_2 and its enhanced visible-light photocatalytic activity, Arab J. Chem. 9: S1706-S1711, 2016.

[47] N. Aman, T. Mishra, R. K. Sahu, J. P. Tiwari: Facile synthesis of thermally stable, mesoporous N doped titanium zirconium oxide nanomaterial with enhanced photocatalytic activity under visible light. J. Mater. Chem. 20: 10876-10882, 2010

[48] X. Yang, Y. Wang, L. Zhang, H. Fu, P. He, D. Han, T. Lawson, X. An: The use of tunable optical absorption plasmonic Au and Ag decorated TiO_2 structures as efficient visible light photocatalysts. Catalysts 10: 139, 2020.

[49] D. Yang, Y. Sun, Z. Tong, Y. Tian, Y. Li, Z. Jiang: Synthesis of Ag/TiO_2 nanotube heterojunction with iImproved visible-light photocatalytic performance inspired by bioadhesion. J. Phys. Chem. C. 119: 5827-5835, 2015.

[50] V. Etacheri, C.D. Valentin, J. Schneider, D. Bahnemann, S.C. Pillai: Visible-light activation of TiO_2 photocatalysts: Advances in theory and experiments, J. Photochem. Photobiol C: Photochem. Rev. 25: 1-29, 2015.

[51] B. S. Chang, A. Martin, B. Thomas, A. Li, R. W. Dorn, J. Gong, A.J. Rossini, M.M. Thuo: Synthesis of interface-driven tunable bandgap metal oxides. ACS Mater. Lett. 2: 1211-1217, 2020.

[52] T. Mishra, L. Wang, R. Hahn, P. Schmuki: In-situ Cr doped anodized TiO_2 nanotubes with increased photocurrent response. Electrochimica Acta 132: 410-415, 2014.

[53] T. Mishra, M. Mahato, Noor Aman, J. N. Patel, R. K. Sahu: Mesoporous WN co-doped titania nanomaterial with enhanced photocatalytic aqueous nitrate removal activity under visible light. Catal Sci. Technol. 1: 609-615, 1011.

[54] J. Low, C. Jiang, B. Cheng, A.A. Al-Ghamdi, J. Yu: A review of direct Z-scheme photocatalysts. Small Method 1: 1700080, 2017.

[55] L. F. Paula, M. Hofer, V. P. B. Lacerda, D. W. Bahnemann, A.O.T. Patrocinio: Unravelling the photocatalytic properties of TiO_2/WO_3 mixed oxides. Photochem. Photobiol. Sci.18: 2469-2483, 2019

[56] H. Wang, L. Zhang, Z. Chen, J. Hu, S. Li, Z. Wang, J. Liu, X. Wang: Semiconductor heterojunction photocatalysts: design, construction and photocatalytic performances. Chem. Soc. Rev. 43: 5234-5244, 2014.

[57] Y. Wang, Q. Wang, X. Zhan, F. Wang, M. Safdar, J. He: Visible light driven type II heterostructures and their enhanced photocatalysis properties: a review. Nanoscale 5: 8326-8339, 2013.

[58] G. Wang, B. Huang, X. Ma, Z. Wang, X. Qin, X. Zhang, Y. Dai, M.-H. Whangbo: $Cu_2(OH)PO_4$, a near-infrared-activated photocatalyst, Angew. Chem. Int. Ed., 52: 1-5, 2013.

[59] W. Jiao, Y. Cheng, J. Zhang, R. Che: Self-assembled 3D hierarchical copper hydroxyphosphate modified by the oxidation of copper foil as a recyclable, wide wavelength photocatalyst. Langmuir 33: 13649-13656, 2017.

[60] D. Magadevan, E Dhivya, N D A Mundari, T Mishra, N Aman: Development of novel TiO_2-$Cu_2(OH)PO_4$ heterojunction as nanophotocatalyst for improved Cr (VI) reduction, J. Environ. Chem. Engg. 7: 102968, 2019.

[61] X. Ning, G. Lu: Photocorrosion inhibition of CdS-based catalysts for photocatalytic overall water splitting. Nanoscale, 12: 1213-1223, 2020.

[62] S. Liu, N. Zhang, Z.-R. Tang, Y.-J. Xu: Synthesis of one-dimensional CdS@TiO_2 core-shell nanocomposites photocatalyst for selective redox: the dual role of TiO_2 shell. ACS Appl. Mater. Inter. 4: 6378-6385, 2012.

[63] R. Acharya, K. Parida: A review on TiO_2/g-C_3N_4 visible-light- responsive photocatalysts for sustainable energy generation and environmental remediation. J. Environ. Chem. Engg. 8: 103896, 2020.

[64] P. Ganguly, S Mathew, L Clarizia, S Kumar R, A Akande, S.J. Hinder, A Breen, S.C. Pillai: Ternary metal chalcogenide heterostructure ($AgInS_2$–TiO_2) nanocomposites for visible light photocatalytic applications, ACS Omega. 5(1): 406–421, 2020.

[65] C. Byrnea, G. Subramanian, S.C. Pillai: Recent advances in photocatalysis for environmental applications. J Environ Chem. Engg. 6: 3531-3555, 2018.

[66] P. Mohapatra, T. Mishra, K.M. Parida: Effect of microemulsion composition on textural and photocatalytic activity of titania nanomaterial. J. Appl. Catal, A 310: 183-189, 2006.

[67] K Urkasame, S Yoshida, T Takanohashi, S Iwamura, I Ogino, S.R. Mukai: Development of TiO_2–SiO_2 photocatalysts having a microhoneycomb structure by the ice templating method. ACS Omega 3: 14274–14279, 2018.

[68] A Kubiak, K Siwińska-Ciesielczyk, T Jesionowski: Titania-based hybrid materials with ZnO, ZrO_2 and MoS_2: a review. Materials 11: 2295, 2018.

[69] L Cheng, Q Xiang, Y Liao H Zhang: CdS-Based photocatalysts. Energy Environ. Sci. 11: 1362-1391, 2018.

[70] M.R. Prairie, L.R. Evans, B. Stange, S.L. Martinez: An investigation of titanium dioxide photocatalysis for the treatment of water contaminated with metals and organic chemicals. Environ. Sci. Technol. 27: 1776-1782, 1993.

[71] S.K. Choi, H.S. Yang, J.H. Kim, H.W. Park: Organic dye-sensitized TiO_2 as a versatile photocatalyst for solar hydrogen and environmental remediation. Appl. Catal. B: Environ. 121–122: 206-213, 2012.

[72] A. Tiwari, U. Pal: Effect of donor-donor-π-acceptor architecture of triphenylamine-based organic sensitizers over TiO_2 photocatalysts for visible-light-driven hydrogen production. Int. J. Hydrogen Energ. 40: 9069, 2015.

[73] Z Wang, X Lang: Visible light photocatalysis of dye-sensitized TiO_2: The selective aerobic oxidation of amines to imines. Appl Catal B: Environ. 224: 404-409, 2018.

[74] L. Murruni, G. Leyva, M.I. Litter: Photocatalytic removal of Pb(II) over TiO_2 and Pt-TiO_2 powders, Catal. Today 129: 127-135, 2007.

[76] C. Maillard-Dupuy, C. Guillard, P. Pichat: The degradation of nitrobenzene in water by TiO_2: kinetics and products; simultaneous elimination of benzamide or phenol or Pb^{2+} cations, New J. Chem. 18: 941-948, 1994.

[76] V.N.H. Nguyen, R. Amal, D. Beydoun: Effect of formate and methanol on photoreduction/ removal of toxic cadmium ions using TiO_2 semiconductor as photocatalyst. Chem. Eng. Sci. 58: 4429-4439, 2003.

[77] X. Wang, S.O. Pehkonen, A.K. Ray: Photocatalytic reduction of Hg(II) on two commercial TiO_2 catalysts. Electrochim. Acta 49: 1435-1444, 2004.

[78] D. Chen, A.K. Ray: Removal of toxic metal ions from wastewater by semiconductor photocatalysis. Chem. Eng. Sci. 56: 1561-1570, 2001.

[79] T.T.Y. Tan, D. Beydoun, R. Amal: Effects of organic hole scavengers on the photocatalytic reduction of selenium anions. J. Photochem. Photobiol. A 159: 273-280, 2003.

[80] X. Zhao, G. Zhang, Z. Zhang: TiO_2-based catalysts for photocatalytic reduction of aqueous oxyanions: State-of-the-art and future prospects. Environ. Int. 136: 105453, 2020.

[81] S. Yamazaki, S. Iwai, J. Yano, H. Taniguchi: Kinetic studies of reductive deposition of copper (II) ions photoassisted by titanium dioxide. J. Phys. Chem. A 105: 11285- 11290, 2001.

[82] I.O. Ekwere: Influence of organic dye ligands on the photocatalytic reduction of copper ions in aqueous solution using UV-nano TiO_2 system. Acad. J. Chem. 5(5): 41-47, 2020.

[83] N. Aman, T. Mishra, J. Hait, R.K. Jana: Simultaneous photoreductive removal of copper (II) and selenium (IV) under visible light over spherical binary oxide photocatalyst. J. Hazard. Mater. 186: 360-366, 2011.

[84] C-C Wang, X Wang, W Liu: The synthesis strategies and photocatalytic performances of TiO_2/MOFs composites: a state-of-the-art review. Chem Eng J, 391: 123601, 2020.

[85] H. Huang, B. Pradhan, J. Hofkens, M B. J. Roeffaers, J A. Steele: Solar-driven metal halide perovskite photocatalysis: design, stability, and performance. ACS Energy Letters 5: 1107-1123, 2020.

[86] B Rahimi, A Ebrahimi: Photocatalytic process for total arsenic removal using an innovative $BiVO_4/TiO_2$/LED system from aqueous solution: Optimization by response surface methodology (RSM). J. Taiwan Inst. Chem. Eng. 101: 64-79, 2019.

[87] M I. Litter: Last advances on TiO_2-photocatalytic removal of chromium, uranium and arsenic. Curr. Opin. Green Sustain. Chem. 6: 150-158, 2017

[88] Z. Li, X. Meng, Z. Zhang: Recent development on MoS2-based photocatalysis: a review. J. Photochem Photobiol C: Photochem Rev. 35: 39-55, 2018.

[89] D. Cambie´, C. Bottecchia, N.J.W. Straathof, V. Hessel, T. Noel: Applications of continuous-flow photochemistry in organic synthesis, material science, and water treatment. Chem. Rev. 116: 10276–10341, 2016.

[90] R. Rakhshaee, J. Darvazeh: Studying role of air bubbles on suspension of hematite particles with three size ranges in plug flow reactor to improve dyes photo degradation compared to conventional packed bed photo reactors. J. Hazard. Mater. 356: 61–72, 2018.

Journal of Metallurgy and Materials Science, Vol. 62, No. 3-4, July-December 2020, pp. 147-153
Printed in India, © NML, ISSN 0972-4257

Some notable experiments of graphene

RANJAN K SAHU*
AMP Division, CSIR-National Metallurgical Laboratory, Jamshedpur-831007, India

Abstract : Graphene is an allotrope of carbon where carbon atoms are attached through sp^2 hybridization in a two-dimensional (2D) plane. Based on the structure, graphene can be visualized as a single sheet of graphite. A. Geim and K. Novoselov successfully isolated free standing monolayer graphene from graphite by scotch tape method for the first time in 2004. This discovery won them the Nobel Prize in physics 2010. However, several inception experiments had been carried out much before its birth by other eminent scientists. In fact, several extended experiments have been performed to understand the properties of graphene after its discovery. This article is a collection of some of the notable pre and post-discovery experiments. In addition, it includes some of the experiments those have been carried out at CSIR-NML.

Keywords*: Graphene; Bio-polymer; Natural carbon source; Photocatalytic method; Ion-bombardment; Scotch tape method*

PRIOR TO DISCOVERY

The first study of graphite exfoliation was reported by the German Scientist C. Schafhaeutl in the year 1840 [1, 2]. He mixed graphite in a solution of nitric and sulphuric acid, subsequently boiled to remove these acids from the solution. He observed that the color of the graphite turned to shiny blue upon reaction with sulphuric and nitric acid. However, this study was limited to observation only without any conclusion. In the year 1859 British chemist Sir Benjamin Brodie aimed to investigate the structure, molecular formula and molecular weight of graphite by studying the reactivity of flake graphite [3, 4]. In the experimental protocol, he heated lamellar graphite with potassium perchlorate and fuming nitric acid at 60°C for 3 to 4 days and repeated the process 3-4 times to ensure complete oxidation. He concluded the following points; (i) the structure of graphite was uneven and composed of carbon, oxygen and hydrogen, (ii) the size of crystals in the perpendicular direction from the ground was extremely thin and it was not possible to receive any reflection by the thickness measurement instrument, (iii) the ignition of the crystal yielded black residue and (iv) this material was dispersible in pure and basic water. Based on these observations, he determined that the molecular weight of graphite is 33. He says that *"This form of carbon should be characterized by a name marking it as a distinct element. I propose to term it Graphon"*. Subsequently, Frenzel and co-workers studied the structural investigation of those samples reported by Brodie using XRD in the year 1934, and they concluded that the intercalation of graphitic layers takes place during the experiment [5]. Few years later, Staudenmaier modified the Brodie's synthesis method, where potassium chlorate was added drop wise to avoid explosion caused by evolution of large amount of gases and heat. In addition, partial amount of fuming H_2SO_4 was added in the place of fuming HNO_3 to enhance the oxidation. So, the modified experiment reduced the release of toxic gases (NO_2, N_2O_4 etc) and increased the reaction rate and the C / O ratio [6]. In the year 1957, Hummers reported a new protocol for the preparation of graphite oxide [7]. This method comprised of the treatment of graphite with the water-free mixture of sulphuric acid, sodium nitrate and potassium permanganate at temperature less than 45°C. This method took less than two hours for complete oxidation of graphite. The color of the graphite oxide solution was footprint to determine the degree of oxidation; yellow bright at high degree of oxidation and green to black hue in the case of poor oxidation. Currently, this is most adoptive method for the conversion of graphite to graphite oxide, which is popularly known as Hummers method.

* Corresponding Author E-mail: rksahu@nmlindia.org

In fact, some eminent groups had carried out theoretical studies to understand the properties of individual graphite layer. In the year 1947, P. R. Wallace for the first time calculated the electronic band structure of individual graphite layer[8]. He reported that in the reciprocal lattice two atoms unit cell constitute the Brillouin Zone with two conical point at the Fermi surface, K and Kε known as Dirac points while the π-π^* band touch at a point. Besides, the electron energy is linearly dependent on the wave vector near the Dirac point. Therefore, graphene is a semimetal or zero-band gap semiconductor. Due to this unique band structure charge carrier in graphene mimic the features of zero mass particles. As a result, the electron mobility in individual graphitic layer is just 300 times less than the speed of light. However, Mermin-Wagner theorem suggested that 2-D materials are thermodynamically unstable in any finite temperature [9], which discouraged the possibility of the formation of individual graphitic layer experimentally. Therefore, the study of Wallace remained just as a fundamental study to understand the electronic properties of individual graphitic layer. In the year 1962 Boehm et al. reduced the suspension of graphite oxide into thin lameller carbon using hydrazine, hydrogen sulphide in dilute alkaline media. This experiment protocol yielded very thin lamellar carbon with small amount of oxygen and hydrogen [10, 11]. In addition, TEM data indicated that the thickness of the thin lameller carbon is around 4.6Å with a little deviation from the thickness of single layer graphene that is observed in the recent studied i.e. 4Å. Though the TEM data suffered some serious experimental errors, Boehm concluded that these films contain single carbon layer.

In 1968 Morgan and Somorjai used low energy electron diffraction (LEED) technique to investigate the adsorption of organic gas on platinum (100) surface at high temperature [12]. The LEED data revealed that the organic gas converted into single and multilayer graphitic carbon sheets. In contrast to the Mermin-Wagner theorem, this study proposed that platinum surface played an important role to stabilize the single layer of graphitic carbon by minimizing the free energy. The observed single layer of carbon on platinum surface by Morgan and Somorjai can be considered to be graphene based on the structural features, even though the term of graphene was not coined by that time. Next, Blakely and co-workers reported that the dissolved carbon of transition metals at high temperature converted into single and multilayer of carbon sheets at the surface [13]. In 1975 van Bommel et al. also observed the formation of single layer graphitic structure at the surface when the single crystal silicon carbide was heated under ultra-high vacuum at and below 800 °C [14]. Around the time of 1980 many reports on single and multilayer carbon with graphitic structure came into lime light. Hence to precise the definition of this material Boehm et al. in 1986 proposed that the single layer of carbon having the graphitic structure or simply the single layer of graphite should be called as "graphene" [15]. In 1997 IUPAC incorporated the suggestion of Boehm et al. in the Compendium of Chemical Technology, and it was suggested that "The term graphene should be used only when the reactions, structural relations or other properties of individual layers are discussed"[16, 17]. Further, Kovtyukhova and co-workers in 1999 made a pretreatment of graphite with H_2SO_4, $K_2S_2O_8$ and P_2O_5 to increase the extent of oxidation [18]. In the same year, Ruoff's group attempted to manipulate the thickness of highly oriented pyrolytic graphite (HOPG) using AFM tip with the goal to achieve single sheet [19, 20]. The results showed that the thickness of prepared graphite was around 200 nm which is equivalent to 600 layers of graphite. Later, Kim's group at Columbia studied the prepared sample from HOPG and could obtained information up to 10 nm thick graphite by a tip less cantilever of AFM, which is equivalent to 30 layers of graphite [21]. Finally, A. Geim and K. Novoselov from the University of Manchester isolated graphene from graphite using micromechanical method or scotch tape method in 2004 [22]. In this method the individual layers were separated out from the HOPG by using a Scotch tape. This is also known as peeling off method as it involves the cleavage of the HOPG layers in to individual layers with the help of a scotch tape. In a typical method the HOPG powder is pressed in the scotch tape and repeated peeling of the HOPG powder bring it down to a single layer. The underlying mechanism of this process is the application of the normal force for several times to peel off HOPG down to single layer. Depending on the extent of cleavage it yielded mono, bi or few layers graphene.

They transferred the individual layer onto silicon wafer and studied the electronic properties. They observed anomalous quantum effect, which is quite similar to those predicted much before theoretically. In addition, they observed that graphene is a semimetal where the conduction band overlaps with the valence band. The mobility and concentration of the charge carrier were determined by the field effect and magneto-resistance measurements. The calculated mobility was 15000 and 60000 $cm^2/V.s$ at 300 and 4 K, respectively. The carrier density was estimated to be $> 10^{12}$ cm^{-2}. The Royal Swedish Academy of Sciences awarded the Nobel prize in physics for 2010 to A. Geim and K. Novoselov for their groundbreaking experiments of graphene. After that, graphene drew attention of many research groups worldwide to explore its utilization towards novel and advanced applications such as opto-electronics, energy storage, photo-voltaic, composite materials, bio-medical, corrosion protection etc.

BEYOND DISCOVERY

After its discovery in 2004, researchers had also attempted to exfoliate graphite via liquid phase exfoliation in order to overcome the criticality and challenges for the volume production of graphene. The sonication assisted liquid phase exfoliation method was reported by Coleman's and Geim's group separately in 2008 [23, 24]. The process involved dispersion of graphite flake in solvent like N, N-dimethyl formamide, N-methylpyrrolidone etc. followed by sonication. Solvents were chosen based on whose surface energy is closer to graphite surface energy, so that the mixing enthalpy will be smaller and exfoliation would be easier. This method also produced graphene. The underlying mechanism of the process is based on the principle of liquid cavitation, in which the cavitation induced bubbles in the solution. The bursting of these bubbles generated shock waves on the graphite surface immediately that led to form the compressive wave. Once the compressive wave spread into the free interface of graphite, a tensile stress wave is reflected back to the body. The generation and bursting of numerous bubbles generates enough tensile stress on the graphite flakes that led to exfoliate of graphite flake and produce graphene sheets. This is a much simpler process for obtaining large scale graphene with respect to the mechanical exfoliation process.

In addition, the remarkable thermal conductivity and mechanical strength properties of free standing graphene sheet were reported by the eminent groups. Balandin measured the thermal conductivity of a free standing single-layer graphene at room temperature using a laser based non-contact technique [25]. In the experiment, the graphene sheet was suspended over a trench of a Si/SiO_2 substrate. The heat was induced by focusing the laser light of excitation wavelength 488 nm at the center of the graphene sheet. The transformation of heat to the Si substrate was negligible as the thermal conductivity of beneath SiO_2 layer is ~1 W/mK. Considering air has negligible thermal conductivity, the following equation was used for determination of the thermal conductivity; $\partial Q/\partial t = -K\phi \nabla T.dS$, where Q is the induced heat transferred over the time t with the cross sectional area S and T is the temperature. The thermal conductivity is found to be ~5.3×10^3 W/mK. The high value of the thermal conductivity suggested that it could be an excellent material for thermal management in electronic devices.

Lee et al. measured the elastic and strength properties of the monolayer graphene membrane using nanoindentation in an atomic force microscope (Model: XE-100, Park systems) [26]. The diamond cantilevers with tip radii of 27.5 and 16.5 nm were used for this study. The spring constant of these cantilevers were calibrated with respect to the reference cantilever. Prior to the nanoindentation experiment, the graphene membrane was scanned by non-contact AFM mode and the tip was placed within 50 nm of the center. Mechanical testing measurement was carried out at constant displacement rate. The acquired data showed no hysteresis loop, indicated the membrane is highly elastic. The breaking force value from the experimental data was calculated to be 2890 nN when the tip radii is 27.5 nm. It was noted that the second and third order stiffness constants are $E^{2D} = 340 \pm 50$ N m^{-1} and $D^{2D} = -690 \pm 120$ N m^{-1}, respectively. The intrinsic strength was calculated using

the equation; $\sigma_m^{2D} = (F E^{2D} / 4\pi R)^{1/2}$ and the value was found to be 40 ± 4 N m^{-1} by considering the thickness of monolayer graphene is 0.335 nm. The Young's modulus and intrinsic stress were estimated to be of $E = 1.0 \pm 0.1$ TPa and $\sigma int = 130 \pm 10$ GPa at a strain of $e = 0.25$. This experiment suggests that graphene is a strongest material ever known in the universe.

EXPERIMENTS MADE AT CSIR-NML

CSIR-NML published the first report of graphene production in 2012 using lotus flower as a carbon source. It was accidental observation made by A. K. Ray. The main intention of the experiment was conversion of $NiCl_2$ to Ni nanoparticles by plant as the enzyme of plant has ability to reduce metal ions and form nanoparticles. However, it was an unsuccessful experiment to produce Ni nanoparticles at room temperature. In next plan of experiments, it was decided to heat the flower petals at temperature more than 1000°C. The obtained product was characterized first using Raman spectroscopy. The Raman data was surprised to all of us, where 2D peak was more intense than D and G peaks and the data were well matched with the earlier reported data for graphene [27]. After that, we designed several other experiments for the production of graphene in order to understand the conversion mechanism from the constituent cellulose structure to graphene. In fact, the same kind of Raman data was observed in the case of conversion hibiscus flower to graphene (Fig.1).

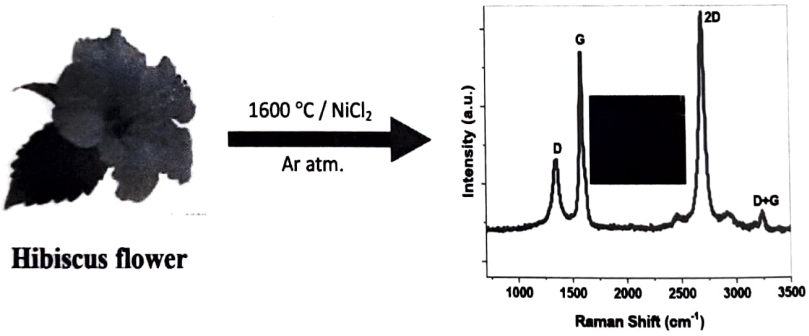

Fig. 1 Experimental protocol and Raman data for the conversion of hibiscus flower to graphene.

We also devised a new experiment for exfoliation of graphene from graphite by photocatalytic reduction [28], where the yellow color graphite oxide solution prepared by Hummers method was reduced using peanut shaped α-Fe_2O_3 particles under visible light. The monodispersed particles with bandgap ~ 2.5 eV was efficient to transfer electrons to the graphite oxide sheet for reduction and exfoliation that led to form large size α-Fe_2O_3 particles embedded thin graphene sheet (Fig. 2). These particles could also be separated from the graphene sheet by centrifuged the solution at 10000 rpm.

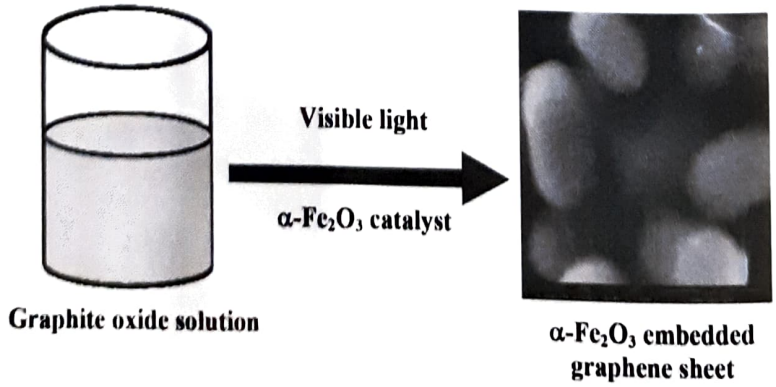

Fig. 2 Experimental protocol for the conversion of graphite oxide solution to graphene sheet by photocatalytic reduction.

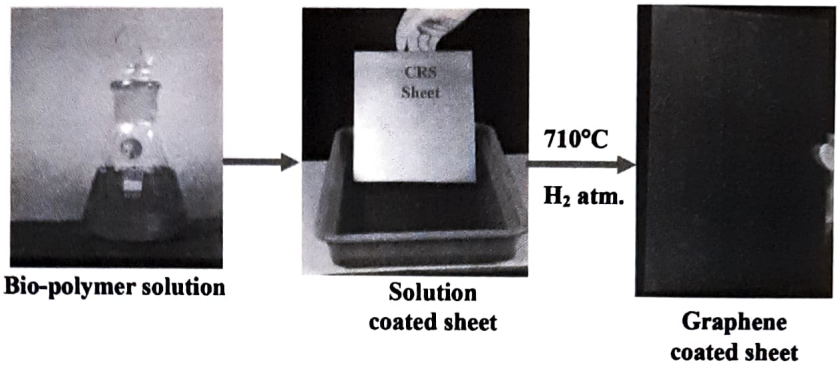

Fig. 3 The schematic representation for the production of graphene coated cold rolled sheet using bio-polymer solution.

Besides, we demonstrated that Ar^+ ion bombardment could be used for conversion of non-aromatic pyrazoline to aromatic pyrazole N-ring of hydrazine reduced graphene sheet at room temperature [29]. Such conversion enhanced the conductivity of the graphene film. In 2014, a simple protocol was developed to produce large area graphene coating over steel substrates using shellac bio-polymer as a carbon source under a collaborative project with Tata Steel, Jamshedpur. The existing batch annealing furnace of Tata Steel was used for the conversion of bio-polymer to graphene over a A4 size cold rolled sheet under the heating conditions of 710°C for 24 hrs in H_2 atmosphere (Fig. 3). Subsequent post-treatment of these coated steel products enabled to enhance the corrosion protection in saline environment. This pioneering work received Tata Innovista Award in 2015 from Tata Sons. In addition, NML also initiated collaboration with M/s- John Keells, Sri Lanka for the direct exfoliation of graphite using collagen protein and the produced graphene is suitable for supercapacitor application.

FUTURE ROADMAP AT CSIR-NML

The functional materials group at CSIR-NML is moving towards with the goal of large scale production of graphene from medium purity Indian flake graphite with high energy storage capacity in the wake of indigenously developed energy storage materials will play a pivotal role in fulfilling the sustainable vision set by India for complete mobility to electric vehicle by 2030. Graphite is one of the key materials used in energy storage applications. Despite India is fifth major producers of flake graphite in the world, existing processed graphite materials are unsuited for high performance energy storage devices. The major drawback of Indian graphite is that it contains silica impurity with the average purity of around 90 %. Even after beneficiation of high grade graphite minerals with modified processing technology by some Indian companies it has been achieved maximum purity up to 94%, which is again below then the required purity (~99%) for energy storage applications. In addition, no efforts have been made by Indian industries to improve the energy storage capacity of natural graphite by devising a new strategy, which further increases the dependency of our electric vehicle manufacturing companies on other countries for energy storage materials and devices. However, the energy storing capacity of Indian flake graphite can be enhanced by improving electrical conductivity and surface area through reducing its thickness along the Z-axis down to few layers and converting the silica impurity to Fe, Co, Ni-silicate functionalized phases containing redox ionic pairs. Such anticipated functionalized graphene would provide a strong support for fabrication of high-performance battery and supercapacitor indigenously.

ACKNOWLEDGEMENT:

Some experimental protocols presented here were financially supported by Tata Steel, Jamshedpur under the collaborative scheme.

REFERENCES:

[1] C. Schafhaeutl: Ueber die verbindungen des kohlenstoffes mit silicium, eisen und anderen metallen, welche die verschiedenen gallungen von roheisen, stahl und schmiedeeisen bilden. J. Prakt. Chem. 21: 129-157, 1840.

[2] C. Schafhaeutl: LXXXVI. On the combinations of carbon with silicon and iron and other metals forming the different species of cast iron, steel and malleable iron. Phil. Mag. 16: 570-590, 1840.

[3] B.C. Brodie: XIII. On the atomic weight of graphite. Philos Trans R Soc London 149: 249-259, 1859.

[4] B.C. Brodie: XXIII.-Researches on the atomic weight of graphite. Q. J. Chem. Soc. 12: 261-268, 1860.

[5] U. Hoffman, A. Frenzel and E. Casalan: Die konstitution der graphitsäure und ihre reaktionen. Ann. Chem. 510: 1-41, 1934.

[6] L. Staudenmaier: Verfahren zur darstellung der graphitsäure. Ber. Dtsch. Chem. Ges. 31: 1481-1487, 1898.

[7] W.S. Hummers and R. E. Offeman: Preparation of graphitic oxide. J. Am. Chem. Soc. 80: 1339-1939, 1958.

[8] P.R. Wallace: The band theory of graphite. Phys. Rev. 71: 622-634, 1947.

[9] N.D. Mermin: Crystalline order in two dimensions. Phys. Rev. 176: 250-254, 1968.

[10] H.P. Boehm, A. Clauss, G.O. Fischer and U. Hofmann: Thin carbon leaves. Naturforsch 17: 150-153, 1962.

[11] H.P. Boehm, A. Clauss, G.O. Fischer and U. Hofmann: The adsorption behavior of very thin carbon films. Anorg. Allg. Chem. 316: 119-127, 1962.

[12] A.E. Morgan and G.A. Somorjai: Low energy electron diffraction studies of gas adsorption on the platinum (100) single crystal surface. Surf. Sci. 12: 405-425, 1968.

[13] J.M. Blakely, J.S. Kim and H.C. Potter: Segregation of carbon to the (100) surface of Nickel, J. Appl. Phys. 41: 2693-2697, 1970.

[14] A.J. van Bommel, J.E. Crombeen and A. van Tooren: LEED and Auger electron observations of the SiC (0001) surface. Surf Sci 48: 463-472, 1975.

[15] H.P. Boehm, R. Setton and E. Stumpp: Nomenclature and terminology of graphite intercalation compounds. Carbon 24: 241-245, 1986.

[16] E. Fitzer, K.-H. Kchling, H.P. Boehm and H. Marsh: Recommended terminology for the description of graphite as a solid. Pure Appl. Chem. 67: 473-506, 1995.

[17] IUPAC in Compendium of Chemical Terminology (Eds.: A.D. McNaught, A. Wilkinson), 2nd ed., Blackwell Scientific, Oxford, 1997.

[18] N.I. Kovtyukhova, P.J. Ollivier, B.R. Martin, T.E. Mallouk, S.A. Chizhik, E.V. Buzaneva, and A.D. Gorchinskiy: Layer-by-layer assembly of ultrathin composite films from micron-sized graphite oxide sheets and polycations. Chem. Mater. 11: 771-778, 1999.

[19] X. K. Lu, H. Huang, N. Nemchuk and R. S. Ruoff: Tailoring graphite with the goal of achieving single sheets. Nanotechnology 10: 269-272, 1999.

[20] X. K. Lu, H. Huang, N. Nemchuk and R.S. Ruoff: Patterning of highly oriented pyrolytic graphite by oxygen plasma etching. Appl. Phys. Lett. 75: 193-197, 1999.

[21] Y.B Zhang, J.P. Small, W.V. Pontius and P. Kim: Fabrication and electric-field-dependent transport measurements of mesoscopic graphite devices. Appl. Phys. Lett. 86: 073104-073107, 2005.

[22] K.S. Novoselov, A.K. Geim, S.V. Morozov, D. Jiang, Y. Zhang, S.V. Dubonos, I V. Grigorieva, A.A. Firsov: Electric field effect in atomically thin carbon films. Science 306: 666-669, 2004.

[23] Y. Hernandez, V. Nicolosi, M. Lotya, F.M. Blighe, Z. Sun, S. De, I.T. McGovern, B. Holland, M. Byrne, Y.K. Gun'Ko, J.J. Boland, P.Niraj, G. Duesberg, S. Krishnamurthy, R. Goodhue, J. Hutchison, V. Scardaci, A.C. Ferrari and J.N. Coleman: High-yield production of graphene by liquid-phase exfoliation of graphite. Nat. Nanotech, 3: 563-568, 2008.

[24] P. Blake, P.D. Brimicombe, R.R. Nair, T.J. Booth, D. Jiang, F. Schedin, L.A. Ponomarenko, S.V. Morozov, H.F. Gleeson, E.W. Hill, A.K. Geim and K.S. Novoselov: Graphene-based liquid crystal device. Nano. Lett. 8:1704-1708, 2008.

[25] A.A. Balandin: Thermal properties of graphene and nanostructured carbon materials. Nat. Mater. 10: 569-581, 2011.

[26] C. Lee, X. Wei, J.W. Kysar, J. Hone: Measurement of the elastic properties and intrinsic strength of monolayer graphene. Science 321: 385-388, 2008.

[27] A.K. Ray, R.K. Sahu, V. Rajinikanth, H. Bapari. M. Ghosh, P. Paul: Preparation and characterization of graphene and Ni-decorated graphene using flower petals as the precursor material. Carbon 50: 4123-4129, 2012.

[28] Y. N. Singhbabu, K. K. Sahu, D. Dadhich, A. K. Pramanick, T. Mishra and R. K. Sahu: Capsule-embedded reduced graphene oxide: synthesis, mechanism and electrical properties. J. Mater. Chem. C 5: 958-966, 2013.

[29] Y. N. Singhbabu, P. Kumari, S. Parida, R. K. Sahu: Conversion of pyrazoline to pyrazole in hydrazine treated N-substituted reduced graphene oxide films obtained by ion bombardment and their electrical properties. Carbon 74: 32-43, 2014.

Preparation of Manuscripts

1. Manuscripts should be sent in MS Word and pdf format.
2. Text should be 12 pt Times New Roman, double-spaced, left justified, A4 sized paper with wide margin.
3. All pages should be numbered consecutively, beginning with page 1, the title page.
4. Tables and figures should be numbered serially. Figures should have legends if applicable.
5. Tables and figures will be placed near their first mention in the text; all tables and figures must be referred to in the manuscript.
6. The following information must be included:
   - Title of the article;
   - Name(s) and initial(s) of author(s)
   - Affiliation(s) of author(s);
   - Name, address, telephone, mobile number and e-mail address of the corresponding author.
   - **Abstract:** Each article should include a brief abstract of 250 words, thatshould highlight the objectives, methods, results, and conclusions of the paper.
   - **Keywords:** To identify the subjects under which the article may be indexed, 6-10 key words should be provided.
   - **References:** In the text, references to the literature should be presented within square bracket indicating the reference number [1]
   - **Paper:**

     [1] J. Singh, A. Kumar: Investigation of structural, morphological and electrochemical properties of mesoporous La_2CuCoO_6 rods fabricated by facile hydrothermal route. Int. J. Miner. Metall. Mater. 27: 987–995, 2020
   - **Book:**

     [2] J.D. Verhoeven: Fundamentals of physical metallurgy, 1st Edition, New York: Wiley, New York, pp. 55-61, 1975
   - **Online document**

     [3] Cory Mitchell: Fractal Indicator Definition and Applications. Technical analysis basic education. Available via https://www.investopedia.com/terms/f/fractal.asp, Retrieved 3 August 2020
   - **Illustrations :** These include photographs, drawings and line art includes graphs, flowcharts, diagrams etcwhich can be reproduced without losing any clarity. Figure legends or captions should follow the order in which they appear in the manuscript, be numbered with Arabic numerals and should not contain a text repeated. The preferred file formats for images and line art are TIF/TIFF and JPG. For good image quality, scanned black & white photographs should be provided as 300 ppi TIFF files and line art should be provided as 600 ppi TIFF files.
   - **Color Figures :** The authors should accept the obligation of bearing the expenses of colour images in the printed version of the journal while no charge is required for their appearance in the electronic version of the journal. Colour illustrations should be provided as scanned TIFF files at a minimum of 300 ppi with a 24-bit colour depth.
   - **Mathematical Equations :** Mathematical equations, suitably numbered, should be inserted in the text through "Equation editor" of MS word as per the example

$$P(e) = \frac{1}{2}\left[1 - erf\left(\frac{K}{2\sqrt{2}}\right)\right] \quad \text{.....(Eq 1)}$$

   - Symbols, Abbreviations, Units, etc.: It is mandatory to define the symbols and acronyms at first mention within the text and also in titles and abstracts. The authors are requested to follow internationally accepted rules for nomenclature, abbreviations, symbols and units.
   - **Computer Code:** Pseudo algorithms, as presented below, with appropriate reference should be submitted.
     - **Title** : To compute power spectral density and corresponding frequency

       Input : Time domain data X(t)

       Output : P
       - Read the signal X(t)
       - Crop the signal and get the length N
       - Supply sampling frequency, f_s
       - Do fast Fourier transformation of the signal

         Xk = fft(X(1:N), f_s);
       - Compute power spectral density and corresponding frequency by

         P = Xk.*conj(Xk) / N;

         f = fs*(1:f_s)/N;

NML PUBLICATIONS

CSIR-National Metallurgical Laboratory (NML) has recently published the following Scientific & Technical books. The year of publication and the price fixed has been shown in the parenthesis respectively. The request for procurement of publication is to be made to the Director, CSIR-National Metallurgical Laboratory, Jamshedpur - 831 007, India (e-mail : director@nmlindia.org) along with the Bank Draft in Favour of Director, NML Jamshedpur, payable at State Bank of India, NML Branch (Code No. 3329) Jamshedpur, India.

1. ***Electronic Waste*** (Eds. R. Singh, A. Das, K.K. Bhattacharyya and N.G. Goswami)	(2010)	(Rs. 950/-, US $100)
2. ***Remaining Life Assessment of Aged Components in Thermal Power Plants and Petrochemical Industries*** (Eds. A.K. Ray, S. Chaudhuri, N.G. Goswami and R.N. Ghosh)	(2008)	(Rs. 950/-, US $100)
3. ***Agglomeration and Charaterization of Iron Bearing Raw Materials*** (Eds. D. Bandyopadhyay, M.C. Goswami, N.G. Goswami and G.K. Mandal)	(2008)	(Rs. 800/-, US $100)
4. ***Extraction of Non-ferrous Metals and their Recycling*** (Eds. R.K. Jana, Abhilash and N.G. Goswami)	(2008)	(Rs. 800/-, US $100)
5. ***Proceedings of the National Workshop on Coal Processing in Hindi*** (Eds. : R. Singh, R.P. Bhagat, (Eds. : R. Singh, R.P. Bhagat, Avimanyu Das, K.K. Bhattacharyya, P.N. Mishra and N.G. Goswami)	(2007)	(Rs. 700/-, US $90)
6. ***Processing of Iron ore*** (Eds. R. Singh, Avimanyu Das and N.G. Goswami)	(2007)	(Rs. 800/-, US $100)
7. ***Special Metal Casting and Forming Processes*** (Eds. K.L. Sahoo, G.K. Mandal, N.G. Goswami and Sukomal Ghosh)	(2007)	(Rs. 800/-, US $100)
8. ***Advanced Gravity Sepration*** (Eds. : R. Singh, A. Das and N.G. Goswami)	(2007)	(Rs. 600/-, US$ 70)
9. ***Synergy of R&D and Marketing*** (Eds. : P.N. Chaudhury, N.V. Satyanarayana, A.Seshu Kumar & N.G. Goswami)	(2003)	(Rs. 800/-, US$ 100)
10. ***Metallurgy in India - A retrospective*** (Eds. : P. Ramachandra Rao and N.G. Goswami)	(2001)	(Rs. 1500/-, US$110)
11. ***Recent Trends in Structural Integrity Assessment*** (Eds. : V.R. Ranaganath, S. Tarafder and Aruna Bahadur)	(2001)	(Rs. 850/-, US$ 100)
12. ***Processing of Fines*** (Eds. : P. Bhattacaryya, R. Singh & N.G. Goswami)	(2000)	(Rs. 1200/-, US$ 115)
13. ***Non Ferrous Metals and Materials*** (Eds. : D.M. Chakrabarti, R.K. Jana, V. Kumar B.D. Pandey & N.G. Goswami)	(2000)	(Rs. 700/-, US$ 100)
14. ***Non Ferrous Extractive Metallurgy in the New Millennium*** (Eds. : P. Ramachandra Rao, Rakesh Kumar, S. Srikanth & N.G. Goswami)	(1999)	(Rs. 1200/-, US$ 115)
15. ***Environmental & Waste Management in Iron & Steel Industries*** (Eds. : A. Bandopadhyay, N.G. Goswami & P. Ramachandra Rao)	(1999)	(Rs. 800/-, US$ 100)
16. ***Fly Ash Utilisation for Value Added Products*** (Eds. : B. Chatterjee, K.K. Singh & N.G. Goswami)	(1999)	(Rs. 600/-, US$ 80)
17. ***Materials Characterization Techniques — Principles and Applications*** (Eds. : G. Sridhar, S. Ghosh Chowdhury & N.G. Goswami)	(1999)	(Rs. 1000/-, US$ 110)
18. ***Environmental & Waste Management in Non-Ferrous Industries*** (Eds. : A. Bandopadhyay, N.G. Goswami & P. Ramachandra Rao)	(1998)	(Rs. 700/-, US$ 100)
19. ***Modern Methods of Chemical Analysis for Minerals, Metals Refractory Materials & Environmental Pollutants*** (Eds. : S.C. Srivastava, K.K. Padhi, L.P. Pandey & N.G. Goswami)	(1998)	(Rs. 300/-, US$ 30)
20. ***Composite Materials*** (Eds. : R.R. Bhat, S. Ghosh & C.S.S. Krishna)	(1998)	(Rs. 500/-, US$ 70)
21. ***Nondestructive Evaluation of Materials*** (Eds. : A. Mitra, N. Parida, D.K. Bhattacharya & (N.G. Goswami)	(1997)	(Rs. 800/-, US$ 100)
22. ***Ferro-Alloys Industreis in the Liberalised Economy*** (Eds. : A.K. Vaish, S.D. Singh, N.G. Goswami & P. Ramachandra Rao)	(1997)	(Rs. 600/-, US$ 80)
23. ***Processing of Fines*** (Eds. : P. Bhattacaryya, R. Singh, K.V. Rao and N.G. Goswami)	(1997)	(Rs. 1000/-, US$ 110)
24. ***Failure Analysis*** (Eds. : S.R. Singh, N. Parida, D.K. Bhattacharya & N.G. Goswami)	(1997)	(Rs. 800/-, US$ 100)
25. ***Computer Applications in Materials & Metallurgical Engineering*** (Eds. : R.N. Ghosh, S. Tarafder & N.G. Goswami)	(1996)	(Rs. 700/-, US$ 100)
26. ***Transport Phenomena in Metallurgical Processes*** (Eds. : S. Prakash & P. Ramachandra Rao)	(1996)	(Rs. 850/-, US$ 100)
27. ***Environmental & Waste Management in Metallugical Industries*** (Eds. : A. Bandopadhyay, N.G. Goswami & P. Ramachandra Rao)	(1996)	(Rs. 700/-, US$ 100)
28. ***Modern Methods of Chemical Analysis for Minerals, Metals, Refractory Materials & Ferro-alloys*** (Eds. : S.C. Srivastava, L.P. Pandey & N.G. Goswami)	(1996)	(Rs. 650/-, US$ 70)
29. ***Boiler Corrosion*** (Eds. : I. Chattoraj, I. Singh, S.K. Narang, D.D.N. Singh & N.G. Goswami)	(1995)	(Rs. 500/-, US$ 70)
30. ***Alternative Charge Materials for Electric Arc & Induction Furnaces*** (Eds. K.N. Gupta, K.K. Mishra, K.K. Singh, A.K. Vaish, S.D. Singh, D. Bandopadhyay & N.G. Goswami)	(1994)	(Rs. 500/-, US$ 70)

ISSN 0974-1267 (Online)
ISSN 0972-4257 (Print)

Published by
CSIR-National Metallurgical Laboratory
Jamshedpur - 831007, Jharkhand, India
www.nmlindia.org